le cnam

University of Salerno
&
Conservatoire national des arts et métiers

PHD SCHOOL IN INDUSTRIAL ENGINEERING (UNISA) - Cycle XXXVIII
ÉCOLE DOCTORALE SCIENCES DES MÉTIERS DE L'INGÉNIEUR (CNAM)

Department of Industrial Engineering (UNISA)
&
Laboratoire de Mécanique des Structure et des Systèmes Couplés (LMSSC/CNAM)

Field of Study: **Industrial Engineering**
Specialization: **Mechanical Engineering**

Doctoral Thesis in :

Isogeometric approaches for fluid–structure coupling in vibroacoustic

Doctoral Thesis of:
Candidate : **LANDI Tommaso**

Supervised by:
Professor **CITARELLA Roberto,** UNISA
Professor **DEÜ Jean-François,** CNAM

and co-supervised by :
PhD **HOAREAU Christophe,** CNAM

Sommario

La presente tesi di dottorato propone una metodologia unificata per l'analisi vibroacustica basata sull'*Analisi Isogeometrica* (IGA), con l'obiettivo di integrare in modo diretto la fase di progettazione geometrica e quella di simulazione numerica. L'interesse scientifico e industriale di tale approccio risiede nella possibilità di superare le limitazioni intrinseche dei metodi tradizionali, come il *Metodo agli elementi finiti* (FEM) e il *metodo agli elementi di contorno* (BEM), che spesso soffrono di errori geometrici, discontinuità di campo e costi computazionali elevati.

La tesi sviluppa un quadro teorico e computazionale completo che coniuga fedeltà geometrica, efficienza numerica e integrazione software di modellazione (CAD), delineando un percorso di ricerca che va dai fondamenti fisico-matematici fino alle applicazioni industriali. Dopo aver definito le equazioni che governano i fenomeni vibroacustici e la relativa formulazione variazionale, il lavoro introduce una rappresentazione isogeometrica rigorosa dei campi strutturali e acustici, evidenziando come la continuità elevata delle funzioni NURBS permetta di ottenere soluzioni a più alto grado di continuità rispetto ai modelli FEM equivalenti.

Uno dei contributi centrali consiste nell'applicazione di un approccio ridotto su base modale, che consente di descrivere il comportamento vibroacustico accoppiato tramite un numero limitato di forme modali. Tale tecnica permette una drastica riduzione del costo computazionale, mantenendo elevata la fedeltà del modello rispetto alla soluzione a pieno ordine (FOM), come dimostrato dai confronti numerici sistematici con IGA e FEM.

Un secondo asse innovativo riguarda l'integrazione diretta tra CAD e IGA, perseguita attraverso un approccio immersivo di raffinamento adattativo basato su spline gerarchiche (HB-splines). In particolare, viene proposta una metodologia per la ricostruzione volumetrica del dominio fluido a partire dalle rappresentazioni di contorno CAD (B-Rep), che consente di estendere la descrizione

geometrica bidimensionale a un modello volumetrico compatibile con l'analisi isogeometrica. Il dominio così generato viene poi accoppiato a un modello strutturale di tipo Kirchhoff–Love, ottenendo un flusso di lavoro completamente automatizzato CAD-to-IGA.

La parte finale della tesi dimostra la validità e la versatilità del metodo attraverso applicazioni in ambiti industriali, in cui l'IGA immersa viene direttamente applicata su modelli CAD reali. I risultati confermano non solo la superiorità dell'IGA in termini di accuratezza nel rappresentare la dinamica del sistema, ma anche la fattibilità di un'integrazione effettiva tra progettazione e analisi, riducendo i tempi di modellazione e aumentando la robustezza del processo simulativo.

Nel suo complesso, la tesi rappresenta un contributo metodologico e applicativo originale nel campo della vibroacustica computazionale, dimostrando come l'Analisi Isogeometrica possa costituire un ponte efficace tra CAD e simulazione numerica. La ricerca apre la strada verso una nuova generazione di strumenti per l'ingegneria vibroacustica, capaci di combinare precisione geometrica, efficienza numerica e integrazione diretta con l'ambiente di progettazione industriale.

Parole chiave : Analisi Isogeometrica, Analisi agli elementi finiti, Vibroacustica computazionale, Accoppiamento struttura–fluido, Integrazione CAD–Analisi, Proiezione su base modale, Simulazione ingegneristica avanzata.

Résumé

Cette thèse de doctorat propose une méthodologie numérique pour les problèmes vibroacoustiques basée sur l'Analyse Isogéométrique (IGA), dans l'objectif d'intégrer directement les phases de conception géométrique et de simulation numérique. L'intérêt scientifique et industriel de cette approche réside dans sa capacité à surmonter les limites intrinsèques des méthodes traditionnelles telles que la Méthode des Éléments Finis (FEM) et la Méthode des Éléments de Frontière (BEM), qui souffrent souvent de difficultés liées à la reconstruction géométrique et à des coûts de calcul élevés. Après avoir défini les équations locales qui gouvernent les phénomènes vibroacoustiques et les formulations variationnelles associées, le travail introduit une représentation isogéométrique rigoureuse des champs de déplacement côté structure et champs de pression côté fluide acoustique, mettant en évidence la manière dont la continuité des fonctions NURBS permet d'obtenir des solutions plus régulières et plus précises que celles fournies par des modèles FEM équivalents. L'une des principales contributions réside dans l'application d'approches de reduction sur bases modales, qui permettent de décrire le comportement vibroacoustique couplé à l'aide d'un nombre limité de modes. Cette technique garantit une réduction drastique du coût de calcul tout en conservant une grande fidélité par rapport à la solution d'ordre complet, comme le démontrent les comparaisons numériques systématiques menées en IGA et en FEM. Une deuxième contribution novatrice concerne l'intégration directe entre la CAO et l'IGA, réalisée au moyen d'une stratégie de raffinement adaptatif immergé basée sur les B-splines hiérarchiques (HB-splines). En particulier, une méthodologie est proposée pour la reconstruction volumique du domaine fluide à partir de représentations frontières CAO (B-Rep), permettant d'étendre une description géométrique bidimensionnelle en un modèle volumique compatible avec l'analyse isogéométrique. Le domaine reconstruit est ensuite couplé à un modèle structurel de coque de Kirchhoff–Love, aboutissant à une chaîne de traitement automatisée, de la CAO à l'IGA. La dernière partie de la thèse démontre la validité et la polyvalence de la méthode à travers des

applications à des géométries complexes, dans lesquels l'IGA immergée est appliquée directement à des modèles CAO réels. Les résultats confirment une intégration efficace entre conception et analyse vibroacoustique, réduisant le temps de modélisation et renforçant la robustesse du processus de simulation. Dans l'ensemble, la thèse constitue une contribution méthodologique et applicative originale dans le domaine de la vibroacoustique numérique, montrant comment l'Analyse Isogéométrique peut servir de passerelle efficace entre la CAO et la simulation numérique. Ce travail ouvre la voie à une nouvelle génération d'outils d'ingénierie vibroacoustique capables de combiner précision géométrique, efficacité numérique et intégration directe dans l'environnement de conception industriel.

Mots-clés: Analyse Isogéométrique, Méthode des Éléments Finis, Vibroacoustique numérique, Couplage fluide–structure, Intégration CAO–Analyse, Réduction modale, Simulation d'ingénierie avancée.

Abstract

This PhD thesis proposes a numerical methodology for vibroacoustic problems based on Isogeometric Analysis (IGA), with the aim of directly integrating the geometric design and numerical simulation stages. The scientific and industrial relevance of this approach lies in its ability to overcome the intrinsic limitations of traditional methods such as the Finite Element Method (FEM) and the Boundary Element Method (BEM), which often suffer from a complex geometric reconstruction and high computational costs. After defining the local governing equations of vibroacoustic phenomena and the associated variational formulation, the work introduces a rigorous isogeometric representation of structural and acoustic fields, highlighting how the high continuity of NURBS functions enables smoother and more accurate solutions compared to equivalent FEM models. One of the main contributions lies in the application of reduced-order modal approaches, allowing the coupled vibroacoustic behaviour to be described through a limited number of modes. This technique guarantees a drastic reduction in computational cost while maintaining high model fidelity with respect to the full-order solution, as demonstrated by systematic numerical comparisons with both IGA and FEM. A second innovative contribution concerns the direct integration between CAD and IGA, pursued through an immersed adaptive refinement approach based on hierarchical B-splines (HB-splines). In particular, a methodology is proposed for the volumetric reconstruction of the fluid domain starting from CAD boundary representations (B-Rep), enabling the extension of a two-dimensional geometric description into a volumetric model compatible with isogeometric analysis. The reconstructed domain is then coupled with a Kirchhoff–Love structural shell model, achieving an automated CAD-to-IGA workflow. The final part of the thesis demonstrates the validity and versatility of the method through applications to complex geometries, in which immersed IGA is directly applied to real CAD models. The results confirm an effective integration between design and vibro-acoustic analysis reducing modeling time and enhancing the robustness of the simulation process. Overall, the thesis represents an original

methodological and applicative contribution to the field of computational vibroacoustics, showing how Isogeometric Analysis can serve as an effective bridge between CAD and numerical simulation. This research paves the way for a new generation of vibroacoustic engineering tools capable of combining geometric precision, numerical efficiency, and direct integration within the industrial design environment.

Keywords: Isogeometric Analysis, Finite Element Method, Computational Vibroacoustics, Fluid–Structure Coupling, CAD–Analysis Integration, Projection on the Modal Basis, Advanced Engineering Simulation.

Contents

List of Tables

List of Figures

Chapter 1

General introduction and goals

This chapter introduces the context, objectives, and structure of the PhD thesis. The research focuses on the development of a comprehensive methodology for vibroacoustic analysis based on Isogeometric Analysis (IGA) and its direct integration with Computer-Aided Design (CAD) representations. After discussing the industrial relevance of vibroacoustic simulations and the limitations of traditional Finite Element and Boundary Element Methods, the chapter outlines how IGA can overcome these issues by unifying the design and analysis stages through CAD-compatible spline functions. The objectives of the work are presented, to enhance vibroacoustic modeling accuracy, reduce computational costs through model reduction techniques, and enable CAD-to-IGA integration using immersed approaches. Finally, the overall organization of the thesis is described, summarizing the contents of each part and highlighting their respective contributions to achieving a seamless design-through-analysis workflow.

Content

1.1 Context of the PhD thesis

Vibroacoustic analysis plays a crucial role in several industries, such as automotive [1, 5], aerospace [6, 7], naval [8], and railway [9] engineering. Acoustic comfort, the subjective perception of interior noise levels and their impact on occupants' well-being, and vibration reduction are both essential factors for product quality and reliability. Accurate vibroacoustic predictions (e.g. coupled vibroacoustic analysis or the noise computed on a frequency range) are necessary for improving passenger comfort, reducing noise emissions, and optimizing lightweight structures. Usually, vibroacoustic simulations are performed using the Finite Element Method (FEM) [1, 5], or, the Boundary Element Method (BEM) [10]. While these approaches are well-established and widely adopted in industrial contexts [11, 12], they suffer from several well-known limitations when applied to complex real-world geometries:

- the need for a complex and time-consuming *meshing* process, particularly when working with Computer-Aided Design (CAD) models generated by industrial design software;
- difficulties in handling highly complex domains, such as internal acoustic cavities with intricate shapes and fluid–structure interfaces, as highlighted in Figure 1.1;
- high computational costs for large-scale three-dimensional problems, with billions of degrees of freedom (DOFs);
- frequency limitations of FEM, since the method is restricted to a given range of wavelengths relative to the mesh discretization.

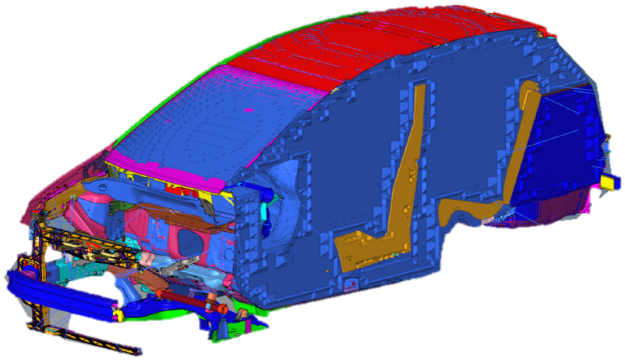

Figure 1.1: Fluid-structure interaction problem in the automotive field [1].

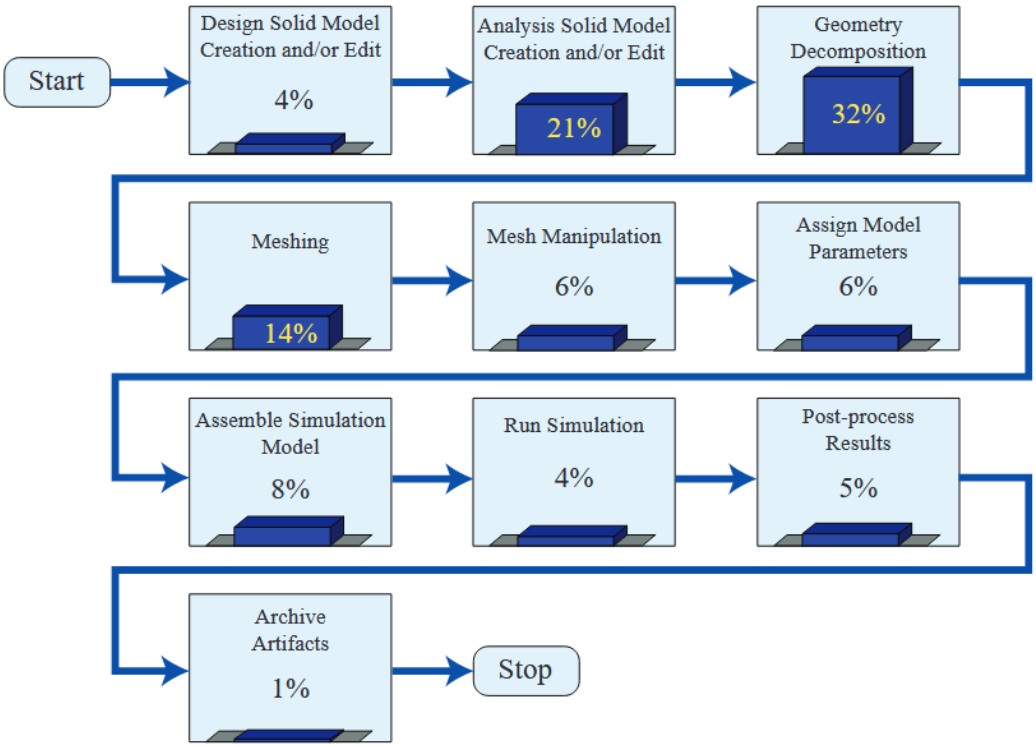

Figure 1.2: Estimation of the relative time costs of each component of the model generation and analysis process at Sandia National Laboratories. Figure from [2].

Over the past decade, the emergence of *Isogeometric Analysis* (IGA) has opened new opportunities for addressing some of these challenges [2]. IGA offers an efficient and accurate alternative to the traditional FEM by using the same mathematical representations, such as Non-Uniform Rational B-Spline (NURBS) or B-splines, employed in CAD to describe both geometry and solution fields. This strong connection between design and analysis stages has the potential to eliminate costly intermediate steps and significantly streamline the simulation workflow, as highlighted in Figure 1.2.

However, a key limitation persists: most commercial CAD systems are based on Boundary Representation (B-Rep) models, which describe only the external surfaces of an object and lack volumetric information [13, 14]. For certain applications, such as the analysis of acoustic cavities, it is essential to evaluate the acoustic field within the enclosed volume, as illustrated in Figure 1.1, typically expressed in terms of the Sound Pressure Level (SPL). This analysis requires access to the internal geometry, since the absence of volumetric data prevents a direct acoustic simulation.

In some cases, however, alternative methods such as the Boundary Element Method (BEM) can be employed, as they only require a surface mesh and do not depend on the volumetric discretization. Nevertheless, BEM formulations present other challenges, including a higher computational cost, since the resulting operators are frequency-dependent and lead to fully populated system matrices, making them less efficient for large-scale or broadband analyses.

1.2 Objectives and content

The present PhD work aims to overcome the aforementioned limitations by developing a fully integrated methodology bridging CAD and numerical vibroacoustic analysis. Beyond theoretical developments, it provides numerical tools and workflows applicable for industrial shapes, following a direction similar to recent approaches in CAD-to-analysis integration, as exemplified by Coreform Flex [15].

This PhD work has several objectives: first, to assess the effectiveness of IGA for vibroacoustic problems; second, to apply modal-based Reduced Order Models (ROM) within the IGA framework, further accelerating the solution of large-scale systems; and third, to leverage on immersed approach to seamlessly integrate CAD geometries with IGA discretizations. This approach enables the automatic generation of a volumetric representation starting solely from the boundary surfaces provided by a CAD model. Thanks to the local refinement capabilities of Hierarchical B-splines (HBs), the computational effort can be focused on the most critical regions of the domain, maintaining high accuracy while controlling the overall number of degrees of freedom.

Once the acoustic cavity has been reconstructed, it can be naturally coupled with a structural model described by the Kirchhoff–Love (KL) shell theory to simulate fluid–structure interaction (FSI) problems. This KL-based coupling represents the first approach adopted in this work; however, alternative strategies are also possible. For instance, both the structure and the acoustic cavity can be built using the Immersed IGA framework, allowing a fully volumetric 3D representation and a consistent coupling between the fluid and the structure.

This coupling is particularly relevant in the automotive sector, where thin panels such as doors, roofs, and dashboards have a strong influence on the acoustic behaviour of the cabin. The developed workflow significantly reduces preprocessing times and simplifies model preparation, making it well-

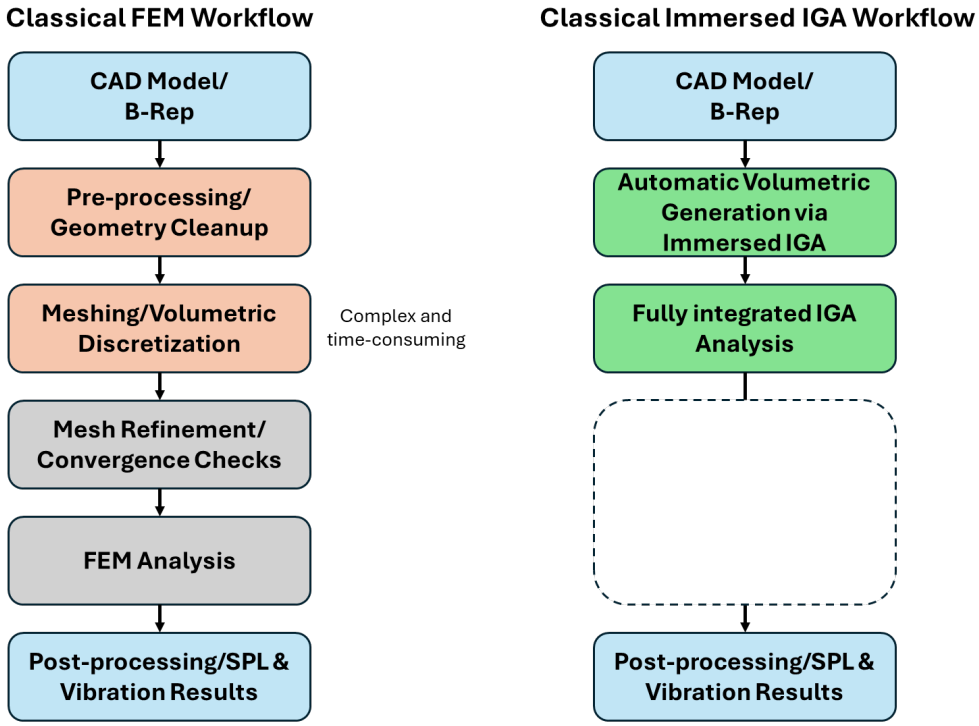

Figure 1.3: From the CAD to analysis: FEM and Immersed IGA workflow

suited for iterative design processes where multiple configurations must be analysed and optimized as shown in Figure 1.3.

Beyond these general objectives, the thesis also introduces two major original contributions to the vibroacoustic simulation community:

- **the first 3D comparison** in vibroacoustic between IGA, FEM, and a semi-analytical reference solution for coupled modal analysis, accompanied by a fully reproducible implementation and open-access code;
- **the first application of Immersed IGA to vibroacoustic problems**, a computationally demanding task that required dedicated algorithmic developments, the corresponding code will be released once the associated publication is completed.

These contributions mark an important step toward the broader integration and practical use of IGA technologies in industrial workflows and beyond.

In summary, this thesis has two primary objectives:

1. to evaluate the benefits of the Isogeometric Analysis (IGA) framework over the traditional FEM approach for vibroacoustic problems in terms of accuracy and computational efficiency;

2. to establish a robust and streamlined workflow that connects CAD representations to IGA-based vibroacoustic simulations, enabling direct analysis of complex geometries in real industrial scenarios.

1.3 Thesis structure

This PhD thesis is organized into two main parts:

- **Vibroacoustic numerical model using IGA with conformal NURBS-suitable analyses**:
  Conformal NURBS-suitable analyses are computational techniques that employ Non-Uniform Rational B-Splines (NURBS) to represent complex geometries in a manner that preserves local angles and shapes. These analyses ensure that the NURBS liines,surfaces and volumes are appropriately parametrized and refined to maintain geometric accuracy and smoothness, which is essential for precise simulations and analyses in engineering and computer-aided design (CAD). The visual explanation of Conformal NURBS-suitable analyses is shown in Figure1.4.

  This first part focuses on the use of B-splines and NURBS for structural, acoustic, and vibroacoustic analyses. It provides the necessary theoretical background, including the governing equations and their variational formulations, and serves as an initial assessment of the advantages of using B-spline- and NURBS-based representations in numerical simulations.
  This part is structured into five chapters:

  - *State of the art of IGA with conformal NURBS-suitable analyses*: presents the state of the art on the use of NURBS functions in numerical analysis;
  - *Governing equation and variational formulation of the internal vibroacoustic problem*: introduces the main governing equations, both in their strong and weak (discretized) forms; moreover it describes the discretization of a vibroacoustic problem using both the isoparametric and isogeometric approaches, highlighting the differences between them;
  - *Reduced order model by projection on modal basis*: presents a model reduction technique employing a modal approach, which significantly reduces computational costs;

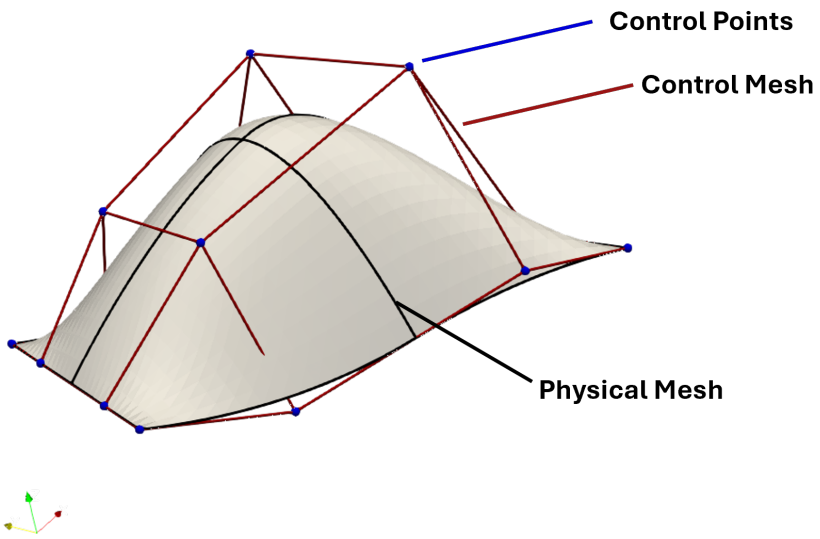

Figure 1.4: NURBS surface (the smooth, curved surface) and its control mesh (the network of blue points and red lines). The control mesh influences the shape of the NURBS surface, and ensuring that this mesh is conformal for accurate analysis and simulation.

  - *IGA vs FEM: 3D numerical examples*: provides two 3D case studies comparing the standard isoparametric approach with the isogeometric one, emphasizing differences in accuracy and computational efficiency;
  - *Conclusion of IGA with conformal NURBS-suitable analyses*: discusses the main results obtained in the first part of the work. Furthermore, the main limitations are discussed, thereby justifying the second part of the manuscript.

- **Vibroacoustic approach using immersed IGA from B-REP CAD/CAE integration**:

  The second part addresses the direct integration between Isogeometric Analysis (IGA) and Computer-Aided Design (CAD), describing the complete workflow required to achieve seamless CAD–CAE interoperability. It also presents the coupling between acoustic and structural domains within an immersed IGA framework.

  This part is divided into five chapters:

  - *State of the Art in CAD-Integrated Isogeometric Analysis*: reviews the state of the art related to the second part of the thesis, highlighting the main techniques proposed in the

literature for reconstructing a 3D volume starting solely from its boundary description;

- *Hierarchical B-Spline approach*: details the methodology developed in this work to reconstruct a three-dimensional volume from its boundary representation;
- *3D coupling strategy*: explains how to couple a volume obtained through the Immersed IGA approach with a structural model formulated according to the Kirchhoff–Love theory;
- *Numerical examples for industrial applications*: presents several numerical examples that demonstrate the applicability of the proposed approach to industrial cases;
- *Conclusion of CAD-integrated isogeometric analysis*: discusses the main results achieved in the second part of the work.

- **Final conclusion and future perspectives**: discusses the final conclusions of the thesis, the open challenges, and the possible directions for future research.

1.4 Graphical abstract

This section provides a graphical overview of the fundamental components of the PhD research. Figure 1.5 illustrates the overall context and the key ingredients of the work, including the use of a modal-based reduced-order approach, the NURBS-suitable formulation, and hierarchical B-splines. Figure 1.6 presents the main computational tools employed throughout the research and the quantities of interest obtained as outputs from the developed framework.

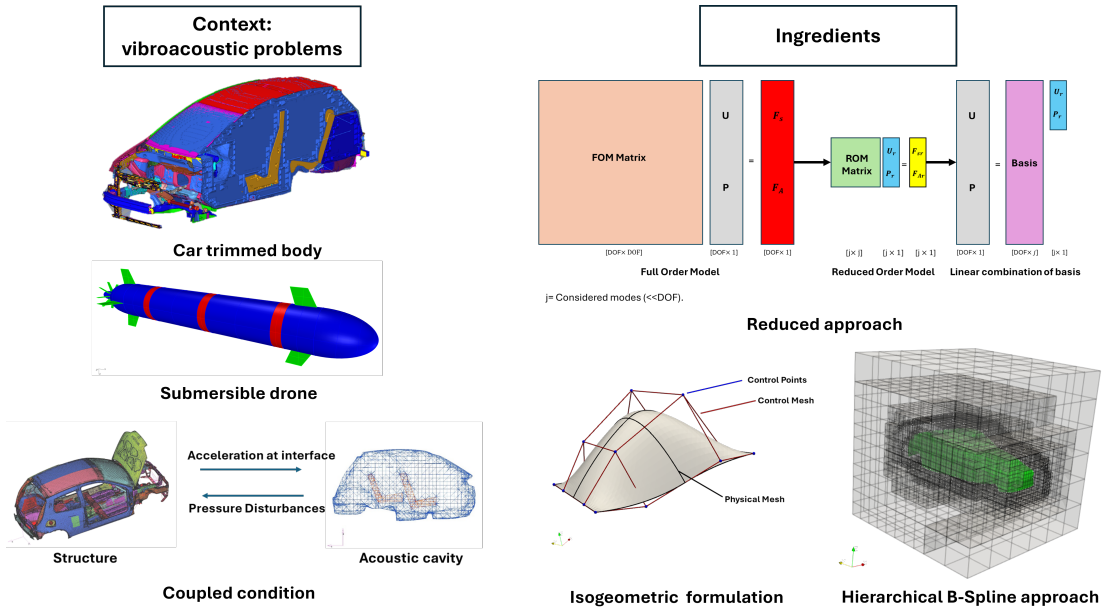

Figure 1.5: Graphical summary of the research context and main ingredients of the thesis: modal-based model reduction, NURBS-suitable analysis, and hierarchical B-splines.

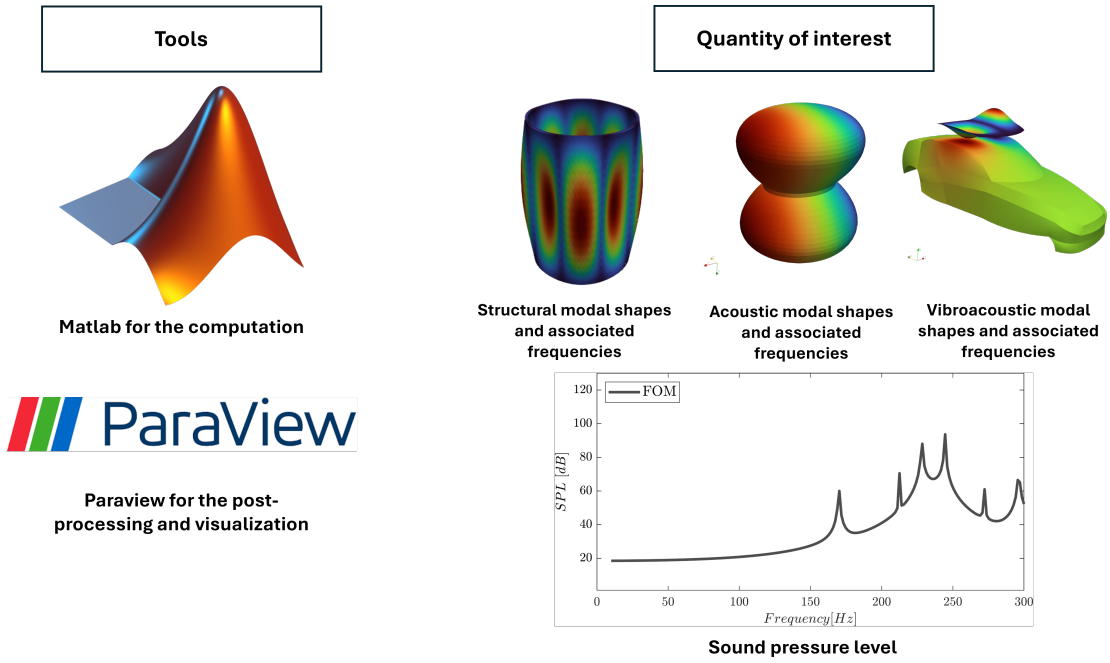

Figure 1.6: Overview of the computational tools and quantities of interest adopted in the developed CAD-integrated vibroacoustic framework.

Part I

Vibroacoustic numerical model using IGA with conformal NURBS-suitable analyses

Chapter 2

State of the art of IGA with conformal NURBS-suitable analyses

This chapter provides a comprehensive overview of the current state of the art in the numerical modeling of vibroacoustic systems, with a particular focus on Isogeometric Analysis (IGA) and conformal NURBS-suitable formulations. Starting from the historical evolution of computational methods for structural–acoustic coupling, the discussion highlights some limitations of traditional Finite Element Method (FEM) approaches and introduces the theoretical foundations and advantages of IGA in terms of geometric exactness, continuity, and spectral accuracy. The chapter then presents the mathematical formulation of NURBS-based basis functions and their use in geometry discretization, establishing the link between CAD representations and numerical analysis. Emerging spline technologies and refinement strategies are reviewed, providing a broader context for recent methodological developments. Finally, the existing research gap in vibroacoustic applications is identified, motivating the comparative analyses and novel contributions developed in this PhD work. Overall, this chapter serves as both a theoretical foundation and a literature review, preparing the ground for the subsequent derivation of the governing equations, variational formulations, and numerical implementations of coupled vibroacoustic problems using IGA and FEM.

Content

2.1 Vibroacoustic modelling: motivation and challenges

The first part of this PhD thesis focuses on the vibroacoustic modeling of coupled structural–acoustic systems using Conformal NURBS-suitable analyses [2]. This research builds upon and extends previous work on vibroacoustic problems, with an emphasis on comparing Isogeometric Analysis (IGA) and the Finite Element Method (FEM) in terms of accuracy, computational efficiency, and suitability for three-dimensional applications [16]. Let assume that the structure is elastic, isotropic, and homogeneous, and that the surrounding fluid (a gas) is compressible, homogeneous, inviscid, and free of viscosity-related dissipative effects.

The study of vibroacoustic problems is crucial in fields such as automotive [1, 17] and aerospace engineering [7, 18], where structural components interact with surrounding fluids, requiring coupled analysis techniques [19, 20, 21, 22, 23, 24].

The reduction of unwanted vibrations is the key in the most of vibroacoustic problems and the damping mechanisms and vibration control strategies have been extensively investigated in [25, 26, 27, 28, 29, 30, 31]. Common computational approaches include the Finite Element Method (FEM) and the Boundary Element Method (BEM). FEM, in particular, is widely used in industrial applications [32, 33, 17] thanks to its strong mathematical foundations, supported by well-established convergence proofs, and its long-standing implementation in commercial and open-source software. Over the years, extensive developments have facilitated its integration into industrial design and simulation workflows. However, despite these advantages, FEM still faces significant challenges when dealing with complex geometries: its meshing process can be cumbersome and time-consuming, and the final solution accuracy often depends heavily on mesh quality and density [34]. To address these limitations, various improvements to FEM, such as Smoothed FEM (S-FEM) [35], have been proposed, introducing gradient smoothing techniques to reduce model stiffness and improve accuracy in coupled structural–acoustic problems.

Over the last decades, the modelling of coupled structural–acoustic systems has evolved considerably, moving from classical finite element approaches toward formulations capable of directly incorporating geometric information from CAD models. While FEM remains the most common choice, its limitations in handling complex geometries and achieving higher-order continuity motivated the development of new numerical frameworks designed to close the gap between CAD and analysis envi-

ronments.

2.2 Potential of Isogeometric Analysis for Natural Frequency Estimation

Isogeometric Analysis (IGA) was introduced [2] with the aim of unifying Computer-Aided Design (CAD) and numerical analysis by using the same mathematical basis functions to represent both geometry and solution fields (e.g., displacement, pressure). The approach relies on B-Splines and Non-Uniform Rational B-Splines (NURBS), the standard representation tools in CAD systems for defining complex curves and surfaces [36]. NURBS offer distinct advantages over classical Lagrange shape functions, including higher continuity, smoothness, and non-negative basis functions, making them particularly well suited for advanced engineering analyses. A detailed discussion of the CAD–analysis gap can be found in [37, 34], while practical implementations of NURBS-based analysis have been discussed in [38]. Although relatively recent, IGA has been successfully applied in several engineering domains, including structural mechanics [39], acoustics [40], electromagnetism [41], shape optimization [42, 43], fluid dynamics [44, 45, 24, 46], and fatigue damage [47], [48].

In the context of structural dynamics, IGA has shown great potential in capturing vibrational behaviour with higher accuracy, as discussed in [2] and illustrated in Figure 2.1. The example reported in this figure compares the first 1000 natural pulsations of a simply supported rod in traction/compression, computed using both IGA and FEM for models with a comparable number of degrees of freedom (approximately 1000 in all cases). Six curves are shown: three obtained with IGA (NURBS basis with polynomial orders $p = 3$, $p = 5$, and $p = 7$) and three obtained with FEM (Lagrange polynomials of the same orders), all evaluated against the analytical reference solution. For a given polynomial order, the IGA results consistently lie closer to the analytical solution than the FEM counterparts across the full range of the first 1000 modes. Moreover, the FEM curves display characteristic irregularities—such as sudden jumps, notably around $n/N = 0.5$ for $p = 7$, which do not appear in the IGA results. This highlights the superior smoothness and accuracy of IGA in representing high-frequency modal content, even when both methods share the same number of degrees of freedom.

In summary, for an equivalent discretization effort, IGA provides significantly more accurate natural frequency predictions than FEM. This observation serves as a strong indication that the advantages

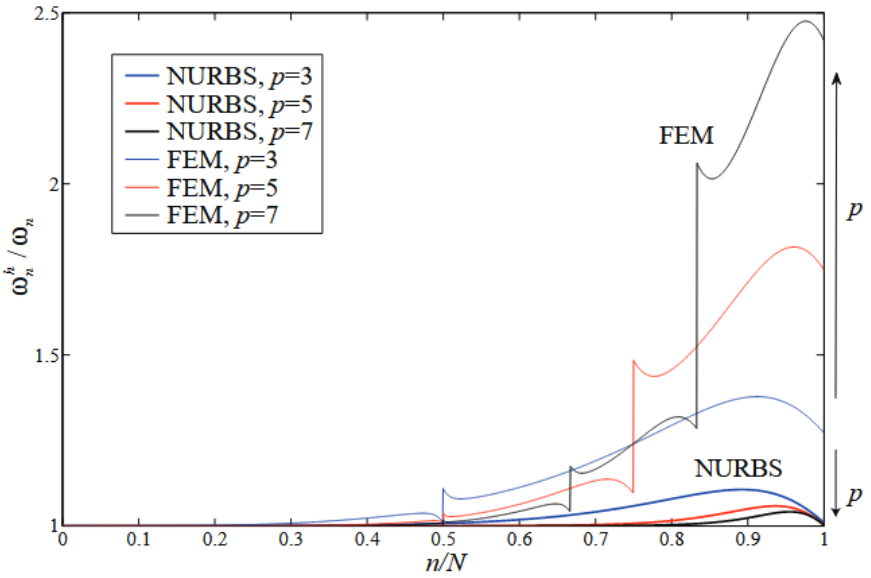

Figure 2.1: Comparison of normalized discrete spectra for a simply supported beam obtained using higher-order finite elements (FEM) and isogeometric analysis with NURBS. The plot shows the discrete eigenfrequencies for each method (mode index $n = 1, 2, \dots$), normalized for direct comparison. The analysis comes from [2].

of IGA can be extended beyond structural dynamics to vibroacoustic analysis, as will be demonstrated in the following sections.

2.3 Use of IGA in engineering application

Studies such as [49] and [50] demonstrated its improved frequency response and its ability to eliminate unwanted spectral artifacts (e.g. the jump observed in Figure 2.1). As discussed in [49] and [51], standard FEM formulations with C_0 continuity tend to diverge in the optical branches as the polynomial order increases, revealing the limitations of high-order FEM in nonlinear and dynamic applications where higher modes play a significant role. Moreover, while FEM with $p = 2$ provides stable results in the low-frequency range, higher-order FEM often diverges at medium-to-high frequencies, whereas IGA maintains accuracy across the full spectral range. Benchmark tests, including the NASA Aluminum Testbed Cylinder, have validated these findings. A related study in [52] also highlights how increased basis continuity enhances solution fidelity, particularly near singular regions. The so-called "k-method" in IGA, which combines polynomial order elevation with subsequent knot insertion, further

improves accuracy over traditional C^0-continuous approaches. Further methodological developments include the introduction of quadrature-free immersed IGA formulations [53], enabling the direct solution of partial differential equations on complex 3D CAD geometries without the need for traditional numerical integration schemes. Other innovations, such as isogeometric collocation methods [54], have reduced computational cost while maintaining accuracy by enforcing equations at collocation points. NURBS-based indirect Boundary Element Methods have also demonstrated higher convergence rates in acoustic problems compared to polynomial-based formulations [55].

Beyond NURBS, several alternative spline bases have been proposed to improve geometric flexibility and local refinement capabilities. For example, [56] developed an IGA framework for 2D linear elasticity using trimmed CAD surfaces, integrating CAD trimming data directly into the analysis process. The Bézier extraction operator introduced in [57] allows IGA formulations to be implemented within C^0 Bézier element structures, facilitating compatibility with standard FEM codes. Locally refined (LR) B-splines [58] and T-splines [59] further extend IGA's versatility by enabling adaptive local refinement for complex 2D and 3D geometries, enhancing computational efficiency.

2.4 Key findings and contributions of this work

The discussion above highlights the evolution from traditional FEM-based approaches toward isogeometric and spline-based analyses capable of bridging the CAD–analysis gap. This methodological transition enables more accurate, smooth, and geometrically consistent modelling of coupled structural–acoustic systems. The research presented in this thesis builds upon these foundations and leads to several key findings.

First, the use of IGA significantly extends the frequency range that can be accurately simulated while maintaining a comparable number of degrees of freedom to standard FEM. Thanks to the higher inter-element continuity and spectral properties of spline spaces, IGA provides improved dispersion characteristics that are particularly beneficial for dynamic and vibroacoustic analyses.

Second, a detailed comparison between semi-analytical solutions, FEM, and IGA has been conducted on a fully three-dimensional vibroacoustic problem. This comparison is performed within a projection-based reduced order modelling framework, enabling a consistent and fair assessment of accuracy, computational cost, and behaviour across methods in both the full and reduced settings.

Finally, an important contribution of this work lies in the substantial code development carried out during the project. The implementation associated with Part I of the thesis is publicly available, providing a complete NURBS-based IGA environment for vibroacoustic simulations and model reduction `vibroacoustic-iga-fem`. The software developed for Part II—which includes immersed formulations, hierarchical refinement, and CAD-integrated representations—will be released following the publication of the related scientific results.

2.5 Introduction to isogeometric discretization

In computational mechanics, the *Finite Element Method* (FEM) has been the dominant numerical framework for decades, providing accurate and robust tools for solving partial differential equations in structural, fluid, and multi-physics applications. Its theoretical maturity, numerical flexibility, and broad implementation base have established FEM as the standard approach for structural and vibroacoustic simulations [60, 61]. However, several limitations persist, particularly in relation to geometry representation, inter-element continuity, and the integration between computer-aided design (CAD) and analysis models. Classical FEM formulations rely on piecewise polynomial basis functions that are only C^0-continuous across element boundaries, as shown in Figure 2.2 which can result in numerical dispersion and loss of smoothness in problems governed by wave propagation, vibration, and acoustic coupling [34, 2]. Moreover, the need to approximate CAD geometries using meshes of linear or quadratic elements introduces additional geometric errors and requires significant preprocessing efforts, such as mesh generation, cleaning, and refinement. To overcome these challenges, the paradigm of *Isogeometric Analysis* (IGA) was introduced in [34] as a unifying framework between CAD and numerical analysis. The main idea of IGA is to employ the same basis functions used in CAD, typically Non-Uniform Rational B-Splines (NURBS), T-splines, or other spline technologies, for both the geometric representation and the field approximation. This approach eliminates the geometry–mesh inconsistency typical of FEM and allows for exact geometry representation while achieving higher global continuity of the solution space [50, 52]. IGA basis functions possess inter-element continuity up to C^{p-1}, as shown in Figure 2.3 which provides clear advantages for vibration and wave propagation problems, including vibroacoustic coupling, by reducing spurious oscillations and improving numerical dispersion characteristics [55, 51, 62]. In addition, the refinement strategies available in IGA, namely h-, p-, and k-refinement, allow for systematic enrichment of the solution

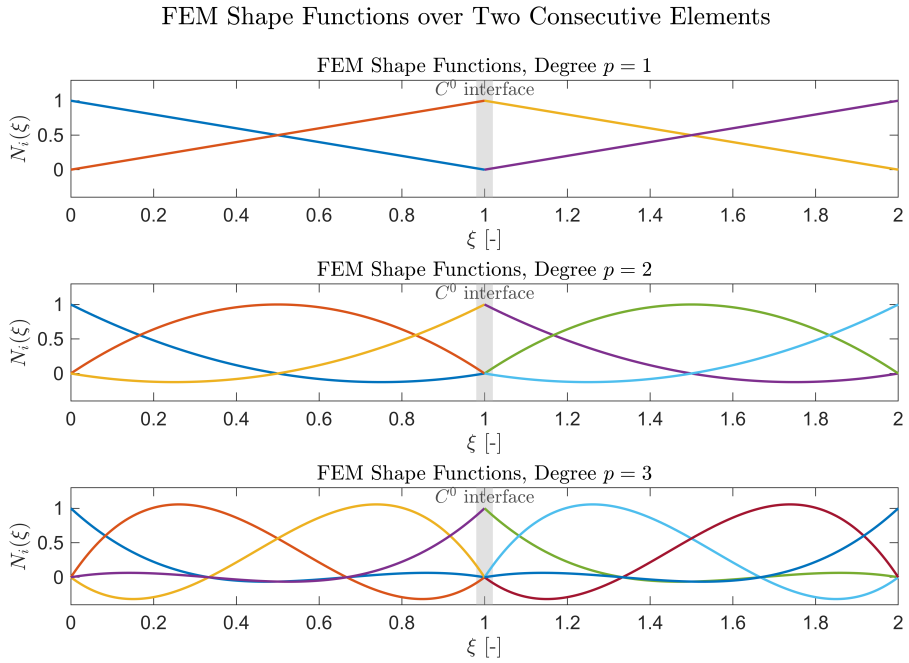

Figure 2.2: Lagrange shape functions of degree $p = 1$,2 and 3 plotted over two consecutive elements. The gray region highlights the interface between elements, where only C^0 continuity is preserved. As the polynomial degree increases, the functions become higher-order within each element, but the inter-element continuity remains limited to C^0, resulting in discontinuous derivatives across the element boundary.

space while maintaining high continuity and geometric accuracy [2]. The three refinement strategies are shown in Figure 2.4.

Despite these advantages, the IGA framework introduces specific challenges related to computational implementation. The increased coupling between degrees of freedom, arising from the smooth and extended support of spline functions, leads to denser system matrices and higher computational cost for assembling and solving linear systems [63]. Furthermore, CAD models are often defined by multiple trimmed NURBS patches, requiring special algorithms to handle non-conforming interfaces and trimmed regions [64].

The advantages of IGA for vibroacoustic and structural–acoustic coupling problems have been demonstrated in several recent studies. In [65], IGA and FEM formulations for coupled cavity–structure systems, are compared, showing that IGA achieves improved accuracy in eigenfrequency prediction with fewer degrees of freedom. In [66], the efficiency of isogeometric discretizations in fluid–structure

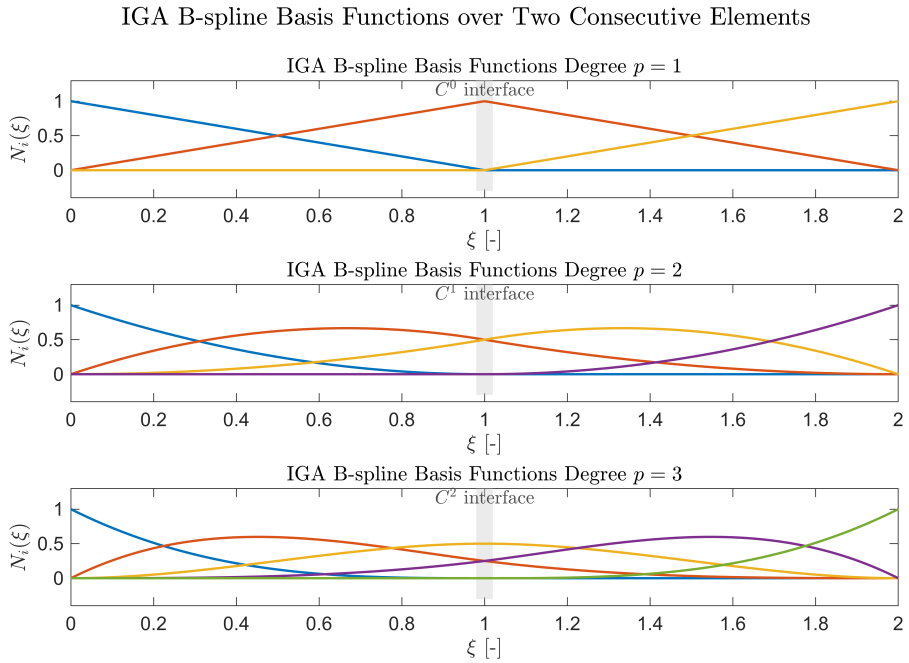

Figure 2.3: IGA B-spline basis functions of degree $p = 1$,2 and 3 plotted over two consecutive elements. The gray region indicates the interface between elements, where the functions remain smooth and continuous. Unlike the FEM case, IGA basis functions maintain up to C^{p-1} continuity across element boundaries, resulting in smoother transitions and higher regularity as the polynomial degree increases.

interaction, for a complex cavity–plate systems, is shown. Similarly, in [67] acoustic scattering problems using IGA combined with infinite elements is analysed, confirming a greater accuracy of the isogeometric basis for high-frequency regimes.

Although IGA is progressively gaining traction in structural dynamics and vibroacoustics, FEM remains predominant in industrial practice due to its mature ecosystem and well-established solver technologies. Ongoing research efforts aim to bridge this gap through efficient preconditioning [63], adaptive refinement, and direct integration of IGA capabilities into existing FEM-based solvers.

In summary, while FEM continues to serve as the reference discretization method for vibroacoustic simulations, IGA represents a promising next-generation framework capable of improving numerical precision, geometric fidelity, and continuity in coupled structural–acoustic problems. The following sections build upon this foundation to present the governing equations and variational formulations of the vibroacoustic problem, followed by their respective FEM and IGA discretizations.

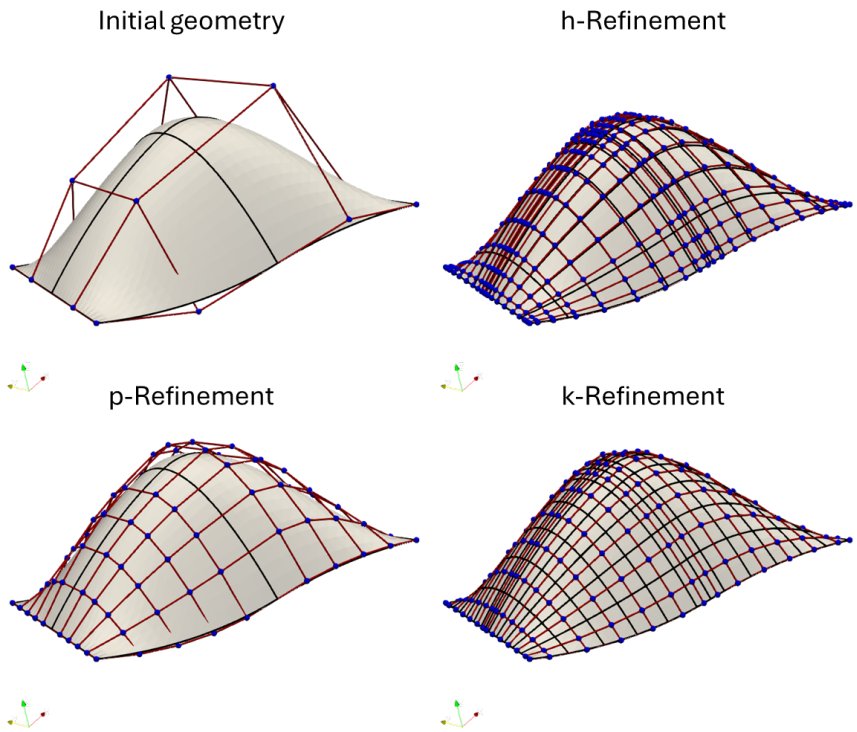

Figure 2.4: Visualization of refinement strategies on the initial geometry. Top-left: initial coarse mesh; top-right: $h-refinement$ (mesh densification); bottom-left: $p-refinement$ (polynomial degree elevation); bottom-right: $k-refinement$, combination of p and h.

2.6 Fundamentals of NURBS-based IGA

The isogeometric approach relies on the definition of NURBS and other mathematical objects. Let's introduce three knot vectors $\boldsymbol{\Xi} = \{\xi_1, \xi_2, ..., \xi_{n+p+1}\}$ with $\boldsymbol{\Xi} \in \mathbb{R}^{n+p+1}$, $\boldsymbol{\mathcal{H}} = \{\eta_1, \eta_2, ..., \eta_{m+q+1}\}$ with $\boldsymbol{\mathcal{H}} \in \mathbb{R}^{m+q+1}$ and $\boldsymbol{\mathcal{Z}} = \{\zeta_1, \zeta_2, ..., \zeta_{l+r+1}\}$ with $\boldsymbol{\mathcal{Z}} \in \mathbb{R}^{l+r+1}$. Here, the index n is the number of B-Spline functions denoted $N_{i,p}$ and the index p corresponds to the degree of the polynomial for the first parameter ξ; m represents the number of B-spline functions denoted $M_{j,q}$ and q corresponds to the degree of the polynomial for this second parameter space associated with η; l represents the number of B-spline functions denoted $L_{k,l}$ and r corresponds to the degree of the polynomial for this third parameter space associated with ζ. B-splines are functions with compact support and they constitute a partition of unity with continuity and regularity properties, as described in [2]. The 3D parametric space is defined by a tensor product of the three knot vectors. The definition of NURBS requires the definition of the weights associated with the tensor $\mathbf{W} = \{w_{i,j,k} \in \mathbb{R}, i, j, k \in [1, n] \times [1, m] \times [1, l]\}$. The

1D B-Spline basis functions $N_i^p(\xi)$ are defined recursively using the Cox-De Book recursion formula:

$$p = 0: \quad N_i^0(\xi) = \begin{cases} 1, & \xi_i \leq \xi < \xi_{i+1}, \\ 0, & \text{otherwise}, \end{cases} \tag{2.1}$$

$$p > 0: \quad N_i^p(\xi) = \frac{\xi - \xi_i}{\xi_{i+p} - \xi_i} N_i^{p-1}(\xi) + \frac{\xi_{i+p+1} - \xi}{\xi_{i+p+1} - \xi_{i+1}} N_{i+1}^{p-1}(\xi). \tag{2.2}$$

To get a NURBS basis $R_i^p(\xi)$ from this function set, a weight w_i is assigned to every B-spline function $N_i^p(\xi)$:

$$R_i^p(\xi) = \frac{N_i^p(\xi) w_i}{W(\xi)} = \frac{N_i^p(\xi) w_i}{\sum_{i=1}^{n} N_i^p(\xi) w_i} \tag{2.3}$$

where $W(\xi)$ is the weighting function.

In the same way, the 2D and 3D NURBS functions are defined as following:

$$R_{i,j}^{p,q}(\xi, \eta) = \frac{N_i^p(\xi) M_j^q(\eta) w_{i,j}}{\sum_{i_w=1}^{n} \sum_{j=1}^{m} N_i^p(\xi) M_j^q(\eta) w_{i,j}} \tag{2.4}$$

$$R_{i,j,k}^{p,q,r}(\xi, \eta, \zeta) = \frac{w_{i,j,k} N_{i,p}(\xi) M_{j,q}(\eta) L_{k,r}(\zeta)}{\sum_{i=1}^{n} \sum_{j=1}^{m} \sum_{k=1}^{l} w_{\hat{i},\hat{j},\hat{k}} N_{\hat{i},p}(\xi) M_{\hat{j},q}(\eta) L_{\hat{k},r}(\zeta)}. \tag{2.5}$$

2.7 Geometry discretization

By introducing a set of control points in 1D $\{\mathbf{B}_i \in \mathbb{R}, i \in [1, n]\}$, the geometry of a curve $\mathbf{C}(\xi)$ in the physical space is represented as a linear combination of 1D NURBS functions:

$$\mathbf{C}(\xi) = \sum_{i=1}^{n} R_i^p(\xi) \mathbf{B}_i \tag{2.6}$$

Table 2.1: Data information to generate IGA and FEM geometry

FEM	IGA
Nodes	Controls points
Elements	Weights
Polynomial order	Patches
	Knot vectors
	Polynomial order

By introducing a set of control points in 2D $\{\mathbf{B}_{i,j} \in \mathbb{R}^2, i,j \in [1,n] \otimes [1,m]\}$, the geometry of a surface $\mathbf{S}(\xi,\eta)$ in the physical space is represented as a linear combination of 2D NURBS functions:

$$\mathbf{S}(\xi,\eta) = \sum_{i=1}^{n}\sum_{j=1}^{m} R_{i,j}^{p,q}(\xi,\eta)\mathbf{B}_{i,j} \tag{2.7}$$

By introducing a set of control points in 3D $\{\mathbf{B}_{i,j,k} \in \mathbb{R}^3, i,j,k \in [1,n]\otimes[1,m]\otimes[1,l]\}$, the geometry of a solid $\mathbf{V}(\xi,\eta,\zeta)$ in the physical space is represented as a linear combination of NURBS functions:

$$\mathbf{V}(\xi,\eta,\zeta) = \sum_{i=1}^{n}\sum_{j=1}^{m}\sum_{k=1}^{l} R_{i,j,k}^{p,q,r}(\xi,\eta,\zeta)\mathbf{B}_{i,j,k} \tag{2.8}$$

The matrix $\mathbf{V}$ corresponds to the physical coordinates of one patch. The 3D IGA discretization using multiple patches is illustrated in Figure 2.5 where the *control net* and the *control points* are represented and the mapping between the reference domain to the physical one is also shown. The knots are depicted in the parametric space and the lines between them, mapped in the physical domain, constitute the edges of an IGA element where the quadrature is performed. In Figure 2.6 a physical domain and reference domain associated to FEM are illustrated for HEXA20 elements. Each element is mapped from the parametric to the physical domain. Each FEM element in the physical domain is function of the nodes positions and of the Lagrange polynomial shape functions. Table 2.1 contains all the data information needed to represent the geometry in the physical domain for both FEM and IGA. It should be noted that connectivity tables must be taken into account; see [2] for details on IGA numbering.

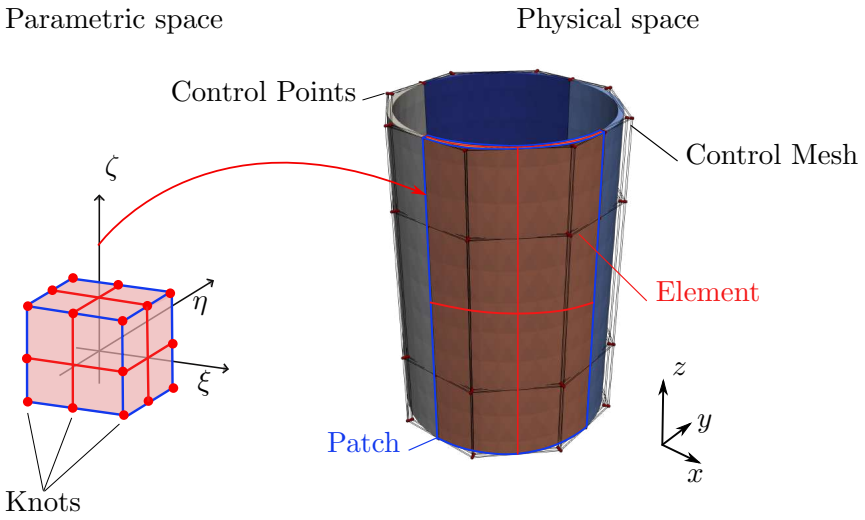

Figure 2.5: IGA mapping from the parametric to the physical space for polynomial order equal to 2

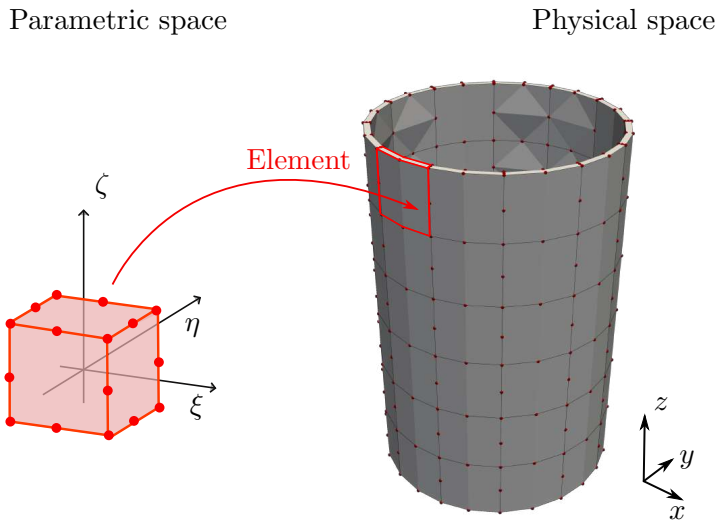

Figure 2.6: FEM mapping from the parametric to the physical space for an HEXA20 element

2.8 IGA research gap in vibro-acoustic

Despite these significant advancements, the literature do not have a 3D demonstration of IGA compared to classic 3D FEM for vibroacoustic applications. Studies such as [68], [69] have addressed vibroacoustic modeling using non-conforming interfaces in IGA, but without fully establishing its comparative advantages. Similarly, [66] examined the vibroacoustic response of a cavity–plate–exterior space system through an isogeometric framework, comparing results with experimental data. Although the findings confirm IGA's potential, inherent experimental uncertainties prevent definitive benchmarking conclusions.

The work presented in Part I of this PhD thesis aims to fill this gap by performing a detailed comparative analysis between IGA and FEM for three-dimensional vibroacoustic problems, validated against a semi-analytical reference solution derived from [70]. This benchmark problem enables a rigorous quantitative assessment of both accuracy and computational efficiency. The semi-analytical reference, based on exact analytical formulations with negligible numerical error, ensures a robust evaluation framework. This research also extends the preliminary study presented in [16], which first compare IGA performance over FEM in vibroacoustic analyses at same polynomial orders.

In contrast to prior studies primarily focused on one- and two-dimensional configurations, the present work emphasizes the benefits of IGA for fully three-dimensional structural, acoustic, and coupled vibroacoustic problems. Furthermore, a modal-based reduced-order modeling approach is introduced and integrated within the IGA framework to significantly reduce computational cost, an essential factor in large coupled systems, where reduced models are key to fast simulations [19], [71]. A related work [72] proposed an IGA–Newmark–POD approach for acoustic wave propagation, demonstrating its stability and convergence. However, existing open-source implementations [73], [74] are limited to uncoupled 1D–3D problems and do not include reduced-order modeling capabilities for coupled systems. For comparison, the study in [75] provided step-by-step FEM and IGA formulations for 1D–2D cases.

To address these limitations, a new computational framework has been developed as part of this thesis, extending the open-source code from [74]. The resulting implementation, publicly available at vibroacoustic-iga-fem, enables reproducibility, transparency, and further research in three-dimensional vibroacoustic modeling using both FEM and IGA, with and without model order reduction.

Chapter 3

Governing equation and variational formulation of the internal vibroacoustic problem

This chapter introduces the fundamental equations governing vibroacoustic phenomena, starting from the physical description of the problem and progressing from the strong form to the weak formulation. The variational framework is then developed, providing a rigorous mathematical foundation for the numerical analysis of coupled structural-acoustic systems. Key operators required for vibroacoustic modeling are introduced and discussed, establishing the theoretical basis for the isogeometric and finite element formulations presented in the subsequent chapters. This chapter serves as a reference point, ensuring a clear understanding of the underlying principles before addressing advanced numerical methodologies.

Content

3.1 Linear vibroacoustic modeling

The internal vibroacoustic problem involves the interaction between an elastic structure and an enclosed acoustic fluid. Its mathematical description requires both the governing differential equations and their corresponding variational formulations. These formulations enable accurate and computationally efficient analyses of coupled structural–acoustic systems. A fundamental reference for the theoretical foundation of such formulations is the work [76], who presented detailed variational forms for interior structural–acoustic vibration problems. Extensions of these formulations have been proposed to address damping and dissipation within internal acoustic cavities [77]. In [78] further refined weak form methods for irregular coupled structural–acoustic systems, emphasizing interface treatment and modal coupling accuracy, are shown.

Recent developments include the comparative study of finite element and isogeometric formulations [65], who analyzed the consistency and numerical convergence of vibroacoustic coupling schemes. Other spectral and variational approaches for internal vibroacoustic problems have been investigated in [62], focusing on multidomain. Isogeometric formulations of plate–cavity vibroacoustic systems were proposed in the recent study [66], highlighting the advantages of displacement–pressure coupling in the weak form. In [79] a systematic derivation of weak integral forms for educational and research applications are provided. Complementary to this, [80] discussed reduced-order modeling strategies for vibroacoustic problems derived from variational formulations.

These contributions collectively establish a comprehensive framework for the derivation, discretization, and implementation of the vibroacoustic variational formulation, forming the theoretical basis for advanced numerical methods such as FEM, BEM, and IGA.

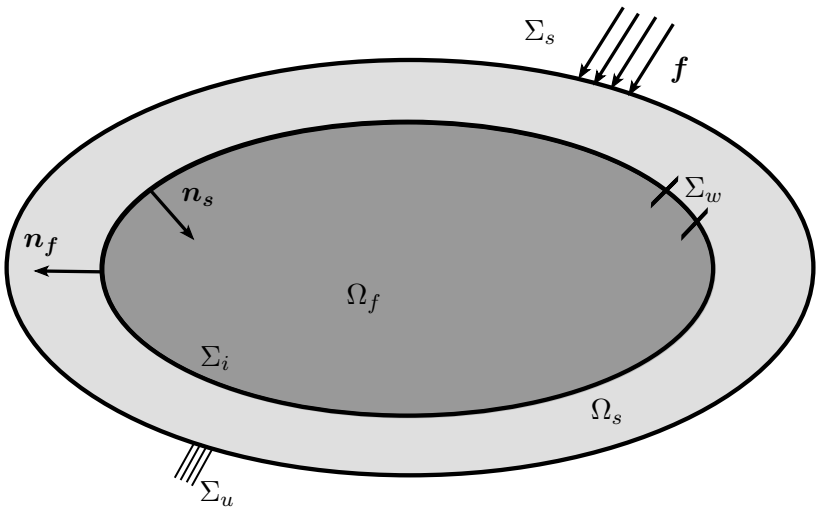

Figure 3.1: Schematization of a generic fluid-structural coupling problem

3.2 Vibroacoustic local equations

The fluid-structure interaction problem is illustrated in Figure 3.1. The problem involves an external structure and an internal fluid, with the two domains interacting at their interface. Referring to Figure 3.1, Ω_s is the structural volumetric domain, Σ_s is the structural surface with prescribed external load, Σ_u is the structural surface with prescribed displacement, Σ_i is the fluid-structure interface, Ω_f is the fluid volumetric domain, Σ_w is the fluid surface with prescribed normal velocity, $\boldsymbol{n_s}$ and $\boldsymbol{n_f}$ are the external normal vectors for the structure and fluid, respectively, and $\boldsymbol{f}$ is the external structural force. For the vibroacoustic problem, several fundamental simplifying assumptions are made. Small displacements in the structure and small fluid pressure variations are considered. All variables are described using harmonic excitations (e.g., sinusoidal), thus the formulation is directly written in the frequency domain using the angular frequency ω. The structure is assumed to be elastic, homogeneous and isotropic, with a linear relationship between stress and strain. The fluid, here a gas, is assumed to be compressible and inviscid, neglecting the dissipative effects associated with viscosity. The gravity effect has also been neglected. After applying all assumptions, it is possible to introduce the linear elastodynamics equations and the boundary conditions for the structure. The purpose is to find $\boldsymbol{u}$, the displacement vector field in $\mathbb{R}^3$, and p, the pressure field in $\mathbb{R}$, satisfying the following

structural equations:

$$\mathbf{div}\boldsymbol{\sigma}(\boldsymbol{u}) + \rho_s\omega^2\boldsymbol{u} = \mathbf{0} \quad \text{in} \quad \Omega_s \tag{3.1}$$

$$\boldsymbol{\sigma}(\boldsymbol{u})\boldsymbol{n_s} - \boldsymbol{f} = \mathbf{0} \quad \text{on} \quad \Sigma_s \tag{3.2}$$

$$\boldsymbol{\sigma}(\boldsymbol{u})\boldsymbol{n_s} + p\boldsymbol{n_s} = \mathbf{0} \quad \text{on} \quad \Sigma_i \tag{3.3}$$

$$\boldsymbol{\varepsilon}(\boldsymbol{u}) - \frac{1}{2}\left(\mathbf{grad}^{\mathrm{T}}\boldsymbol{u} + \mathbf{grad}\boldsymbol{u}\right) = \mathbf{0} \quad \text{in} \quad \Omega_s \tag{3.4}$$

$$\boldsymbol{u} = \mathbf{0} \quad \text{on} \quad \Sigma_u \tag{3.5}$$

$$\boldsymbol{\sigma}(\boldsymbol{u}) - \boldsymbol{\mathcal{C}} : \boldsymbol{\varepsilon}(\boldsymbol{u}) = \mathbf{0} \quad \text{in} \quad \Omega_s. \tag{3.6}$$

Eq. (3.1) corresponds to the dynamic equilibrium equation in the Ω_s domain involving pulsation ω and density ρ_s. Eq. (3.2) corresponds to the stress boundary conditions on a part of the edge Σ_s and ensures the balance of forces at the surface where $\boldsymbol{f}$ is a given surface stress vector. Eq. (3.3) describes the boundary conditions on the surface Σ_i that separates the structure domain Ω_s from the fluid one Ω_f and represents the coupling equation. Eq. (3.4) expresses the kinematic relationship between $\boldsymbol{u}$ and the strain $\boldsymbol{\varepsilon}$ within the solid domain. Eq. (3.5) corresponds to a homogeneous Dirichlet boundary condition on the surface Σ_u. Eq. (3.6) represents the material constitutive law and expresses the relationship between the Cauchy stress $\boldsymbol{\sigma}$ and the strain $\boldsymbol{\varepsilon}$. The notation $\boldsymbol{\mathcal{C}}$ represents a material-dependent fourth-order tensor which depends on the Young Modulus E and the Poisson ratio ν. In the following, the linear acoustic equations are presented in the absence of external acoustic sources.

$$\Delta p + \frac{\omega^2}{c_0^2}p - \boldsymbol{f} = 0 \quad \text{in} \quad \Omega_f \tag{3.7}$$

$$\mathbf{grad}p \cdot \boldsymbol{n_f} - \rho_f\omega^2\boldsymbol{u} \cdot \boldsymbol{n_f} = 0 \quad \text{on} \quad \Sigma_i \tag{3.8}$$

$$\mathbf{grad}p \cdot \boldsymbol{n_f} = 0 \quad \text{on} \quad \Sigma_w \tag{3.9}$$

Eq. (3.7) represents the Helmholtz wave equation under the above assumptions, where ω is the pulsation and c_0 is the sound speed in the fluid. Eq. (3.8) corresponds to the continuity of the normal velocity on fluid-structure interface as the fluid is supposed inviscid. Eq. (3.9) corresponds to Eq. (3.8) written for a rigid fixed interface. These equations, combined with the equations describing the behavior of the elastic structure, model a coupled fluid-structure system and allow to analyze its vibroacoustic behavior. For more details see [19].

3.3 Coupled variational formulation

This section is devoted to the weak formulation of the coupled fluid-structure problem. Let's introduce a virtual displacement field denoted by $\delta\boldsymbol{u} \in \mathcal{C}_u$ and a virtual pressure field $\delta p \in \mathcal{C}_p$, where $\mathcal{C}_u$ and $\mathcal{C}_p$ are function spaces of sufficiently regular functions. Mathematically, this is expressed considering $\delta\boldsymbol{u} = \mathbf{0}$ on Σ_u. From the previous local equations (from Eqs. (3.1) to (3.9)) and after some mathematical manipulations, it is possible to formulate the variational formulation in terms of displacement and pressure such that:

$$k(\boldsymbol{u}, \delta\boldsymbol{u}) - \omega^2 m(\boldsymbol{u}, \delta\boldsymbol{u}) - c(p, \delta\boldsymbol{u}) - f(\delta\boldsymbol{u}) = 0, \qquad \forall \delta\boldsymbol{u} \in \mathcal{C}_u \tag{3.10}$$

$$h(p, \delta p) - \omega^2 q(p, \delta p) - \omega^2 \rho_f c(\delta p, \boldsymbol{u}) = 0, \qquad \forall \delta p \in \mathcal{C}_p. \tag{3.11}$$

The terms given in Eq. (3.10) are the following:

$$k(\boldsymbol{u}, \delta\boldsymbol{u}) = \int_{\Omega_s} \boldsymbol{\varepsilon}(\delta\boldsymbol{u}) : \boldsymbol{\mathcal{C}} : \boldsymbol{\varepsilon}(\boldsymbol{u})\, dV \tag{3.12}$$

$$m(\boldsymbol{u}, \delta\boldsymbol{u}) = \int_{\Omega_s} \rho_s\, \delta\boldsymbol{u} \cdot \boldsymbol{u}\, dV \tag{3.13}$$

$$c(p, \delta\boldsymbol{u}) = \int_{\Sigma_i} \delta\boldsymbol{u} \cdot p\boldsymbol{n_s}\, dS \tag{3.14}$$

$$f(\delta\boldsymbol{u}) = \int_{\Sigma_s} \delta\boldsymbol{u} \cdot \boldsymbol{f}\, dS \tag{3.15}$$

and the ones in Eq. (3.11) are such that:

$$h(p, \delta p) = \int_{\Omega_f} \mathbf{grad}\delta p \cdot \mathbf{grad} p\, dV \tag{3.16}$$

$$q(p, \delta p) = \int_{\Omega_f} \frac{1}{c_0^2} p\, \delta p\, dV \tag{3.17}$$

$$c(\delta p, \boldsymbol{u}) = \int_{\Sigma_i} \boldsymbol{u} \cdot \delta p\, \boldsymbol{n_f}\, dS \tag{3.18}$$

Eq. (3.12) is the virtual structural potential energy, Eq. (3.13) is the virtual structural kinetic energy, Eq. (3.14) is the virtual coupling energy for the structural side, Eq. (3.15) is the virtual structural external energy. Due to the analogy between the structure and the fluid, Eqs. (3.16) and (3.17) can be introduced as the virtual acoustic potential energy and the virtual acoustic kinetic energy, respectively. Eq. (3.18) is the virtual coupling energy for the acoustic side.

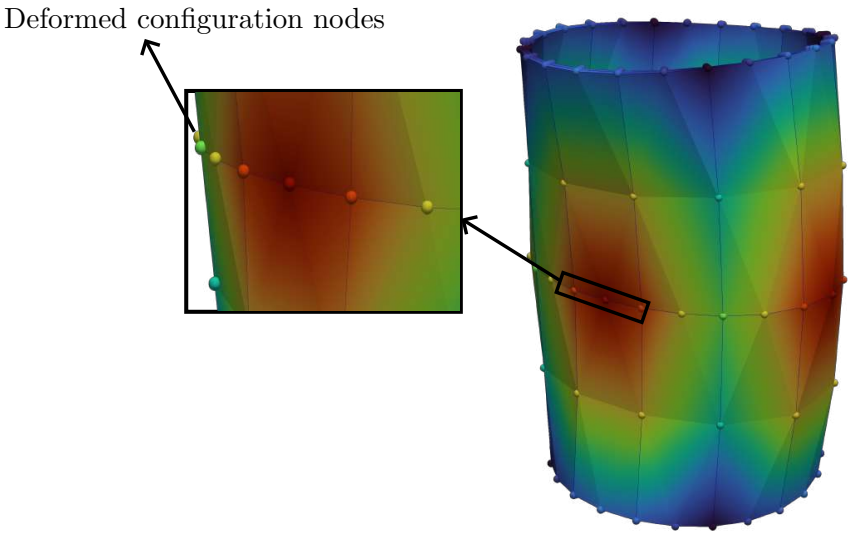

Figure 3.2: FEM field representation

3.4 Field discretization and discretized coupled problem

Let's introduce the discretized fields $\boldsymbol{u}^h$ and p^h and the related virtual fields $\delta\boldsymbol{u}^h$ and δp^h. For sake of simplicity, the same index h is chosen for IGA and FEM discretization, as in the following equations:

$$\boldsymbol{u}^h = \mathbf{N}_s\mathbf{u} \quad \text{and} \quad \delta\boldsymbol{u}^h = \mathbf{N}_s\delta\mathbf{u} \tag{3.19}$$

$$p^h = \mathbf{N}_f\mathbf{p} \quad \text{and} \quad \delta p^h = \mathbf{N}_f\delta\mathbf{p} \tag{3.20}$$

where $\mathbf{N}_s$ and $\mathbf{N}_f$ contains either the FEM shape functions or the IGA shape functions. The unknown vectors $\mathbf{u}$ and $\mathbf{p}$ are the unknown nodal values for FEM or the unknown values defined at the control points for IGA. The FEM and IGA functional field representation, for a cylinder modal shape, is shown in Figs. 3.2 and 3.3, respectively.

The problem to be solved can be written in the matrix form using the Eqs. from (3.1) to (3.18), taking into account the isoparametric and isogeometric discretization defined from Eqs. (3.19) and

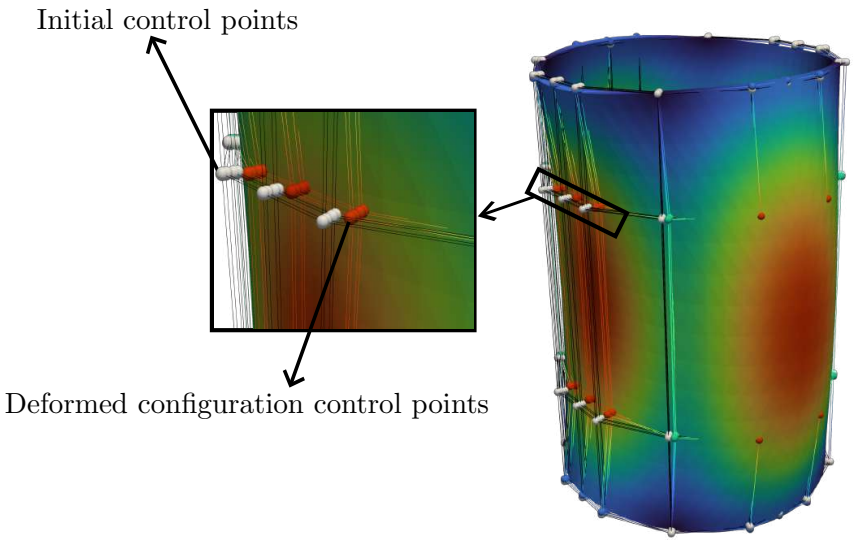

Figure 3.3: IGA field representation

(3.20). Thus, the following operators are obtained :

$$k(\delta\mathbf{u}^{\mathbf{h}}, \mathbf{u}^{\mathbf{h}}) = \delta\mathbf{u}^T \mathbb{K}\mathbf{u} \quad \Rightarrow \quad \mathbb{K} : \text{Structural Stiffness Matrix} \tag{3.21}$$

$$m(\delta\mathbf{u}, \mathbf{u}) = \delta\mathbf{u}^T \mathbb{M}\mathbf{u} \quad \Rightarrow \quad \mathbb{M} : \text{Structural Mass Matrix} \tag{3.22}$$

$$c(\delta\mathbf{u}, p) = \delta\mathbf{u}^T \mathbb{C}\mathbf{p} \quad \Rightarrow \quad \mathbb{C} : \text{Coupling Matrix} \tag{3.23}$$

$$f(\delta\mathbf{u}) = \delta\mathbf{u}^T \mathbf{f} \quad \Rightarrow \quad \mathbf{f} : \text{External Structural Force} \tag{3.24}$$

$$h(p, \delta p) = \delta\mathbf{p}^T \mathbb{H}\mathbf{p} \quad \Rightarrow \quad \mathbb{H} : \text{Acoustic Stiffness Matrix} \tag{3.25}$$

$$q(\delta p, p) = \delta\mathbf{p}^T \mathbb{Q}\mathbf{p} \quad \Rightarrow \quad \mathbb{Q} : \text{Acoustic Mass Matrix} \tag{3.26}$$

The matrices $\mathbb{K}$ and $\mathbb{H}$ are positive semi-definite, the kernel of $\mathbb{K}$ is of dimension six in 3D, and the kernel of $\mathbb{H}$ is of dimension one. The matrix $\mathbb{M}$ is positive definite. From Eqs. (3.21) to (3.26), the operator can be written for both IGA and FEM according to the discretization form:

$$\left(\begin{bmatrix} \mathbb{K} & -\mathbb{C} \\ \mathbf{0} & \mathbb{H} \end{bmatrix} - \omega^2 \begin{bmatrix} \mathbb{M} & \mathbf{0} \\ \rho_f \mathbb{C}^T & \mathbb{Q} \end{bmatrix} \right) \begin{bmatrix} \mathbf{u} \\ \mathbf{p} \end{bmatrix} = \begin{bmatrix} \mathbf{f} \\ \mathbf{0} \end{bmatrix}. \tag{3.27}$$

In both FEM and IGA cases, the matrix formulation has the same matrix form. Note that $\mathbb{K}$, $\mathbb{M}$, $\mathbb{H}$, $\mathbb{Q}$, $\mathbb{C}$, can be written in both IGA and FEM according to the discretization. The Gaussian

quadrature, which is a numerical integration technique to get an approximate value of a definite integral, need the selection of an appropriate number of integration points as a function of the used polynomial order. For more details on the Gaussian quadrature in FEM and IGA, see [32] and [2], respectively.

3.5 Numerical vibroacoustic analysis

This section presents a numerical application of a fully coupled vibroacoustic problem solved using the Isogeometric Analysis (IGA) framework. The objective is to evaluate the accuracy, computational efficiency, and numerical properties of the IGA formulation for coupled fluid–structure systems. Two main analyses are carried out: the coupled eigenvalue analysis and the frequency response function (FRF) computation.

A deliberately simple geometry is selected for this study. This choice serves two purposes. First, it allows a clear and transparent illustration of the proposed methodology without the additional complexity that may obscure the interpretation of the results. Second, the geometry can be easily reproduced by other researchers, facilitating verification and comparison of the numerical approach. It is important to emphasise that the methodology developed in this work has also been applied and tested on more complex geometries in later sections, confirming its robustness and broader applicability beyond this introductory example.

3.5.1 Geometry and material parameters

The test configuration consists of a thin elastic plate coupled with an enclosed acoustic cavity, as shown in Figure 3.4. The main physical parameters of both the structural and the acoustic domains are summarized in Table 3.1. The plate is clamped along all four edges, while the cavity boundaries are assumed acoustically rigid, except at the fluid–structure interface where the coupling occurs. A preliminary mesh convergence study was performed to ensure the accuracy of the solution within the investigated frequency range (0–300Hz). The adopted structural and acoustic discretizations were verified to provide converged results, and the interface meshes were constructed to be fully compatible, guaranteeing a consistent fluid–structure coupling within the IGA framework.

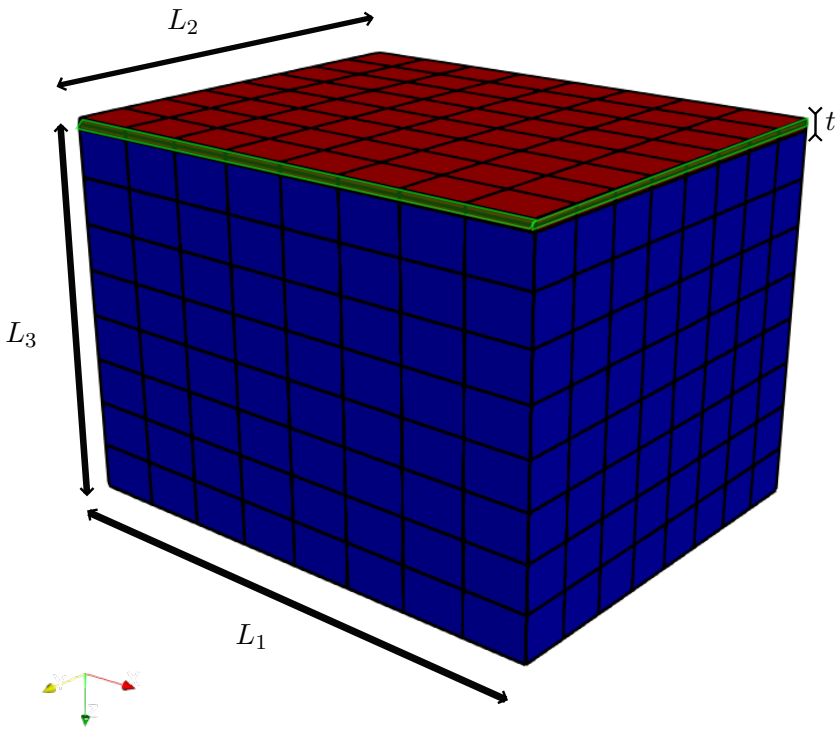

Figure 3.4: Vibroacoustic problem under investigation. The structure is in red and the acoustic cavity is in blue. On the green are all the displacements are clamped.

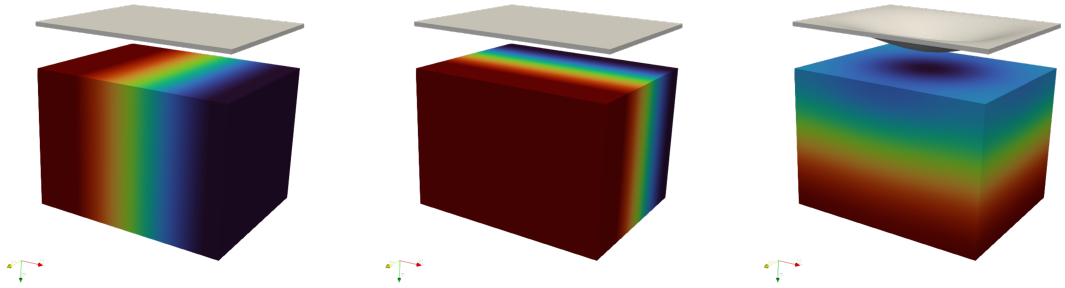

Figure 3.5: First three non-zero vibroacoustic mode shapes.

3.5.2 Coupled vibroacoustic eigenvalue analysis

The coupled eigenvalue problem is solved to determine the natural frequencies and mode shapes of the fully coupled vibroacoustic system using the IGA discretization. Representative coupled modes are analyzed to highlight how the presence of the acoustic cavity affects the structural dynamic behavior and vice versa.

The governing coupled system to be solved is expressed in Equation 3.28:

$$\left(\begin{bmatrix} \mathbb{K} & -\mathbb{C} \\ \mathbf{0} & \mathbb{H} \end{bmatrix} - \omega^2 \begin{bmatrix} \mathbb{M} & \mathbf{0} \\ \rho_f \mathbb{C}^T & \mathbb{Q} \end{bmatrix} \right) \begin{bmatrix} \mathbf{u} \\ \mathbf{p} \end{bmatrix} = \begin{bmatrix} \mathbf{0} \\ \mathbf{0} \end{bmatrix}, \tag{3.28}$$

As shown in Equation 3.28, the coupled fluid–structure problem leads to a *non-symmetric* system due to the presence of the coupling matrix $\mathbb{C}$. Consequently, its solution is more computationally demanding compared to standard symmetric eigenvalue problems.

The modal analysis of the system provides the natural frequencies and corresponding coupled mode shapes. Table 3.2 reports the first seven coupled eigenfrequencies together with the domain (structural or fluid) where the response is dominant. Moreover the coupled vibroacoustic problem is solved using a commercial software (Patran/Nastran) and the results are aligned with the ones obtained from the IGA approach. Figure 3.5 illustrates the first three vibroacoustic modes.

Table 3.1: Structural and fluid material properties.

$\rho_s \left[\frac{kg}{m^3}\right]$	$\rho_f \left[\frac{kg}{m^3}\right]$	$c_0 \left[\frac{m}{s}\right]$	E [Pa]	ν[-]	$L_1[m]$	$L_2[m]$	$L_3[m]$	$t[m]$
2700	1.2	340	$7{\cdot}10^{10}$	0.3	1	0.8	0.7	0.02

Table 3.2: First seven vibroacoustic natural frequencies obtained through an IGA approach and Patran/Nastran and their dominant domain.

Mode number	f_c [Hz]	f_{PatNat} [Hz]	Dominant domain
1	0.00	0.00	F
2	169.98	169.95	F
3	212.48	212.27	F
4	228.23	228.12	S + F
5	244.43	244.00	F
6	272.12	272.75	F
7	296.30	296.28	F

Since the density of the fluid (air) is relatively low, its influence on the structural dynamics is negligible. Conversely, the structure strongly affects the acoustic pressure field within the cavity. This behavior is particularly evident in the third non-zero mode at 228.23 Hz, where the structural deformation dominates the coupled response, imposing its modal shape on the acoustic field.

3.5.3 Frequency response function (FRF) analysis

The Frequency Response Function (FRF) is computed to evaluate the dynamic behavior of the coupled vibroacoustic system under harmonic excitation. The objective of this analysis is to assess how the structure and the enclosed acoustic cavity respond to a time-harmonic load applied on the structural surface (see Figure 3.6). The pressure field within the acoustic cavity is analyzed in terms of both the pressure amplitude per unit force and the corresponding Sound Pressure Level (SPL).

The FRF is obtained by solving a series of linear systems over a range of excitation frequencies, according to the following algorithm:

Here, $\mathbf{K}_h$ and $\mathbf{M}_h$ denote the global stiffness and mass matrices of the coupled system, $\mathbf{F}_{\text{tot}}$ is the external load vector, and ω_n represents the circular frequency at each frequency step. The total computational cost therefore depends on both the size of the system matrices, directly related to the total number of degrees of freedom and on the number of frequency steps n_{step} to be evaluated. Indeed, the above linear system must be solved n_{step} times, once for each excitation frequency, which can lead to a significant computational burden for fine frequency resolutions or large-scale models.

The frequency sweep is performed over the range 0–300 Hz, covering the main resonance modes of

Algorithm 1 Frequency Response Function (FRF) algorithm with computational time for the considered problem

procedure FRF($f_{\min}, f_{\max}, n_{\text{step}}, p, q, r, n_{ex}, n_{ey}, n_{ez}, uknot, vknot, wknot, c_0, \rho_s, \rho_f, \nu, E$)
    Compute matrices
    Compute $\mathbb{H}$ ▷ time $t_H = 1.2\ s$
    Compute $\mathbb{Q}$ ▷ time $t_Q = 1.2\ s$
    Compute $\mathbb{K}$ ▷ time $t_K = 1.6\ s$
    Compute $\mathbb{M}$ ▷ time $t_M = 1.6\ s$
    Compute $\mathbb{C}$ ▷ time $t_C = 0.5\ s$
    Rearrange system matrices
    Rearrange $\mathbf{K}_h$, $\mathbf{M}_h$
    Loop over frequency domain
    for $n = 1$ **to** n_{step} **do**
        Compute $\omega_n = 2\pi f_n$
        Solve $(\mathbf{K}_h - \omega_n^2 \mathbf{M}_h)\mathbf{U}_n = \mathbf{F}_{\text{tot}}$ ▷ time $t_{\text{sol}} = 95\ s$
    end for
    return $\mathbf{U}_n$ containing displacement $\mathbf{U}$ and pressure $\mathbf{P}$
end procedure

the coupled system identified in the previous eigenvalue analysis.

Within the acoustic cavity, the computed pressure field is post-processed to obtain the Sound Pressure Level (SPL), which is defined as:

$$SPL = 20 \log_{10} \left(\frac{p_{\text{rms}}}{p_0} \right) \quad [\text{dB}], \tag{3.29}$$

where p_{rms} is the root mean square of the acoustic pressure, and $p_0 = 2 \times 10^{-5}$ Pa is the reference pressure in air.

The computed FRF (Figure 3.7) and SPL (Figure 3.8) distributions allow the identification of resonance peaks and provide insight into the coupled vibroacoustic behavior of the system.

The peaks shown in Figures 3.7 and 3.8 are identical for both FRFs and occur precisely at the calculated modal frequencies. It is worth noting that these peaks do not diverge to infinity, as would theoretically occur in an undamped system, because the FRFs are evaluated on a discrete set of frequency steps; the finite resolution of this frequency grid naturally limits the apparent peak amplitude.

3.5.4 Computational performance and discussion

This subsection presents a quantitative assessment of the computational performance of the coupled vibroacoustic analysis. Both the eigenvalue problem and the Frequency Response Function (FRF)

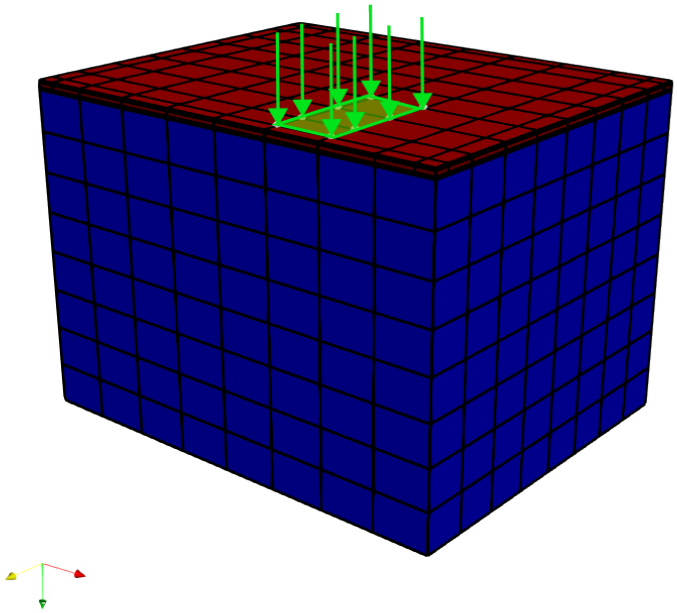

Figure 3.6: Applied harmonic forces on the structural net patch. The arrows indicate the structural surface forces.

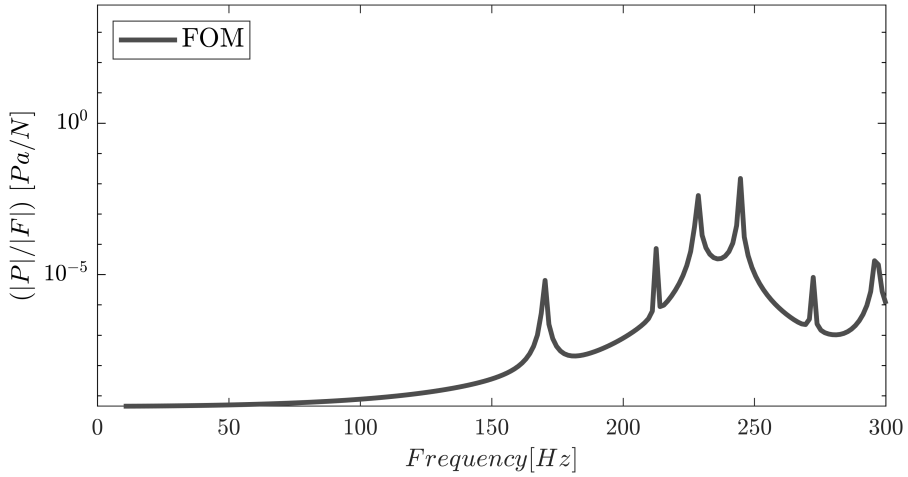

Figure 3.7: Computed Frequency Response Function (FRF) of the coupled vibroacoustic system, expressed as pressure amplitude per unit excitation force. The resonance peaks correspond to the coupled natural frequencies.

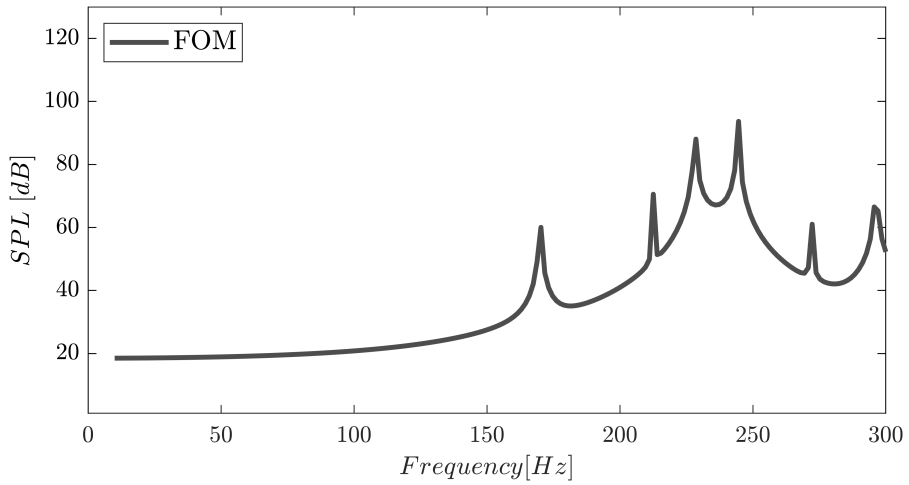

Figure 3.8: Sound Pressure Level (SPL) distribution within the acoustic cavity, computed over the 0–300 Hz frequency range. The SPL peaks confirm the resonance frequencies identified in the FRF.

computation were carried out using the IGA discretization described earlier.

The structural and acoustic stiffness ($\mathbf{K}_h$) and mass ($\mathbf{M}_h$) matrices exhibit a typical sparse pattern, as illustrated in Figures 3.9 and 3.10, where only a small fraction of the total entries are non-zero. This sparsity is advantageous for memory efficiency, as it allows the use of optimized storage schemes and sparse solvers; however, it also leads to irregular data access patterns that can affect numerical performance on large-scale systems. Moreover, despite their sparse nature, the overall coupled matrix remains *non-symmetric* due to the presence of the coupling operator $\mathbb{C}$ (see Equation 3.28). This lack of symmetry not only increases the computational cost of direct solvers, which must handle non-Hermitian systems, but can also deteriorate the conditioning of the problem, thereby impacting both the convergence rate and numerical stability of iterative algorithms.

The coupled system involves a total of 2303 degrees of freedom (DOFs), resulting in global matrices of size 2303×2303.

Table 3.3 summarizes the average computational times for the modal and FRF analyses. While the eigenvalue computation already requires a significant amount of time, the FRF analysis is considerably more expensive, since the linear system

$$(\mathbf{K}_h - \omega_n^2 \mathbf{M}_h)\mathbf{U_n} = \mathbf{F_{tot}} \tag{3.30}$$

must be solved repeatedly for each frequency step in the investigated range (0–300 Hz).

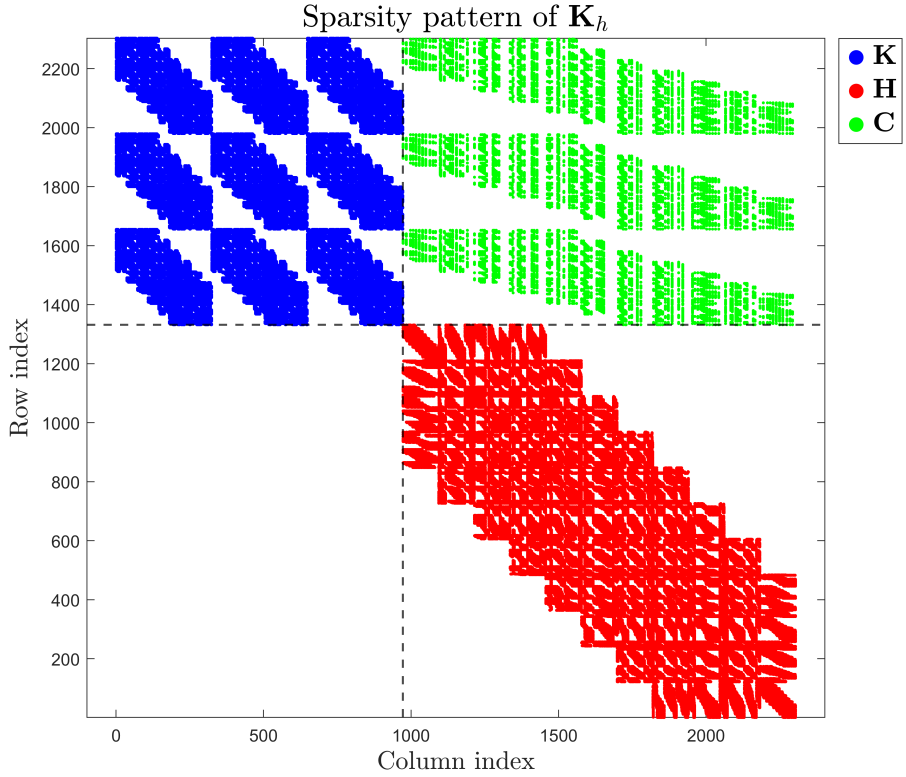

Figure 3.9: Sparsity pattern of the global stiffness $\mathbb{K}_h$.

Table 3.3: Computational times for the vibroacoustic analyses.

Analysis type	Number of frequency steps / modes	Computation time $[s]$
Coupled eigenvalue analysis	all modes	130
FRF computation (0–300 Hz)	200 frequency steps	95

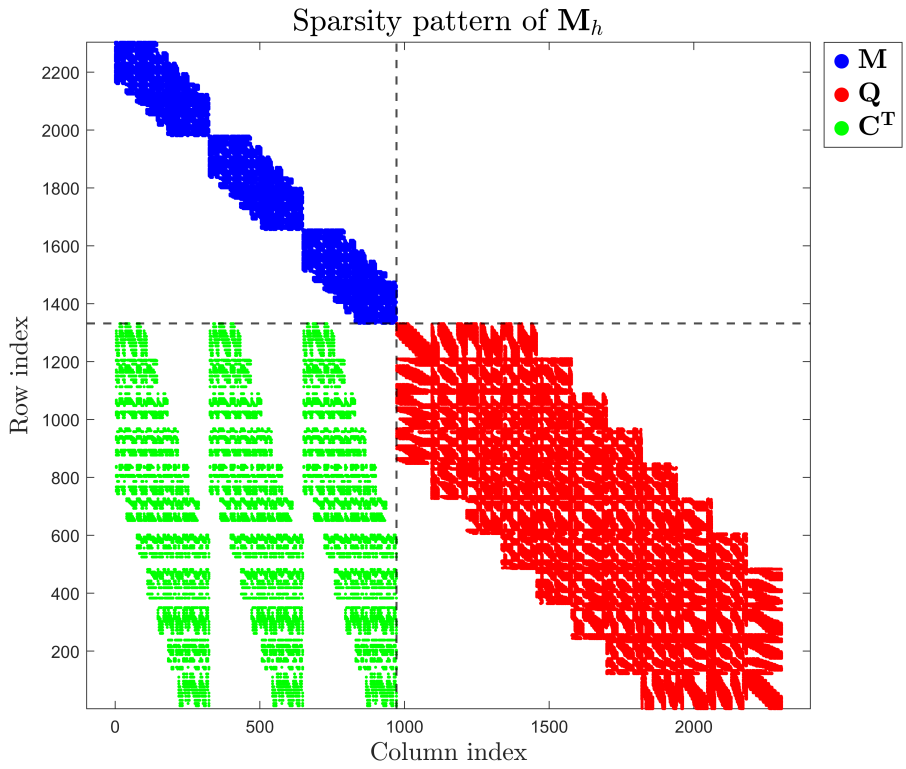

Figure 3.10: Sparsity pattern of the global stiffness $\mathbb{M}_h$.

In this configuration, the coupled eigenvalue analysis required approximately $130s$, while the FRF computation took around $95s$ for 200 frequency steps. These results demonstrate that the computational time is quite long considering the size of the problem (2303×2303).

Moreover, Figure 3.11 illustrates the computational cost associated with assembling the acoustic and structural matrices, as well as the time required to compute the FRF response (considering 200 frequency steps), as the number of degrees of freedom increases. As shown in the figure, the assembly time is negligible compared to the FRF computation time. This behaviour is mainly related to the size of the system: when the number of degrees of freedom is moderate, the computational cost of the FRF evaluation remains significantly higher than that of matrix assembly. In particular, the non-symmetric nature of the coupled operator and the need to solve the system multiple times for different frequencies make broadband simulations computationally demanding. Therefore, it becomes essential to introduce efficient numerical reduction techniques.

The next chapter addresses this issue through the development of a Reduced Order Model (ROM) based on a modal projection approach, which substantially decreases the number of unknowns while

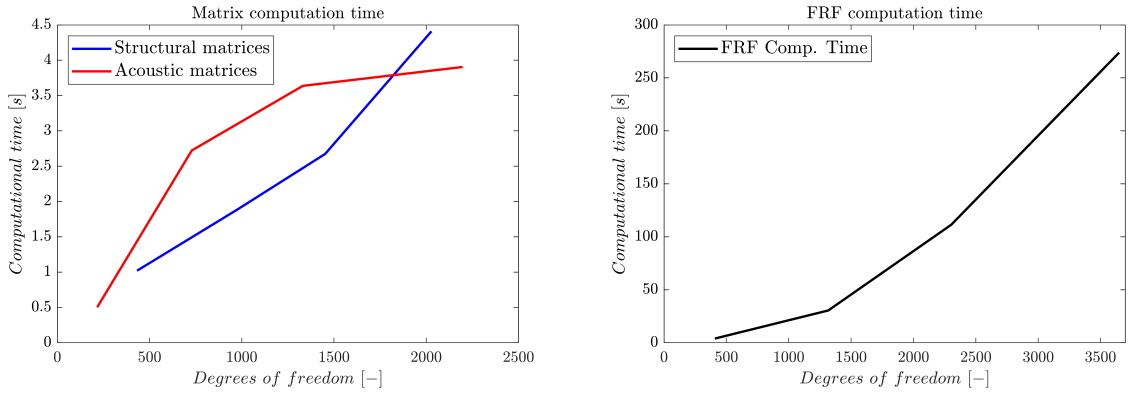

Figure 3.11: Computational time required for the assembly of acoustic and structural matrices and for the evaluation of the FRF (200 frequency steps) as a function of the system degrees of freedom.

preserving the physical accuracy of the coupled response.

3.6 Conclusion and motivation for Reduced Order Models (ROMs)

This numerical example demonstrates the capability of the Isogeometric Analysis (IGA) framework to accurately capture coupled vibroacoustic phenomena, providing a smooth and consistent representation across both structural and acoustic domains. The fully coupled formulation ensures physical fidelity, particularly in the prediction of natural frequencies, mode shapes, and frequency response functions of the system.

Nevertheless, the computational performance analysis highlights a critical limitation of the full-order IGA approach. Even for a relatively simple configuration, consisting of a single thin plate coupled with a small acoustic cavity, the required computational time for both the eigenvalue analysis and the frequency response computation is considerable. As the physical model becomes more complex, involving larger domains, finer discretizations, or additional coupling interfaces, the size and density of the system matrices ($\mathbf{K}_h$, $\mathbf{M}_h$) increase rapidly. This growth leads to prohibitively high memory demands and solution times, especially in broadband frequency analyses where the linear system must be solved for a large number of frequency steps.

Furthermore, the non-symmetric nature of the coupled problem adds an additional layer of complexity, requiring solvers capable of handling non-Hermitian matrices and further increasing computational effort. Consequently, while the full IGA model provides a high-fidelity representation, it becomes impractical for large-scale or parametric studies where multiple analyses are required.

To overcome these challenges, the next chapter introduces a modal-based Reduced Order Model (ROM) formulation. This approach aims to drastically reduce computational costs while preserving the essential coupled dynamics of the system. By projecting the full-order system onto a reduced modal subspace, the ROM enables efficient frequency-domain simulations and opens the way for advanced applications such as optimization, sensitivity analysis, and uncertainty quantification in coupled vibroacoustic problems.

Chapter 4

Reduced order model by projection on modal basis

This chapter presents the methodology employed for the solution of vibroacoustic problems through the use of structural and acoustic mode shapes. The approach, grounded in modal analysis, provides an efficient and accurate framework for the investigation of coupled vibroacoustic systems. The theoretical formulation is outlined in detail, emphasizing its applicability and the range of physical quantities that can be consistently reconstructed within this setting. Particular attention is devoted to the computational advantages of the modal approach, most notably the substantial reduction in the size of the algebraic system and the consequent decrease in computational cost. Furthermore, an illustrative application is included, in which a reduced-order model is developed and critically assessed through a systematic comparison with the reference full-order model (FOM) obtained via isogeometric analysis (IGA). This example not only demonstrates the effectiveness of the reduction procedure but also highlights its potential for integration with both finite element and isogeometric frameworks in more advanced applications.

Content

4.1 Introduction to reduced models

Reduced Order Models (ROMs) have emerged as an essential approach in computational mechanics for efficiently simulating complex dynamical systems, particularly in vibroacoustics and fluid-structure interaction problems. The primary goal of ROMs is to decrease the computational burden while retaining the essential dynamic characteristics of the full-order system. This need arises especially in high-fidelity simulations, where full-scale finite element models can involve millions of degrees of freedom and prohibitively long computational times [81, 82]. For instance, when computing the pressure distribution inside an acoustic cavity using a direct frequency-domain approach, one must solve a sequence of linear systems at each frequency step, as illustrated by the algorithm 1

The computational cost therefore depends both on the size of the system matrices $\mathbf{K}_h$ and $\mathbf{M}_h$, which are directly related to the total number of degrees of freedom, and on the number of frequency steps n_{step} to be evaluated.

Several methodologies for model reduction exist in the literature, each with its advantages and limitations. One of the most classical and widely used approaches is the *projection onto a modal basis*, where the system's response is approximated by a linear combination of a limited number of structural and acoustic or coupled structural-acoustic modes [83, 27, 16]. This method benefits from the physical interpretability of the retained modes and is particularly effective when the dynamics are dominated by low-frequency modes. Modal truncation can be enhanced using techniques such as frequency weighting, damping-adapted modes, or enriched modal bases to improve accuracy in specific frequency bands [26].

Beyond modal projection, several other ROM strategies have been developed. *Proper Orthogonal Decomposition* (POD) constructs the reduced basis from snapshots of the full-order system, capturing the most energetic modes of the system's response [72]. This approach is often combined with Galerkin or Petrov-Galerkin projections to yield a computationally efficient reduced system. Another popular technique is *Balanced Truncation*, commonly used in control theory, which reduces the system while preserving input-output behavior and energy measures [81]. Similarly, *Krylov subspace methods* approximate the system response in the frequency domain and are particularly advantageous for parametric studies or systems with frequency-dependent behavior [27].

Recent research has also explored hybrid and adaptive ROMs, combining multiple reduction tech-

niques to improve efficiency and accuracy. For instance, projection-based ROMs can be coupled with isogeometric analysis or finite element discretizations, enabling high-fidelity simulation with significantly reduced computational costs [16, 65]. Reduced models have been successfully applied to structural-acoustic coupling, piezoelectric damping systems, and flow-excited cavities, demonstrating their versatility and practical relevance in engineering applications [27, 66].

In summary, ROMs represent a powerful framework to tackle the computational challenges posed by complex vibroacoustic systems. Among the various techniques, projection on modal bases remains a robust and physically meaningful approach, while alternative methods such as POD, balanced truncation, and Krylov-based techniques offer complementary tools for specialized problems or for systems where modal dominance is not guaranteed.

4.2 Projection on decoupled systems

In the present work, the reduced order model is obtained using the modes of the decoupled systems namely on one hand, acoustic modes of the cavity with rigid fixed interfaces, and on the other hand, structural modes in vacuo, see [19], [81], [82]. Therefore, two eigenvalues problems must be solved, one for the structure, Equation (4.1) and one for the acoustic cavity, Equation (4.2):

$$\left(\mathbb{K} - \omega^2 \mathbb{M}\right) \boldsymbol{\phi}^s = 0 \tag{4.1}$$

$$\left(\mathbb{H} - \omega^2 \mathbb{Q}\right) \boldsymbol{\phi}^f = 0 \tag{4.2}$$

In both eigenvalue analyses the mass and stiffness matrices are symmetrical and thus the eigenvalue problem is carried out, in a straightforward manner, using the Lanczos method. From the eigenvalue solution of the two decoupled systems, the eigenvectors and eigenfrequencies of the two systems are obtained (Equations (4.3) and (4.4)):

$$\boldsymbol{\Phi}_s = \begin{bmatrix} \vdots & & \vdots \\ \boldsymbol{\phi}_1^s & \dots & \boldsymbol{\phi}_{m_s}^s \\ \vdots & & \vdots \end{bmatrix}_{(n_s \times m_s)} \quad \text{and} \quad \boldsymbol{\omega}_s = \begin{bmatrix} \vdots \\ \omega_i^s \\ \vdots \end{bmatrix}_{(m_s \times 1)} \tag{4.3}$$

and

$$\boldsymbol{\Phi}_f = \begin{bmatrix} \vdots & & \vdots \\ \boldsymbol{\phi}_1^f & \dots & \boldsymbol{\phi}_{m_f}^f \\ \vdots & & \vdots \end{bmatrix}_{(n_f \times m_f)} \quad \text{and} \quad \boldsymbol{\omega}_f = \begin{bmatrix} \vdots \\ \omega_i^f \\ \vdots \end{bmatrix}_{(m_f \times 1)} \tag{4.4}$$

Leveraging on the aforementioned eigenvectors, obtained from the decoupled modal analyses, it is possible to switch from the Full Order Model (FOM) to the Reduced Order Model [19]. The latter is based on the following assumptions:

$$\mathbf{u} \simeq \boldsymbol{\Phi}_s \boldsymbol{\alpha} \quad \text{and} \quad \mathbf{p} \simeq \boldsymbol{\Phi}_f \boldsymbol{\beta} \tag{4.5}$$

Substituting Equations (4.5) in Equation (3.27), the following reduced vibroacoustic problem, in a fully coupled configuration and in the absence of external forces, is obtained:

$$\left(\begin{bmatrix} \mathbb{K}_r & -\mathbb{C}_r \\ \mathbf{0} & \mathbb{H}_r \end{bmatrix} - \omega^2 \begin{bmatrix} \mathbb{M}_r & \mathbf{0} \\ \rho_f \mathbb{C}_r^T & \mathbb{Q}_r \end{bmatrix} \right) \begin{bmatrix} \boldsymbol{\alpha} \\ \boldsymbol{\beta} \end{bmatrix} = \begin{bmatrix} \mathbf{0} \\ \mathbf{0} \end{bmatrix} \tag{4.6}$$

where:

$$\begin{aligned} \mathbb{M}_r = \boldsymbol{\Phi}_s^T \mathbb{M} \boldsymbol{\Phi}_s, \quad \mathbb{Q}_r = \boldsymbol{\Phi}_f^T \mathbb{Q} \boldsymbol{\Phi}_f, \quad \mathbb{C}_r = \boldsymbol{\Phi}_s^T \mathbb{C} \boldsymbol{\Phi}_f \\ \mathbb{K}_r = \boldsymbol{\Phi}_s^T \mathbb{K} \boldsymbol{\Phi}_s, \quad \mathbb{H}_r = \boldsymbol{\Phi}_f^T \mathbb{H} \boldsymbol{\Phi}_f \end{aligned} \tag{4.7}$$

Equations (4.7) represent the reduced operators. The size of the new (reduced) matrices is much smaller than that of the original (full) ones, which allows for a much faster resolution of the problem.

The eigenvalue analysis of the reduced system leads to the coupled vibroacoustic eigenfrequecies:

$$\boldsymbol{\omega} = \begin{bmatrix} \vdots \\ \omega_i \\ \vdots \end{bmatrix}_{((m_s+m_f)\times 1)} \tag{4.8}$$

The quantities of interest ($\boldsymbol{\omega_s}$,$\boldsymbol{\omega_f}$ and $\boldsymbol{\omega}$) given in Equations (4.3), (4.4) and (4.8) are computed and compared to the semi-analytical ones in the following section.

4.3 3D numerical example

4.3.1 Methodology

In this section, the vibroacoustic problem introduced in the Section 3.5 is analysed using both the full-order model (FOM) and reduced-order model (ROM) formulations based on modal projection, increasing the number of modes taken into account. The problem under investigation is the same shown in Figure 3.4 and the geometrical and material properties are the same shown in Table 3.1. The study aims to assess the capability of the modal-based ROM to accurately reproduce the coupled vibroacoustic behaviour while significantly reducing computational time.

The analysis focuses on a frequency range between 0 and 300 Hz. To evaluate the influence of the modal truncation on the accuracy of the ROM, three different reduced models are considered:

- **ROM$_1$** – including all structural and acoustic modes within the frequency range [0–300] Hz (range of interest);
- **ROM$_2$** – including all structural and acoustic modes within 1.5 times the range of interest, [0–450] Hz;
- **ROM$_3$** – including all structural and acoustic modes within twice the range of interest, [0–600] Hz.

Each ROM is constructed by projecting the decoupled acoustic and structural modes. The reference coupled eigenvalue problem is the same solved in Section 3.5. Subsequently, a frequency response function (FRF) analysis is performed to evaluate both the overall of the pressure response per unit structural excitation (P/F) and the associated sound pressure level (SPL) inside the acoustic cavity. Finally, the accuracy of each reduced model is assessed by comparing the coupled natural frequencies, the FRF, and the SPL with the reference full-order model (FOM). The L_2-norm of the error is computed to quantify the deviation between the ROM and FOM solutions, and the computational times of each simulation are compared to demonstrate the efficiency of the reduced models. The overall workflow adopted for the vibroacoustic analysis is schematically illustrated in Figure 4.1. The diagram summarizes all the main stages of the numerical procedure, from the definition of the physical problem and the computation of the full-order reference solution to the construction, projection, and validation of the reduced-order models (ROMs).

4.3.2 Acoustic and structural natural frequencies

Before solving the coupled vibroacoustic problem, the structural and acoustic subsystems are analyzed independently in order to obtain their uncoupled modal characteristics. The modal analysis of each subdomain provides the natural frequencies and mode shapes that will later be used to construct the reduced-order bases for the coupled system.

The free vibration problem for the **structural domain** can be formulated as in Equation 4.1 and for the **acoustic domain** in Equation 4.2.

The eigenvectors $\boldsymbol{\phi}^s$ and $\boldsymbol{\phi}^f$ represent the structural and acoustic mode shapes, respectively.

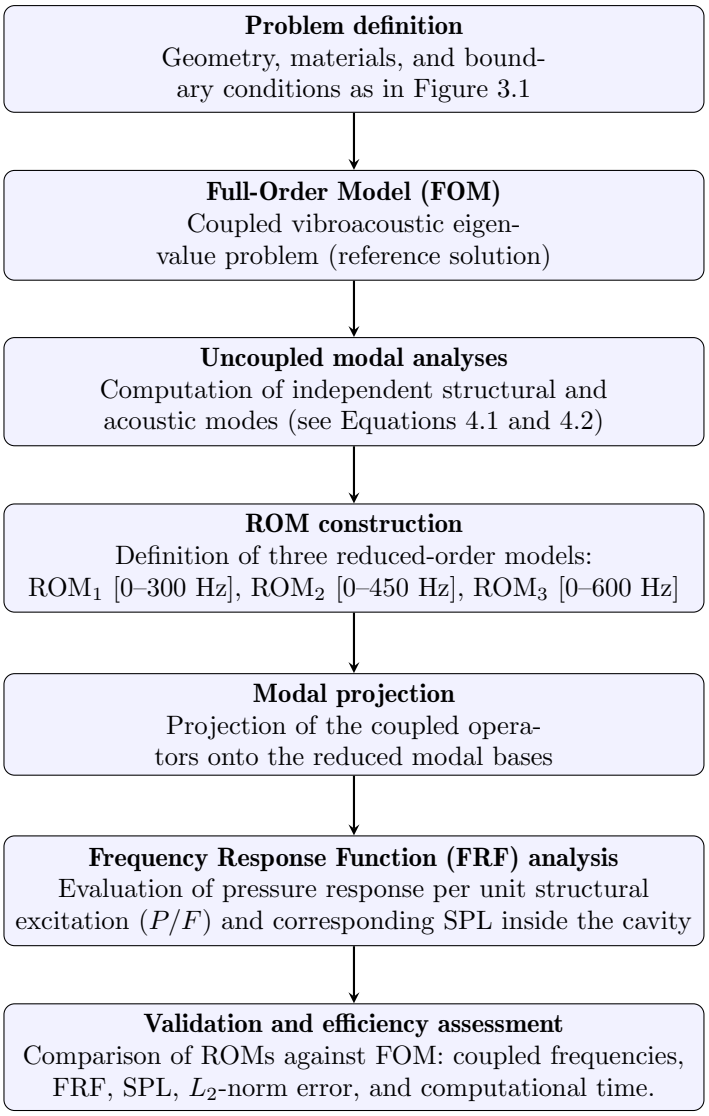

Figure 4.1: Schematic representation of the methodology used for the vibroacoustic analysis with FOM and ROMs.

Tables 4.1 and 4.2 summarize the first ten natural frequencies for the acoustic and structural subsystems, respectively. The results highlight the significantly different dynamic ranges of the two domains: the acoustic cavity exhibits its first mode at 0 Hz (rigid-body pressure mode), whereas the structural component starts vibrating at higher frequencies.

Table 4.1: First ten acoustic natural frequencies.

Mode number	f_{aco} [Hz]
1	0.00
2	170.00
3	212.50
4	242.86
5	272.13
6	296.44
7	322.70
8	340.00
9	364.74
10	400.94

Table 4.2: First ten structural natural frequencies.

Mode number	f_{str} [Hz]
1	229.97
2	403.61
3	525.33
4	682.59
5	694.72
6	952.50
7	984.00
8	1129.10
9	1150.50
10	1377.60

Figure 4.2 illustrates the first three uncoupled mode shapes for both the structural and acoustic systems.

The modal analyses confirm that both the structural and acoustic models exhibit well-converged results, with stable eigenvalues and consistent spatial distributions of the mode shapes. In particular,

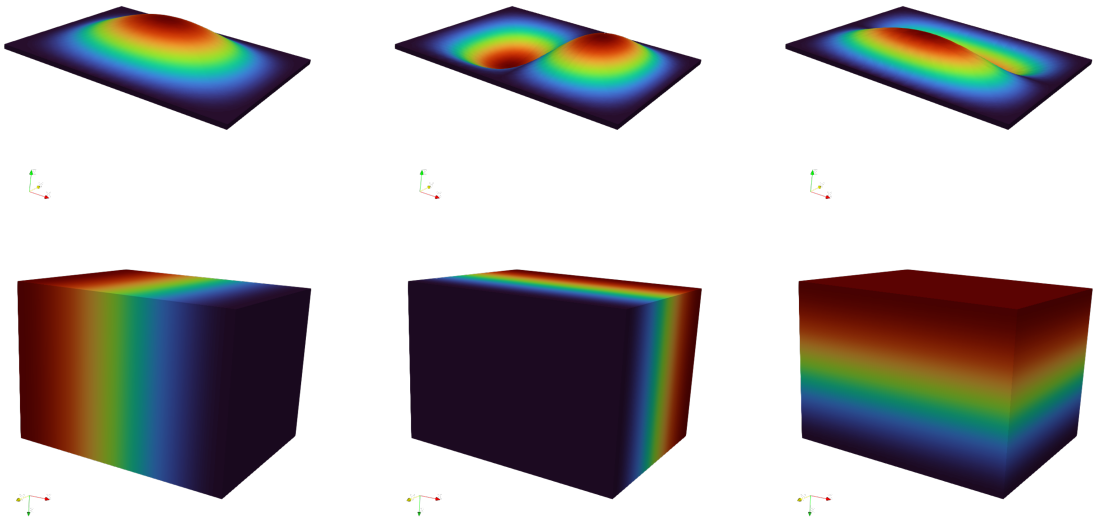

Figure 4.2: First three structural (up) and acoustic (bottom) mode shapes.

it has been observed that convergence is achieved when considering all modes up to approximately twice the frequency range of interest (i.e., up to 600 Hz in this study).

4.3.3 Full-Order vs Reduced-Order: natural modes and frequency response

To further assess the effectiveness of the proposed Reduced Order Models (ROMs), a forced response analysis is carried out and compared with the reference Full Order Model (FOM). The analysis aims to evaluate the acoustic pressure field inside the cavity resulting from a structural excitation applied to a portion of the structure surface.

The acoustic response is quantified in terms of the *Sound Pressure Level* (SPL), defined as:

$$SPL = 20 \log_{10} \left(\frac{p_{\text{rms}}}{p_0} \right) \text{ dB} \tag{4.9}$$

where p_{rms} is the root mean square pressure amplitude and $p_0 = 2 \times 10^{-5}$ Pa is the reference sound pressure, corresponding approximately to the threshold of human hearing at 1 kHz. The SPL provides a logarithmic measure of the perceived intensity of a sound and is widely used in vibroacoustic evaluations.

The applied excitation is illustrated in Figure 3.6. Numerically, a unitary pressure load was imposed in the z-direction on selected structural control points within the green area, as highlighted

in the Figure 3.6.

The problem is solved first using the full coupled formulation (FOM) and then through three reduced-order models (ROMs) built by projecting the coupled system onto the modal bases obtained from the uncoupled analyses:

- **ROM1**: includes all structural and acoustic modes in the frequency range [0–300] Hz;
- **ROM2**: includes all modes up to 1.5 times the range of interest ([0–450] Hz);
- **ROM3**: includes all modes up to 2 times the range of interest ([0–600] Hz).

To solve the same coupled problem through a reduced-order approach, the following algorithm summarizes the main steps of the modal-based ROM procedure.

Algorithm 2 Reduced-Order Model (ROM) via modal projection

procedure ROM($f_{\min}, f_{\max}, f_{\text{cut}}, n_{\text{step}}, p, q, r, n_{ex}, n_{ey}, n_{ez}, uknot, vknot, wknot, c_0, \rho_s, \rho_f, \nu, E$)
  Compute system matrices
  Compute $\mathbb{H}, \mathbb{Q}, \mathbb{K}, \mathbb{M}, \mathbb{C}$ ▷ t_H, t_Q, t_K, t_M, t_C
  Uncoupled modal analyses
  Solve structural eigenproblem $(\mathbb{K} - \omega^2\mathbb{K})\phi^s = 0$ ▷ time $t_{ModStr} = 3.3\ s$
  Solve acoustic eigenproblem $(\mathbb{H} - \omega^2\mathbb{Q})\phi^f = 0$ ▷ time $t_{ModAco} = 3.1\ s$
  Mode selection (ROM type)
  if ROM1 **then** $f_{\text{cut}} = 300$ Hz
  else if ROM2 **then** $f_{\text{cut}} = 1.5\, f_{\max}$
  else if ROM3 **then** $f_{\text{cut}} = 2\, f_{\max}$
  end if
  Retain modes with $f_{s,i}, f_{a,j} \leq f_{\text{cut}}$
  Form reduced modal bases $\widetilde{\Phi}_s$, $\widetilde{\Phi}_a$
  Model reduction
  Compute reduced matrices: $\mathbb{K}_{\mathbb{ROM}}, \mathbb{M}_{\mathbb{ROM}}, \mathbb{H}_{\mathbb{ROM}}, \mathbb{Q}_{\mathbb{ROM}}, \mathbb{C}_{\mathbb{ROM}}$
  Compute $\mathbf{F_{ROM}}$
  Frequency sweep
  for $n = 1$ **to** n_{step} **do**
    $\omega_n = 2\pi f_n$
    Solve $(\mathbf{K}_{\text{ROM}} - \omega_n^2\mathbf{M}_{\text{ROM}})\mathbf{U}_{\text{ROM}} = \mathbf{F}_{\text{ROM}}$ ▷ time $t_{solROM} = negligible$
    Recover full solution $\mathbf{U}_n = [\phi^s; \phi^f]\mathbf{U}_{\text{ROM}}$
  end for
  return $\mathbf{U}_n$ with **U** and **P**
end procedure

The corresponding coupled natural frequencies obtained from the FOM and the three ROMs are

Table 4.3: Comparison between coupled frequencies obtained with the Full Order Model (FOM) and the three Reduced Order Models (ROMs).

		ROM1 [0–300]Hz		ROM2 [0–450]Hz		ROM3 [0–600]Hz	
Mode	f_{FOM} [Hz]	f_{ROM1} [Hz]	error [%]	f_{ROM2} [Hz]	error [%]	f_{ROM3} [Hz]	error [%]
1	0.00	0.00	0.00	0.00	0.00	0.00	0.00
2	169.98	170.00	0.014	169.98	0.002	169.98	0.0005
3	212.48	212.50	0.009	212.48	0.005	212.48	0.001
4	228.23	228.54	0.140	228.37	0.090	228.37	0.061
5	244.43	244.48	0.019	244.45	0.006	244.45	0.009
6	272.12	272.13	0.004	272.13	0.004	272.13	0.004
7	296.30	296.44	0.050	296.30	0.015	296.30	0.001

summarized in Table 4.3. It can be observed that, even with a limited number of modes, the reduced models reproduce the reference results with very good accuracy.

Figures 4.3 and 4.4 show the Frequency Response Function (FRF) obtained from both the full and reduced models. Figure 4.3 presents the pressure amplitude per unit excitation force, while Figure 4.4 shows the corresponding sound pressure level (SPL) inside the cavity. All the reduced-order models (ROMs) provide a satisfactory approximation of the coupled vibroacoustic response; however, only the most enriched model (ROM3) is able to accurately reproduce all the resonance peaks observed in the full-order model (FOM). In particular, ROM1 and ROM2 fail to capture certain acoustic resonances because the corresponding structural mode, effectively excited by the applied load, is not included in their reduced modal basis. As a result, the expected acoustic peaks are absent in their frequency response functions.

If one wishes to improve the accuracy of ROM1 and ROM2 without significantly extending the modal range, the reduced bases could be enriched by including the quasi-static response of the acoustic field induced by the structural modes. This enrichment, however, requires solving a set of linear systems for each structural mode to obtain the corresponding quasi-static fluid response, leading to a noticeable increase in computational cost. For this reason, such an extension is not considered in the present study.

Despite the higher number of retained modes in ROM3, the computational cost remains practically unchanged compared to the simpler reduced models, confirming the effectiveness and scalability of the proposed modal reduction strategy as shown in Figure 4.4.

To quantitatively assess the quality of the reduced models, the relative L_2-norm error with respect

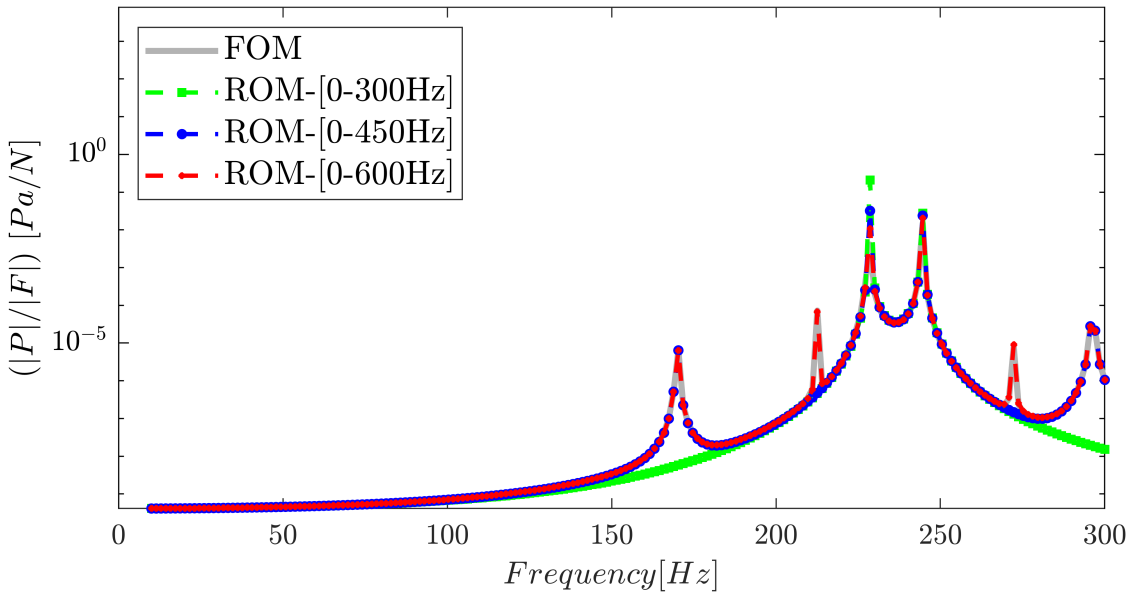

Figure 4.3: Frequency Response Function (FRF) of the acoustic cavity: comparison between FOM and ROMs.

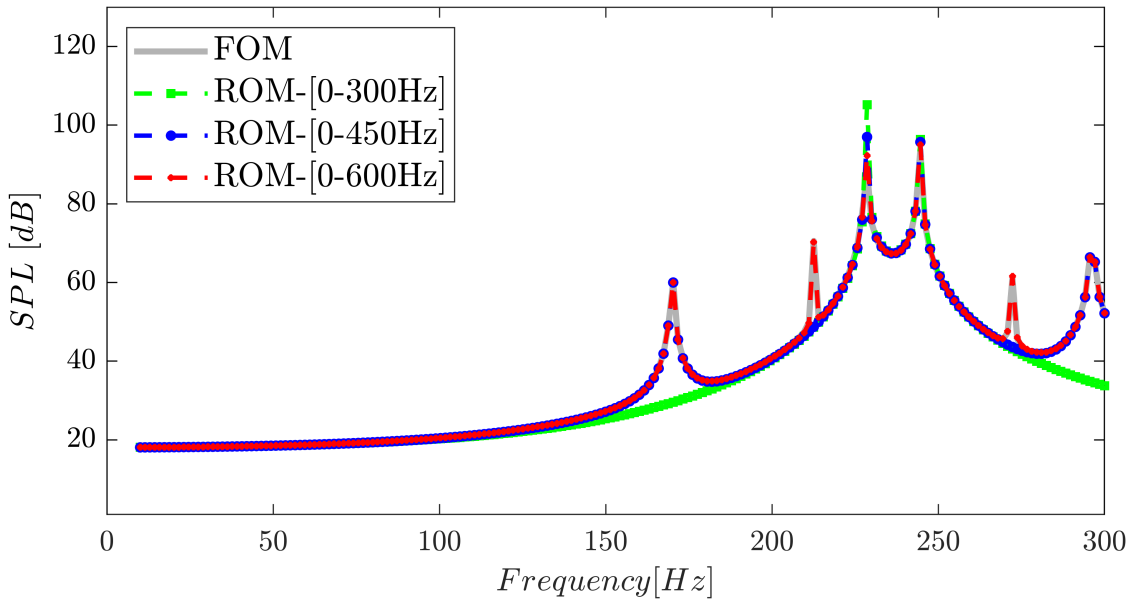

Figure 4.4: Sound Pressure Level (SPL) inside the acoustic cavity: comparison between FOM and ROMs.

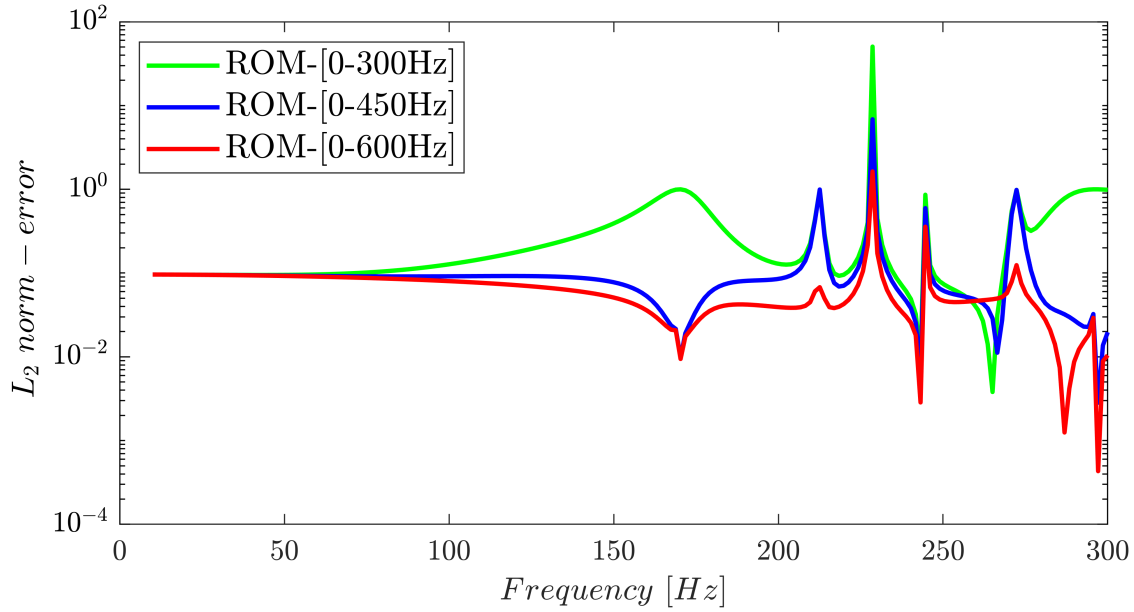

Figure 4.5: Comparison of the L_2-norm error between the Reduced Order Models (ROMs) and the Full Order Model (FOM).

to the FOM is computed and reported in Figure 4.5. The error decreases as the modal subspace is enriched, confirming that the projection-based ROMs retain the essential dynamics of the coupled problem.

From a computational perspective, the reduction in model order results in a drastic decrease in solution time, as shown in Table 4.4. While the full-order analysis requires about 95 seconds (for 200 frequency steps), the ROM-based simulations are carried out, considering an off-line phase to compute the basis ($3.3s$ for the structure and $3.1s$ for the acoustic modes). Then, knowing the basis, the FRF is computed in fraction of seconds. The latter computational time is a function of the number of selected acoustic and structural modes (which remain very small in the frequency of interest compared to the DOFs of the system). The ROM-model approximates the FOM without any significant loss of accuracy, except at the resonance frequency since no damping have been added to the system. Nevertheless, for the same frequency steps, the ROM should always converge toward the FOM by adding enough modes.

The results clearly demonstrate that the modal-based reduced models are capable of reproducing both the modal and forced responses of the coupled vibroacoustic system with excellent accuracy and a dramatic reduction in computational cost. In this example, selecting structural and acoustic modes up

Table 4.4: Computation time for the full-order model (FOM) and the three reduced-order models (ROMs). The value $6.4s$ corresponds to the time to compute the structural and acoustic modal analysis. In parenthesis, the speed up factor of ROM compared to the FOM is also reported.

t_{FOM} [s]	t_{ROM1}[s]	t_{ROM2} [s]	t_{ROM3} [s]
95	0.02+6.4 (14.8)	0.10+6.4 (14.6)	0.15+6.4 (14.5)

to approximately twice the frequency range of interest proves sufficient to accurately approximate the full-order model (FOM) within the reduced-order framework, yielding an efficient yet reliable ROM.

Although additional techniques exist for further enriching the reduced basis—such as

- including the static response at $\omega = 0$ in the structural subspace;
- complementing the basis with the fluid response associated with each structural mode using a pseudo-inverse operator—these approaches come with an increased computational burden in the offline phase.

While such enrichments may improve accuracy, especially in strongly coupled regimes, they require extra calculations that partially offset the efficiency gained from model reduction. For this reason, these techniques are not incorporated here, in order to keep the proposed workflow simple, lightweight, and easy to reproduce. Nevertheless, their integration represents a promising direction for future research and the further enhancement of vibroacoustic reduced-order modelling strategies.

4.4 Computational Efficiency and Scalability Considerations

The computational speed-up obtained with the present reduction strategy strongly depends on the size of the FOM and the number of selected modes. A key advantage of this approach is that structural and acoustic eigenmodes are computed separately, which is significantly cheaper than performing a fully coupled vibroacoustic eigenanalysis. Nevertheless, as the number of degrees of freedom increases, several contributions drive the computational cost:

- the CPU time associated with solving the full system;
- the cost of computing a sufficiently large set of eigenvalues and eigenvectors;

- the effort required to assemble the operators for both the FOM and the ROM.

The methodology remains highly efficient as long as the number of modes within the frequency band of interest remains small compared to the total number of degrees of freedom. However, this assumption may not hold for systems with very large acoustic domains or for structures made of extremely compliant materials (e.g., foams or viscoelastic layers), where a substantially larger modal basis may be needed to achieve the desired accuracy. Nevertheless, the integration of enriched modal bases and alternative reduction strategies represents a promising direction for future research and for further enhancing the accuracy and robustness of vibroacoustic reduced-order modelling.

4.5 Conclusion on projection on modal basis

To conclude, the projection of the coupled vibroacoustic problem onto the structural and acoustic modal bases has proven to be an effective strategy to drastically reduce the computational cost while maintaining a high level of accuracy. The comparison between the full-order model (FOM) and the reduced-order models (ROMs) has shown that the modal approach is able to accurately reproduce both the uncoupled and the coupled dynamic behaviour of the system. In particular, in the given example, by including all structural and acoustic modes up to approximately twice the frequency range of interest, seems enough to well reconstruct the coupled behaviour, but this should be the subject of further investigations with other parameters. Furthermore, in the shown example, the third reduced model (ROM3) provides an almost identical response to that of the full model, both in terms of natural frequencies and frequency response functions (FRFs). The analysis also highlights that the simpler reduced models (ROM1 and ROM2), although computationally cheaper, may fail to capture specific resonances when the excited structural mode does not efficiently couple with the retained acoustic subspace. While their accuracy could be improved by enriching the reduced bases with the quasi-static acoustic responses associated with the structural modes, such an approach would require solving additional linear systems and therefore partially compromise the computational advantage of the reduction process. Overall, the modal projection approach demonstrates a remarkable balance between efficiency and accuracy. It enables a significant reduction in the system size and computational time, by several orders of magnitude, without affecting the physical fidelity of the results. This methodology thus represents a solid foundation for the development of more advanced and parametric

Reduced Order Models (ROMs), which will be used in the next chapters to enable fast and accurate simulations.

Chapter 5

IGA vs FEM: 3D numerical examples

This chapter presents numerical examples for a variety of vibroacoustic applications. A detailed comparison between the Finite Element Method (FEM) and Isogeometric Analysis (IGA) is carried out, focusing on natural frequencies and overall system response. The objective is to highlight the advantages of IGA over FEM in terms of computational efficiency and accuracy. Comparisons are performed for coupled vibroacoustic problems as well as for purely acoustic and purely structural cases. Where available, analytical solutions are used for validation, while reference solutions are otherwise obtained using highly refined FEM models with a large number of degrees of freedom. This chapter provides a practical demonstration of the theoretical concepts discussed in previous chapters and sets the stage for evaluating the performance of IGA in realistic vibroacoustic scenarios.

Content

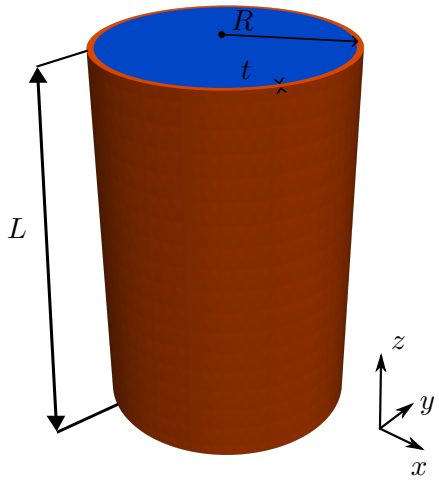

Figure 5.1: Fluid cavity (in blue) surrounded by a solid structure (in red)

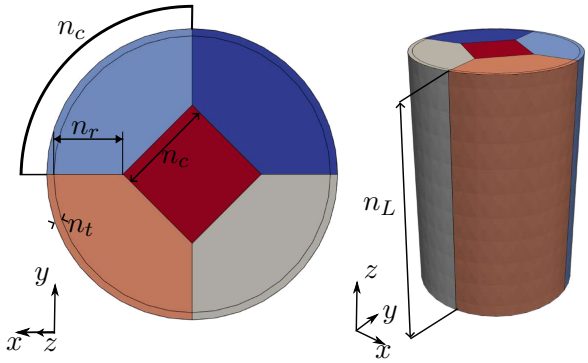

Figure 5.2: Structure and fluid design and its subdivisions

5.1 3D computations of cylinder filled with fluid

The problem under investigation is illustrated in Figure 5.1, where a fluid cavity is enclosed by a structure. As shown in Figure 5.2, the fluid cavity and the surrounding structure are respectively split in five and four subdomains, each highlighted by a different color. This subdivision ensures that only HEXA elements are generated during the meshing process (structured mesh). In Figure 5.2, n_c, n_L, n_t and n_r represent the number of elements in the circumferential, axial, thickness and radial direction, respectively. For sake of simplicity, $n_L = n_c = n_r$ is imposed. The cavity and the structure have compatible meshes at their interface. The geometric and material properties of the structure and fluid are shown in Table 5.1, where ρ_s is the structural density, ρ_f is the fluid density, c_0 is the sound speed in the considered fluid, E is the Young Modulus, ν is the Poisson coefficient, R is the

Table 5.1: Structural and fluid material and geometrical properties

$\rho_s \left[\frac{kg}{m^3}\right]$	$\rho_f \left[\frac{kg}{m^3}\right]$	$c_0 \left[\frac{m}{s}\right]$	E [Pa]	ν[-]	R[m]	t[m]	L[m]
2700	1.2	340	$7{\cdot}10^{10}$	0.3	1	0.05	3

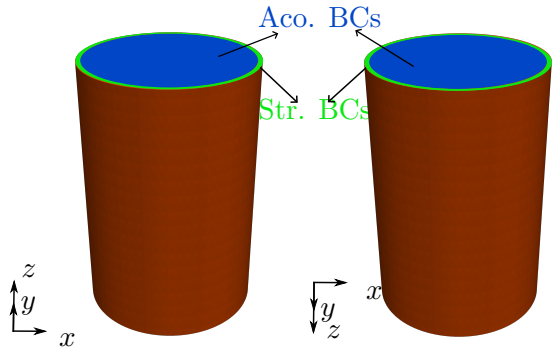

Figure 5.3: Structural and acoustic boundary conditions: only the axial structural displacements are allowed at the top and bottom cylinder part (green area); the acoustic normal velocity is imposed equal to 0 for the top and bottom fluid sections (blue area)

hollow cylinder external radius, t is the thickness and L is the height.

5.1.1 Problem modeling

The authors' methodology is based on comparing solutions from IGA and FEM with the semi-analytical ones [70]. In the latter, the process for obtaining the eigenfrequencies of a structural hollow cylinder is outlined, followed by analyses of the acoustic cavity and the vibroacoustic problem. The MATLAB code was developed by the authors to compute the analytical eigenfrequencies for the structural, acoustic, and vibroacoustic problem. For the FEM analysis, a polynomial interpolation of order two was imposed for all computations. The reason of that has been carefully explained in the Section 2. In contrast, for IGA, polynomial orders ranging from two to seven were considered.

The boundary conditions (BCs) imposed for the problem under consideration are shown in Figure 5.3. These BCs are consistent with those adopted in [70].

5.1.2 Structural results

In this section, only the structural problem is analyzed. The methodology follows the approach described in Section 5.1.1. For FEM analysis, a gradual increase of number of elements is performed,

Table 5.2: Structural FEM models, related numbers of free degrees of freedom and element discretization

FEM with p=2	n_c	n_t	DOFs
mod.1	7	2	6244
mod.2	8	2	8192
mod.3	11	2	15620
mod.4	13	2	21892
mod.5	15	2	29220
mod.6	17	2	37604

Table 5.3: Structural IGA models, related numbers of free degrees of freedom and element discretization

IGA	p=2			p=3			p=4			p=5			p=6			p=7		
	n_c	n_t	DOFs	n_c	n_t	DOFs	n_c	n_t	DOFs	n_c	n_t	DOFs	n_c	n_t	DOFs	n_c	n_t	DOFs
mod.1	10	2	5632	8	2	5800	8	2	7040	6	2	5800	5	2	5800	4	2	5800
mod.2	13	2	9184	12	2	11480	11	2	11480	9	2	9880	8	2	9880	6	2	8400
mod.3	16	2	13600	15	2	17000	14	2	17000	12	2	15040	10	2	13200	7	2	9880
mod.4	24	2	29600	18	2	26040	17	2	23600	15	2	21280	13	2	19080	10	2	15040

resulting in six distinct models. Table 5.2 shows the six models, detailing the degrees of freedom (DOFs) and the element number in each direction. For IGA analysis, on the other hand, a k-refinement ([2]) is performed. This refinement is based on a preliminary increase of the polynomial order followed by a gradual increase of knots number. Along the thickness, the polynomial order is increased only up to three, since the thickness is small and therefore there is no need for further refinement. For IGA analysis, four models are constructed for each polynomial order and the number of DOFs are shown in Table 5.3. After obtaining the analytical structural eigenfrequencies of the system from [70], and calculating the eigenfrequencies for each FEM and IGA system considered, it is possible to evaluate their percentage error against the reference solution (in this scenario it is the semi-analytical one), according to Equation (5.1).

$$\text{Error } [\%] = \left| \left(\frac{\text{freq}_{(\text{IGA/FEM})}}{\text{freq}_{\text{REFERENCE}}} - 1 \right) \times 100 \right| \tag{5.1}$$

Figures 5.4 and 5.5 show the percentage error on the eigenfrequencies calculated through FEM and IGA against the reference solution. The first 51 distinct structural modes are under investigation for this analysis. For the calculation, the maximum acceptable error is set at 1%. Another relevant

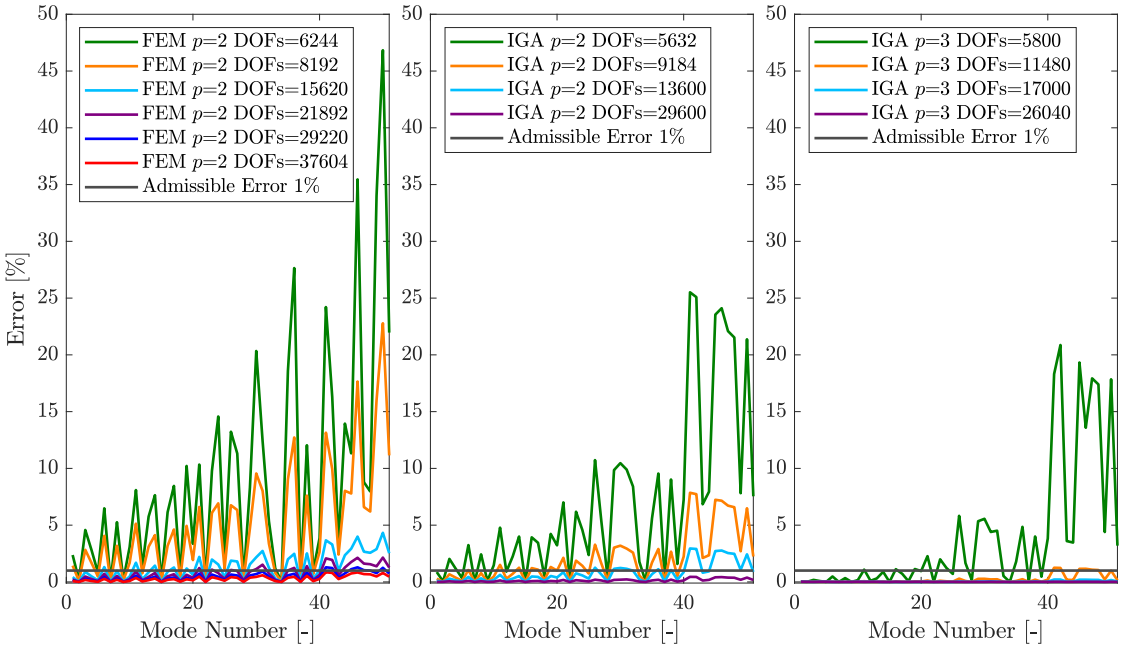

Figure 5.4: Structural eigenmodes percentage error using FEM with $p = 2$ and IGA with p=2 and p=3

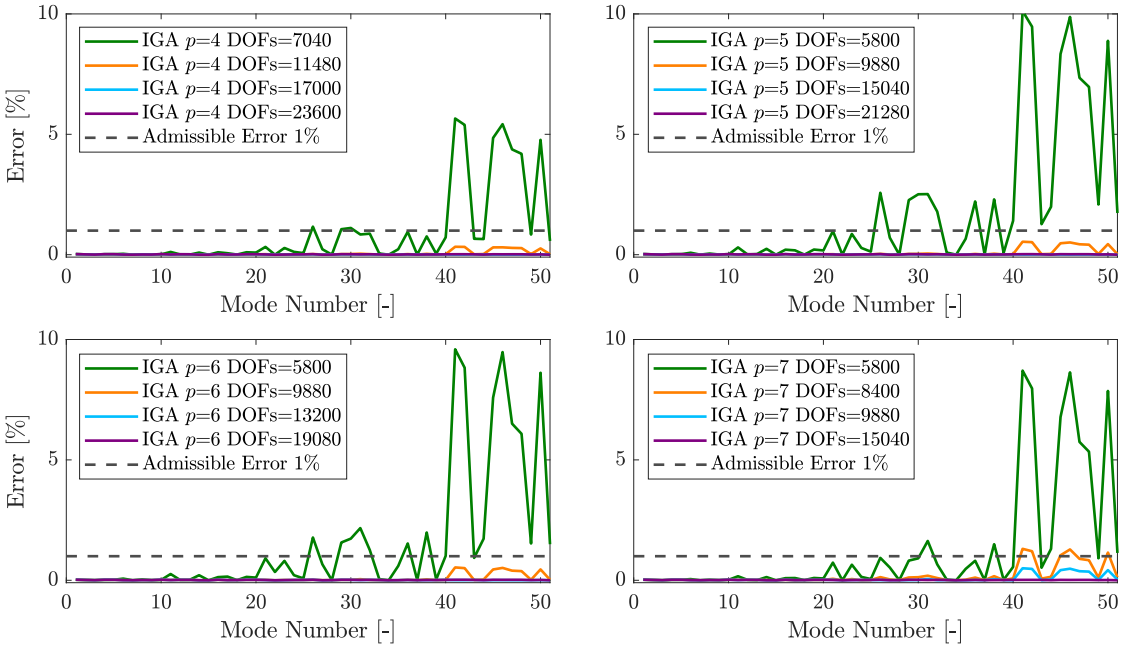

Figure 5.5: Structural eigenmodes percentage error using IGA with p=4, p=5, p=6 and p=7

Table 5.4: Structural FEM time details

FEM with p=2	t_{tot}^{str} $[s]$	t_{ref}^{str} [%]	t_{mat}^{str} [%]	t_{an}^{str} [%]
mod.1	131.5	0.08	0.68	99.24
mod.2	168.1	0.02	0.37	99.61
mod.3	396.2	0.02	0.34	99.64
mod.4	731.5	0.01	0.24	99.75
mod.5	895.7	0.01	0.26	99.73
mod.6	$1.4{\cdot}10^3$	0.01	0.21	99.78

factor to consider is the computational time of FEM and IGA. The total computational time can be expressed as:

$$t_{tot}^{str/aco/vibro} = \sum_i t_i^{str/aco/vibro} \tag{5.2}$$

In Equation (5.2) $t_{tot}^{str/aco/vibro}$ is the computation time in the structural, acoustic and vibroacoustic case. Regarding the structural FEM or IGA, t_{tot}^{str} is given by the sum of the meshing time (pre-processing) t_{ref}^{str}, the matrix construction time t_{mat}^{str}, and the time required to solve the linear problem in Equation (4.1) t_{an}^{str}. For a rational benchmarking between FEM and IGA, the computational time plays a crucial role. Tables 5.4, 5.5, and 5.6 present the total computational times for FEM and IGA, highlighting the percentage contribution of each intermediate time, relative to the total time: it is evident that the analysis time (t_{an}^{str}) is significantly higher than the others. This gap decreases as the polynomial order increases, since the computational time for assembling the elementary matrices, is directly linked to the number of Gauss integration points, which, in turn, is set at $p+1$. Figure 5.6 illustrates the total computational structural time for FEM and IGA. However, to gain an effective understanding, it is necessary to analyse Figure 5.6 with reference to the computational burden and Figures 5.4 and 5.5 for the corresponding accuracy. By analyzing these figures, it becomes evident that, to achieve a maximum error of 1%, the FEM requires the use of the most refined model, whereas for IGA with $p = 4$, the second model is sufficient. Referring then to Figure 5.6 for the total computational structural time, the second IGA model exhibits a lower time compared to the sixth FEM model.

Additionally, Figure 5.7 illustrates the convergence rate evaluated on several structural modes. Furthermore, Table 5.7 presents the frequency and wave numbers for each mode from the analytical solution, and Figure 5.8 displays the corresponding modal shapes. Moreover, Figure5.7 shows that,

Table 5.5: Structural IGA time details for p=2, p=3 and p=4

IGA	$p=2$				$p=3$				$p=4$			
	t^{str}_{tot} [s]	t^{str}_{ref} [%]	t^{str}_{mat}[%]	t^{str}_{an}[%]	t^{str}_{tot}[s]	t^{str}_{ref}[%]	t^{str}_{mat}[%]	t^{str}_{an}[%]	t^{str}_{tot}[s]	t^{str}_{ref}[%]	t^{str}_{mat}[%]	t^{str}_{an}[%]
mod.1	120.8	0.27	9.09	90.64	292.8	0.08	1.51	98.41	565.9	0.02	1.86	98.12
mod.2	188.5	0.07	0.94	98.9	862.9	0.02	0.87	99.11	$1.3{\cdot}10^3$	0.01	1.56	98.43
mod.3	358.4	0.05	0.72	99.23	$1.5{\cdot}10^3$	0.02	0.81	99.17	$2.2{\cdot}10^3$	0.03	1.45	98.52
mod.4	$1.7{\cdot}10^3$	0.06	0.48	99.46	$2.2{\cdot}10^3$	0.02	0.81	99.17	$3.5{\cdot}10^3$	0.02	1.37	98.61

Table 5.6: Structural IGA time details for p=5, p=6 and p=7

IGA	$p=5$				$p=6$				$p=7$			
	t^{str}_{tot} [s]	t^{str}_{ref} [%]	t^{str}_{mat}[%]	t^{str}_{an}[%]	t^{str}_{tot}[s]	t^{str}_{ref}[%]	t^{str}_{mat}[%]	t^{str}_{an}[%]	t^{str}_{tot}[s]	t^{str}_{ref}[%]	t^{str}_{mat}[%]	t^{str}_{an}[%]
mod.1	533.5	0.02	5.18	94.8	704.7	0.01	11.74	88.25	830.3	0.02	14.18	85.8
mod.2	$1.1{\cdot}10^3$	0.01	5.74	94.25	$1.8{\cdot}10^3$	0.01	9.69	90.30	$1.6{\cdot}10^3$	0.01	15.04	84.95
mod.3	$2.4{\cdot}10^3$	0.01	4.51	95.48	$2.1{\cdot}10^3$	0.01	12.63	87.36	$2.2{\cdot}10^3$	0.01	15.45	84.54
mod.4	$2.8{\cdot}10^3$	0.02	5.8	94.18	$3.6{\cdot}10^3$	0.02	12.68	87.3	$4.2{\cdot}10^3$	0.01	16.03	83.96

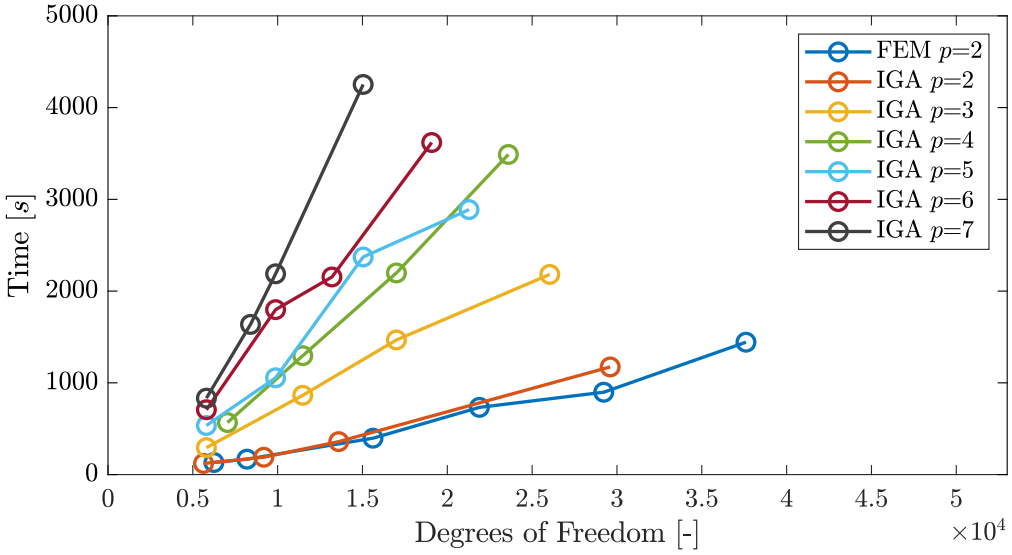

Figure 5.6: FEM and IGA total structural time (t^{str}_{tot})

Table 5.7: Exact frequencies of four structural modes and their wave numbers. m=axial wave number, n=circumferential wave number

mode number	m	n	freq[Hz]
6	1	5	314.0351
14	2	6	495.0992
21	1	7	612.3130
51	4	8	996.2362

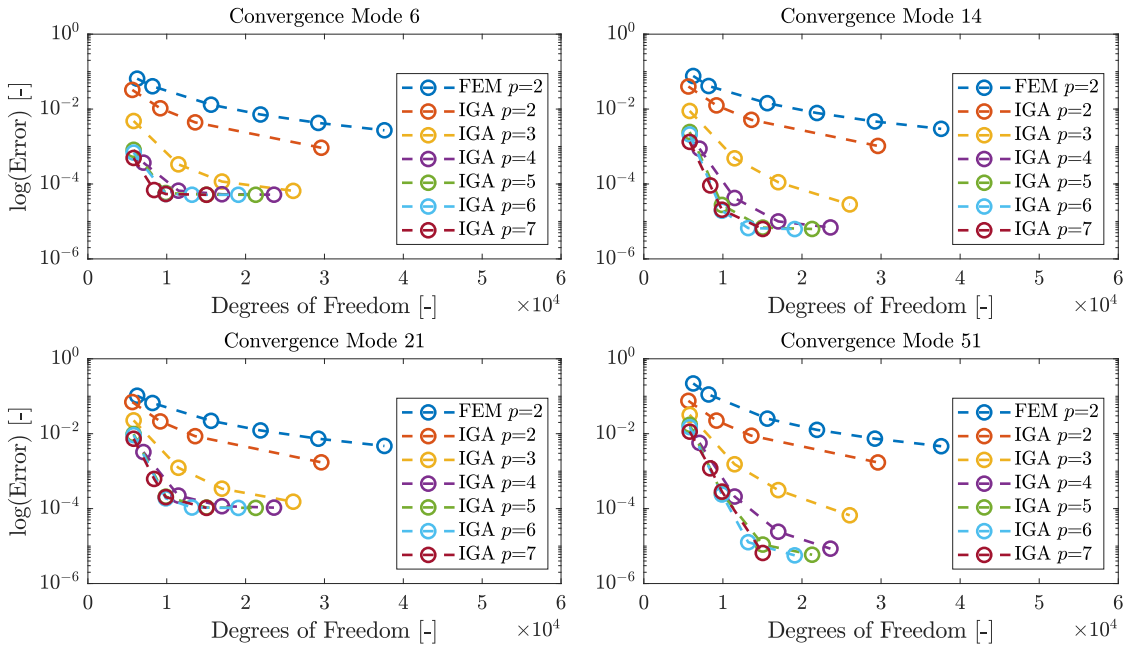

Figure 5.7: Convergence analysis of four structural modes

also when analyzing the eigenfrequencies convergence rate for the selected modes, the IGA approach performs much better than the FEM one. Additionally, it is shown that in IGA, once the polynomial degree reaches $p = 4$, the rate of convergence does not increase significantly. This observation was also noted by [34].

5.1.3 Acoustic results

The same methodology that has been used for the structure is used for the fluid, as detailed in the following. Again for the FEM, six models are created (keeping the order of the polynomial equal to two) as illustrated in Table 5.8. For the isogeometric models, as done for the structure, four models are created (Table 5.9), increasing the polynomial order from two to seven. The percentage error, calculated by Equation (5.1), considering the first 45 distinct numerical (FEM and IGA) and analytical fluid eigenfrequencies, is shown in Figures 5.9 and 5.10. A maximum acceptable error of 1% is set in relation to the calculated eigenfrequencies. To evaluate the acoustic computational time, it is possible to refer to the Equation (5.2) and introduce the total acoustic computational FEM and IGA time t_{tot}^{aco}, which is given by the sum of the meshing time t_{ref}^{aco}, the matrix construction time t_{mat}^{aco}, and the time required to solve the linear problem in Equation (4.2), t_{an}^{aco}. For a consistent

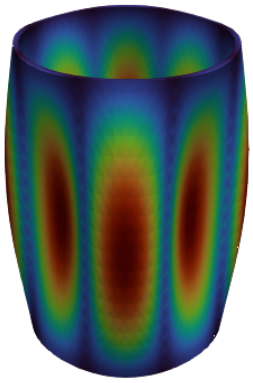

(a) Modal shape of the 6th mode at 314.0351 Hz with m=1 and n=5

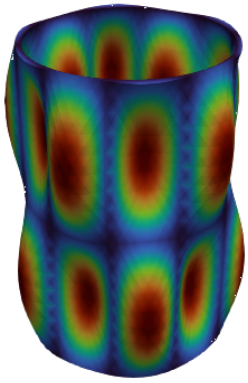

(b) Modal shape of the 14th mode at 495.0992 Hz with m=2 and n=6

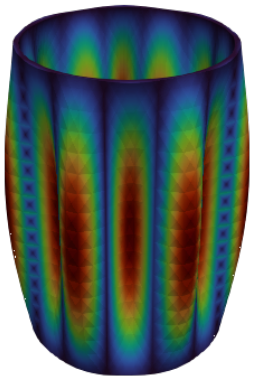

(c) Modal shape of the 21st mode at 612.3130 Hz with m=1 and n=7

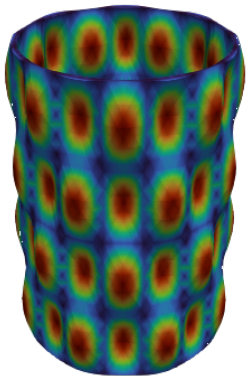

(d) Modal shape of the 51st mode at 996.2362 Hz with m=4 and n=8

Figure 5.8: Modal shapes of the four structural modes reported in Table 5.7. The peaks are highlighted in red while the nodal planes are in blue

Table 5.8: Fluid FEM models, related numbers of free degrees of freedom and element discretization

FEM with p=2	n_c	DOFs
mod.1	7	7932
mod.2	8	11633
mod.3	11	29228
mod.4	13	47568
mod.5	15	72316
mod.6	17	104432

Table 5.9: Fluid IGA models, related numbers of free degrees of freedom and element discretization

IGA	p=2		p=3		p=4		p=5		p=6		p=7	
	n_c	DOFs	n_c	DOFs	n_c	DOFs	n_c	DOFs	n_c	DOFs	n_c	DOFs
mod.1	10	7536	8	5731	8	7536	6	5731	5	5731	4	5731
mod.2	13	15135	12	15135	11	15135	9	12208	8	12008	6	9685
mod.3	16	26640	15	26640	14	26640	12	22321	10	18496	10	12208
mod.4	24	82576	18	49456	17	42861	15	36880	13	31483	10	22321

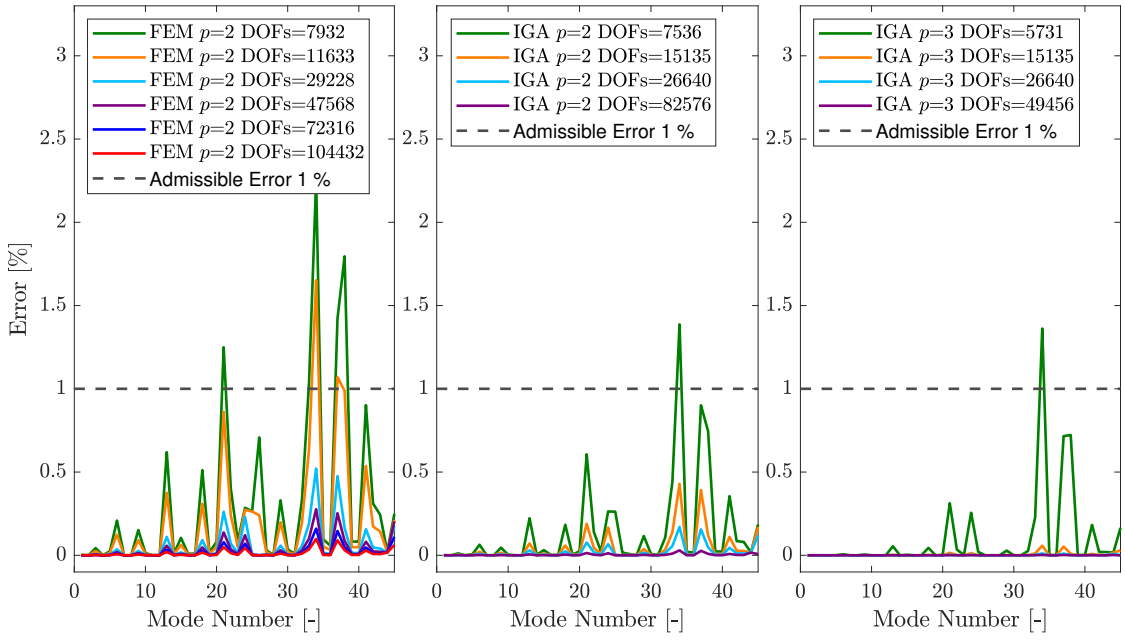

Figure 5.9: Acoustic eigenmodes percentage error using FEM with $p = 2$ and IGA with p=2 and p=3

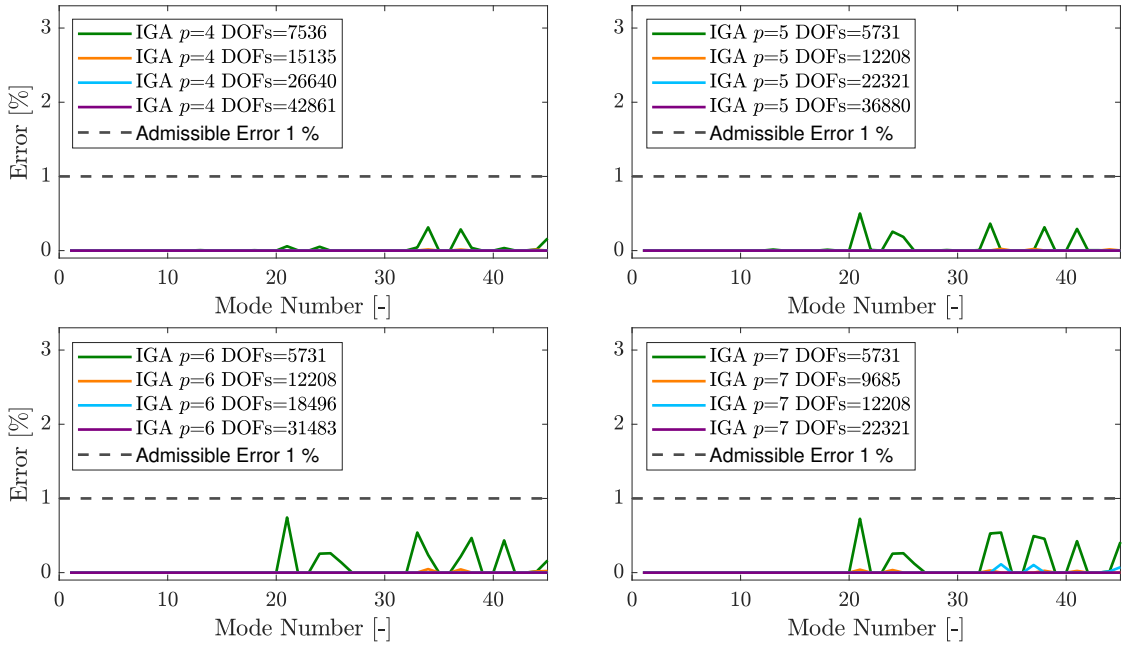

Figure 5.10: Acoustic eigenmodes percentage error using IGA with p=4, p=5, p=6 and p=7

benchmarking between FEM and IGA, the computational time must be also considered, as done for the structure. Tables 5.10, 5.11, and 5.12 present the total acoustic computational times for FEM and IGA, to solve the acoustic problem, highlighting the percentage contribution of each individual time. From these tables, it is evident that the analysis time (t_{an}^{aco}) is significantly higher than the others. This gap decreases as the polynomial degree increases, for the same reason explained for the structural analysis. Figure 5.11 illustrates the total acoustic computational time for FEM and IGA. By analyzing Figures 5.9, 5.10 and 5.11 , it becomes evident that, to achieve a maximum error of 1%, the FEM requires the use of the third model, whereas for IGA with $p = 5$, the first model is sufficient, with a consequent advantage in terms of computational time provided by the latter (the first IGA model exhibits a lower total computation time compared to the third FEM model). Figure5.12 illustrates the convergence rate of four acoustic modes. Table 5.13 provides the analytical values and wave numbers for each mode, while Figure5.13 shows the corresponding modal shapes. For the fluid domain, a similar behavior to that has been observed in the structural analysis is noted: in IGA, increasing the polynomial order beyond a certain value (e.g., $p = 5$) does not significantly enhances the convergence rate.

Table 5.10: Acoustic FEM time details

FEM with p=2	t_{tot}^{aco} $[s]$	t_{ref}^{aco} [%]	t_{mat}^{aco} [%]	t_{an}^{aco} [%]
mod.1	32.1	0.27	0.75	98.98
mod.2	61.7	0.21	0.74	99.05
mod.3	412.6	0.08	0.82	99.1
mod.4	783.3	0.08	0.73	99.1
mod.5	$2.1{\cdot}10^3$	0.05	0.92	99.03
mod.6	$4.3{\cdot}10^3$	0.04	0.84	99.12

Table 5.11: Acoustic IGA time details for p=2, p=3 and p=4

IGA	$p=2$				$p=3$				$p=4$			
	t_{tot}^{aco} $[s]$	t_{ref}^{aco} [%]	t_{mat}^{aco}[%]	t_{an}^{aco}[%]	t_{tot}^{aco}[s]	t_{ref}^{aco}[%]	t_{mat}^{aco}[%]	t_{an}^{aco}[%]	t_{tot}^{aco}[s]	t_{ref}^{aco}[%]	t_{mat}^{aco}[%]	t_{an}^{aco}[%]
mod.1	120.8	0.24	2.62	97.14	43.2	0.45	11.17	88.38	105.1	0.34	13.05	86.61
mod.2	189.1	0.4	2.73	96.87	269.6	0.33	5.46	94.21	434.5	0.27	8.02	91.71
mod.3	360.8	0.7	2.61	96.69	671.3	0.41	4.34	95.25	$1.1{\cdot}10^3$	0.31	6.48	93.21
mod.4	$1.2{\cdot}10^3$	3.73	2.66	93.61	$1.8{\cdot}10^3$	0.41	2.97	96.62	$2.8{\cdot}10^3$	0.33	5.79	93.88

Table 5.12: Acoustic IGA time details for p=5, p=6 and p=7

IGA	$p=5$				$p=6$				$p=7$			
	t_{tot}^{aco} $[s]$	t_{ref}^{aco} [%]	t_{mat}^{aco}[%]	t_{an}^{aco}[%]	t_{tot}^{aco}[s]	t_{ref}^{aco}[%]	t_{mat}^{aco}[%]	t_{an}^{aco}[%]	t_{tot}^{aco}[s]	t_{ref}^{aco}[%]	t_{mat}^{aco}[%]	t_{an}^{aco}[%]
mod.1	118.7	0.24	13.9	85.86	235.4	0.16	14.77	85.07	238.7	0.18	38.89	60.93
mod.2	448.1	0.22	12.2	87.58	958.8	0.13	14.42	85.45	$1.2{\cdot}10^3$	0.1	26.35	73.55
mod.3	$1.4{\cdot}10^3$	0.23	9.46	90.31	$1.8{\cdot}10^3$	0.17	15.45	84.38	$2.0{\cdot}10^3$	0.09	24.73	75.18
mod.4	$3.3{\cdot}10^3$	0.29	9.25	90.46	$4.5{\cdot}10^3$	0.21	15.07	84.72	$6.6{\cdot}10^3$	0.1	23.8	76.1

Table 5.13: Exact frequencies of four fluid modes and their wave numbers. m=axial wave number, n=circumferential wave number, k=radial wave number

mode number	m	n	k	freq[Hz]
6	3	0	0	170
21	5	0	0	283.3333
30	2	4	0	323.4004
40	1	5	0	369.8055

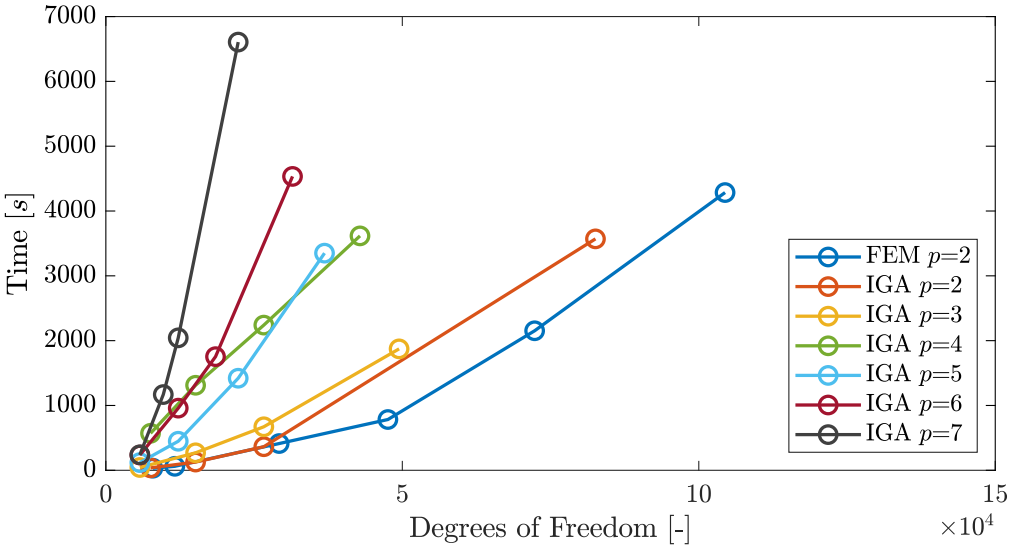

Figure 5.11: FEM and IGA total acoustic time (t_{tot}^{aco})

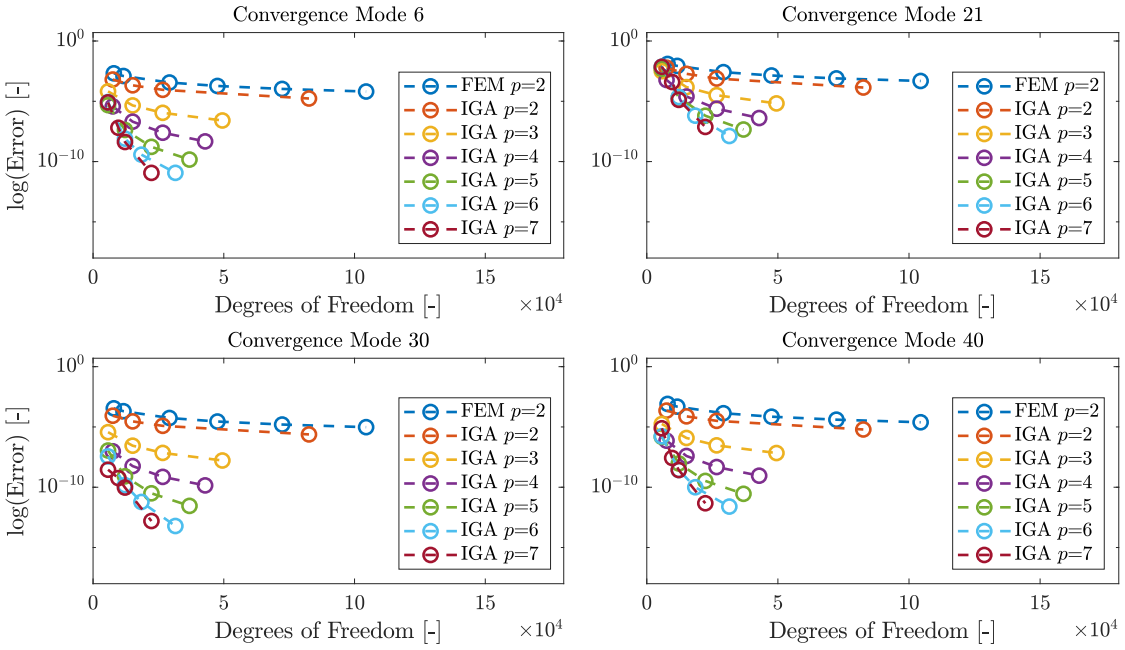

Figure 5.12: Convergence analysis of four fluid modes

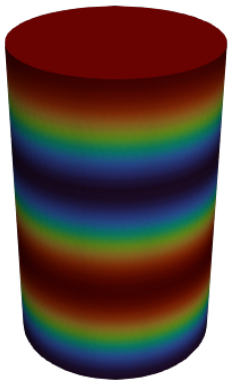

(a) Modal shape of the 6th mode at 170 Hz with m=3, n=0 and k=0

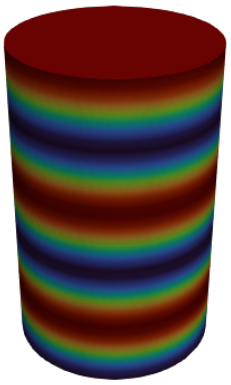

(b) Modal shape of the 21th mode at 283.3333 Hz with m=5, n=0 and k=0

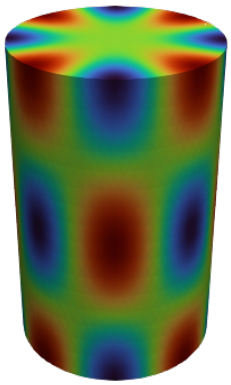

(c) Modal shape of the 30th mode at 323.4004 Hz with m=2, n=4 and k=0

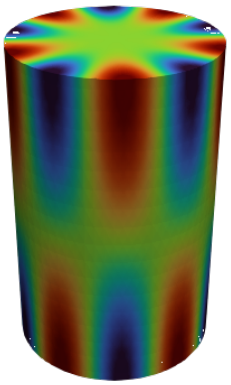

(d) Modal shape of the 40th mode at 369.8055 Hz with m=1, n=5 and k=0

Figure 5.13: Modal shapes of the four fluid modes reported in Table 5.13. The positive peaks are in red, the negative ones are in blue and the nodal planes are in light green.

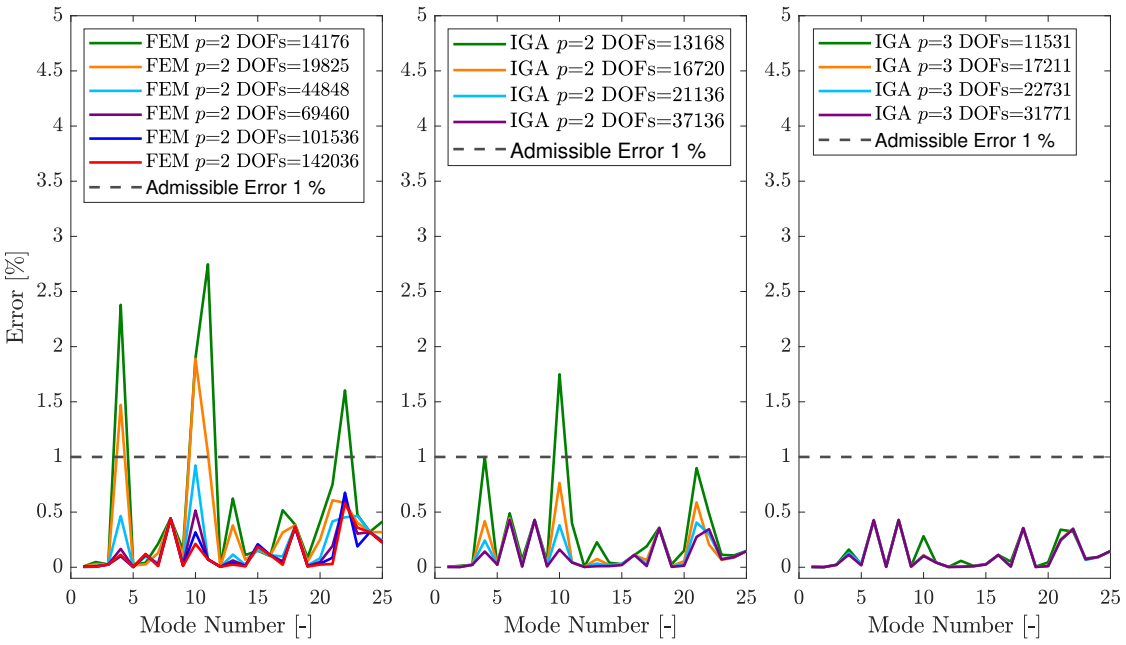

Figure 5.14: Vibroacoustic eigenmodes percentage error using FEM with p=2 and IGA with p=2 and p=3

5.1.4 Vibroacoustic results

This section tackles the vibroacoustic problem. The fluid-structural coupling, shown in Figure 5.1, is solved using an analytical approach [70] and a numerical one (FEM and IGA). When FEM or IGA methods are used, the modal approach is exploited. When using a modal approach (Section 5), the choice of an appropriate number of structural and acoustic modes is crucial. For the problem under consideration, a range [0-230]Hz has been chosen and all acoustic and structural modes in the [0-500]Hz range are considered. The error of the first 25 distinct vibroacoustic frequencies is shown in Figures 5.14 and 5.15. For coupled fluid-structural modes, the isogeometric approach achieves higher accuracy with fewer degrees of freedom. To evaluate the vibroacoustic computational time, it is possible to refer to the Equation (5.2) and introduce the total vibroacoustic computational FEM and IGA time t_{tot}^{vibro}, which is given by the sum of the meshing time t_{ref}^{vibro} (which is the sum of t_{ref}^{str} and t_{ref}^{aco}), the matrix construction time t_{mat}^{vibro} (t_{mat}^{str}+ t_{mat}^{aco}+ t_C, where t_C is the time to construct the coupling matrix $\mathbb{C}$), and the time required to solve the linear problems in Equation (4.1) and (4.2), t_{an}^{vibro}. Again, for a consistent benchmarking between FEM and IGA, the computational time must be considered. Tables 5.14, 5.15, and 5.16 present the total computational times for FEM and IGA, to solve the

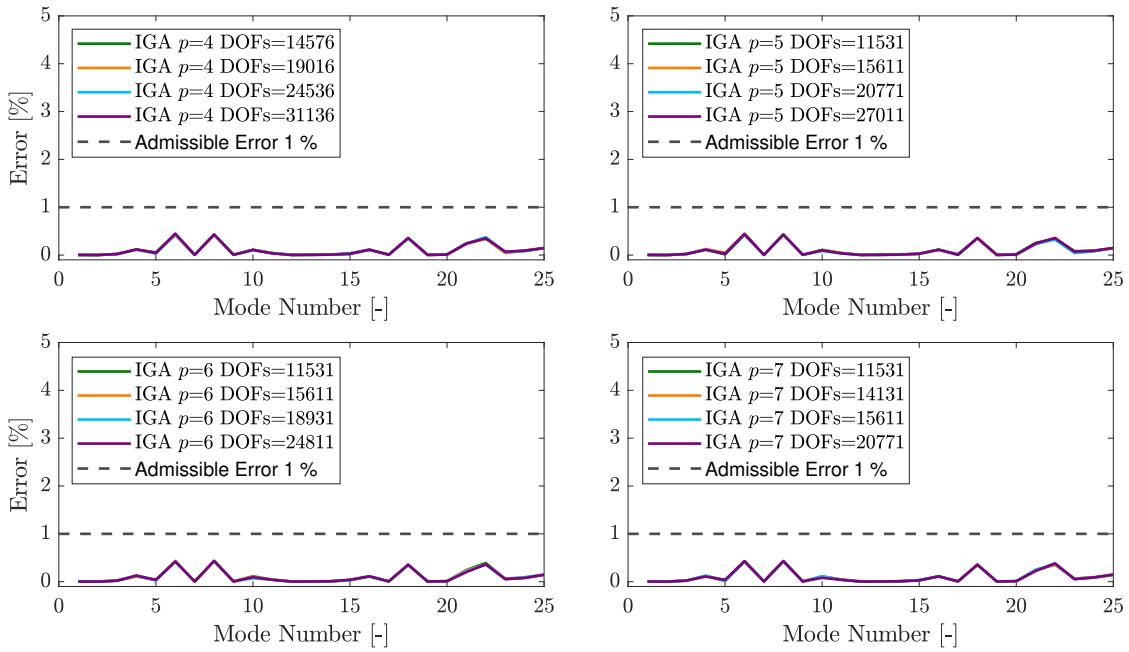

Figure 5.15: Vibroacoustic eigenmodes percentage error using IGA with p=4, p=5, p=6 and p=7

vibroacoustic problem, highlighting the percentage contribution of each individual time. From these tables, it is evident that the analysis time (t_{an}^{vibro}), which refers to the evaluation of the modal basis for the reduced problem, is significantly higher than the others. This gap decreases as the polynomial degree increases for the same reason explained before. Figure 5.16 illustrates the total computation time for FEM and IGA. As expected, the computational time increases with the polynomial degree. By analyzing Figures 5.16, 5.14 and 5.15 it becomes evident that, to achieve a maximum error of 1%, the FEM requires the use of the third model, whereas for IGA with p=3, the first model is sufficient, with a consequent advantage in terms of computational time (the first IGA model exhibits a lower total computational time compared to the third FEM model). Figure5.17 illustrates the convergence rate of four vibroacoustic modes. Table 5.17 provides the analytical values and wave numbers for each mode. In addition, a diagram is provided to understand how frequencies and modal shapes change, when using a decoupled rather than a coupled approach (Figure5.18). The coupled modal shapes are shown in Figure5.18 and their corresponding frequencies are reported in Table 5.18 with highlight of the dominant domain. The frequencies of the coupled vibroacoustic modes highlighted in Table5.18 do not vary substantially from the frequencies of the corresponding decoupled modes. The modal shapes, however, vary strongly when the dominant domain is the structural one. The same behavior

Table 5.14: Vibroacoustic FEM time details

FEM with p=2	t_{tot}^{vibro} $[s]$	t_{ref}^{vibro} [%]	t_{mat}^{vibro} [%]	t_{an}^{vibro} [%]
mod.1	163.7	0.12	1.24	98.64
mod.2	229.9	0.07	0.89	99.04
mod.3	809.36	0.05	0.64	99.3
mod.4	$1.5{\cdot}10^3$	0.05	0.55	99.4
mod.5	$3.1{\cdot}10^3$	0.04	0.42	99.54
mod.6	$5.7{\cdot}10^3$	0.04	0.33	99.63

Table 5.15: Vibroacoustic IGA time details with p=2, p=3 and p=4

IGA	$p=2$				$p=3$				$p=4$			
	t_{tot}^{vibro} $[s]$	t_{ref}^{vibro} [%]	t_{mat}^{vibro}[%]	t_{an}^{vibro}[%]	t_{tot}^{vibro}[s]	t_{ref}^{vibro}[%]	t_{mat}^{vibro}[%]	t_{an}^{vibro}[%]	t_{tot}^{vibro}[s]	t_{ref}^{vibro}[%]	t_{mat}^{vibro}[%]	t_{an}^{vibro}[%]
mod.1	158.8	0.38	9.28	90.34	336.9	0.12	3.03	96.85	672.4	0.07	3.8	96.13
mod.2	315.9	0.28	2.38	97.34	$1.1{\cdot}10^3$	0.09	2.08	97.83	$1.7{\cdot}10^3$	0.08	3.33	96.59
mod.3	722.93	0.37	1.78	97.85	$2.1{\cdot}10^3$	0.14	2.01	97.85	$3.3{\cdot}10^3$	0.12	3.25	96.63
mod.4	$4.7{\cdot}10^3$	0.97	0.85	98.18	$4.0{\cdot}10^3$	0.2	1.88	97.92	$6.3{\cdot}10^3$	0.16	3.46	96.38

Table 5.16: Vibroacoustic IGA time details with p=2, p=3 and p=4

IGA	$p=5$				$p=6$				$p=7$			
	t_{tot}^{vibro} $[s]$	t_{ref}^{vibro} [%]	t_{mat}^{vibro}[%]	t_{an}^{vibro}[%]	t_{tot}^{vibro}[s]	t_{ref}^{vibro}[%]	t_{mat}^{vibro}[%]	t_{an}^{vibro}[%]	t_{tot}^{vibro}[s]	t_{ref}^{vibro}[%]	t_{mat}^{vibro}[%]	t_{an}^{vibro}[%]
mod.1	653.8	0.06	6.98	92.96	942.3	0.05	12.7	87.25	$1.1{\cdot}10^3$	0.06	19.91	80.03
mod.2	$1.5{\cdot}10^3$	0.07	7.89	92.04	$2.7{\cdot}10^3$	0.05	11.53	88.42	$2.8{\cdot}10^3$	0.05	19.94	80.01
mod.3	$3.8{\cdot}10^3$	0.09	6.53	93.38	$3.9{\cdot}10^3$	0.09	14.12	85.79	$4.2{\cdot}10^3$	0.05	20.11	79.84
mod.4	$6.2{\cdot}10^3$	0.17	7.82	92.01	$8.1{\cdot}10^3$	0.13	14.21	85.66	$1.1{\cdot}10^4$	0.06	20.92	79.02

Table 5.17: Exact frequencies of four vibroacoustic modes and their wave numbers. m=axial wave number, n=circumferential wave number, k=radial wave number

mode number	m	n	k	freq[Hz]
7	3	0	0	169.9932
9	3	1	0	199.7362
13	4	0	0	226.6577
17	4	1	0	249.7371

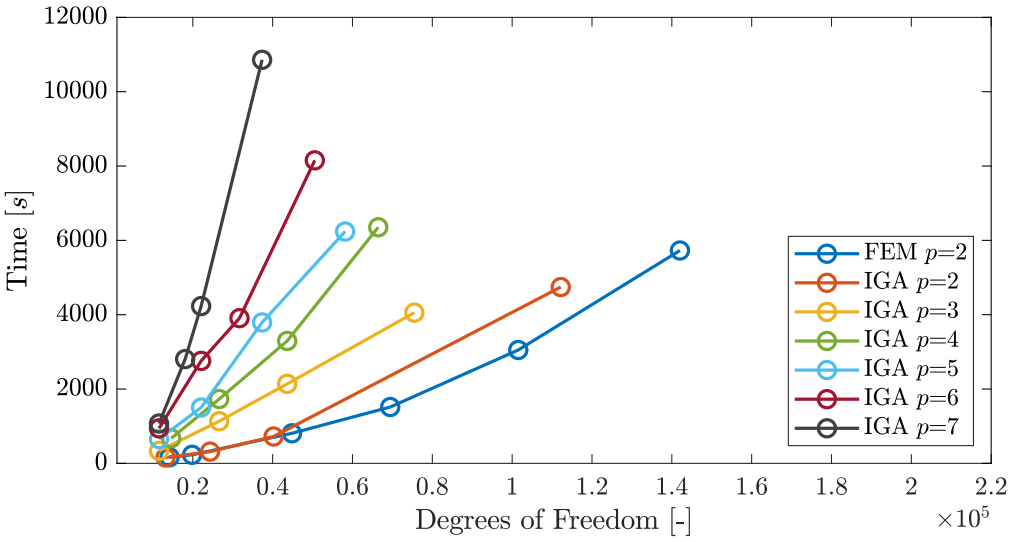

Figure 5.16: Total vibroacoustic time t_{tot}^{vibro}

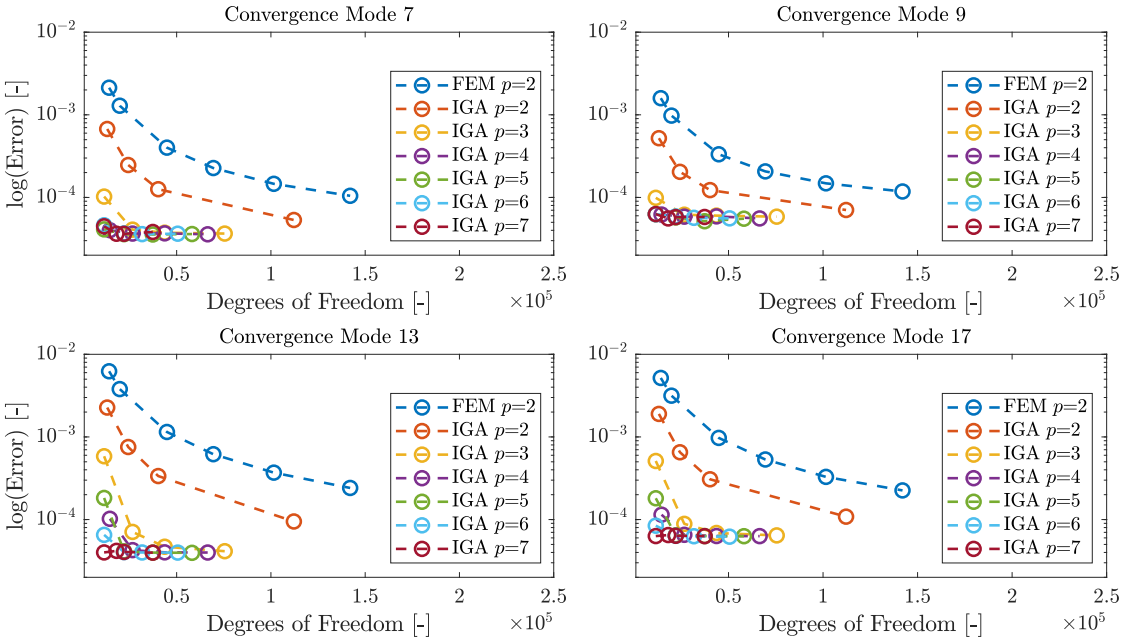

Figure 5.17: Convergence analysis of four vibroacoustic modes

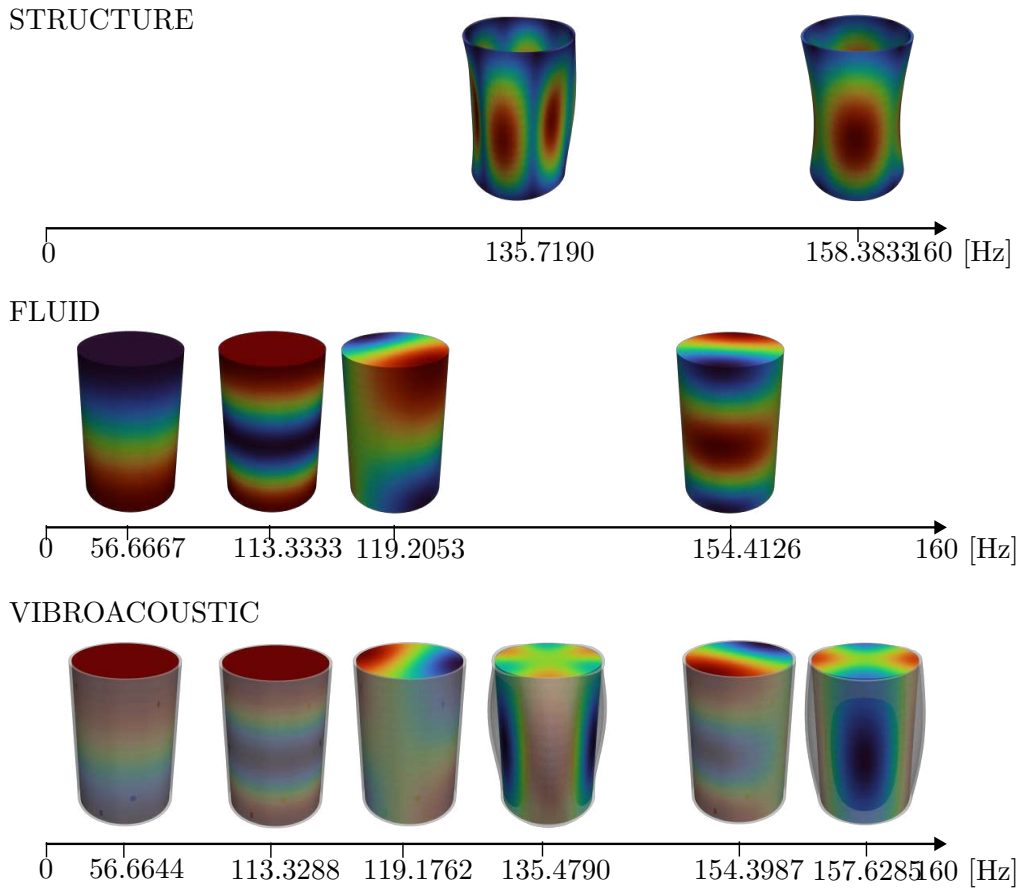

Figure 5.18: Structural, acoustic and vibroacoustic modes up to 160 Hz

Table 5.18: Frequencies of coupled and uncoupled systems

Structure Modes [Hz]	Fluid Modes [Hz]	Coupled Modes [Hz]	Dominant Domain
-	56.6667	56.6644	F
-	113.3333	113.3288	F
-	119.2053	119.1762	F
135.7190	-	135.4790	S+F
-	154.4126	154.3987	F
158.3833	-	157.6285	S+F

Table 5.19: Structural and fluid material properties for simplified vehicle model application

$\rho_{sc}\left[\frac{kg}{m^3}\right]$	$\rho_{fc}\left[\frac{kg}{m^3}\right]$	$c_0\left[\frac{m}{s}\right]$	E_c [Pa]	ν_c[-]
7860	1.2	340	$2.1{\cdot}10^{12}$	0.3

is highlighted in [82]. In fact, although the frequencies of coupled vs. decoupled modes do not vary substantially, it is evident that when a structural mode is present, the fluid response is closely related to the structural modal shape. For instance, the vibroacoustic mode at 56.6644 Hz corresponds to the acoustic mode at 56.6667 Hz and the modal shape is just related to the acoustic domain, in fact there is no structural response due to the acoustic field. On the other hand, the vibroacoustic mode at 135.7190 Hz, corresponds to the structural mode at 135.7190 Hz and the fluid response due to this latter mode is evident from Fig 5.18. This result justifies the initial hypothesis of weak coupling and the consequent use of the decoupled modes.

5.2 3D computations of simplified vehicle model

The problem under investigation is illustrated in Figure 5.19, which represents a classical vibroacoustic problem in the automotive field. The vehicle dynamic is crucial to evaluate the perceived comfort of the users [1].The material properties of the car structure and fluid are shown in Table 5.19. These values have been calibrated to get realistic frequencies. The boundary conditions imposed for the simplified vehicle model under consideration are shown in Figure 5.19. The geometrical properties, which can be useful to replicate the car design, are highlighted in Appendix A and can be also obtained from the code vibroacoustic-iga-fem.

5.2.1 Problem modeling

The authors' methodology is based on comparing solutions from IGA and FEM with an overkilled FEM solution (192966 and 390538 structural and acoustic DOFs, respectively). For the FEM analysis, a polynomial interpolation of order two was imposed for all computations whilst, for IGA, polynomial orders ranging from two to seven were considered. Also for this application, the same discretization is imposed in all directions (n_c), except for the structural thickness, where a different number of elements is used (n_t). The cavity and the structure have compatible meshes at their interface. For this

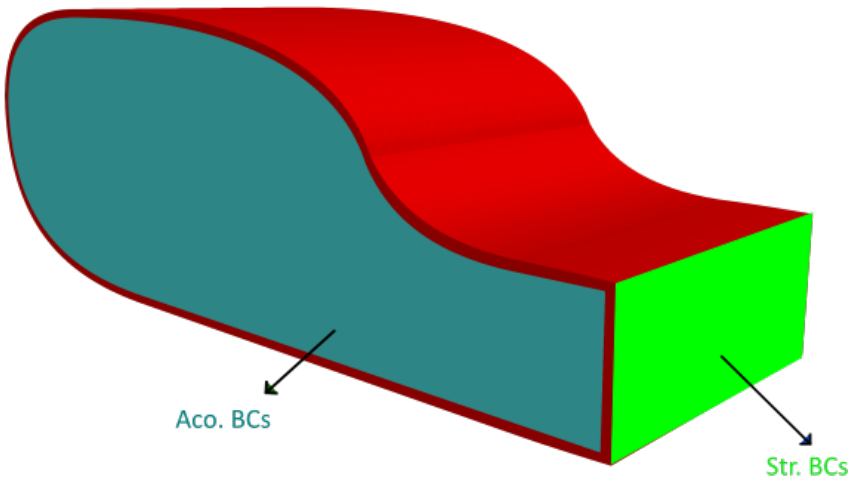

Figure 5.19: Geometry and boundary conditions for the simplified vehicle model application. On the light green area all the displacements are fixed whilst, on the blue area, the acoustic normal velocity is imposed equal to zero

application the frequency range of interest is [0-150]Hz and therefore to reconstruct the vibroacoustic eigenfrequencies through the projection of modal basis, all the structural and acoustic modes, in the range [0-300]Hz, are taken into account. The considered range is consistent with a realistic automotive application [1].

5.2.2 Structural results

In this section, only the structural problem is analysed. The methodology follows the approach described in Section 5.1.1. For FEM analysis, a gradual increase of number of elements is performed, resulting in six distinct models. Table 5.20 shows the six models, detailing the degrees of freedom (DOFs) and the element number in each direction. For IGA analysis, four models are constructed for each polynomial order and the number of DOFs are shown in Table 5.21. After obtaining the reference structural eigenfrequencies of the system from an overkilled FEM solution, and calculating the eigenfrequencies for each FEM and IGA system considered, it is possible to evaluate their percentage error, according to Equation (5.1). Figures 5.20 and 5.21 show the percentage error on the eigenfrequencies calculated through FEM and IGA against the reference solution. The first 13 structural modes, that have been found out in the considered range (0-300 Hz), are under investigation for this analysis. Tables 5.22, 5.23, and 5.24 present the total computational times for FEM and

Table 5.20: Structural FEM models, related numbers of free degrees of freedom and element discretization for the simplified vehicle model application

FEM with p=2	n_c	n_t	DOFs
mod.1	4	2	5709
mod.2	5	2	8652
mod.3	6	2	12201
mod.4	7	2	16356
mod.5	8	2	21117
mod.6	10	2	32457

Table 5.21: Structural IGA models, related numbers of free degrees of freedom and element discretization for the simplified vehicle model application

IGA	p=2			p=3			p=4			p=5			p=6			p=7		
	n_c	n_t	DOFs	n_c	n_t	DOFs	n_c	n_t	DOFs	n_c	n_t	DOFs	n_c	n_t	DOFs	n_c	n_t	DOFs
mod.1	6	2	6192	4	2	5901	2	2	4212	2	2	5901	2	2	7872	2	2	10125
mod.2	8	2	9960	6	2	10125	4	2	7872	3	2	7872	3	2	10125	3	2	12660
mod.3	10	2	14616	8	2	15477	8	2	18576	6	2	15477	5	2	15477	5	2	18576
mod.4	15	2	30141	14	2	38301	12	2	33792	10	2	29565	9	2	35865	7	2	25620

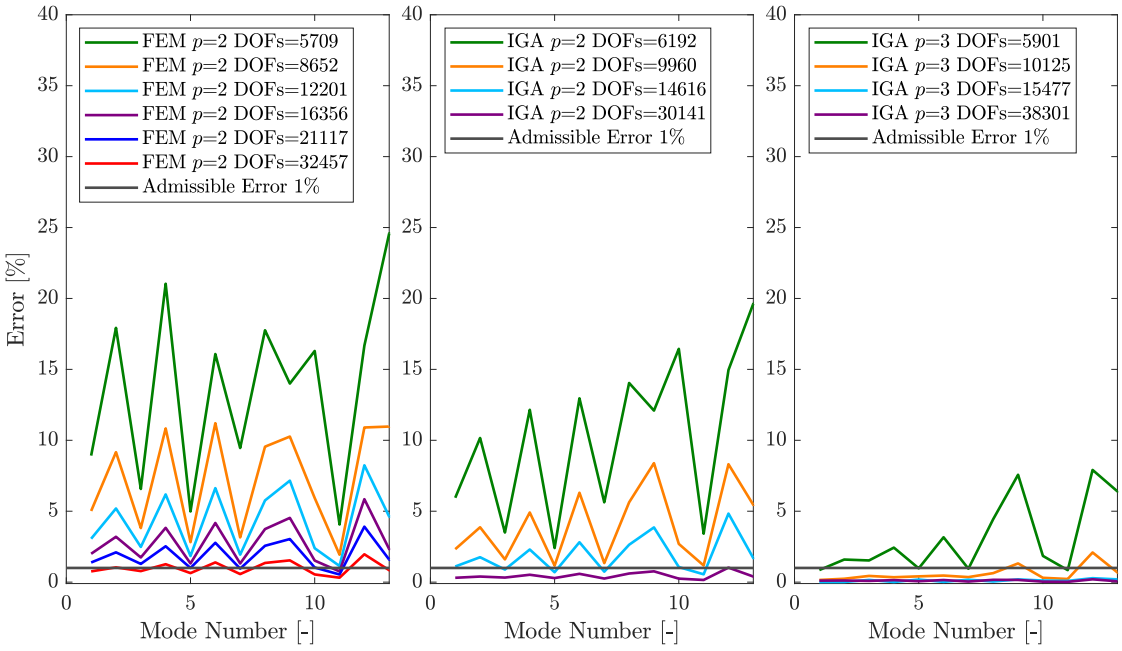

Figure 5.20: Structural eigenmodes percentage error using FEM with $p = 2$ and IGA with p=2 and p=3 for the simplified vehicle model application

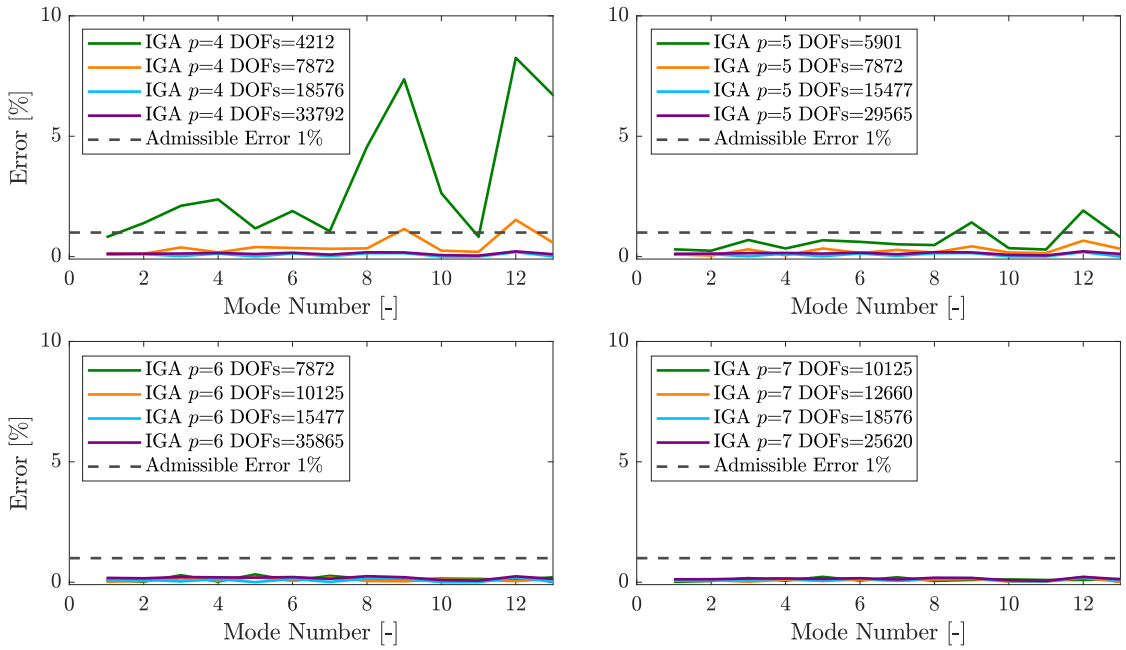

Figure 5.21: Structural eigenmodes percentage error using IGA with p=4, p=5, p=6 and p=7 for the simplified vehicle model application

IGA, highlighting the percentage contribution of each intermediate time, relative to the total time. For this application the analysis (t_{an}^{str}) and matrices construction time (t_{mat}^{str}) have the same order of magnitude. This result is consistent with what was expected, considering that just few modes have been requested during the analysis. The Figure 5.22 illustrates the total computational structural time for FEM and IGA. However, to gain an effective understanding, it is necessary to analyse Figure 5.22 with reference to the computational burden and Figures 5.20 and 5.21 for the corresponding accuracy. By analyzing these figures, it becomes evident that, to achieve a maximum error of 1%, the FEM requires the use of the most refined model (that for some frequencies is not even enough), whereas for IGA with $p = 5$, the first model is sufficient. Referring then to Figure 5.22 for the total computational structural time, the first IGA model exhibits a lower time compared to the sixth FEM model.

Additionally, Figure 5.23 illustrates the convergence rate evaluated on several structural modes. Furthermore, Table 5.25 presents the frequency for each mode of the reference overkilled solution, and Figure 5.24 displays the corresponding modal shapes.

Moreover, Figure5.23 shows that, also when analyzing the eigenfrequencies convergence rate for the selected modes, the IGA approach performs much better than the FEM one. Additionally, it is shown that in IGA, once the polynomial degree reaches $p = 3$, the rate of convergence does not

Table 5.22: Structural FEM time details for the simplified vehicle model application

FEM with p=2	t_{tot}^{str} $[s]$	t_{ref}^{str} [%]	t_{mat}^{str} [%]	t_{an}^{str} [%]
mod.1	1.96	6.56	34.85	58.59
mod.2	2.29	1.05	30.23	68.72
mod.3	3.48	1.15	28.41	70.44
mod.4	4.71	1.03	26.59	72.38
mod.5	6.53	0.93	24.16	74.91
mod.6	11	0.87	22.34	76.79

Table 5.23: Structural IGA time details for p=2, p=3 and p=4 for the simplified vehicle model application

IGA	$p=2$				$p=3$				$p=4$			
	t_{tot}^{str} $[s]$	t_{ref}^{str} [%]	t_{mat}^{str}[%]	t_{an}^{str}[%]	t_{tot}^{str}[s]	t_{ref}^{str}[%]	t_{mat}^{str}[%]	t_{an}^{str}[%]	t_{tot}^{str}[s]	t_{ref}^{str}[%]	t_{mat}^{str}[%]	t_{an}^{str}[%]
mod.1	4.74	2.80	70.48	26.72	4.75	0.38	85.59	13.03	1.79	0.70	68.25	31.05
mod.2	4.29	2.39	46.90	50.71	3.16	1.70	58.54	39.76	2.20	1.31	72.43	26.26
mod.3	6.45	1.52	43.14	55.34	5.20	1.43	55.89	42.68	6.53	1.05	65.56	33.39
mod.4	15.84	2.19	36.55	61.26	15.86	2.08	46.44	51.48	15.18	1.01	59.79	39.20

Table 5.24: Structural IGA time details for p=5, p=6 and p=7 for the simplified vehicle model application

IGA	$p=5$				$p=6$				$p=7$			
	t_{tot}^{str} $[s]$	t_{ref}^{str} [%]	t_{mat}^{str}[%]	t_{an}^{str}[%]	t_{tot}^{str}[s]	t_{ref}^{str}[%]	t_{mat}^{str}[%]	t_{an}^{str}[%]	t_{tot}^{str}[s]	t_{ref}^{str}[%]	t_{mat}^{str}[%]	t_{an}^{str}[%]
mod.1	1.11	0.74	83.44	28.00	2.52	0.38	91.79	7.83	4.32	2.23	92.74	5.03
mod.2	1.41	1.55	74.19	24.26	2.03	1.61	77.91	20.48	2.69	1.14	83.17	15.69
mod.3	5.32	0.69	77.04	22.27	4.79	0.69	82.09	17.22	7.10	0.52	86.65	12.83
mod.4	12.92	0.7	71.21	28.09	13.73	0.48	79.16	20.36	12.32	0.45	85.50	14.05

Table 5.25: Exact frequencies of four structural modes

mode number	freq[Hz]
4	68.1810
8	154.6168
9	176.3456
12	250.6239

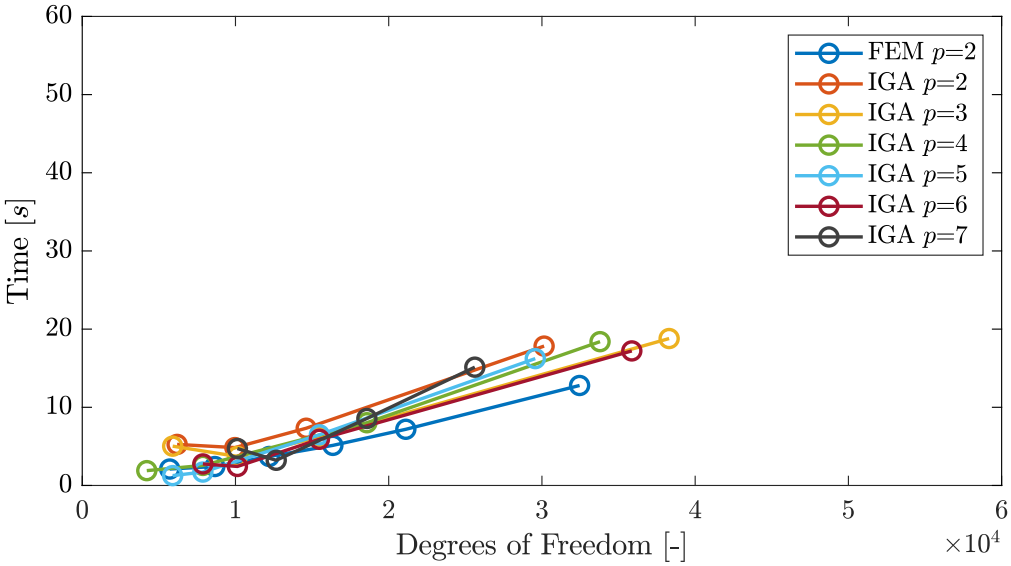

Figure 5.22: FEM and IGA total structural time (t_{tot}^{str}) for the simplified vehicle model application

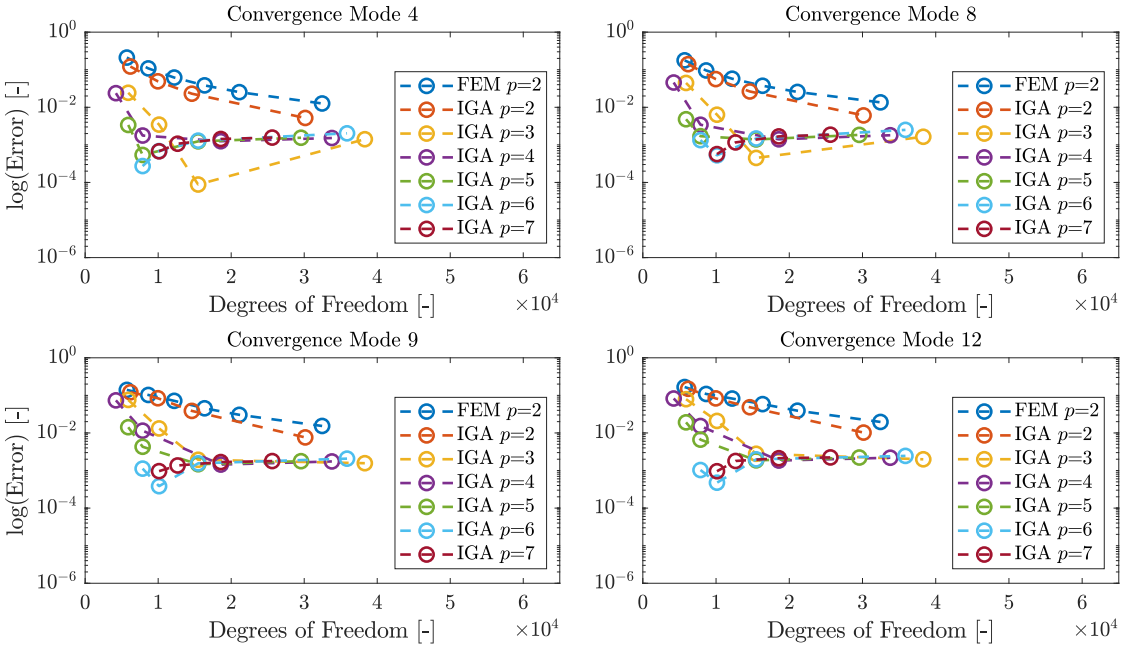

Figure 5.23: Convergence analysis of four structural modes

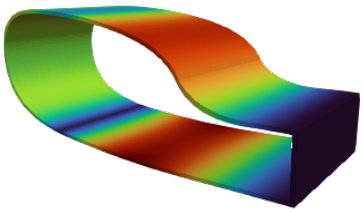

(a) Modal shape of the 4th mode at 68.1810 Hz

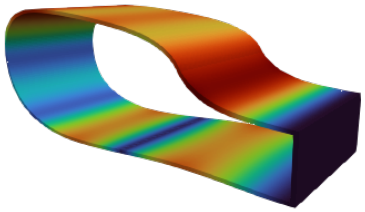

(b) Modal shape of the 8th mode at 154.6168 Hz

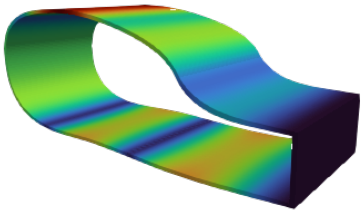

(c) Modal shape of the 9th mode at 176.3456 Hz

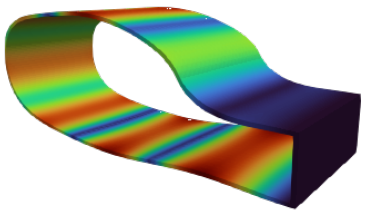

(d) Modal shape of the 12th mode at 250.6239 Hz

Figure 5.24: Modal shapes of the four structural modes reported in Table 5.25. The peaks are highlighted in red while the nodal planes are in blue

increase significantly.

5.2.3 Acoustic results

The same methodology that has been used for the structure is used for the fluid, as detailed in the following. Again for the FEM, six models are created (keeping the order of the polynomial equal to two) as illustrated in Table 5.26. For the isogeometric models, as done for the structure, four models are created (Table 5.27), increasing the polynomial order from two to seven. The percentage error, calculated by Equation (5.1), considering the first 23 numerical (FEM and IGA) and reference

Table 5.26: Fluid FEM models, related numbers of free degrees of freedom and element discretization for the simplified vehicle model application

FEM with p=2	n_c	DOFs
mod.1	4	3329
mod.2	5	6186
mod.3	6	10333
mod.4	7	16010
mod.5	8	23457
mod.6	10	44621

Table 5.27: Fluid IGA models, related numbers of free degrees of freedom and element discretization for the simplified vehicle model application

IGA	p=2		p=3		p=4		p=5		p=6		p=7	
	n_c	DOFs	n_c	DOFs	n_c	DOFs	n_c	DOFs	n_c	DOFs	n_c	DOFs
mod.1	6	1536	4	1029	2	648	2	1029	2	1536	2	2187
mod.2	8	3000	6	2187	4	1536	3	1536	3	2187	3	3000
mod.3	10	5184	8	3993	8	5184	6	3993	5	3993	5	5184
mod.4	15	14739	14	14739	12	12288	10	10125	9	10125	7	8232

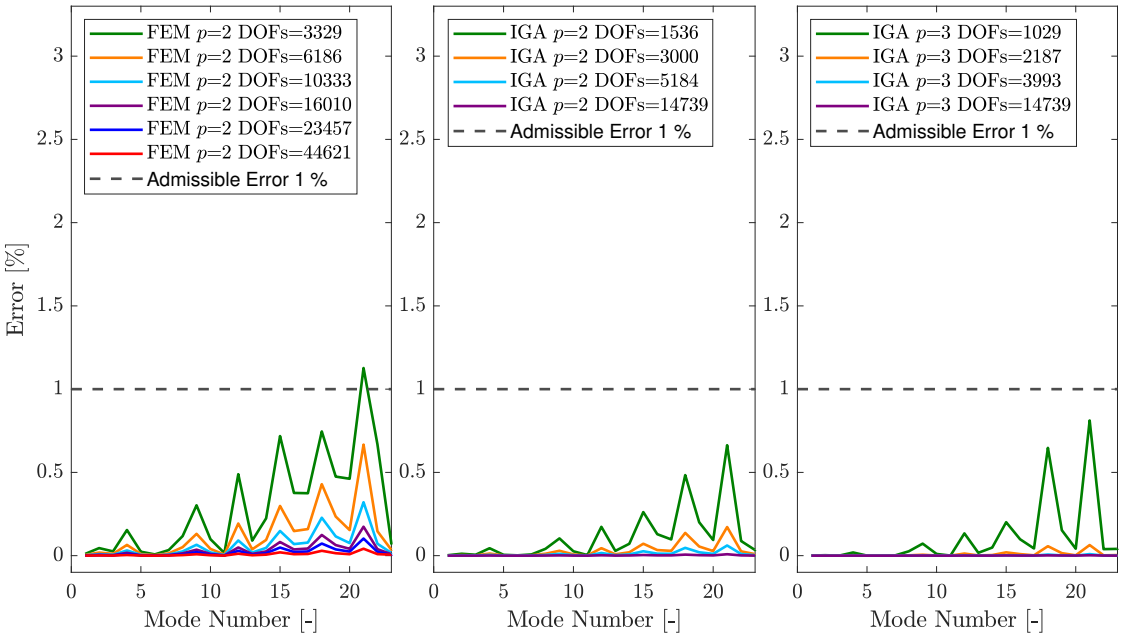

Figure 5.25: Acoustic eigenmodes percentage error using FEM with $p = 2$ and IGA with p=2 and p=3 for the simplified vehicle model application

fluid eigenfrequencies, is shown in Figures 5.25 and 5.26. Only the first 23 fluid modes are taken into account, as they fall within the considered range (0-300 Hz).

A maximum acceptable error of 1% is set in relation to the calculated eigenfrequencies. To evaluate the acoustic computational time, it is possible to refer to the Equation (5.2). Tables 5.28, 5.29, and 5.30 present the total acoustic computational times for FEM and IGA, to solve the acoustic problem, highlighting the percentage contribution of each individual time. Figure 5.27 illustrates the total acoustic computational time for FEM and IGA. By analyzing Figures 5.25, 5.26 and 5.27, it becomes evident that, to achieve a maximum error of 1%, the FEM requires the use of the second

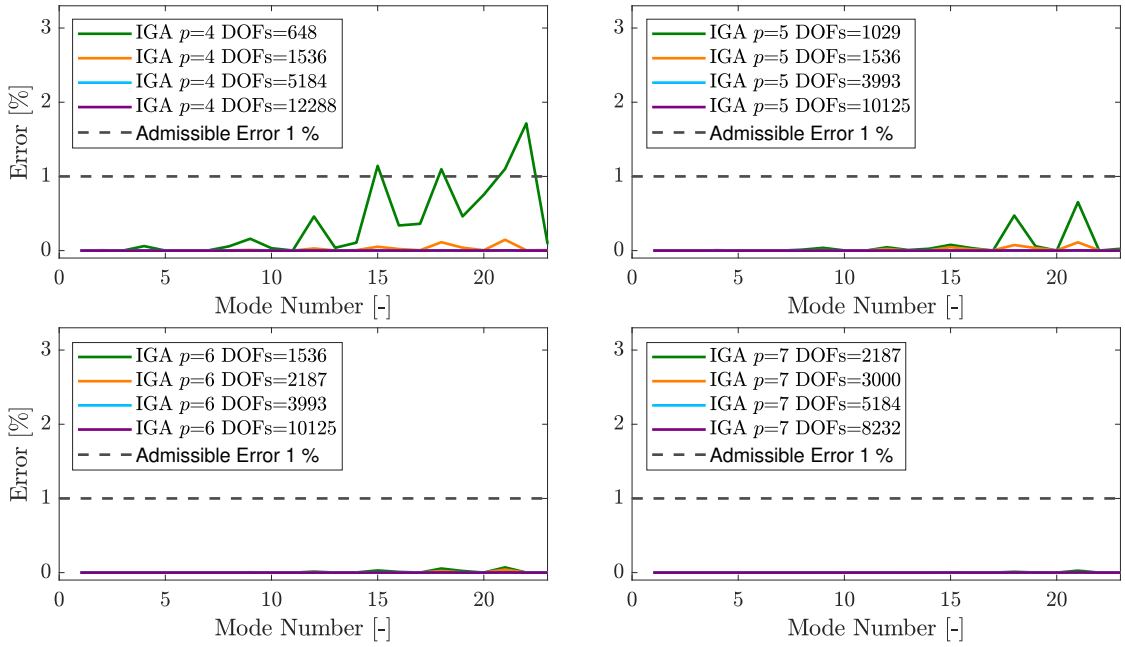

Figure 5.26: Acoustic eigenmodes percentage error using IGA with p=4, p=5, p=6 and p=7 for the simplified vehicle model application

model, whereas for IGA with $p = 3$, the first model is sufficient, with a consequent advantage in terms of computational time provided by the latter (the first IGA model exhibits a lower total computation time compared to the second FEM model).

Figure5.28 illustrates the convergence rate of four acoustic modes. Table 5.31 provides the reference values, while Figure5.29 shows the corresponding modal shapes. For the fluid domain, a similar behavior to that has been observed in the structural analysis is noted: in IGA, increasing the polynomial order beyond a certain value (e.g., $p = 4$) does not significantly enhances the convergence rate.

Table 5.28: Acoustic FEM time details for the simplified vehicle model application

FEM with p=2	t_{tot}^{aco} $[s]$	t_{ref}^{aco} [%]	t_{mat}^{aco} [%]	t_{an}^{aco} [%]
mod.1	12.30	0.3	21.93	77.77
mod.2	32.06	0.16	29.07	70.77
mod.3	78.23	0.11	28.67	71.22
mod.4	151.30	0.09	33.08	66.83
mod.5	323.83	0.06	35.72	64.22
mod.6	$1.13{\cdot}10^3$	0.04	42.14	57.82

Table 5.29: Acoustic IGA time details with p=2, p=3 and p=4 for the simplified vehicle model application

IGA	$p=2$				$p=3$				$p=4$			
	t_{tot}^{aco} $[s]$	t_{ref}^{aco} [%]	t_{mat}^{aco}[%]	t_{an}^{aco}[%]	$t_{tot}^{aco}[s]$	t_{ref}^{aco}[%]	t_{mat}^{aco}[%]	t_{an}^{aco}[%]	$t_{tot}^{aco}[s]$	t_{ref}^{aco}[%]	t_{mat}^{aco}[%]	t_{an}^{aco}[%]
mod.1	4.69	1.98	40.94	57.08	4.04	0.86	42.25	56.89	2.12	0.77	58.37	40.86
mod.2	4.38	4.24	71.64	24.12	16.45	0.58	16.43	82.99	4.03	0.58	44.22	55.20
mod.3	6.79	6.47	72.34	21.19	57.07	0.33	10.70	88.97	62.47	0.27	16.05	83.68
mod.4	19.21	19.38	71.80	8.82	744.7051	0.33	3.58	96.09	361.55	0.29	9.26	90.45

Table 5.30: Acoustic IGA time details with p=5, p=6 and p=7 for the simplified vehicle model application

IGA	$p=5$				$p=6$				$p=7$			
	t_{tot}^{aco} $[s]$	t_{ref}^{aco} [%]	t_{mat}^{aco}[%]	t_{an}^{aco}[%]	$t_{tot}^{aco}[s]$	t_{ref}^{aco}[%]	t_{mat}^{aco}[%]	t_{an}^{aco}[%]	$t_{tot}^{aco}[s]$	t_{ref}^{aco}[%]	t_{mat}^{aco}[%]	t_{an}^{aco}[%]
mod.1	0.92	0.53	82.66	16.81	1.23	0.56	81.41	18.03	1.69	0.91	81.32	17.77
mod.2	2.07	0.62	65.44	33.94	2.82	0.50	69.72	29.78	3.65	0.38	76.90	22.72
mod.3	19.92	0.39	32.74	66.87	10.99	0.40	54.59	45.01	16.82	0.31	64.51	35.18
mod.4	172.05	0.23	17.36	82.41	122.40	0.20	27.44	72.36	52.92	0.18	44.49	55.33

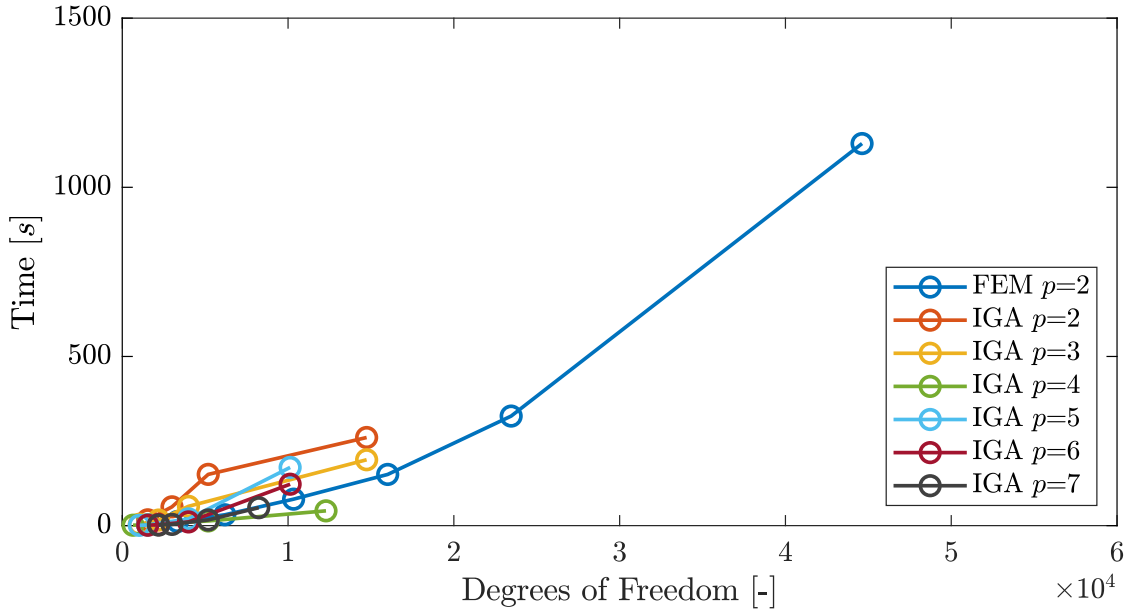

Figure 5.27: FEM and IGA total acoustic time (t_{tot}^{aco}) for the simplified vehicle model application

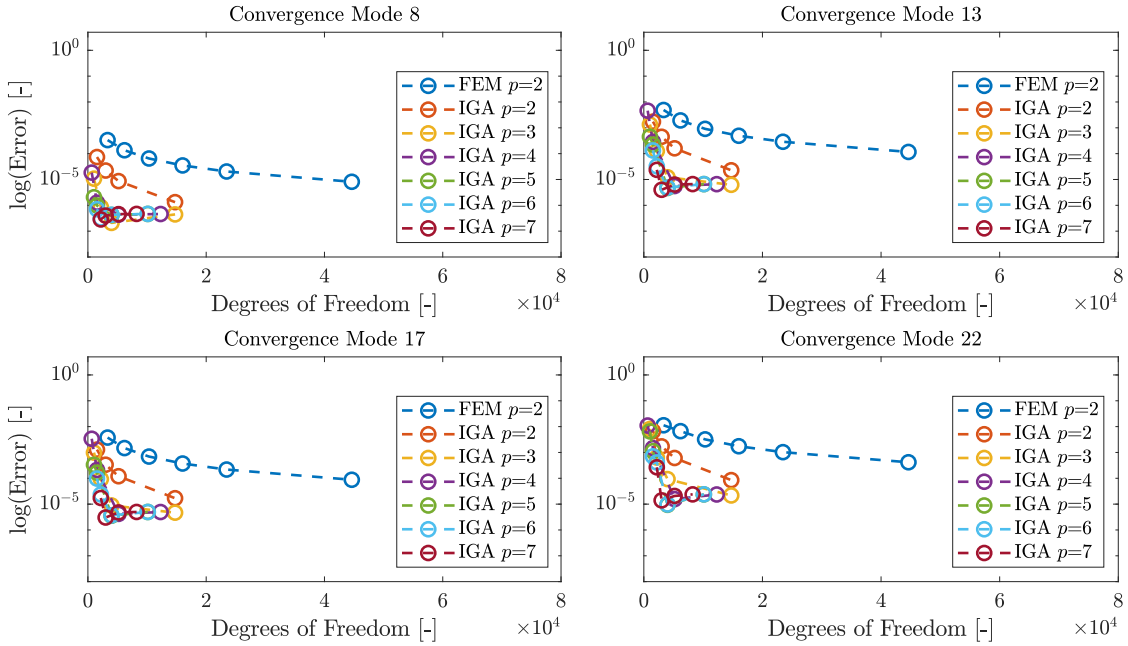

Figure 5.28: Convergence analysis of four fluid modes

Table 5.31: Exact frequencies of four fluid modes

mode number	freq[Hz]
8	173.4525
13	236.4959
17	275.6806
22	298.1761

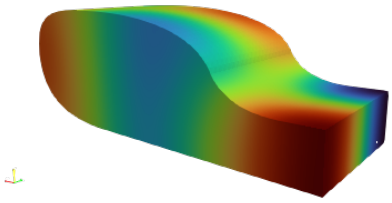

(a) Modal shape of the 8th mode at 173.4525 Hz

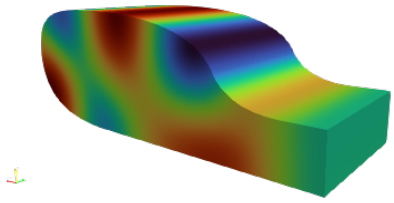

(b) Modal shape of the 13th mode at 236.4959 Hz

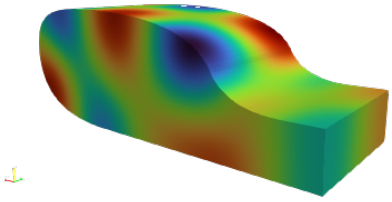

(c) Modal shape of the 17th mode at 275.6806 Hz

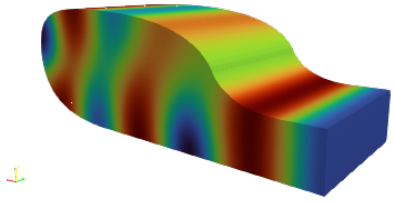

(d) Modal shape of the 22nd mode at 298.1761 Hz

Figure 5.29: Modal shapes of the four fluid modes reported in Table 5.31. The positive peaks are in red, the negative ones are in blue and the nodal planes are in light green.

5.2.4 Vibroacoustic results

This section tackles the vibroacoustic problem. The fluid-structural coupling, shown in Figure 5.19, is solved using both FEM and IGA. For the problem under consideration, a range [0-150]Hz has been chosen and all acoustic and structural modes in the [0-300]Hz range are considered. For this application, 13 structural and 23 acoustic modes are considered. The error of the first 36 vibroacoustic frequencies is shown in Figures 5.30 and 5.31. For coupled fluid-structural modes, the isogeometric approach achieves higher accuracy with fewer degrees of freedom. To evaluate the vibroacoustic computational time, it is possible to refer to the Equation (5.2). Again, for a consistent benchmarking between FEM and IGA, the computational time must be considered. Tables 5.32, 5.33, and 5.34 present the total computational times for FEM and IGA, to solve the vibroacoustic problem, highlighting the percentage contribution of each individual time. Figure 5.32 illustrates the total computation time for FEM and IGA. As expected, the computational time increases with the polynomial degree. By analyzing Figures 5.30, 5.31 and 5.32, it becomes evident that, to achieve a maximum error of 1%, the FEM requires the use of the sixth model, whereas for IGA with p=4, the second model is sufficient,

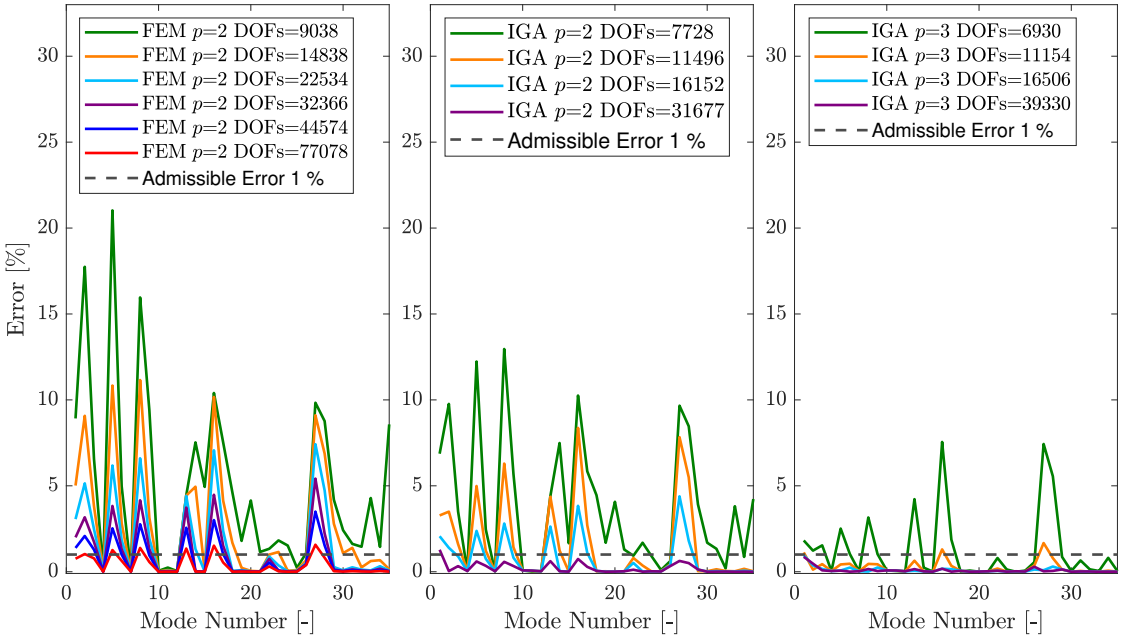

Figure 5.30: Vibroacoustic eigenmodes percentage error using FEM with p=2 and IGA with p=2 and p=3 for the simplified vehicle model application

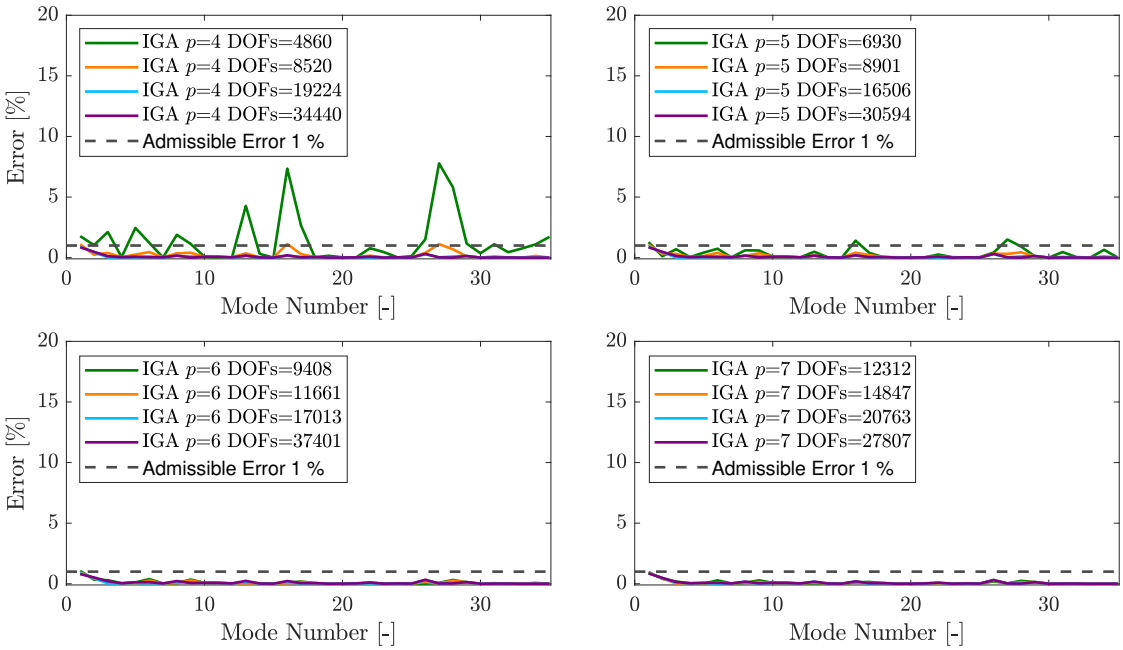

Figure 5.31: Vibroacoustic eigenmodes percentage error using IGA with p=4, p=5, p=6 and p=7 for the simplified vehicle model application

Table 5.32: Vibroacoustic FEM time details for the simplified vehicle model application

FEM with p=2	t_{tot}^{vibro} $[s]$	t_{ref}^{vibro} [%]	t_{mat}^{vibro} [%]	t_{an}^{vibro} [%]
mod.1	14.30	1.16	8.77	90.07
mod.2	34.48	0.22	4.32	95.46
mod.3	81.94	0.15	2.71	97.14
mod.4	156.43	0.12	2.06	97.82
mod.5	331.01	0.08	1.38	98.54
mod.6	$1.14{\cdot}10^3$	0.04	0.78	99.18

Table 5.33: Vibroacoustic IGA time details with p=2, p=3 and p=4 for the simplified vehicle model application

IGA	$p=2$				$p=3$				$p=4$			
	t_{tot}^{vibro} $[s]$	t_{ref}^{vibro} [%]	t_{mat}^{vibro}[%]	t_{an}^{vibro}[%]	t_{tot}^{vibro}[s]	t_{ref}^{vibro}[%]	t_{mat}^{vibro}[%]	t_{an}^{vibro}[%]	t_{tot}^{vibro}[s]	t_{ref}^{vibro}[%]	t_{mat}^{vibro}[%]	t_{an}^{vibro}[%]
mod.1	22.41	1.01	25.78	73.21	9.06	0.58	67.26	32.16	2.84	0.69	66.16	33.15
mod.2	60.41	0.48	9.44	90.08	20.16	0.74	25.32	73.94	6.59	0.79	56.73	42.48
mod.3	158.80	0.34	5.40	94.26	63.22	0.42	5.75	83.83	70.50	0.34	22.42	77.24
mod.4	$1.08{\cdot}10^3$	0.38	2.18	97.44	763.50	0.36	4.84	94.80	379.95	0.31	12.05	87.64

with a consequent advantage in terms of computational time (the second IGA model exhibits a lower total computational time compared to the sixth FEM model). Figure5.33 illustrates the convergence rate of four vibroacoustic modes and the Table 5.17 provides the reference values, while Figure5.34 shows the corresponding modal shapes.

In addition, a diagram is provided to understand how the eigenvalues and modal shapes, at low frequencies, change when using a decoupled rather than a coupled approach (Figure5.35). The coupled modal shapes are shown in Figure5.35 and their corresponding frequencies are reported in Table 5.36

Table 5.34: Vibroacoustic IGA time details with p=2, p=3 and p=4 for the simplified vehicle model application

IGA	$p=5$				$p=6$				$p=7$			
	t_{tot}^{vibro} $[s]$	t_{ref}^{vibro} [%]	t_{mat}^{vibro}[%]	t_{an}^{vibro}[%]	t_{tot}^{vibro}[s]	t_{ref}^{vibro}[%]	t_{mat}^{vibro}[%]	t_{an}^{vibro}[%]	t_{tot}^{vibro}[s]	t_{ref}^{vibro}[%]	t_{mat}^{vibro}[%]	t_{an}^{vibro}[%]
mod.1	2.18	0.60	84.25	15.15	3.98	0.41	89.05	10.54	6.41	1.74	90.17	8.09
mod.2	3.79	0.91	71.46	27.63	5.25	0.89	75.21	23.90	6.87	0.65	81.13	18.22
mod.3	26.41	0.43	44.62	54.95	16.90	0.46	65.38	34.16	25.39	0.35	72.75	26.90
mod.4	188.28	0.26	22.50	77.24	139.62	0.22	34.33	65.45	68.06	0.22	54.21	45.57

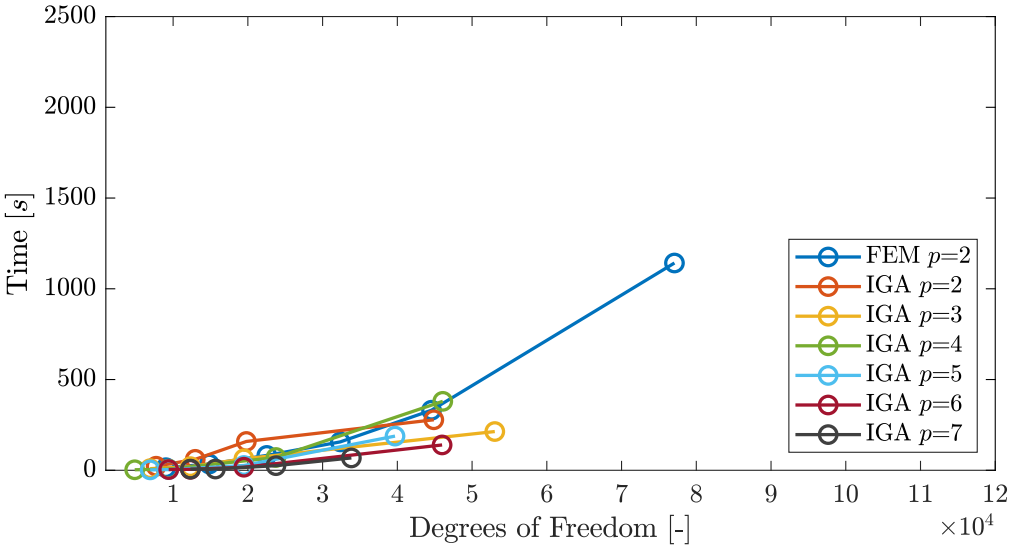

Figure 5.32: Total vibroacoustic time for the simplified vehicle model application t_{tot}^{vibro}

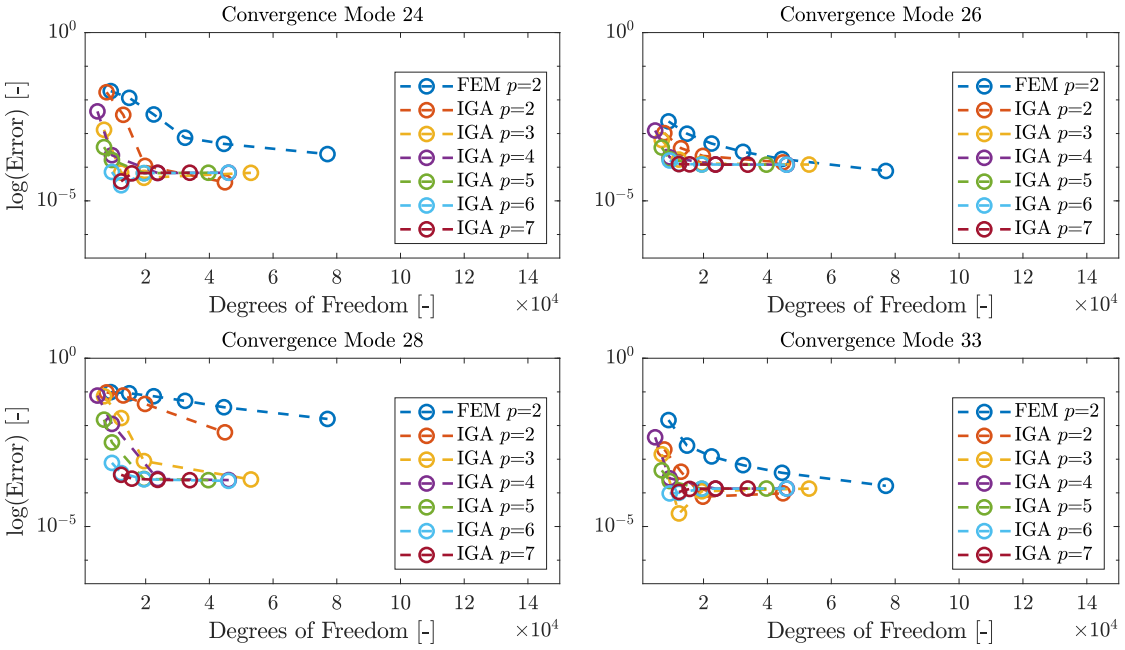

Figure 5.33: Convergence analysis of four vibroacoustic modes

Table 5.35: Exact frequencies of four vibroacoustic modes

mode number	freq[Hz]
24	236.5151
26	247.4812
28	251.6978
33	288.8451

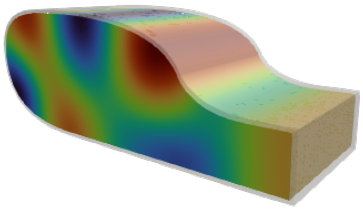

(a) Modal shape of the 24th mode at 236.5151 Hz

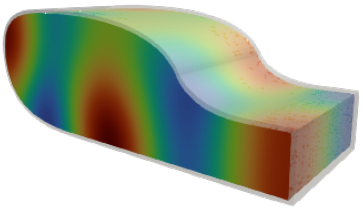

(b) Modal shape of the 26th mode at 247.4812 Hz

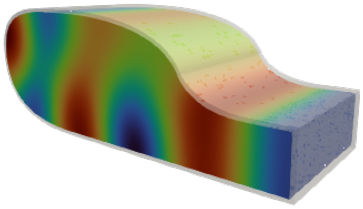

(c) Modal shape of the 27th mode at 251.6978 Hz

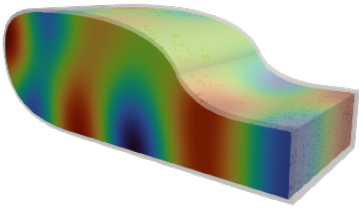

(d) Modal shape of the 32nd mode at 288.8451 Hz

Figure 5.34: Modal shapes of the four vibroacoustic modes reported in Table 5.35. The positive peaks are in red, the negative ones are in blue and the nodal planes are in light green.

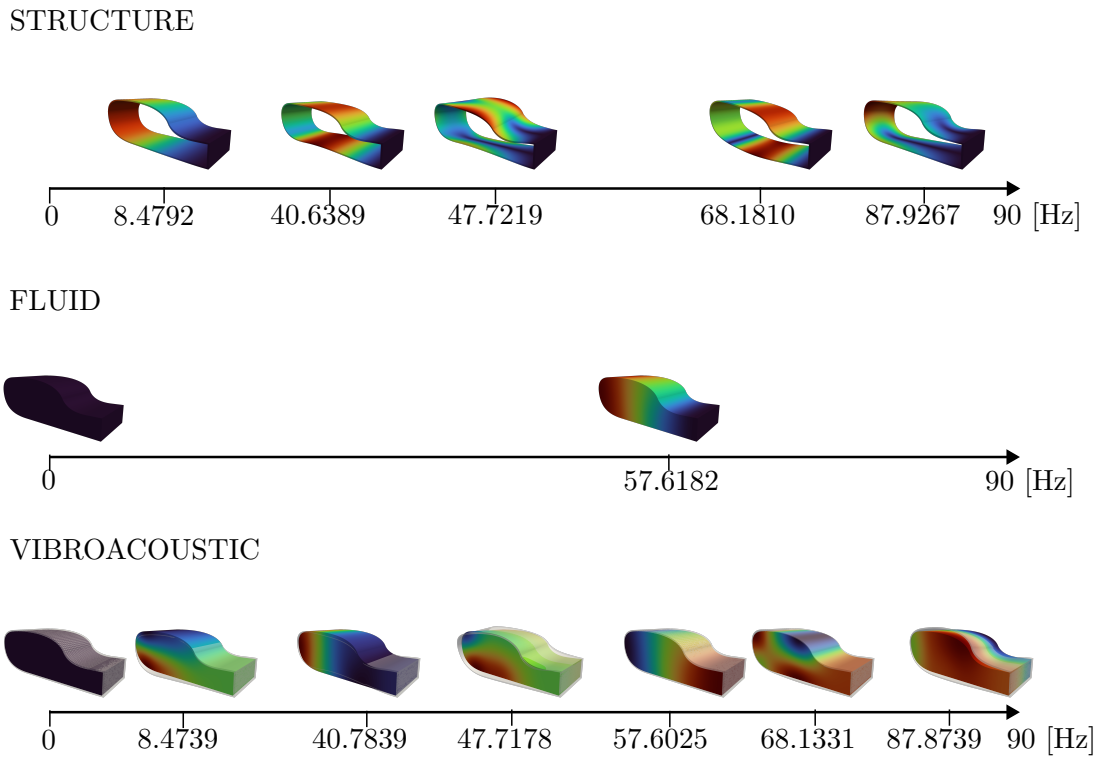

Figure 5.35: Structural, acoustic and vibroacoustic car modes up to 90 Hz

with highlight of the dominant domain.

The frequencies of the coupled vibroacoustic modes highlighted in Table 5.36 do not vary substantially from the frequencies of the corresponding decoupled modes. The same considerations that have been made for the previous example (hollow cylinder filled with fluid) might be done for this scenario.

Table 5.36: Frequencies of coupled and uncoupled systems for the simplified vehicle model application

Structure Modes [Hz]	Fluid Modes [Hz]	Coupled Modes [Hz]	Dominant Domain
-	0	0	F
8.4792	-	8.4739	S+F
40.6389	-	40.7839	S+F
47.7219	-	47.7178	S+F
-	57.6182	57.6025	F
68.1810	-	68.1331	S+F
87.9267	-	87.8739	S+F

Chapter 6

Conclusion of IGA with conformal NURBS-suitable analyses

In the first part of this work, the fundamental principles of isogeometric analysis (IGA) and its main differences with the finite element method (FEM) were presented. A modal-based formulation was also introduced to reduce the computational cost without compromising accuracy. Preliminary results for acoustic, structural, and vibroacoustic problems were compared between the IGA and FEM approaches. The findings showed that IGA achieves comparable or even better accuracy with a significantly lower computational cost, primarily due to the smaller number of degrees of freedom required for the same level of precision. This advantage was consistently observed across structural, acoustic, and vibroacoustic cases, confirming the strong potential of IGA as a more efficient numerical framework.

Moreover, the introduction of a modal-based Reduced Order Model (ROM) formulation further enhanced the computational efficiency of the coupled vibroacoustic analyses. This combined IGA–ROM approach allowed a substantial reduction in solution time while maintaining excellent accuracy in the representation of the coupled modes and frequency response functions (FRFs). Such results demonstrate that IGA, especially when integrated with ROM strategies, represents a powerful and scalable tool for vibroacoustic simulations.

However, several limitations remain, mainly related to the use of a conformal NURBS-suitable analysis. In this framework, the geometry of each domain must be explicitly defined by specifying the *control points*, *weights*, and *knot vectors* that describe the NURBS basis functions. While this procedure is suitable for simple or idealized geometries, it becomes impractical for complex or real-

istic configurations. The manual definition of these parameters is time-consuming, error-prone, and incompatible with industrial-scale models where geometric descriptions are usually imported directly from CAD environments.

Therefore, the main bottleneck of the current IGA implementation lies in the lack of a direct CAD/IGA integration. Bridging this gap is essential to fully exploit the potential of IGA, enabling the direct use of CAD-defined NURBS geometries for analysis without intermediate meshing or manual parameterization. This limitation will be addressed in the second part of this work through the adoption of an *Immersed IGA* framework, which overcomes the need for conformal parameterizations and allows efficient analysis of complex geometries.

Overall, the results obtained in this first part confirm the strong potential of isogeometric analysis as a robust and accurate computational tool. Even in its current form, IGA outperforms conventional FEM in terms of accuracy–cost ratio, and its efficiency is further enhanced when coupled with modal-based model reduction techniques. These encouraging outcomes motivate the continued development toward a more flexible, CAD-integrated IGA formulation capable of handling realistic engineering configurations.The codes used to reproduce these analyses are available open source at: `vibroacoustic-iga-fem`.

Part II

Vibroacoustic approach using immersed IGA from B-REP CAD/CAE integration

Chapter 7

State of the Art in CAD-Integrated Isogeometric Analysis

This chapter reviews the current state of the art in CAD-integrated isogeometric analysis (IGA), focusing on *immersed approaches* that enable direct use of CAD geometries without conforming mesh generation. After introducing the concept of Boundary Representation (B-REP) and its role in CAD-IGA integration, several immersed methods are analyzed, including the Cut Finite Element Method (CutFEM), the Extended Finite Element Method (X-FEM), and the Finite Cell Method (FCM). Adaptive refinement techniques such as hp-adaptivity and hierarchical splines are discussed as key strategies to improve both accuracy and computational efficiency. The chapter concludes by identifying current research gaps in CAD-integrated IGA workflows, specifically regarding robust geometry handling, adaptive refinement, and efficient coupling for vibroacoustic simulations, which directly motivate the methodological developments presented in Part II of this thesis.

Content

7.1 Introduction and motivation

Part II of this thesis focuses on the development of a robust workflow for vibroacoustic analysis that integrates CAD geometries directly into isogeometric analysis (IGA). The main objective is to establish a design-through-analysis methodology that allows the use of Boundary Representation (B-REP) CAD models in IGA simulations without the need for laborious conforming mesh generation.

In a B-REP model, a solid object is represented by its bounding surfaces, explicitly defining vertices, edges, and faces. These surfaces are usually described parametrically (e.g., using NURBS), allowing precise representation of complex geometries. This representation, which follows standard formats such as IGES and STEP, provides a precise and compact way to encode complex geometries commonly used in CAD systems [36, 13, 84].

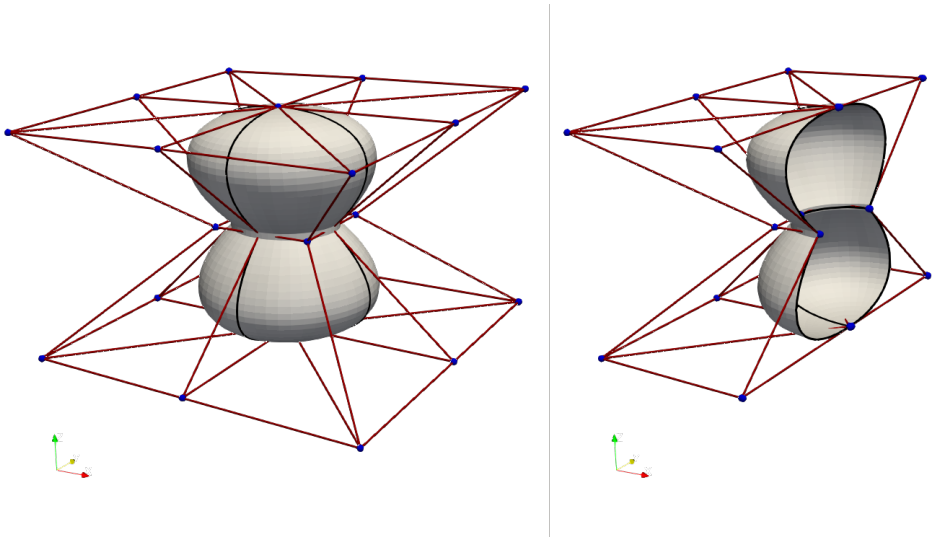

Figure 7.1: Example of a solid object from CAD shown on the left and its sectional view on the right. The black lines represent the B-REP elements, the red lines indicate the control mesh used in isogeometric analysis, and the blue points mark the control points of the B-REP surfaces.

However, the only boundary representation becomes critical in vibroacoustic applications involving enclosed cavities, where the evaluation of the acoustic pressure field inside the fluid domain is required. Without volumetric information, the internal acoustic response, typically represented in terms of Sound Pressure Level (SPL), cannot be directly computed from the CAD model.

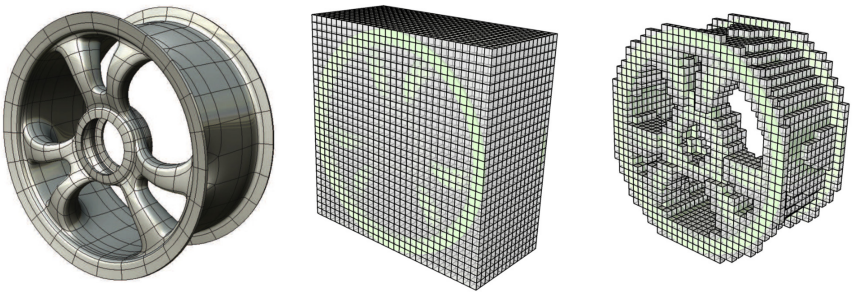

Figure 7.2: Schematic representation of the immersed method. On the left, the original CAD geometry is shown. In the center, the geometry is immersed into a background computational mesh. On the right, the elements of the mesh that lie inside the physical domain (active elements) are highlighted. Image from [3].

7.2 Immersed methods for CAD-based analysis

Traditional finite element methods (FEM) often require meshes that closely follow the shape of the domain. For complex geometries, this often means significantly refining the mesh to accurately capture all features, which increases computational cost and pre-processing effort. Immersed methods overcome the limitations of traditional FEM by decoupling the computational mesh from the geometry. In these methods, the mesh does not need to conform to the exact boundaries of the domain; instead, the physical domain is "immersed" into a background mesh, and the governing equations are modified to account for the considered elements, as shown in Figure 7.2. This allows direct use of CAD models in simulations while preserving geometric accuracy [85].

7.2.1 Cut Finite Element Method (CutFEM)

Among immersed methods, the *Cut Finite Element Method (CutFEM)* [86, 87] allows the computational mesh to intersect the physical domain arbitrarily. In this approach, only the portion of each element that lies inside the physical domain contributes to the weak formulation. Elements intersected by the boundary, known as *cut elements*, may lead to ill-conditioned system matrices due to their small physical volume. To address this, CutFEM employs stabilization strategies such as *ghost penalty* terms and *Nitsche's method* to enforce boundary conditions weakly and ensure numerical stability. Since boundary conditions are applied directly on the true interface, CutFEM provides accurate boundary representations and is well-suited for problems with evolving geometries or moving interfaces, without the need to regenerate a conforming mesh.

7.2.2 Extended Finite Element Method (X-FEM)

The *Extended Finite Element Method (X-FEM)* [88, 89] also belongs to the family of unfitted approaches but follows a different philosophy. Instead of modifying the integration domain, X-FEM enriches the standard finite element approximation space with additional functions that capture discontinuities, cracks, or embedded interfaces within elements. This makes X-FEM particularly effective in vibroacoustic and structural-acoustic simulations involving complex internal features, where the mesh does not conform to discontinuities.

7.2.3 Finite Cell Method (FCM)

The *Finite Cell Method (FCM)* [90, 91, 92, 93] adopts a fictitious-domain strategy. The physical domain is embedded within a larger, simple background mesh, typically Cartesian, and the material outside the physical domain is assigned a very small stiffness through a penalization parameter. The weak form is integrated over the entire extended domain, with the fictitious region contributing negligibly to the system matrix. Unlike CutFEM, which explicitly enforces boundary conditions on the true interface, FCM avoids explicit boundary treatment and relies on accurate numerical integration near the immersed boundary to capture geometry effects. This approach is particularly advantageous for structural or vibroacoustic analyses of highly complex geometries, where generating a body-fitted mesh would be computationally prohibitive [3].

7.3 Adaptive refinement strategies in IGA

7.3.1 Hp-adaptive methods

Hp-adaptive methods [3] enhance both accuracy and efficiency by combining local mesh refinement (h-refinement) with polynomial enrichment (p-refinement). In practice, this means that in regions where the solution varies rapidly or near geometric singularities, the mesh can be refined and the polynomial order of the basis functions increased simultaneously. Figure 7.3 illustrates this concept on a vehicle wheel.

While hp-adaptivity is highly effective for capturing local solution details in complex CAD-derived domains, its main limitation lies in the increased complexity of managing varying polynomial orders and ensuring smooth transitions between elements.

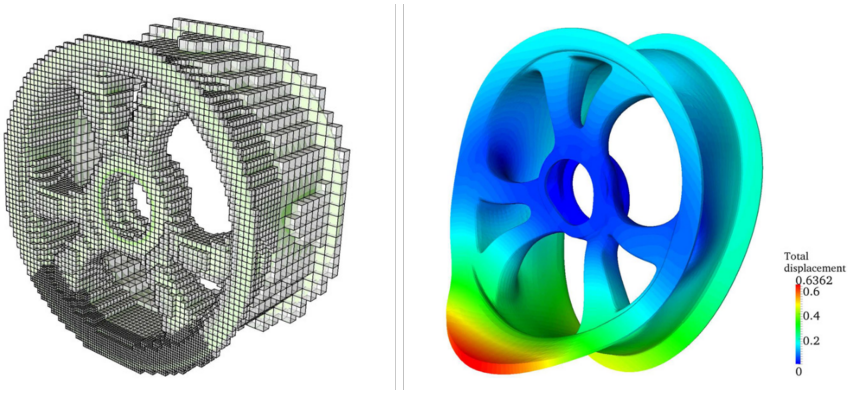

Figure 7.3: Example of hp-adaptive refinement on a vehicle wheel [3]. Hierarchical refinement increases resolution in regions with high solution gradients (e.g., contact and edges), while smoother regions use coarser elements.

7.3.2 Hierarchical B-splines (HB-splines)

Within the IGA framework, *Hierarchical B-splines (HB-splines)* [4] are chosen in this work as the primary basis for adaptive refinement. Unlike hp-adaptive methods, HB-splines provide local adaptivity while preserving the inherent smoothness and continuity of the spline basis. This allows refinement in selected regions without altering the global representation or introducing additional complexity. HB-splines thus strike a practical balance between flexibility and simplicity, enabling efficient implementation in CAD-to-IGA workflows.

7.3.3 Other immersed IGA techniques

Other immersed IGA techniques, such as *Truncated Hierarchical B-splines (THB-splines)* [94, 95], can improve locality and reduce redundancy, but at the cost of more complex basis management. Similarly, multigrid solvers and iterative preconditioners [96] are essential for efficiently solving large linear systems arising from high-order and cut-element discretizations.

7.4 Summary and identified research gaps

This review highlights how immersed approaches, CutFEM, X-FEM, and FCM, enable the use of CAD geometries in numerical simulations without the need for conforming meshing. However, several challenges remain before fully automated CAD-to-IGA workflows can be achieved:

- **Geometry integration:** Existing immersed IGA frameworks often rely on simplified or manually pre-processed geometries when validating against classical FEM or when demonstrating their potential integration in engineering workflows. As a result, benchmark problems are frequently based on idealized or artificially simplified CAD shapes rather than on full B-REP models. This limits the assessment of immersed IGA methods on truly industrial geometries, where issues such as trimmed surfaces, complex topology, and geometric inconsistencies pose significant challenges that current approaches are not yet able to handle in a fully automated way.

- **Stability and conditioning:** Cut-element formulations still face issues with ill-conditioned system matrices and integration errors near complex interfaces.

- **Adaptive refinement:** Although HB- and THB-splines provide a solid mathematical framework for local adaptivity, fully automated and robust refinement strategies for immersed IGA are still under active development. This concerns both theoretical aspects—such as understanding limitations, ensuring stability near cut elements, and defining reliable refinement criteria—and practical ones. To the best of the authors' knowledge, no open-source or commercial implementations currently offer a complete and mature adaptive refinement pipeline for immersed IGA, making this an open area of research from both the algorithmic and software perspectives.

- **Fluid–structure coupling:** Efficient coupling of immersed fluid and structural domains for vibroacoustic problems remains computationally demanding and methodologically open.

These gaps directly motivate the developments presented in Part II of this thesis, where a robust CAD-to-IGA integration framework based on hierarchical B-splines and immersed vibroacoustic coupling is proposed.

Chapter 8

Hierarchical B-Spline approach

Most CAD systems describe geometries only through boundary representations (B-Rep), lacking the volumetric information required for numerical analysis. This chapter introduces a methodology to reconstruct the volumetric domain directly from CAD boundaries using Hierarchical B-Splines (HB-splines). The approach combines geometric flexibility, local refinement, and computational efficiency, enabling adaptive representation of acoustic cavities.

Content

8.1 Introduction and state of the art on Hierarchical B-Spline

8.1.1 Fundamentals of Hierarchical B-Splines

A pivotal advancement within IGA is the development of Hierarchical B-splines (HB-splines), which extend traditional B-splines by introducing a hierarchical structure that allows for local refinement. This capability is crucial for accurately capturing the intricate details of acoustic domains without the need for conforming meshes, which are often cumbersome to generate and manage. HB-splines can be understood as an evolution of standard B-splines that introduces adaptability into the spline space. Traditional B-splines are globally refined, meaning that increasing the resolution in one region increases the number of control points everywhere. HB-splines, instead, allow for local refinement, activating finer basis functions only where needed. This results in a more efficient and targeted representation of the solution space.

Mathematically, let $\{N_{i,p}(\xi)\}$ denote a set of B-spline basis functions of degree p defined on a knot vector Ξ. HB-splines are constructed hierarchically over a sequence of nested spline spaces:

$$V^0 \subset V^1 \subset V^2 \subset \cdots \subset V^L \tag{8.1}$$

where each level l corresponds to a refinement of the previous space V^{l-1}. The hierarchical basis is then built by activating only those basis functions whose support intersects a region of interest Ω^l at level l, while deactivating the coarser functions in that region, as shown in Figure 8.1:

$$\mathcal{H} = \bigcup_{l=0}^{L} \{N_{i,p}^l \in V^l : \text{supp}(N_{i,p}^l) \subset \Omega^l \setminus \Omega^{l+1}\}. \tag{8.2}$$

This hierarchical construction enables local refinement without globally increasing the number of degrees of freedom, providing both flexibility and computational efficiency [4]. The latter is shown in Figure 8.2.

8.1.2 Advantages and state of the art

The adoption of HB-splines in immersed IGA offers several advantages:

- *Local refinement:* increases resolution only where higher accuracy is required (e.g., near boundaries or interfaces);

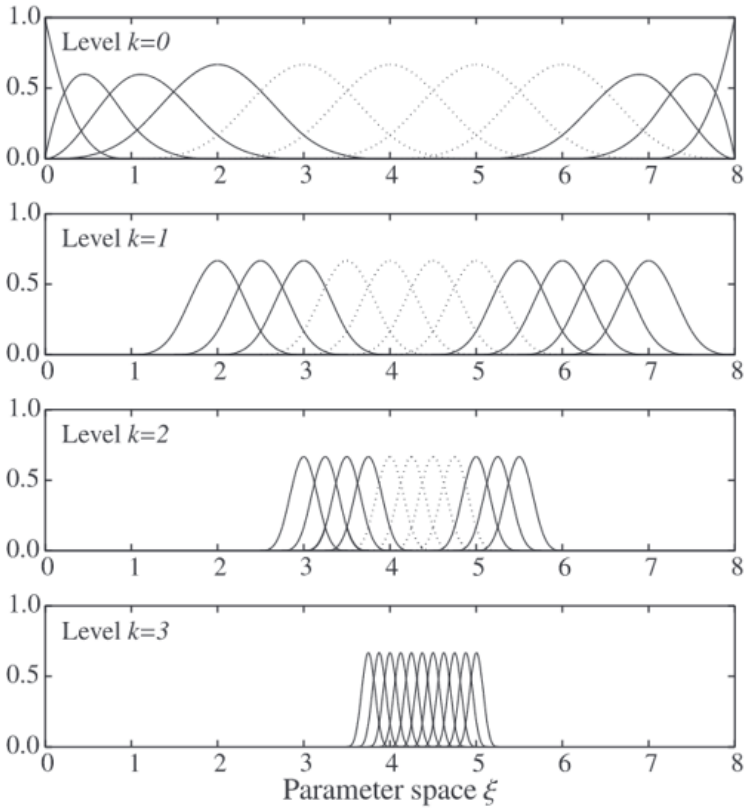

Figure 8.1: Illustration of HB-spline refinement in 1D from [4]. Local refinement is introduced only in a specific region, increasing resolution without affecting the entire domain.

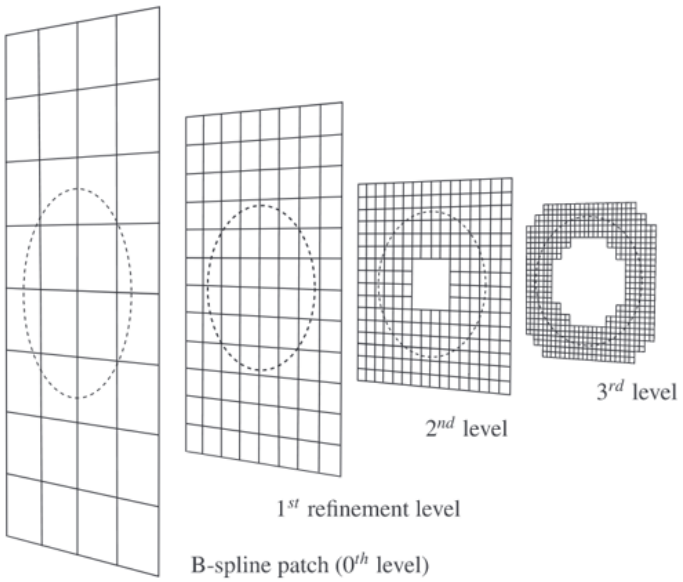

Figure 8.2: Hierarchical refinement levels for a 2D example (plate with circular inclusion) [4]. The refinement is concentrated around the circular region of interest, illustrating typical hierarchical grid generation in two dimensions.

- *Improved precision:* hierarchical refinement captures local field variations more accurately;
- *Reduced computational cost:* refinement affects only a subset of the domain;
- *Geometric flexibility:* spline-based representation allows accurate modeling of complex geometries;
- *Overall efficiency:* fewer degrees of freedom lead to faster and more stable analyses.

Recent works have explored the potential of HB-splines in immersed and adaptive IGA frameworks e.g., [97, 98, 99] demonstrating their effectiveness across various physics (heat transfer, acoustics, and multi-material systems). However, their direct application to immersed IGA for acoustic cavity analysis remains limited, and this research aims to fill that gap by extending the methodology to volumetric reconstruction and vibroacoustic coupling.

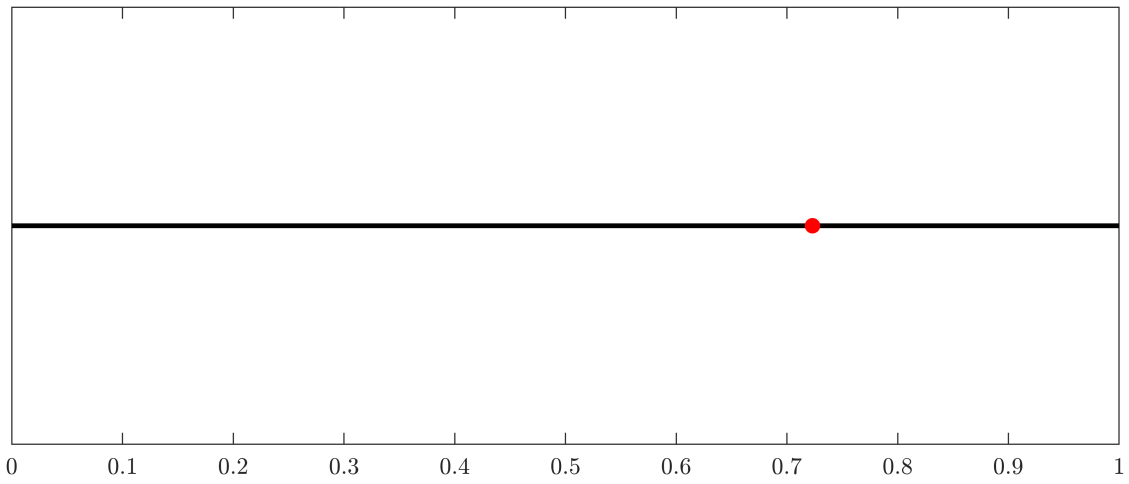

Figure 8.3: Rod under investigation. The cut location point is indicated by the red marker.

Table 8.1: Structural parameter for the rod.

E $[Pa]$	ρ $[\frac{kg}{m^3}]$	$L[m]$	x_{stop} $[m]$	p [-]	n^0_{elem}
1.0	1.0	1.0	0.7231	6	8

8.2 Computation of operators and integrations

8.2.1 1D Traction–Compression rod

In this section, a tensile–compressive rod of length $L = 1$ is analysed. The rod is fixed at its left end and it is cut at an arbitrary point, in this case $x_{stop} = 0.7231$, as highlighted in Figure 8.3. After that, a modal analysis is performed. The obtained results are then compared with those from an exact solution. The procedure adopted in the hierarchical B-spline framework is organized into a sequence of computational steps. Each step is designed to progressively build the multi-level data structure, establish the local-to-global mapping of basis functions, and finally assemble the global stiffness and mass operators with appropriate domain penalization. The overall workflow is summarized in Algorithm 3.

For the analysed example, for the sake of simplicity, material parameters such as Young's modulus and density are set to unity. The adopted parameter values are summarized in Table 8.1.

Considering six levels (the initial level plus five refinement levels), the total number of basis functions is shown in Figure 8.4.

Algorithm 3 Hierarchical B-spline construction and operator assembly with domain penalization

Require: Initial number of elements n_0, spline degree p, number of levels n_{level}, split position x_{stop}

Initialization
Create root of data tree: `data_tree` = tree(0)

1. Hierarchical mesh generation
for $l = 1$ to $n_{\text{level}} + 1$ **do**
    Build knot vector and connectivity table for level l
    Identify element e_{stop} intersected by x_{stop}
    Determine elements to split: $e_{\text{split}} = [e_{\text{stop}} - p : e_{\text{stop}} + p]$ and split them into two elements
    Update hierarchical data tree with child nodes for each split element
    Determine kept basis functions and store local connectivity in `LEVEL`(l)
end for

2. Construction of integration paths
for all leaf nodes in `data_tree` **do**
    Traverse parent nodes to define element paths across levels
    Store `path_elem` and `path_level` for each integration domain
end for

3. Local-to-global indexing
Initialize global and local index vectors
for $l = 1$ to $n_{\text{level}} + 1$ **do**
    Map local basis indices `ind_kept_local` to global numbering
    Update `LEVEL`(l).*ind_kept_global* and corresponding connectivity tables
    identify the number of basis to take into account following AppendixB
end for

4. Operator assembly with penalization
Initialize $\mathbf{K} = \mathbf{0}$, $\mathbf{M} = \mathbf{0}$, and `dofu_tot` = $\mathbf{0}$
for all integration paths i **do**
    Collect global and local connectivity across all levels in the path
    For each Gauss point:

- Map Gauss point gp to physical coordinate x_{gp}
- **If** x_{gp} is inside the physical domain:
  - Set $\alpha = 1$
  - Store associated DOFs in `dofu_tot`
- **Else (outside domain):**
  - Apply penalization factor $\alpha \in [10^{-8}, 10^{-12}]$
  - Use α to penalize the local operators
- Assemble into global matrices: $\mathbf{K}$ and $\mathbf{M}$

end for

Output: Hierarchical operators $\mathbf{K}$, $\mathbf{M}$, and active DOF set `dofu_tot`

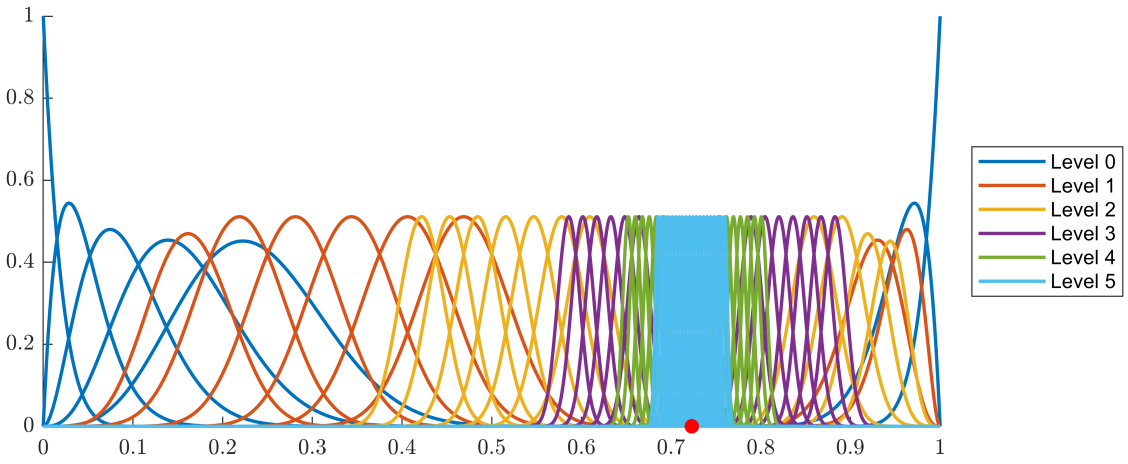

Figure 8.4: Total considered basis functions.

Figure 8.5: Graphical representation of the hierarchical data tree obtained for the 1D rod problem.

Figure 8.5 illustrates the data tree structure obtained for this example. It is worth noting that the tree follows a binomial hierarchy: in one dimension (1D) each element is split into two sub-elements, in two dimensions (2D) each element is divided into four, and in three dimensions (3D) each element is subdivided into eight, forming an octree structure.

Figure 8.6 shows all the Gauss points of the considered problem. The Gauss points located outside the domain are penalized, while the integration is performed only on those lying inside the physical region. This penalization mitigates the artificial stiffness introduced by non-physical zones, ensuring a more consistent mechanical response and improving the conditioning of the stiffness matrix.

From a computational perspective, the assembly of the stiffness and mass matrices could be further accelerated. Indeed, elements that lie sufficiently far from the physical boundary x_{stop} correspond to degrees of freedom that are not included in `dofu_tot`; such regions do not contribute to the final system. These elements can therefore be identified prior to the integration loop, allowing one to skip their evaluation entirely and significantly reduce the computational cost of assembling K and M.

Figure 8.7 shows the first two numerical and analytical mode shapes, while Table 8.2 reports the

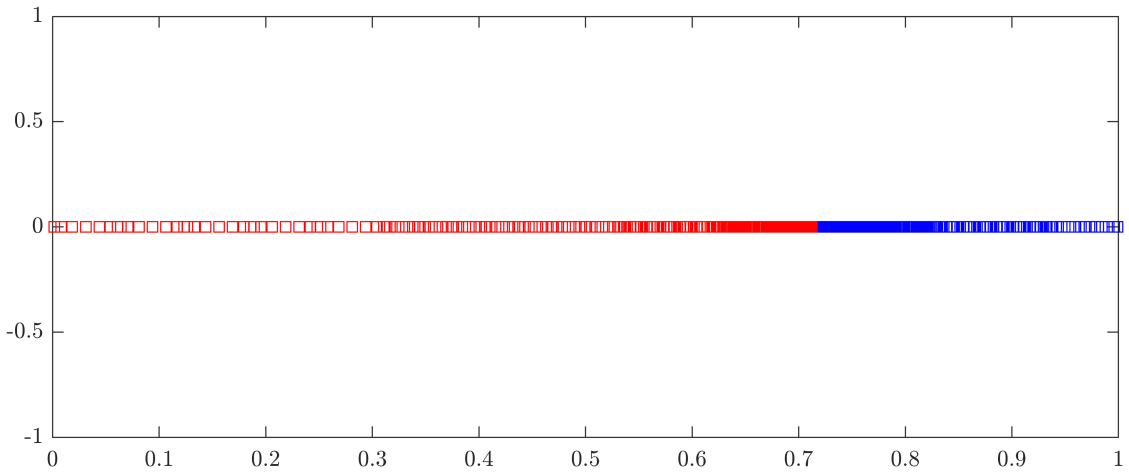

Figure 8.6: All Gauss points. Only the ones inside the domain (in red) are taking into account during the integration while the others (in blue) are penalized.

Table 8.2: First five structural numerical and analytical frequencies and corresponding percentage error.

$f_{an}(Hz)$	$f_{num}(Hz)$	**Error** (%)
0.346	0.346	0.03
1.037	1.037	0.03
1.729	1.729	0.03
2.420	2.420	0.03
3.112	3.112	0.03

computed frequency values along with the corresponding error with respect to the exact solution.

8.2.1.1 Advantages of HBs over the Finite Cell Method approach

The approach discussed above could also be applied in a global refinement (Finite Cell Method approach) rather than a local one. However, this strategy would involve solving the problem on a very fine mesh, which is generally unnecessary since it refines regions that are not of primary interest. Using this global approach, by varying the polynomial degree p, one obtains the error on the first five frequencies, which is shown in Figure 8.8.

To achieve the same level of accuracy between the locally refined (HBs) and the uniformly refined solutions (FCM), a relative error of approximately 0.03% must be considered. To reach this error level, the locally refined approach requires a problem with only 43 degrees of freedom, whereas the uniform refinement demands about 200 degrees of freedom. Although this result is expected, it serves

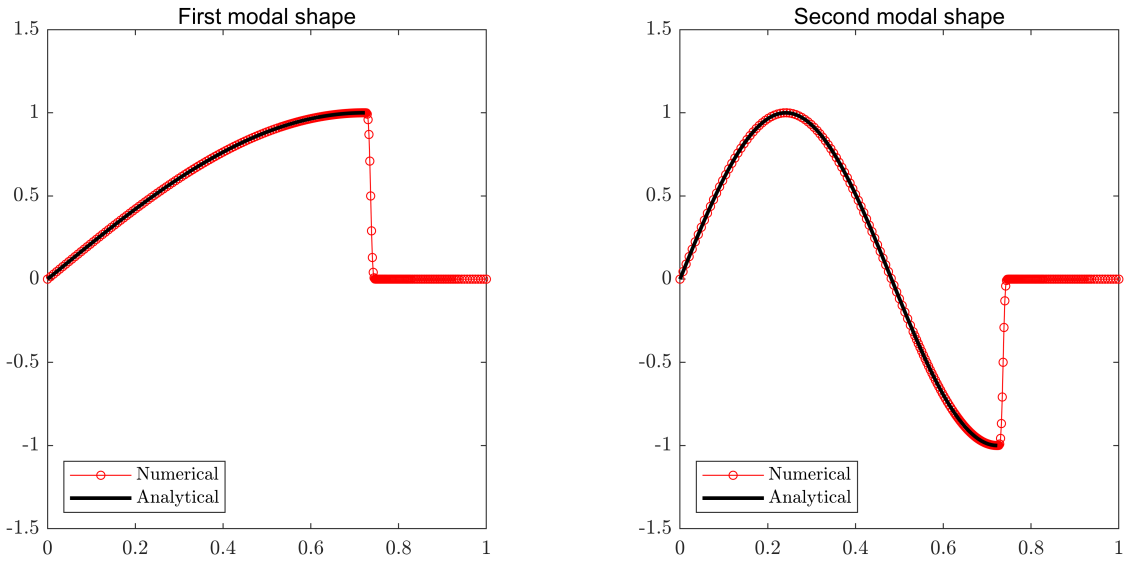

Figure 8.7: First two structural modal shapes.

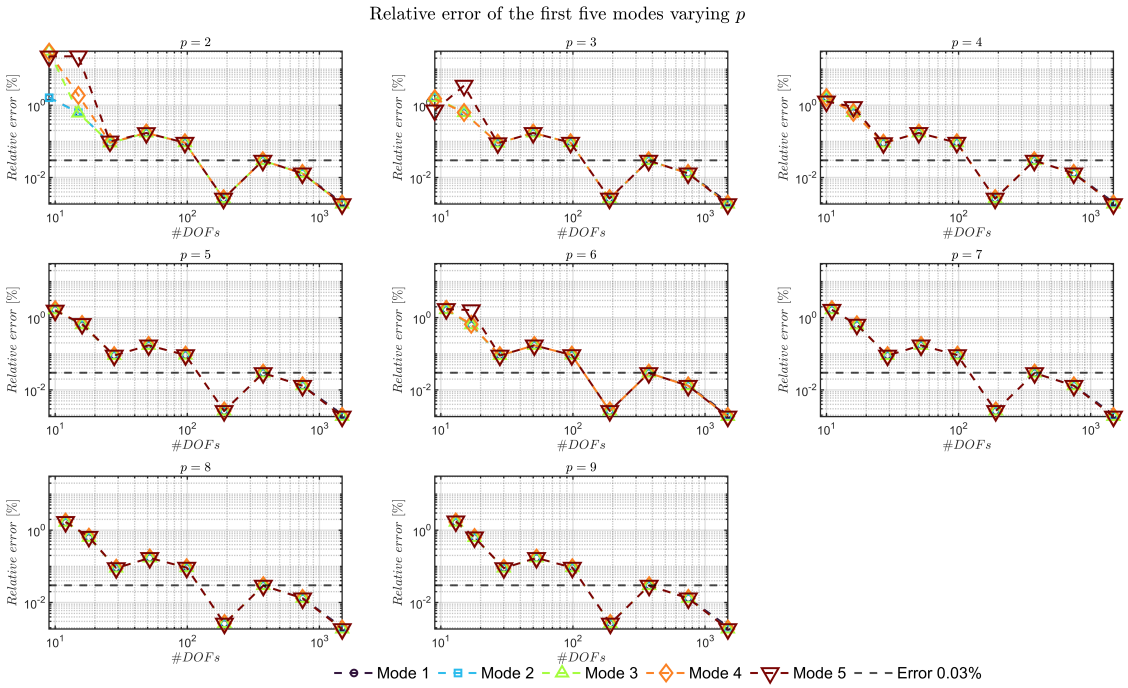

Figure 8.8: Percentage error of the first 5 modes varying p. These results are obtained performing a uniform meshing (finite cell method approach) along the entire rod.

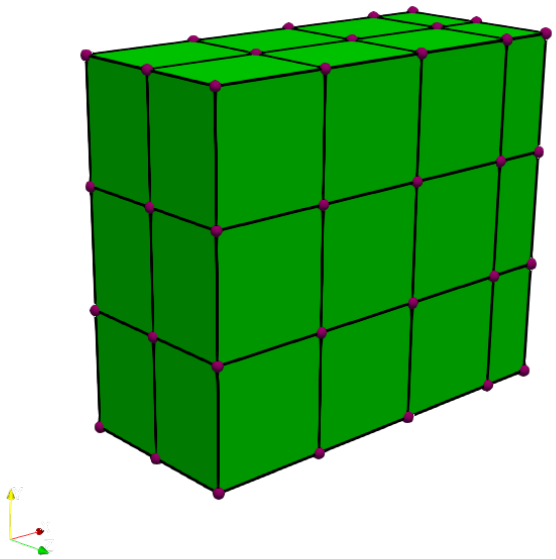

Figure 8.9: B-Rep geometry extracted from the CAD file.

to justify the adopted approach. Naturally, this phenomenon becomes even more pronounced as the complexity of the system increases.

8.2.2 Computation of 3D immersed IGA: rectangular acoustic cavity

This section is devoted to the use of Hierarchical B-Spline for a three-dimensional geometry. Consider a geometry obtained from CAD software, as illustrated in Figure 8.9, which provides only the boundary representation of the domain.

The dimensions of the geometry are $0.3 \times 0.7 \times 0.6$. For this example, all parameters (density, and sound speed) are set to 1, and different cases, with different HBs levels, are considered. The procedure to be followed consists of:

The workflow of the process described above is illustrated in Figures 8.10, 8.11 and 8.12 for three cases, corresponding to an increasing number of hierarchical levels considered in the analysis.

Figure 8.13 shows the distribution of the Gauss points, highlighting the ones inside the domain of interest for the three considered cases in Figures 8.10, 8.11 and 8.12. The numerical integration is

Algorithm 4 Algorithm for 3D Immersed Isogeometric Analysis - Part 1

Input: Number of levels n_{level}, geometric domain (L_1, L_2, L_3), initial subdivisions (n_{ex}, n_{ey}, n_{ez}), polynomial degrees (p, q, r), cloud of x_{stop} identify as V
Output: Hierarchical structures `LEVEL`, **K**, **M** and DOFs

Step 1: Initialization of the multilevel hierarchy
for $lvl = 1$ **to** $n_{level} + 1$ **do**
    Generate 3D linear mesh (`nodes`, `elems`) with subdivisions scaled by 2^{lvl-1}
    Construct knot vectors $(uKnot, vKnot, wKnot)$ and NURBS basis functions of order (p, q, r)
    Store geometric and topological data in `LEVEL(lvl)`
end for

Step 2: Construction of the hierarchical data structure (Data Tree)
Initialize `data_tree` with a root node
for $lvl = 1$ **to** $n_{level} + 1$ **do**
    Identify elements intersected by refinement a cloud set points V that define the geometry (split elements)
    Determine sets of kept and refined elements in (x, y, z) directions
    if $lvl < n_{level} + 1$ **then**
        Generate child elements (8 per split element because it is in 3D)
        Update `data_tree` with parent–child relations
    end if
    Update per-level element sets: `keep`, `split`, `removed`
end for

Step 3: Construction of multilevel connectivity
for each level lvl **do**
    Build 3D connectivity between elements, nodes, and basis functions (according to B)
    Determine hierarchical relations between consecutive levels
    Compute global identification vectors for active basis functions
end for
Obtain the global map `index_global` and 1D hierarchical structure `LEVEL1D`

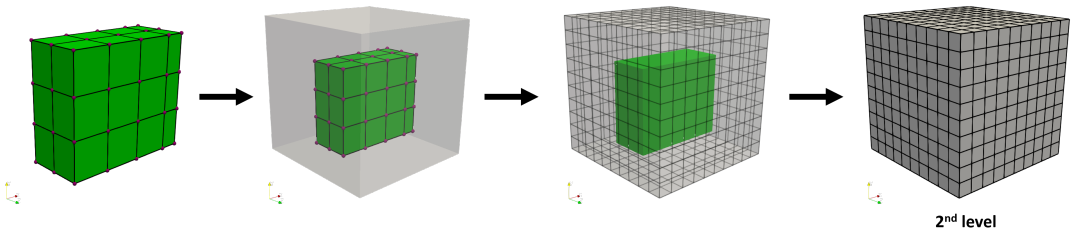

Figure 8.10: Workflow for the case with polynomial degree $p = 1$ and two hierarchical levels. The elements of the first level are completely replaced by those of the second level.

Algorithm 5 Algorithm for 3D Immersed Isogeometric Analysis - Part 2 (continued)

Step 4: Construction of integration points and domains

for each leaf element in `data_tree` **do**
    Generate Gaussian integration points in the parametric domain
    If the integrated element is on the boundary, the integration points must be increased to get a better approximation, otherwise $p+1$ is sufficient
    Compute hierarchical leaf–root paths for immersed integration
    Store coordinates and weights in `integration` and `roots`
end for

Step 5: Assembly of global matrices

for each level lvl **do**
    for each active element **do**
        Evaluate NURBS basis functions and their derivatives
        Compute Jacobian and geometric transformations
        if integration point lies inside the immersed geometry **then**
            Accumulate local stiffness and mass contributions (K_e, M_e)
        else
            Apply penalization factor $\alpha \in [10^{-8}, 10^{-12}]$
        end if
        Assemble (K_e, M_e) into global matrices (K, M)
    end for
end for

Step 6: Final output

Return global matrices (K, M), total volume, and hierarchical data structures `LEVEL`, `data_tree`, and `index_global`

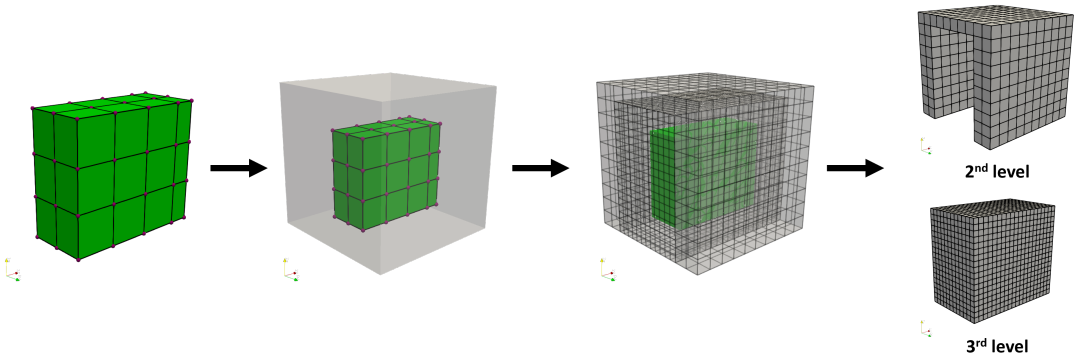

Figure 8.11: Workflow for the case with polynomial degree $p = 1$ and three hierarchical levels. Also in this case, the elements of the first level are completely replaced by those of the higher levels.

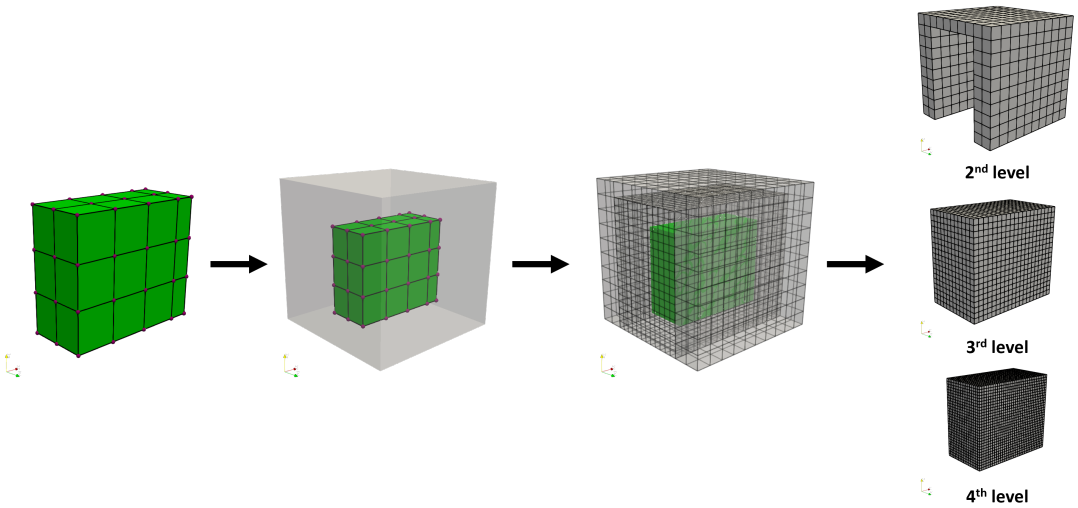

Figure 8.12: Workflow for the case with polynomial degree $p = 1$ and four hierarchical levels. As before, the elements of the first level are entirely replaced by those of the subsequent levels.

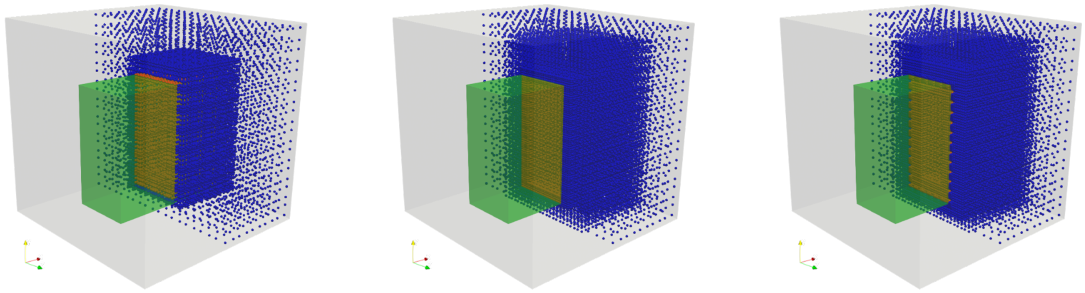

Figure 8.13: Distribution of the Gauss points considered in the hierarchical analysis with polynomial degree $p = 1$. From left to right: two, three, and four hierarchical levels are used, respectively. In blue the penalized Gauss points, in orange the not-penalized Gauss points.

carried out only on the internal points, while the external ones are penalized.

Figure 8.14 shows the convergence of the first ten computed modes obtained by varying the polynomial degrees p, q, and r from 1 to 3, while increasing the number of hierarchical levels in the analysis, respect to the analytical solution which is available for this problem. Furthermore, Figure 8.15 illustrates the first three, non-zero, numerical mode shapes.

Figure 8.16 shows the degrees of freedom and the computational costs (including hierarchical level construction time, matrix assembly time, and system solution time for the modal analysis) for the cases considered.

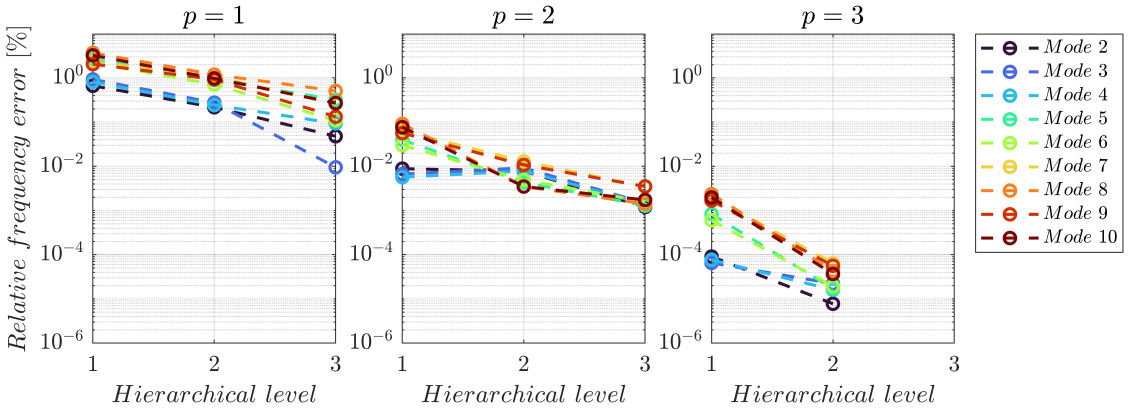

Figure 8.14: Convergence of the first ten computed eigenmodes obtained by varying the polynomial orders p, q, and r from 1 to 3, while increasing the number of hierarchical levels in the analysis. The subfigures correspond respectively to $p = 1$ (left), $p = 2$ (center), and $p = 3$ (right). The vertical axis represents the relative error with respect to the exact solution, whereas the horizontal axis indicates the number of hierarchical levels considered.

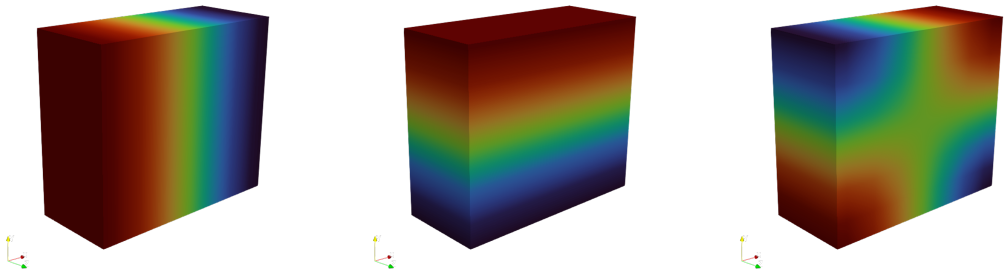

Figure 8.15: First three non-zero acoustic modal shapes.

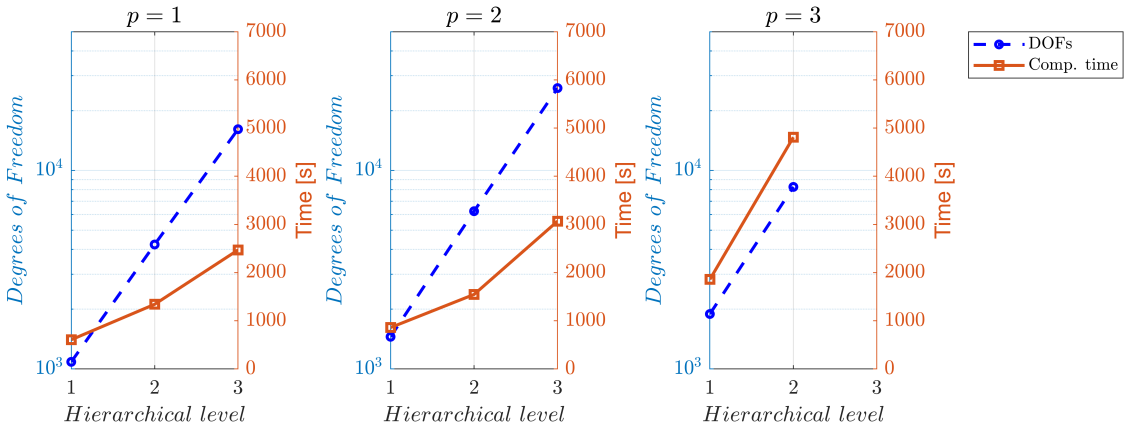

Figure 8.16: Degrees of freedom (left axis) and computational costs (right axis) for the considered cases. The computational costs include the time to build the hierarchical levels, assemble the matrices, and solve the system.

As the number of hierarchical levels increases, the computational times become significant, as shown in Figure 8.16. This is mainly due to the fact that the code was implemented in MATLAB and can still be optimized. The computational time is mainly due to the assembly of matrix because of:

- a lot of basis are coupled at many hierarchical levels;
- for each basis, the B-Spline functions are called form an external tool.

As a future way to reduce the computational time, the use of compiled C or C++ or FORTRAN might be helpful.

Chapter 9

3D coupling strategy

The accurate and efficient coupling between fluid and structural domains represents one of the most challenging aspects of modern computational mechanics, particularly in the context of vibroacoustic and fluid–structure interaction (FSI) analyses. This chapter presents a three-dimensional coupling strategy that combines immersed isogeometric analysis for the fluid domain with Kirchhoff–Love shell formulations. For the structure and for multi-patches Kirchhoff–Love geometry, a method to ensure the geometry continuity (G^1) is proposed. The hybrid approach (Immersed IGA and B-Rep) exploits the exact geometric representation provided by NURBS or B-REP data, while maintaining high-order continuity and smoothness at the interface. The proposed method allows for a direct and seamless integration between the CAD model of the structure and the volumetric spline-based description of the surrounding acoustic or fluid cavity. The developed coupling approach is validated through a vibroacoustic benchmark problem, where the numerical results are compared against those obtained from the commercial software Patran–Nastran. The excellent agreement between the two sets of results confirms the robustness and accuracy of the proposed immersed isogeometric coupling strategy.

Content

9.1 Introduction and State of the Art of Coupling Strategies for FSI

9.1.1 Motivation and Problem Context

The accurate simulation of fluid–structure interaction (FSI) problems involving thin-walled structures is of significant importance in computational mechanics. This study focuses on exploiting Boundary Representation (B-REP) CAD data: structural components and interfaces that can be described as surfaces are modeled directly from B-REP geometry, while the fluid cavity is represented volumetrically using HB-splines within the immersed IGA framework. This allows a natural integration between CAD-based surface models and volumetric spline representations, preserving thin-shell behavior.

9.1.2 Kirchhoff-Love Shells and Immersed Fluid Approaches

The Kirchhoff–Love (KL) shell formulation assumes that normals to the midsurface remain straight and normal after deformation, neglecting transverse shear. Within IGA, KL shells are particularly suitable because spline basis functions inherently satisfy the C^1-continuity requirements [100, 101, 102, 103]. On the fluid side, immersed isogeometric methods embed the physical boundary within a fixed background mesh and enforce interface conditions weakly via penalty, Nitsche, or Lagrange-multiplier techniques [104, 105, 106, 107]. These approaches enable the treatment of complex or moving geometries without boundary-fitted meshes [99, 98, 108, 109].

9.1.3 Coupling Strategies and Contributions of This Work

Coupling fluid and structure can be achieved via monolithic or partitioned schemes. Monolithic approaches solve the coupled system at once, while partitioned methods iterate between fluid and structure. Ensuring consistent interface kinematics and dynamics is crucial, especially for non-matching discretizations [110]. Coupling volumetric fluid domains with 2D KL shells introduces additional challenges due to the geometric mismatch. Recent works [111, 112] address weak enforcement of coupling conditions using Nitsche's method for thin shells. Building on these foundations, this thesis couples a 3D fluid cavity obtained via Immersed IGA with a KL shell directly extracted from CAD. This methodology preserves exact geometric correspondence and combines the high-order accuracy of KL shells with the flexibility of immersed IGA for complex fluid domains.

9.2 Notions on Kirchhoff-Love shell theory

9.2.1 Assumptions and geometric representation

The structure is modelled as a shell defined by a curved surface denoted by Σ. A material point, denoted by $\boldsymbol{X} \in \mathbb{R}^3$, is associated with a pair of curvilinear coordinates (θ^1, θ^2) belonging to the intervals $\mathcal{I}1$ and $\mathcal{I}2$, such that:

$$\boldsymbol{X} = \boldsymbol{X}(\theta^1, \theta^2). \tag{9.1}$$

The displacement field $\boldsymbol{u} \in \mathbb{R}^3$ of the shell mid surface is defined as follows:

$$\boldsymbol{u} = \boldsymbol{u}(\theta^1, \theta^2). \tag{9.2}$$

9.2.2 Weak formulation for linear problems

For reference, the structure is assumed to be thin through its thickness t, which is considered constant. Transverse shear deformation is neglected in comparison with the elastic strain energy. Consequently, a normal vector to the midsurface in the reference configuration remains normal after deformation.

The virtual work of the internal forces with respect to a reference configuration can therefore be expressed as the sum of membrane and bending contributions, as follows:

$$-k(\delta\boldsymbol{u}, \boldsymbol{u}) = -\int_{\Sigma} \left(\delta\boldsymbol{\varepsilon}(\delta\boldsymbol{u}) : \mathbf{N}(\boldsymbol{u}) + \delta\boldsymbol{\kappa}(\delta\boldsymbol{u}) : \mathbf{M}(\boldsymbol{u})\right), dS. \tag{9.3}$$

Here, $\delta\boldsymbol{\varepsilon}$ denotes the virtual membrane strain tensor, $\mathbf{N}$ the in-plane stress resultant tensor, $\delta\boldsymbol{\kappa}$ the virtual change in curvature associated with bending, and $\mathbf{M}$ the bending moment tensor.

Under the assumption of small perturbations, the corresponding differential operators can be written as:

$$\delta\boldsymbol{\varepsilon}(\delta\boldsymbol{u}) = \mathcal{B}_{\text{mem}}, \delta\boldsymbol{u}, \qquad \mathbf{N}(\boldsymbol{u}) = t, \boldsymbol{D}, \mathcal{B}_{\text{mem}}, \boldsymbol{u}, \qquad \delta\boldsymbol{\kappa}(\delta\boldsymbol{u}) = \mathcal{B}_{\text{ben}}, \delta\boldsymbol{u}, \qquad \mathbf{M}(\boldsymbol{u}) = \frac{t^3}{12}, \boldsymbol{D}, \mathcal{B}_{\text{ben}}, \boldsymbol{u}. \tag{9.4}$$

For the sake of clarity, the explicit forms of the differential operators $\mathcal{B}_{\text{mem}}$, $\mathcal{B}_{\text{ben}}$, and $\boldsymbol{D}$ are omitted here. These operators are defined in terms of quantities derived from differential geometry, and their computation relies on covariant and contravariant bases together with the associated metric tensors [100, 101].

9.2.3 Kirchhoff-Love numerical example

In this section, four examples of the application of the Kirchhoff–Love formulation are presented. In particular, the first example is a plate consisting of a single patch. The second example, instead, is a plate composed by two equal patches, the third consists of two different patches and the fourth consists of a cylinder composed of four different patches. In the last two cases, it is necessary to enforce a G^1 continuity at the interfaces between the patches as explained in [2]. The G^1 continuity (geometric tangent-continuity) means that two curves or surface patches meet in a way such that:

- They have positional continuity (they share the same point or edge): this is G^0;
- In addition, their tangent directions at the common boundary are the same (i.e., the tangent vectors are collinear and pointing in the same direction), thus the transition appears smooth without a sharp corner.

In other words: the patches may still differ in curvature (so the rate of change of the tangent might change across the interface), but at the interface the tangent plane (for surfaces) or tangent line (for curves) matches. This is often used in CAD, geometric modelling and isogeometric analysis to guarantee visually smooth or physically compatible joins between patches.

9.2.3.1 Kirchhoff-Love plate

In this section, the problem illustrated in Figure 9.1 is analysed. The plate has dimensions of 0.7×0.6 m, and its mechanical and geometrical properties are summarized in Table 9.1. The plate is clamped along its four edges.

A modal analysis was carried out on the plate, and the computed results were compared with the analytical solutions. The first nine analytical frequencies are reported in Table 9.2

The relative errors for the first nine modes are shown in Figure 9.2, while the mode shapes corresponding to the first six natural frequencies are illustrated in Figure 9.3.

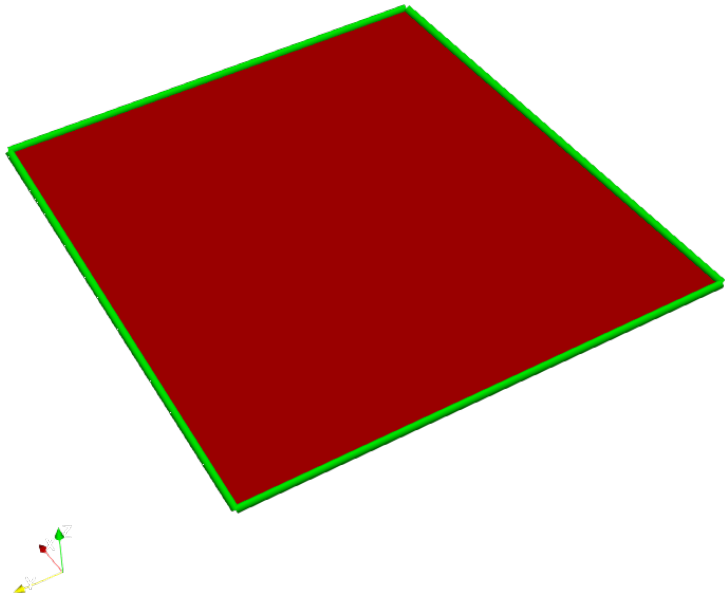

Figure 9.1: Geometry of the Kirchhoff–Love plate considered for the modal analysis. In the green area, all the displacements are clamped.

Table 9.1: Material and geometrical properties of the plate.

E [Pa]	ρ [$\frac{kg}{m^3}$]	t [m]	ν [-]
2.1×10^{11}	7860	0.005	0.3

Table 9.2: First nine analytical frequencies for the plate shown in Figure 9.1.

Mode number	f_{an} [Hz]
1	59.20
2	134.41
3	161.57
4	236.79
5	259.77
6	332.20
7	362.14
8	407.41
9	435.27

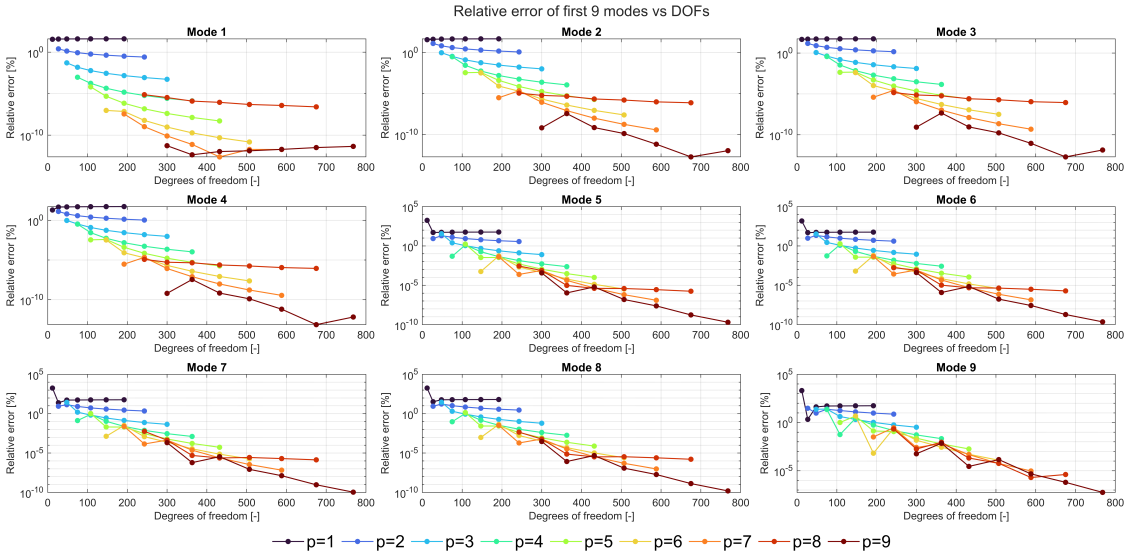

Figure 9.2: Comparison between numerical and analytical results: relative errors for the first nine modes varying the polynomial order and increasing the degrees of freedom.

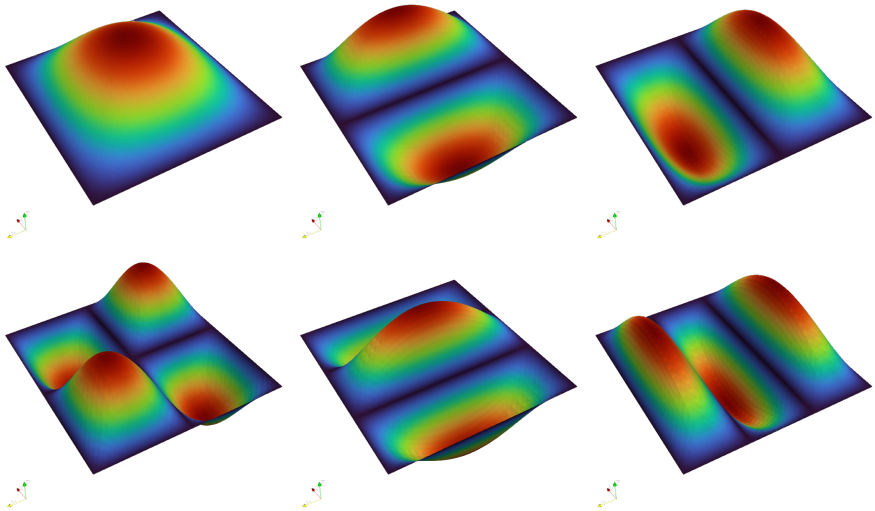

Figure 9.3: First six mode shapes obtained from the modal analysis of the Kirchhoff–Love plate.

As clearly shown in Figure 9.2, increasing the polynomial degree leads to faster convergence of the model. The same behaviour was previously observed in the 3D case.

9.2.3.2 Kirchhoff-Love plate divided in two equal patches

In this section, the same problem studied in the previous section is solved again, but this time considering that the plate is composed of two equal subplates as shown in Figure 9.4. In this case, a G^1 continuity condition must be enforced. The material properties are the same shown in Figure 9.1.

The approach used is that of the Local Lagrange Multipliers (LLM). In computational mechanics (and related numerical methods), Lagrange multipliers are introduced to enforce constraints by augmenting the system with additional unknowns (the multiplier values) and equations so that the constraint is satisfied exactly [113, 114]. A localized Lagrange multiplier approach refers to the strategy where these multipliers are applied locally (for example at the interface of sub-domains, patches or non-matching meshes) rather than enforcing a global coupling of all variables. For instance, when two patches meet and share nodes or when meshes do not align exactly, localized multipliers can act at those interface nodes to impose continuity or compatibility conditions without strongly coupling the entire systems. Using localized Lagrange multipliers has benefits such as preserving modularity of software components (each patch or domain solver can be relatively independent) and facilitating coupling of different discretizations (e.g., non-matching meshes) while still enforcing the constraint interface.

In this context (patch coupling in an isogeometric structure), the localized multipliers enforce matching of displacements across patch boundaries, ensuring continuity or compatibility across patches without merging all degrees of freedom into one monolithic system.

The applied algorithm, to enforce the G^1 continuity is explained in Algorithm 6.

Considering that the analytical solution frequencies are those reported in Table 9.2, Figure 9.5 shows the error between the frequencies obtained by modeling two plates and enforcing a G^1 continuity at their interface, and the analytical solution. Furthermore, Figure 9.6 illustrates the first three mode shapes, highlighting the two patches as well.

Even when considering two different plates and enforcing a G^1 continuity through local Lagrange multipliers (LLM), the obtained results are in excellent agreement with the analytical solutions. The

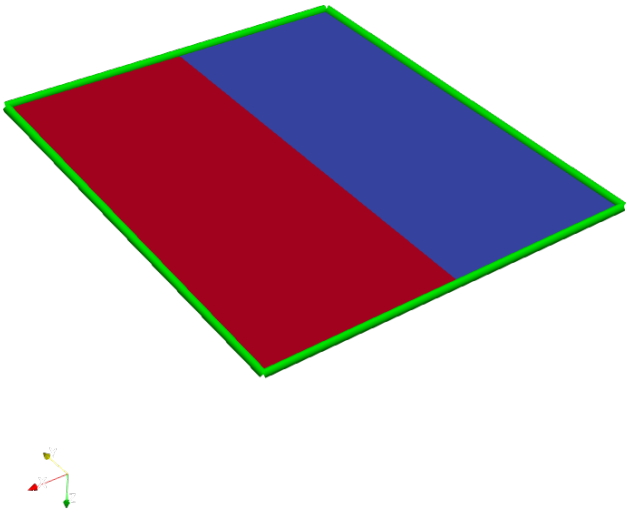

Figure 9.4: Geometry of the plate shell composed by two equal NURBS patches (highlighted with two different colours). The interfaces between patches are coupled through a G^1 continuity constraint. The green area is clamped.

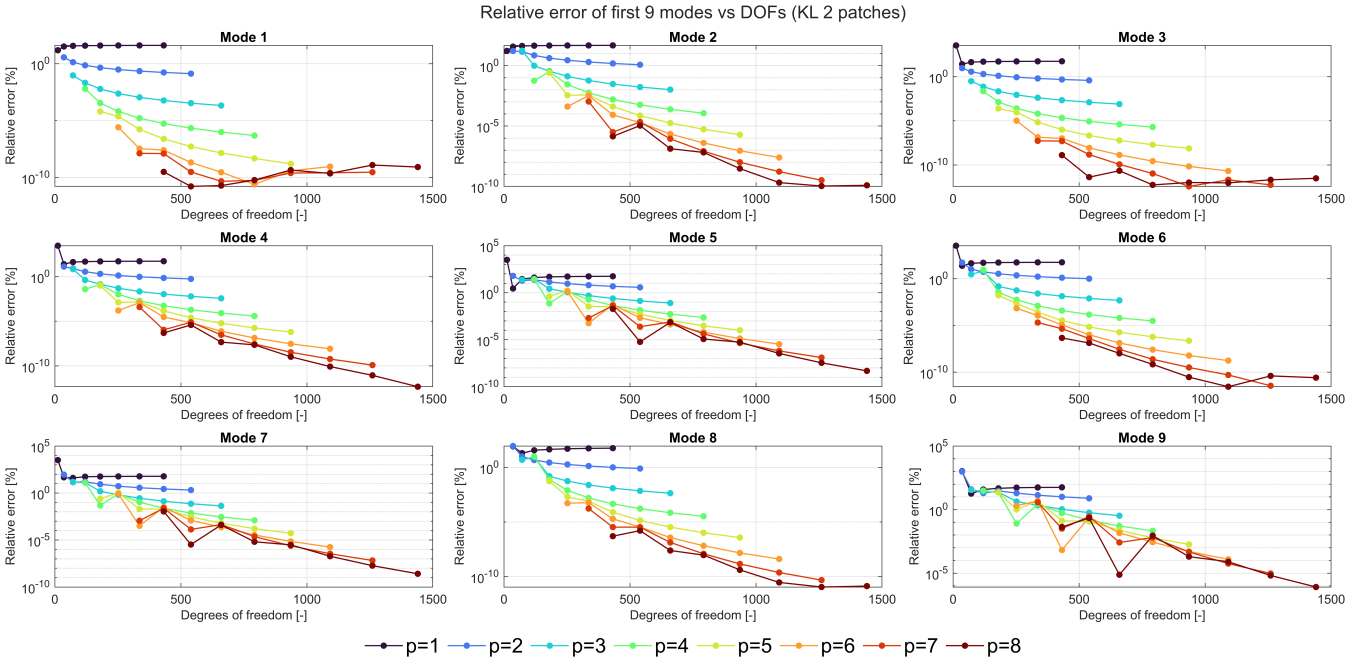

Figure 9.5: Comparison between numerical and analytical results: relative errors for the first nine modes varying the polynomial order and increasing the degrees of freedom.

Algorithm 6 Modal Analysis of 2D NURBS Structures with Constraints and Lagrange Multipliers

Input: Initial NURBS, refinement parameters, material properties (E, ν, ρ, t), number of Gauss points $noGPs$, geometric boundary constraints.
Output: Natural frequencies and mode shapes.
Refine NURBS uniformly along x and y:
Increase the polynomial order
Add more control points
Compute elemental stiffness and mass matrices for each patch:
for $i = 1$ to number of patches **do**
    $[K_i, M_i] \leftarrow$ compute 2D Kirchhoff-Love matrices
    Store K_i, M_i
end for
Assemble global matrices K and M from patch-wise contributions.
Identify constrained nodes based on boundary coordinates.
Determine local and global free degrees of freedom $dofu$ for each patch.
Identify connections between patches and shared nodes:
Find patch combinations with common nodes
Construct constraint matrices B and L_{inter} to link shared nodes.
Assemble extended Lagrangian matrices $K_{\text{lag}}, M_{\text{lag}}$ including constraints:

$$K_{\text{lag}} = \begin{bmatrix} K & B & 0 \\ B^T & 0 & -L_b \\ 0 & -L_b^T & 0 \end{bmatrix}, \qquad M_{\text{lag}} = \begin{bmatrix} M & 0 & 0 \\ 0 & 0 & 0 \\ 0 & 0 & 0 \end{bmatrix}$$

where

$$L_b = B^T L_{\text{inter}}.$$

Apply additional constraints via B^{con}.
Select global free degrees of freedom $dofu$.
Solve the reduced generalized eigenvalue problem:
$[vecp, valp] \leftarrow eigs(K_{lag}^T(dofu, dofu), M_{lag}^T(dofu, dofu), nbmode)$
Compute natural frequencies:
$freq \leftarrow \sqrt{diag(valp)}/(2\pi)$
Sort frequencies and corresponding mode shapes.

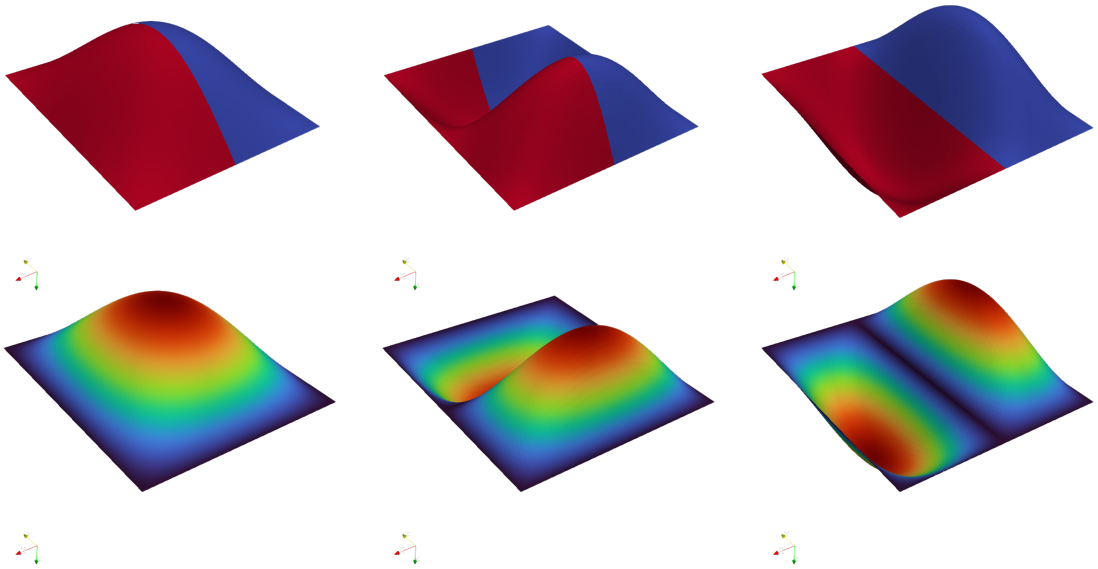

Figure 9.6: First three mode shapes of the plate shell obtained from the Kirchhoff–Love formulation with G^1 continuity enforcement across patch interfaces.

drawback in this case is that, in order to enforce G^1 continuity, additional degrees of freedom must be introduced into the system (approximately 10% more).

9.2.3.3 Kirchhoff-Love plate divided in two different patches

This section investigates the same problem as the previous one, but considering that the two patches have different sizes, as shown in Figure 9.7.

Figure 9.8 shows the error obtained in this case with respect to the reference solution, while Figure 9.9 presents the first three mode shapes.

Also for this application, the results are perfectly consistent with those obtained in the previous sections.

9.2.3.4 Kirchhoff-Love cylinder with four patches

In this section, a cylindrical shell composed of four patches is analysed (see Figure 9.10). The patches are connected along their interfaces, where a G^1 continuity condition is imposed to ensure smooth geometric and displacement transitions across the boundaries. The geometrical and material

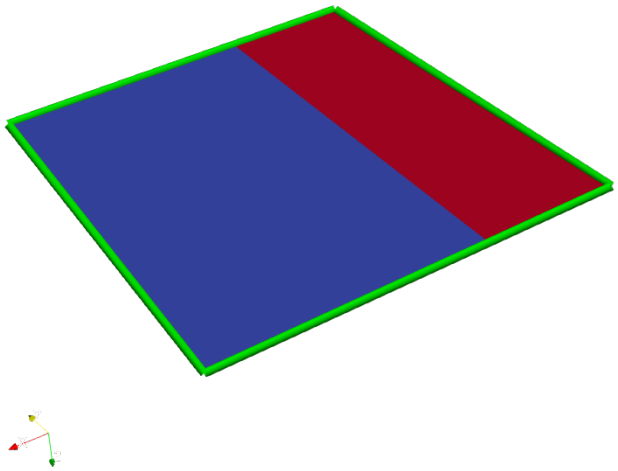

Figure 9.7: Geometry of the plate shell composed by two different NURBS patches (highlighted with two different colours). The interfaces between patches are coupled through a G^1 continuity constraint. The green area is clamped.

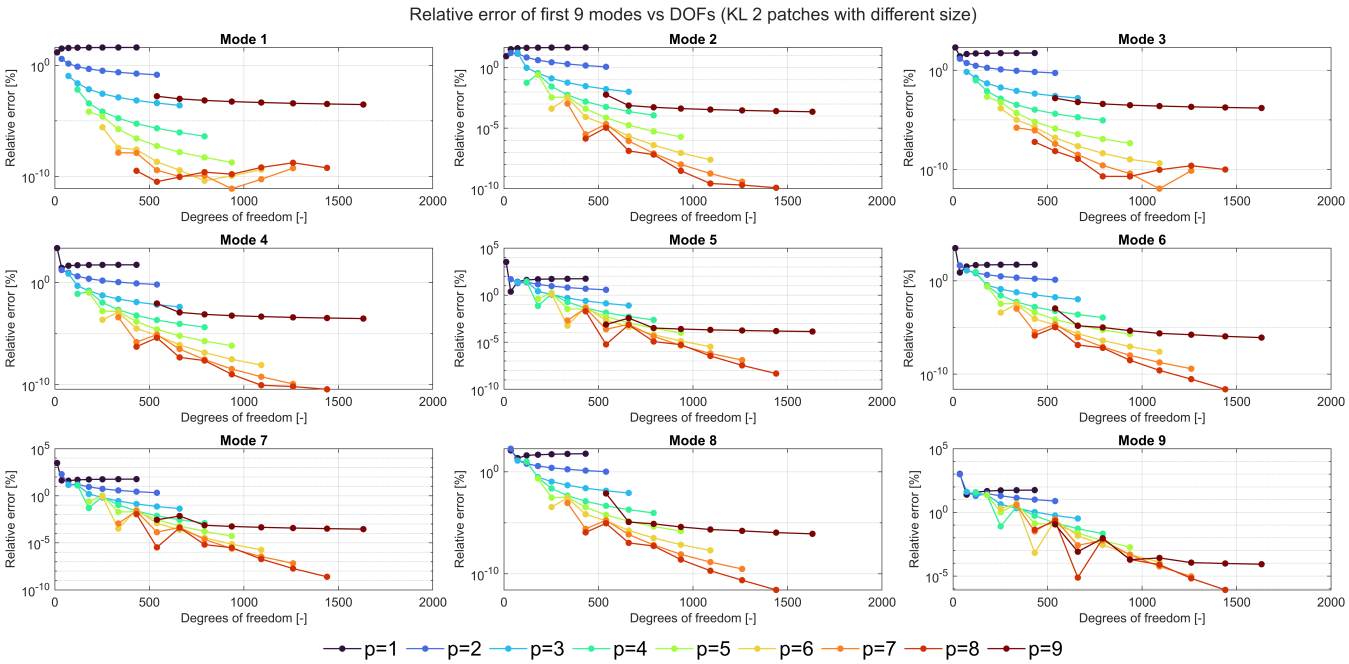

Figure 9.8: Comparison between numerical and analytical results: relative errors for the first nine modes varying the polynomial order and increasing the degrees of freedom.

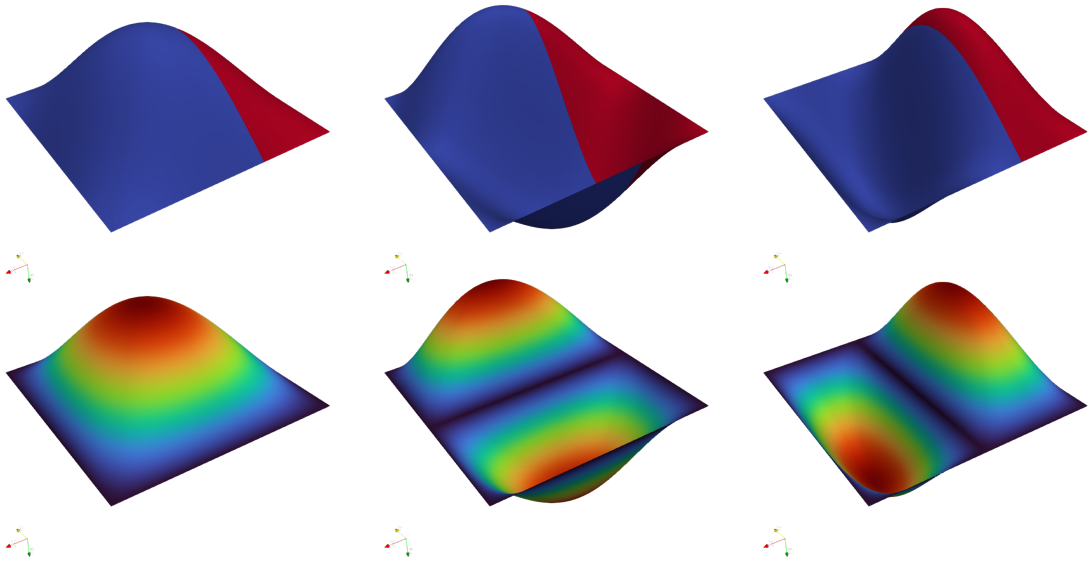

Figure 9.9: First three mode shapes of the plate shell obtained from the Kirchhoff–Love formulation with G^1 continuity enforcement across patch interfaces.

Table 9.3: Material and geometrical properties of cylinder.

E [Pa]	ρ [$\frac{kg}{m^3}$]	t [m]	ν [-]	R [m]	L [m]
7.0×10^{10}	7860	0.005	0.3	1	3

properties are reported in Table 9.3. The considered mesh for the analysis is shown in Figure 9.11.

Table 9.4 presents the analytical and numerical results obtained for this problem, highlighting the error between the two sets of results.

Table 9.4: First nine analytical and numerical natural frequencies of the cylinder and its relative error.

Mode number	f_{an} [Hz]	f_{num} [Hz]	err [%]
1	15.14	15.14	0.02
2	15.14	15.14	0.02
3	18.49	18.49	0.08
4	18.49	18.49	0.08
5	19.00	19.00	0.01
6	19.00	19.00	0.01
7	25.45	25.45	0.26
8	25.45	25.45	0.26
9	34.46	34.40	0.30

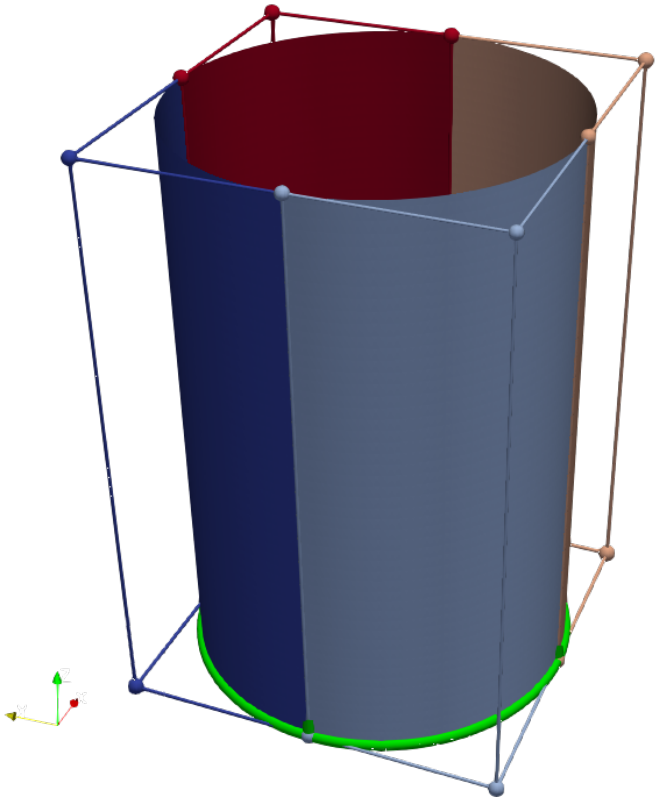

Figure 9.10: Geometry of the cylindrical shell composed of four NURBS patches (highlighted with four different colours). The interfaces between patches are coupled through a G^1 continuity constraint. The green area, at the bottom of the cylinder, is clamped.

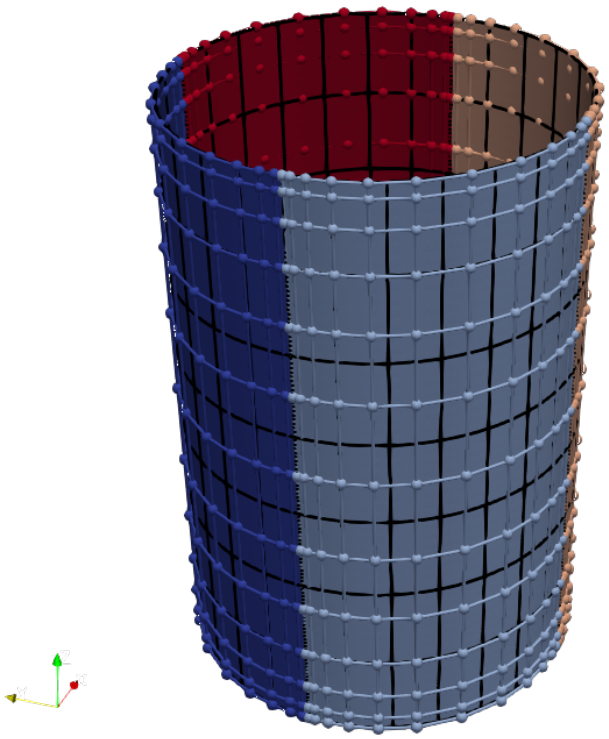

Figure 9.11: Considered mesh for the analysis. The control mesh and the control points are highlighted for each patch.

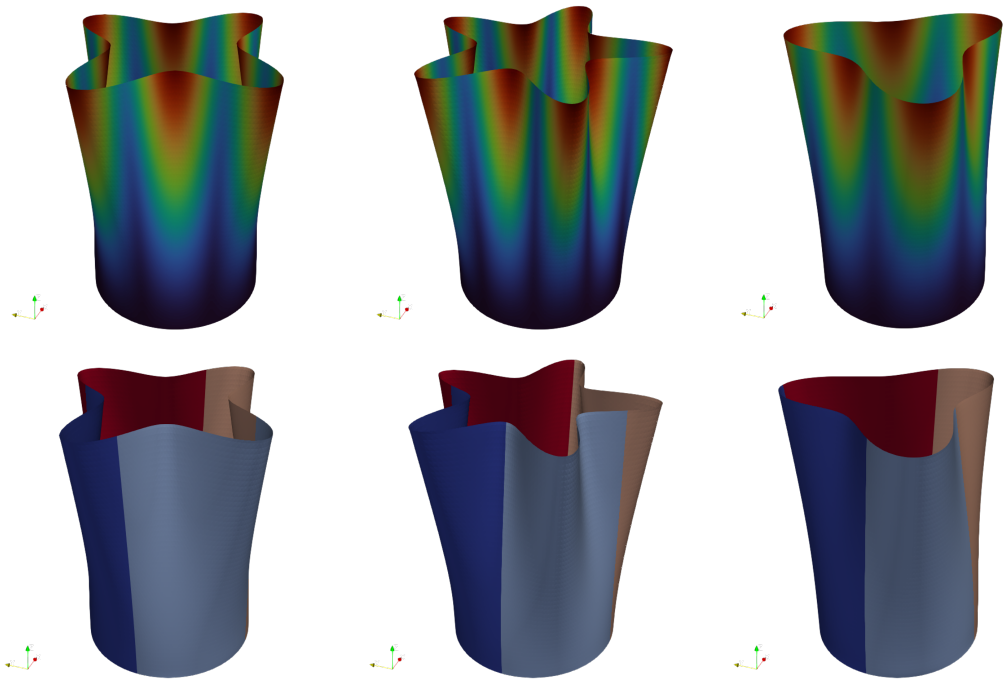

Figure 9.12: First three mode shapes of the cylindrical shell obtained from the Kirchhoff–Love formulation with G^1 continuity enforcement across patch interfaces.

Table 9.4 reports the analytical and numerical results obtained for this problem, highlighting the error between the two. In conclusion, the results obtained for this example are consistent with the reference ones.

9.2.3.5 Limitations

Although it has been demonstrated that a G^1 continuity condition can be successfully applied between patches modeled with the Kirchhoff–Love formulation, its generalization to an arbitrary number of patches has not been fully investigated in this work, representing a current limitation of the work. It is worth noting that an automated and robust implementation for the coupling of multiple patches is essential to extend the applicability of the method to more complex geometries and large-scale industrial models. Future developments should therefore focus on the definition of systematic algorithms for multi-patch connectivity management, capable of automatically enforcing G^1 or higher-order continuity conditions. Such an extension would allow for the creation of fully smooth and geometrically consistent models, further enhancing the accuracy and efficiency of isogeometric

vibroacoustic analyses. Moreover, the ability to handle complex multi-patch configurations in an automated manner would significantly strengthen the CAD-to-IGA integration process, paving the way for its use in real engineering design workflows.

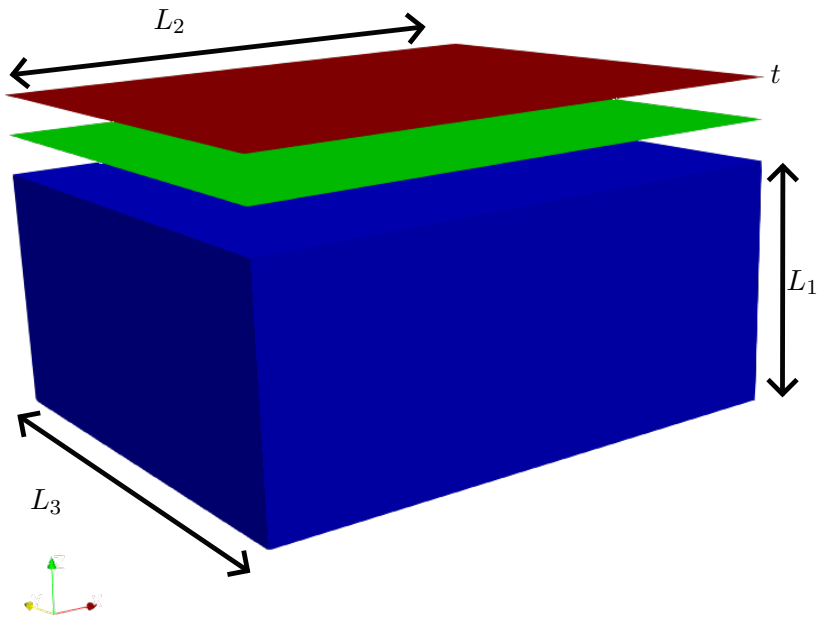

Figure 9.13: Exploded view of the coupled structural–acoustic model. The structural domain (red), the interface (green), and the acoustic cavity (blue) are displayed separately to highlight the three interacting regions.

9.3 Adopted coupling approach

Once the acoustic cavity is generated using HBS, it could be coupled with a structure to perform vibroacoustic analysis. The structure can also be modelled using HBS (for a 3D structure) or with shell elements. In the case studied here, the structure is modeled with shell elements using a Kirchhoff-Love formulation. The shell structural geometry can be directly extracted from the CAD model. A classic coupling problem is shown in Figure 9.13. It represents the acoustic cavity obtained in the previous section and a flat structural component.

In the continuous weak formulation, the coupling terms are expressed as in 3.14 and 3.18.

However, we are now working in a *discretized context*, where the interface Σ_i is represented by a NURBS surface. The displacement field $\boldsymbol{u}$ and the corresponding virtual displacement field $\delta\boldsymbol{u}$ are

approximated using NURBS shape functions and denoted by $\boldsymbol{u}^h$ and $\delta\boldsymbol{u}^h$, respectively. These are defined as in 3.19 and can be expressed also as:

$$\boldsymbol{u}^h(\boldsymbol{\xi}_s) = \sum_{i=1}^{n_s} R_i(\boldsymbol{\xi}_s)\, \boldsymbol{u}_i = \mathbf{R}(\boldsymbol{\xi}_s)\, \mathbf{u} \tag{9.5}$$

$$\delta\boldsymbol{u}^h(\boldsymbol{\xi}_s) = \sum_{i=1}^{n_s} R_i(\boldsymbol{\xi}_s)\, \delta\boldsymbol{u}_i = \mathbf{R}(\boldsymbol{\xi}_s)\, \delta\mathbf{u} \tag{9.6}$$

where $\boldsymbol{\xi}_s$ is the coordinate in the 2D parametric space $\boldsymbol{\xi}_s = (\xi_s, \eta_s)$, and $\mathbf{R}$ is the matrix of NURBS shape functions, given by:

$$\mathbf{R} = \begin{bmatrix} R_1 & 0 & 0 & \dots & R_{n_s} & 0 & 0 \\ 0 & R_1 & 0 & \dots & 0 & R_{n_s} & 0 \\ 0 & 0 & R_1 & \dots & 0 & 0 & R_{n_s} \end{bmatrix} \tag{9.7}$$

Here, $\boldsymbol{u}_i$ is a vector containing the unknown displacement values at the control points:

$$\boldsymbol{u}_i = [u_1, v_1, w_1, \dots, u_{n_s}, v_{n_s}, w_{n_s}]^T. \tag{9.8}$$

The **pressure field** is defined over a three-dimensional domain that contains the surface interface, which is subdivided using HBS (Hierarchical B-splines). It is expressed as:

$$p^h = \underbrace{\sum_{i=1}^{n_0} S_i^0(\boldsymbol{\xi}_f)\, p_i^0}_{\text{Level 0}} + \dots + \underbrace{\sum_{i=1}^{n_L} S_i^L(\boldsymbol{\xi}_f)\, p_i^L}_{\text{Level L}} \tag{9.9}$$

$$= \mathbf{S}\,\mathbf{p} \tag{9.10}$$

where $\boldsymbol{\xi}_f$ is the coordinate in the 3D parametric space $\boldsymbol{\xi}_f = (\xi_f, \eta_f, \zeta_f)$, $\mathbf{S}$ is the global matrix of HBS shape functions (defined later), and $\mathbf{p}$ is the vector of pressure unknowns (not located at control points). This vector is organized as:

$$\mathbf{p} = \begin{bmatrix} \mathbf{p}^0 \\ \vdots \\ \mathbf{p}^k \\ \vdots \\ \mathbf{p}^L \end{bmatrix}, \qquad \mathbf{p}^k = \begin{bmatrix} p_1^k \\ \vdots \\ p_{n_k}^k \end{bmatrix}. \tag{9.11}$$

Finally, the global HBS shape function matrix $\mathbf{S}$ is assembled as:

$$\mathbf{S} = [\,\mathbf{S}^0, \ldots, \mathbf{S}^k, \ldots, \mathbf{S}^L\,], \tag{9.12}$$

where each block $\mathbf{S}^k$ is defined by:

$$\mathbf{S}^k = [\,S_1^k, \ldots, S_{n_k}^k\,]. \tag{9.13}$$

The main objective is to construct the coupling matrix $\mathbb{C}$, which enables the analysis of vibroacoustic problems. To build this matrix, an integration domain must first be defined. The coupling is performed at the Gauss points of the NURBS interface surface, which are defined in the 2D parametric space of the solid. In general, an integration over a 2D IGA surface involves two transformations:

$$\int_{\Sigma_i} f(\boldsymbol{x})\, dS = \int_{\hat{\Sigma}_i} f(\boldsymbol{x}(\boldsymbol{\xi}_s))\, J_1(\boldsymbol{\xi}_s) J_2(\boldsymbol{\xi}_s)\, d\hat{S} \tag{9.14}$$

$$\simeq \sum_{g=1}^{nG} f(\boldsymbol{x}(\boldsymbol{\xi}_g))\, J_1(\boldsymbol{\xi}_g) J_2(\boldsymbol{\xi}_g) w_g, \tag{9.15}$$

where J_1 is the mapping from the parametric space to the physical space, J_2 accounts for the transformation to the surface in 3D space, and w_g are the Gauss weights. In our case, the integration is defined as:

$$c(p, \delta\boldsymbol{u}) = \int_{\Sigma_i} p\,\boldsymbol{n} \cdot \delta\boldsymbol{u}\, dS \tag{9.16}$$

$$= \int_{\hat{\Sigma}_i} p^h(\boldsymbol{\xi}_f(\boldsymbol{\xi}_s))\,\boldsymbol{n} \cdot \delta\boldsymbol{u}^h(\boldsymbol{\xi}_s)\, J_1(\boldsymbol{\xi}_s) J_2(\boldsymbol{\xi}_s)\, d\hat{S} \tag{9.17}$$

$$\simeq \sum_{g=1}^{nG} p^h(\boldsymbol{\xi}_f(\boldsymbol{\xi}_g))\,\boldsymbol{n} \cdot \delta\boldsymbol{u}^h(\boldsymbol{\xi}_g)\, J_1(\boldsymbol{\xi}_g) J_2(\boldsymbol{\xi}_g) w_g \tag{9.18}$$

$$\simeq \delta\mathbf{u}^T \left[\sum_{g=1}^{nG} \mathbf{R}^T(\boldsymbol{\xi}_g)\,\mathbf{n}\,\mathbf{S}(\boldsymbol{\xi}_f(\boldsymbol{\xi}_g))\, J_1(\boldsymbol{\xi}_g) J_2(\boldsymbol{\xi}_g) w_g \right] \mathbf{p}, \tag{9.19}$$

where: $\boldsymbol{\xi}_s = (\xi_s, \eta_s)$ are the coordinates in the 2D parametric space of the solid, $\boldsymbol{\xi}_f = (\xi_f, \eta_f, \zeta_f)$ are the coordinates in the 3D parametric space of the fluid, $\mathbf{R}$ and $\mathbf{S}$ are the NURBS and HBS shape function matrices, respectively, and $\mathbf{n}$ is the outward normal vector to the interface.

Once the integration domain is set, the next step is to evaluate the structural NURBS basis functions in the 2D parametric space ($\mathbf{R}^T(\boldsymbol{\xi}_g)$) and the hierarchical B-spline basis functions in the 3D parametric space of the fluid ($\mathbf{S}(\boldsymbol{\xi}_f(\boldsymbol{\xi}_g))$).

This approach is illustrated in Figure 9.14.

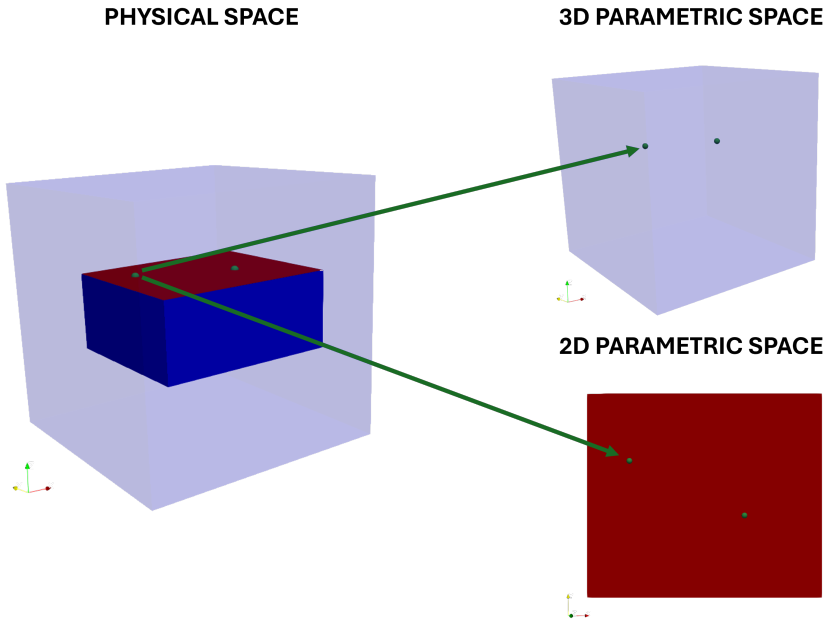

Figure 9.14: Coupling integration. In green is the Gauss point to be integrated and then the corresponding coordinates in the 2D and 3D parametric space.

Table 9.5: Structural and acoustic parameters for the problem illustrated in Figure 9.13.

E [Pa]	ρ_s $[\frac{kg}{m^3}]$	ν [-]	$L_1 \times L_2 \times L_3$ [m]	ρ_f $[\frac{kg}{m^3}]$	c_0
4×10^6	7860	0.3	$0.3 \times 0.7 \times 0.6$	1.0	1.0

Table 9.6: First five vibroacoustic numerical frequencies and its relative error, obtained through the proposed method and Patran-Nastran.

$f_{num}(Hz)$	$f_{PatNat}(Hz)$	**Error** (%)
0	0	0
0.2588	0.2603	0.0057
0.5861	0.5832	0.0050
0.7046	0.7019	0.0039
0.7163	0.7170	0.0010
0.8361	0.8360	0.0001
1.0325	1.0263	0.0060
1.1010	1.1017	0.0007

For the problem shown in Figure 9.13, whose dimensions and the properties of the acoustic cavity and the structure are reported in Table 9.5, a coupled modal analysis is carried out. The number of hierarchical levels to construct the fluid cavity is set to two. The results obtained in terms of natural frequencies and eigenvalues are compared with those obtained using a commercial software (Patran–Nastran [115, 116]). The frequencies of the aforementioned problem are shown in Table 9.6 while the modal shapes are shown in Figure 9.15.

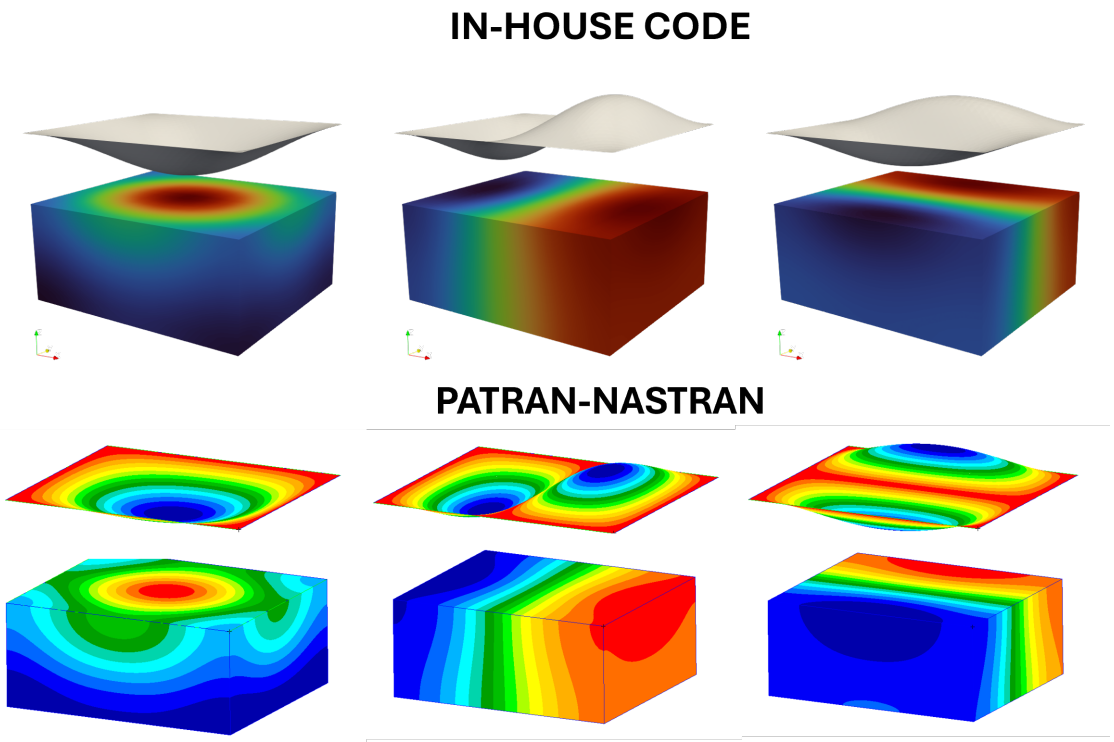

Figure 9.15: Vibroacoustic mode shapes obtained using the proposed coupled modal analysis method compared with the corresponding results computed with the commercial software Patran–Nastran.

Chapter 10

Numerical examples for complex shapes

This chapter is dedicated to the applications and possible integrations between CAD and IGA. Several industrial examples will be presented, showing how isogeometric analysis can be directly integrated with CAD. Modal coupling analyses will also be shown, which are useful for studying the dynamics of both coupled and uncoupled systems. In particular, different case studies will be discussed, ranging from the automotive to the marine fields. For each of these, immersed IGA will be employed in combination with CAD models, thus providing a direct integration between design and analysis. These examples are meant not only to demonstrate the technical feasibility of a CAD–IGA interaction, but also to highlight its potential impact in industrial practice. Indeed, by bridging the gap between design and analysis, this approach shows that seamless integration is achievable and paves the way towards more efficient, reliable, and innovation-oriented workflows.

Content

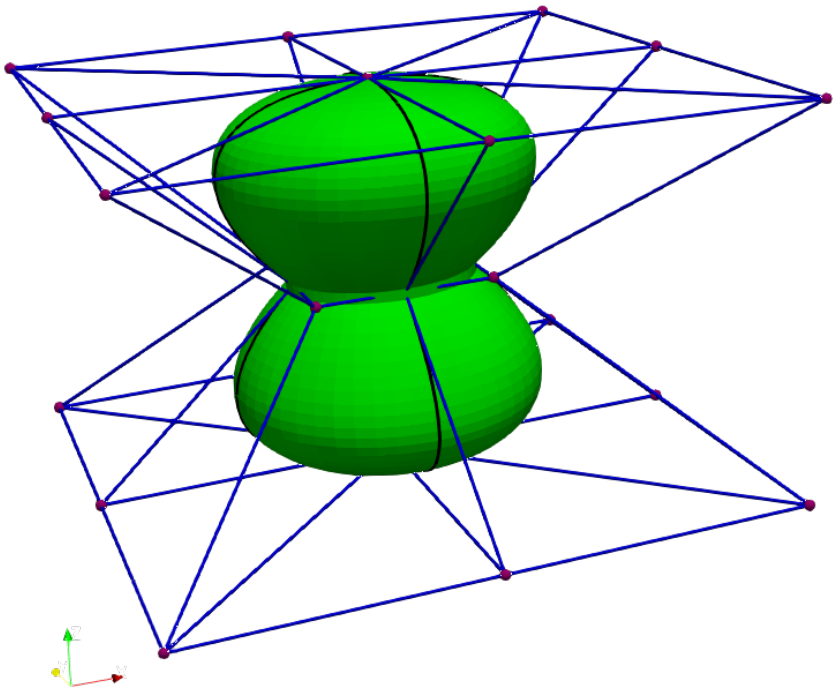

Figure 10.1: Pot-shaped geometry extracted from CAD software.

10.1 Pot-shaped acoustic cavity

The first example under investigation is shown in Figure 10.1. The geometry represents a pot-shaped acoustic cavity, for which the acoustic modal shapes want to be analyzed. As already described in the previous chapters, when the geometry is extracted from the CAD environment, only the boundary representation is transferred.

Considering that at least six linear elements per wavelength are required to obtain a good approximation of the acoustic modes, four hierarchical levels are constructed. These are shown in Figure 10.2.

Since no analytical solution is available for this problem, the reference solution used to validate the proposed model is obtained through a FEM approach with a commercial software package (Patran-Nastran). The properties for the analysis are reported in Table 10.1, while Figure 10.3 highlights all the considered integration points, derived from the different hierarchical levels, that are considered in

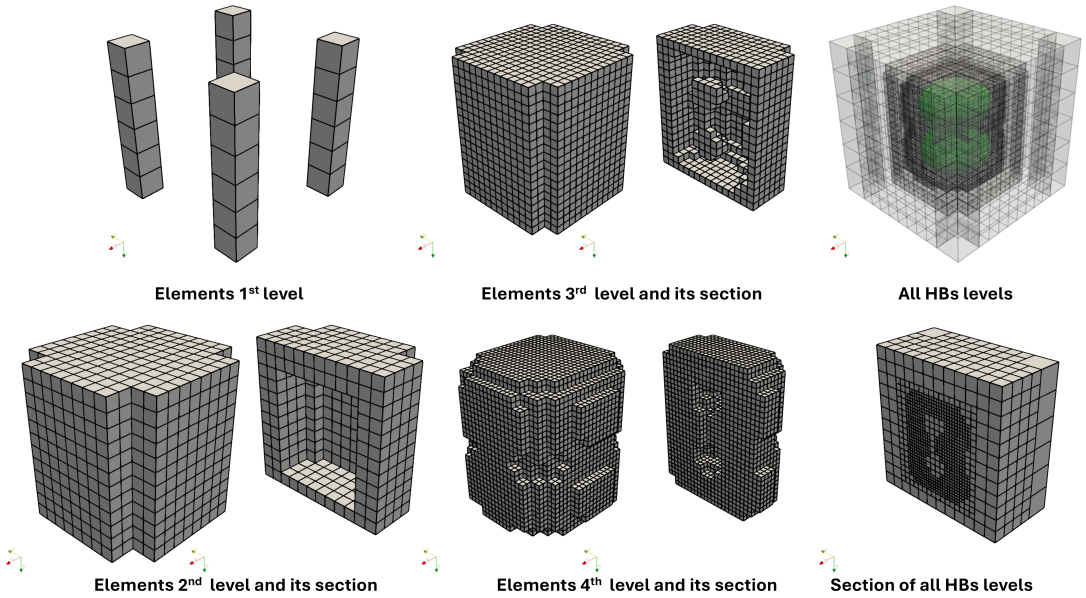

Figure 10.2: Hierarchical B-Spline levels and its sections.

Table 10.1: Pot-shaped acoustic properties.

$\rho_f\ [\frac{kg}{m^3}]$	$c_0\ [\frac{m}{s}]$	$level$
1	340	4

the numerical procedure.

Table 10.2 reports the first ten natural acoustic frequencies of the system, obtained both with the proposed Immersed method and with the commercial software. In addition, Figure 10.4 shows the first four modal shapes computed using Immersed IGA and the commercial software.

10.2 Submersible drone acoustic cavity

The second example under investigation is shown in Figure 10.5. The geometry represents a simplified car acoustic cavity, for which the acoustic modal shapes want to be analyzed.

Considering that at least six linear elements per wavelength are required to obtain a good approximation of the acoustic modes, four hierarchical levels are constructed. These are shown in Figure 10.6.

Since no analytical solution is available for this problem, the reference solution used to validate the proposed model is obtained through a FEM approach with a commercial software package (Patran-

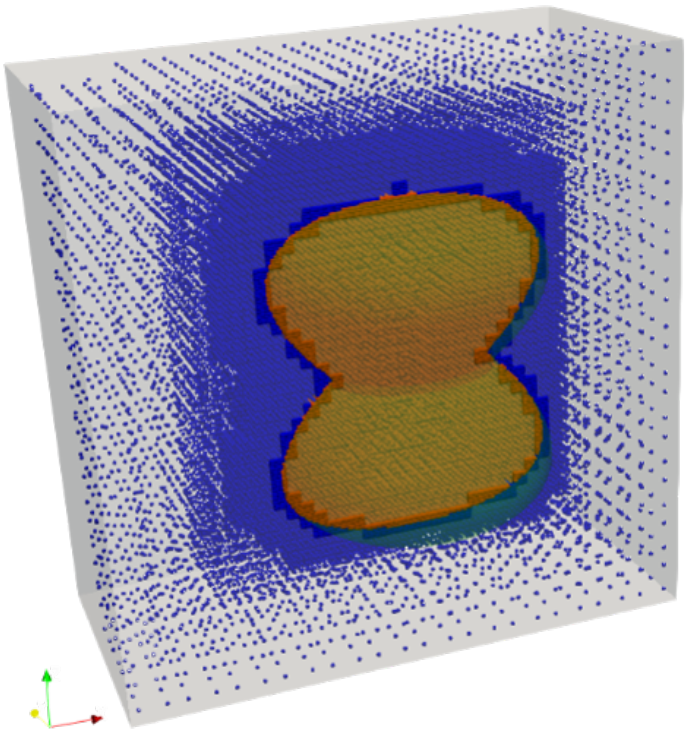

Figure 10.3: Gauss points for the pot-shaped geometry. In blue the penalized Gauss points, in orange the not-penalized Gauss points.

Table 10.2: First ten acoustic numerical and reference frequencies, and the corresponding percentage error.

f_{PatNas} **[Hz]**	f_{num} **[Hz]**	**Error** (%)
0	0	0
255.08	256.62	0.60
497.12	498.01	0.18
537.37	538.77	0.26
538.95	539.97	0.19
570.45	571.99	0.27
732.00	734.46	0.34
830.74	835.93	0.62
838.76	840.91	0.26
841.19	846.38	0.62

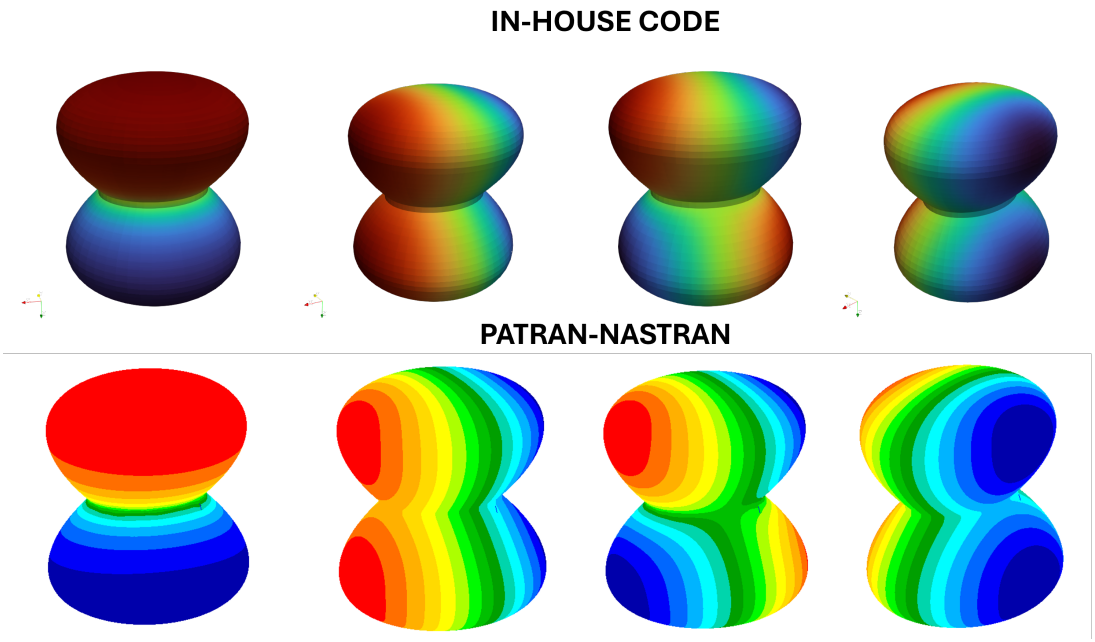

Figure 10.4: Comparison of first four non-zero modes between the proposed immersed IGA method and Patran-Nastran.

Table 10.3: Submersible drone acoustic properties.

ρ_f $[\frac{kg}{m^3}]$	c_0 $[\frac{m}{s}]$	*level*
1	340	4

Nastran). The properties for the analysis are reported in Table 10.3, while Figure 10.7 highlights all the considered integration points, derived from the different hierarchical levels, that are considered in the numerical procedure.

Table 10.4 reports the first ten natural acoustic frequencies of the system, obtained both with the proposed Immersed method and with the commercial software. In addition, Figure 10.8 shows the first four modal shapes computed using Immersed IGA and the commercial software.

10.3 Car-shaped acoustic cavity

The third example under investigation is shown in Figure 10.9. The geometry represents a simplified car acoustic cavity, for which the acoustic modal shapes want to be analyzed.

Considering that at least six linear elements per wavelength are required to obtain a good approxi-

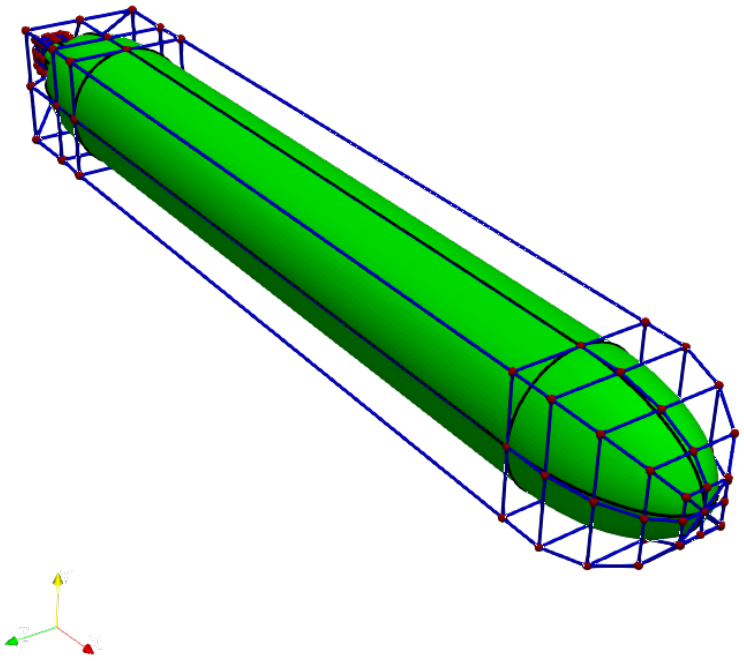

Figure 10.5: Submersible drone geometry extracted from CAD software.

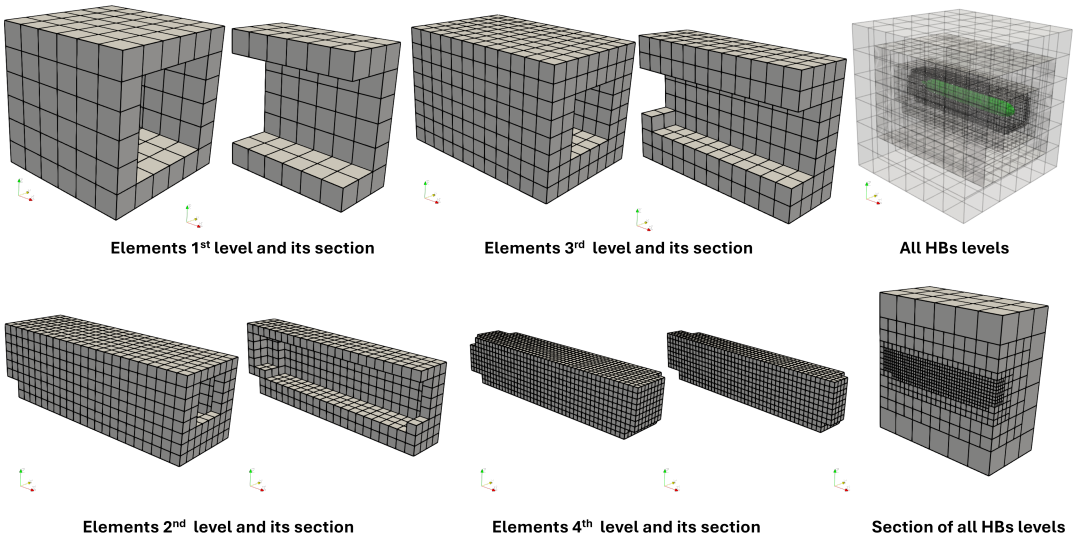

Figure 10.6: Hierarchical B-Spline levels and its sections.

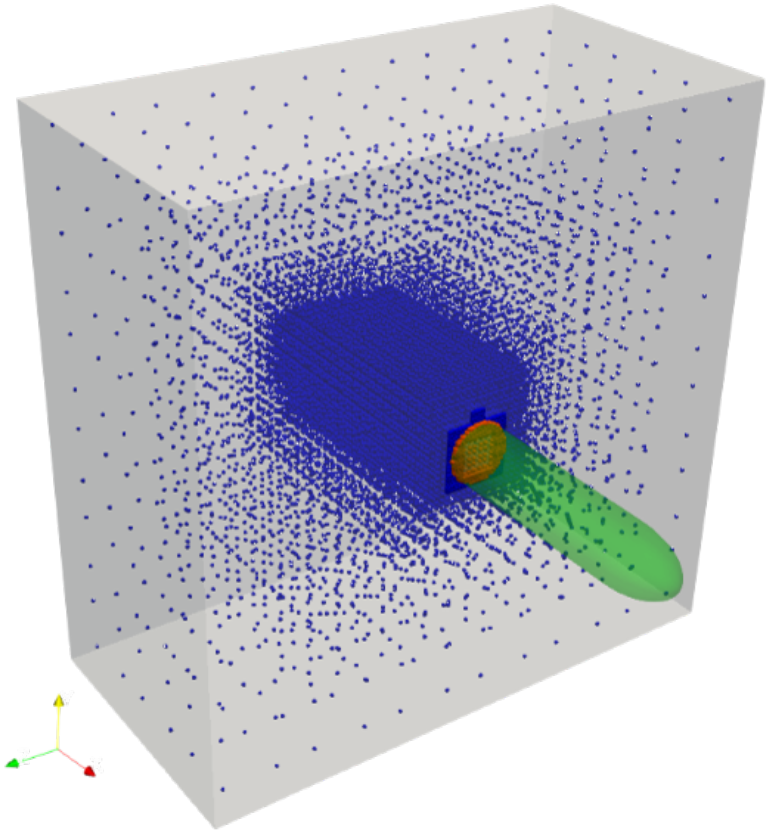

Figure 10.7: Gauss points for the submersible drone geometry. In blue the penalized Gauss points, in orange the not-penalized Gauss points.

Table 10.4: First ten acoustic numerical and reference frequencies, and the corresponding percentage error.

f_{PatNas} **[Hz]**	f_{num} **[Hz]**	**Error** (%)
0	0	0
236.36	236.74	0.16
470.91	472.03	0.24
701.52	704.30	0.39
924.97	931.45	0.70
1133.27	1149.06	1.39
1305.02	1343.68	2.96
1456.88	1504.65	3.28
1643.35	1682.76	2.40
1847.92	1891.32	2.35

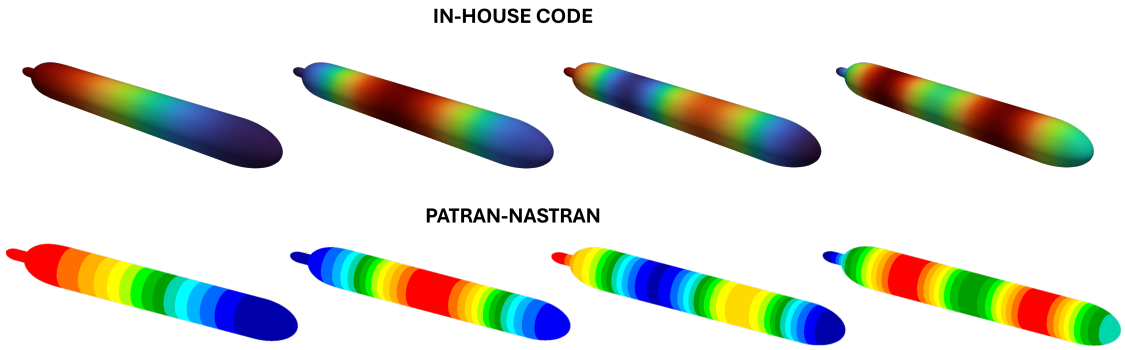

Figure 10.8: Comparison of first four non-zero modes between the proposed immersed IGA method and Patran-Nastran.

Table 10.5: Simplified car acoustic properties.

$\rho_f \ [\frac{kg}{m^3}]$	$c_0 \ [\frac{m}{s}]$	$level$
1	340	4

mation of the acoustic modes, four hierarchical levels are constructed. These are shown in Figure 10.10.

Since no analytical solution is available for this problem, the reference solution used to validate the proposed model is obtained through a FEM approach with a commercial software package (Patran-Nastran). The properties for the analysis are reported in Table 10.5, while Figure 10.11 highlights all the considered integration points, derived from the different hierarchical levels, that are considered in the numerical procedure.

Table 10.6 reports the first ten natural acoustic frequencies of the system, obtained both with the proposed Immersed method and with the commercial software. In addition, Figure 10.12 shows the first four modal shapes computed using Immersed IGA and the commercial software.

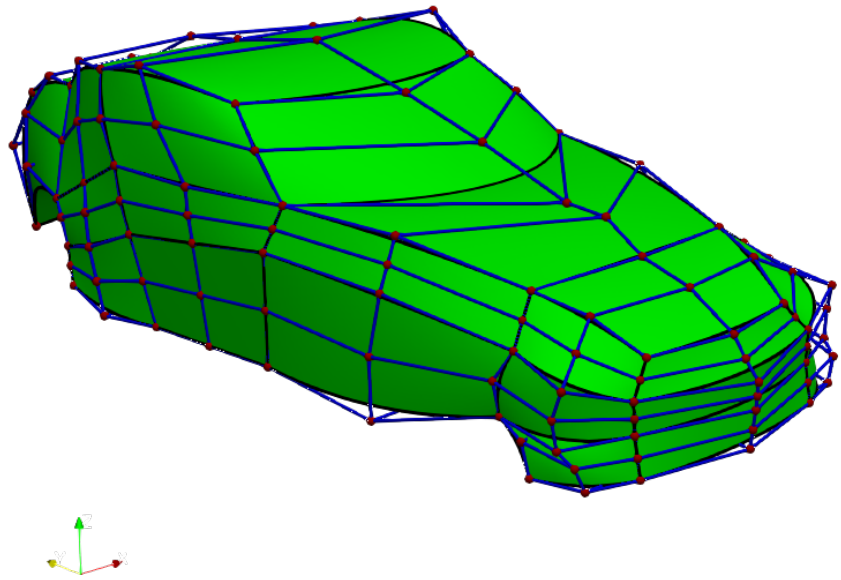

Figure 10.9: Car geometry extracted from CAD software.

Table 10.6: First ten acoustic numerical and reference frequencies, and the corresponding percentage error.

f_{PatNas} **[Hz]**	f_{num} **[Hz]**	**Error** (%)
0	0	0
250.03	250.13	0.04
400.87	401.56	0.17
544.14	545.06	0.17
561.04	562.56	0.27
656.04	657.00	0.15
747.69	751.96	0.57
771.50	773.50	0.26
843.32	845.46	0.25
855.55	857.97	0.28

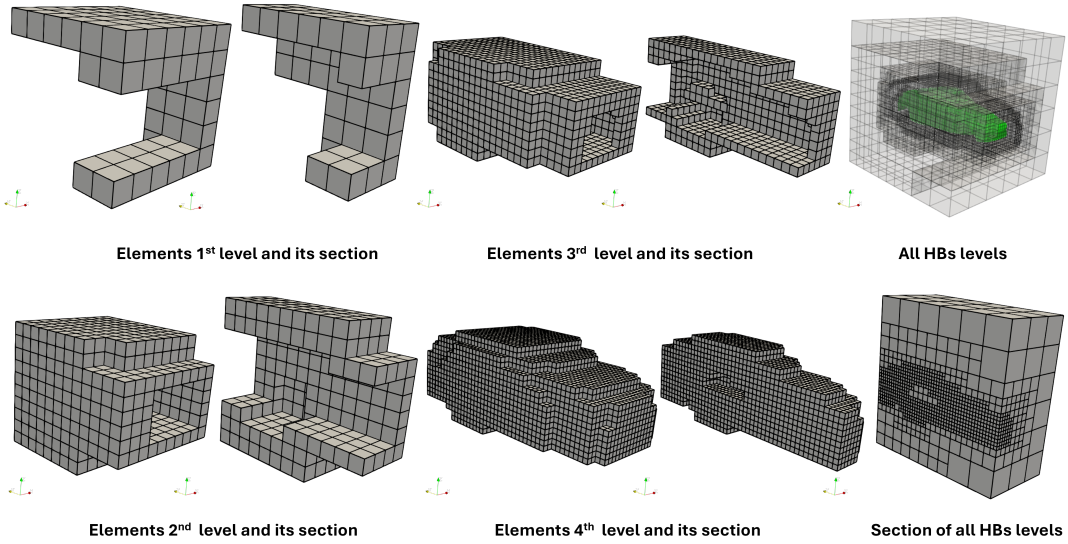

Figure 10.10: Hierarchical B-Spline levels and its sections.

10.3.1 Vibroacoustic model and methodology

In this section, a vibroacoustic analysis is performed, including both a coupled modal analysis and a Frequency Response Function (FRF) evaluation, considering the geometry of the car. In order to account for the entire vehicle structure, G^1 continuity conditions must be imposed at the interfaces between the patches. However, this operation is not within the scope of the present work and therefore represents one of its limitations.

In many industrial applications, such as those in the NVH (Noise, Vibration, and Harshness) field, it is often necessary to investigate the dynamic behavior of individual panels when they are detached from the rest of the structure. For this reason, an analysis of this type is carried out here, focusing on a single panel of the vehicle, which is shown in Figure 10.13. The objective is to assess how this panel influences the cavity modes and how it transfers energy—and consequently, noise—inside the vehicle (FRF). The same approach is adopted in [117].

Concerning the boundary conditions applied to the structure, the acoustic cavity is considered acoustically rigid, except for the region coupled with the structural surface. The structural panel itself is constrained along all four edges, as shown in Figure 10.14.

Table 10.7 reports the material properties of the acoustic cavity and the structural panel considered in the analyses.

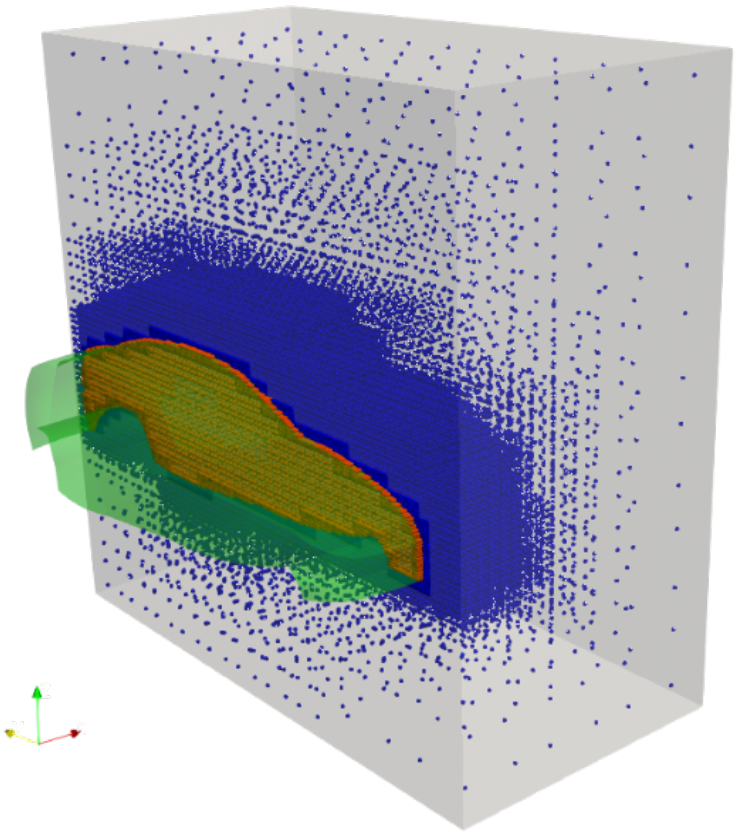

Figure 10.11: Gauss points for the car geometry. In blue the penalized Gauss points, in orange the not-penalized Gauss points.

10.3.2 Vibroacoustic modal analysis

The frequency range of interest is set between 0 and 400 Hz, which corresponds to the typical bandwidth investigated in automotive vibroacoustic studies. The aim of the analysis is to determine the coupled structural–acoustic modes and to evaluate the acoustic cavity response induced by a structural excitation.

To achieve this objective while ensuring computational efficiency, a reduced-order modelling strategy is adopted. Specifically, the coupled problem is projected onto a modal subspace constructed from

Table 10.7: Structural and acoustic parameters for the problem illustrated in Figure 10.13.

E [Pa]	ρ_s $[\frac{kg}{m^3}]$	ν [-]	t $[m]$	ρ_f $[\frac{kg}{m^3}]$	c_0 $[\frac{m}{s}]$
5.0×10^9	7860	0.3	0.005	1.0	340.0

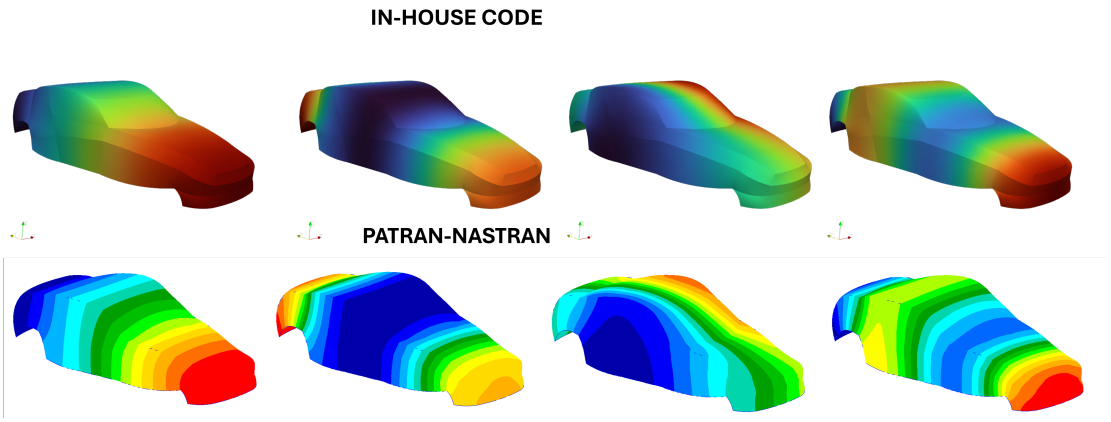

Figure 10.12: Comparison of first four non-zero modes between the proposed immersed IGA method and Patran-Nastran.

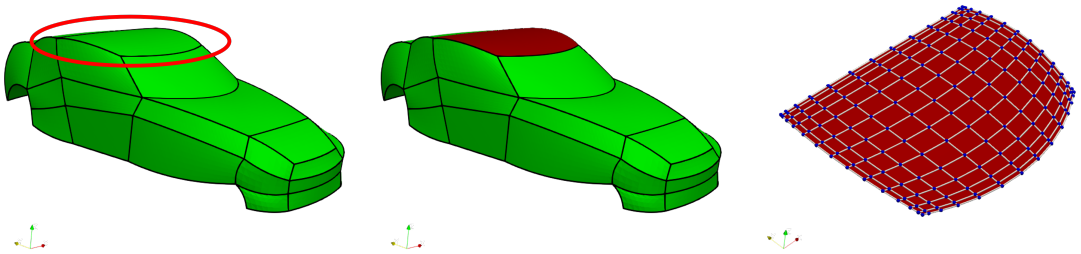

Figure 10.13: Overview of the vehicle shell geometry (in green). The panel under investigation is highlighted in red. On the right, the same panel is shown separately with its corresponding NURBS patch and control points network.

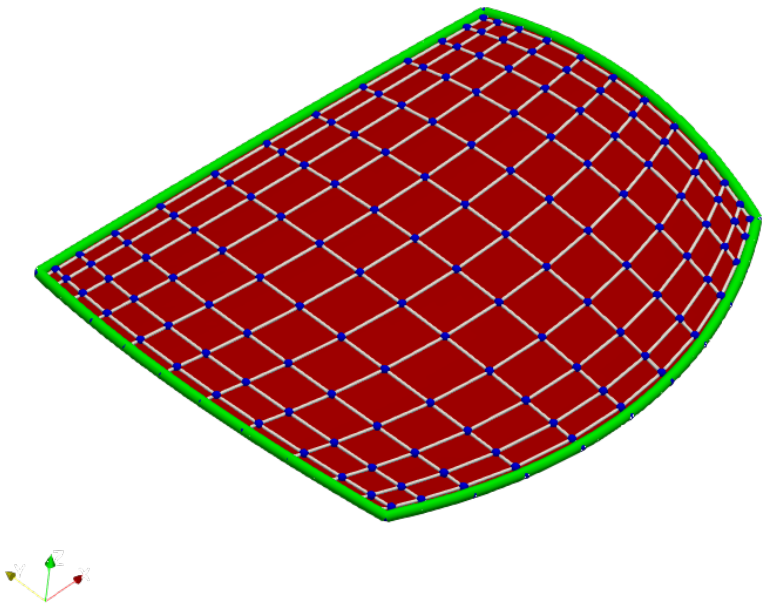

Figure 10.14: Geometry of the car rooftop panel considered for the analysis. The green areas along the edges indicate the regions where all displacements are constrained. These boundary conditions are consistent with the global vehicle dynamics, as the rooftop is connected to other structural components in those areas.

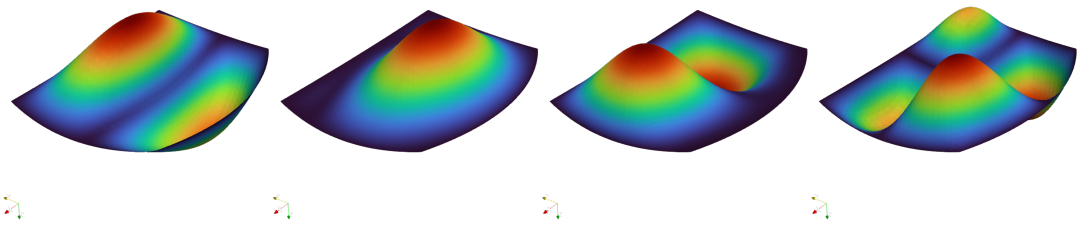

Figure 10.15: First four structural mode shapes of the rooftop panel obtained from the modal analysis. The mode shapes are arranged in ascending order of their corresponding natural frequencies.

both structural and acoustic modes within the 0–800 Hz frequency range, corresponding to twice the target bandwidth. The rationale behind the selection of this frequency range has been extensively discussed in Chapter 4.

The acoustic modes employed in the present analysis correspond to those previously computed and listed in Table 10.6, whereas the associated mode shapes are illustrated in Figure 10.12.

For the structural component shown in Figure 10.14, a structural modal analysis is performed. The results, in terms of natural frequencies and corresponding mode shapes, are reported in Table 10.8 and Figure 10.15, respectively.

Table 10.8: First seven natural frequencies of the rooftop panel obtained from the structural modal analysis.

Mode number	f_{num} [Hz]
1	198.39
2	239.27
3	272.14
4	312.40
5	347.87
6	388.49
7	441.13

Furthermore, a coupled modal analysis is performed using the modal reduction approach described by Equation 4.6. Table 10.9 presents the natural frequencies of the coupled modes, specifying the predominant domain (structural or fluid) associated with each mode. The corresponding coupled mode shapes are illustrated in Figure 10.16.

Table 10.9: First eight vibroacoustic natural frequencies and dominant domain.

Mode number	f_c [Hz]	Dominant domain
1	0	F
2	198.39	S + F
3	250.13	S + F
4	272.14	F
5	312.40	S + F
6	347.87	S + F
7	388.48	S + F
8	401.56	F

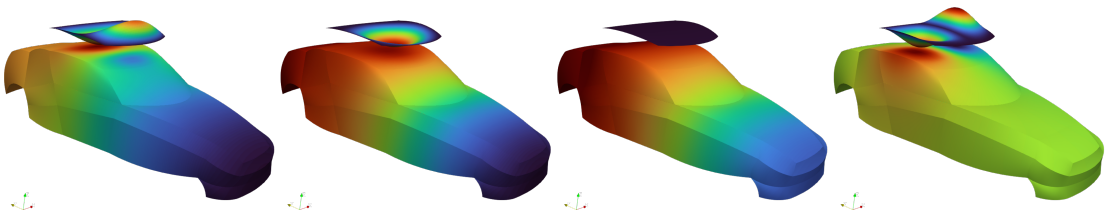

Figure 10.16: First four non-zero vibroacoustic mode shapes obtained from the modal analysis. The mode shapes are arranged in ascending order of their corresponding natural frequencies.

From this figure, it can be clearly observed—as expected—that when a structural mode is present, the acoustic cavity is influenced by it and responds with a compatible modal shape. Conversely, when the mode is predominantly acoustic, the cavity alone is not capable of exciting the structure.

10.3.3 Frequency response function

In this section, a frequency response analysis is carried out on the model shown in Figure 10.17. The problem is solved using both a full-order model (FOM) approach and a reduced-order model (ROM) approach, considering all the modes contained within twice the frequency range of interest.

The results, expressed in terms of the overall acoustic pressure response per unit of external excitation force, are presented in Figure 10.18.

Figure 10.18 also illustrates the mode shapes associated with each pressure peak, highlighting the coupling between the acoustic and structural domains. As can be observed, when a pressure peak occurs—particularly in regions corresponding to the driver or passenger positions—its amplitude

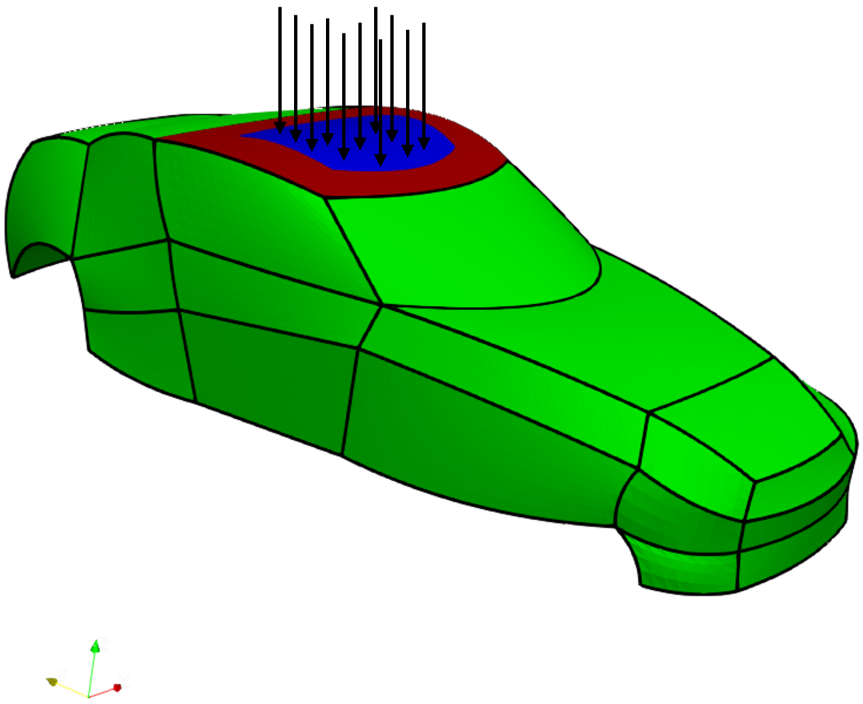

Figure 10.17: External forces applied to the structural panel for the frequency response analysis (FRF). The excitation points are defined on the outer surface of the model.

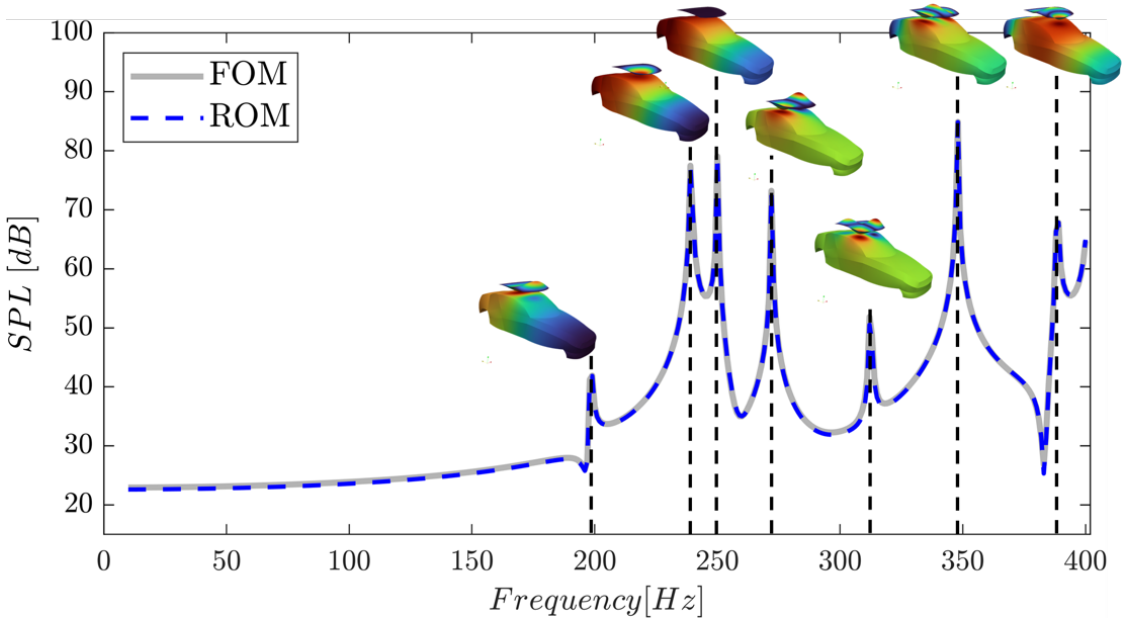

Figure 10.18: Frequency Response Function (FRF) of the coupled structural–acoustic system. The figure also highlights the mode shapes corresponding to each pressure peak, showing both the structural and acoustic responses.

should be minimized, since excessive acoustic pressure in these zones may lead to undesirable noise inside the vehicle [1]. However, the mitigation of such effects lies beyond the scope of the present study.

Chapter 11

Conclusion of CAD-Integrated isogeometric analysis

Part II of this thesis has presented the methodological and computational developments aimed at enabling a seamless integration between Computer-Aided Design (CAD) and Isogeometric Analysis (IGA) for vibroacoustic simulations. The research addressed several key challenges that currently limit the industrial adoption of IGA, particularly those related to geometry representation, domain reconstruction, and multi-physics coupling. A comprehensive review of the state of the art in CAD-integrated IGA was provided, with a particular focus on immersed approaches. Moreover, the review identified the need for adaptive refinement strategies and robust coupling mechanisms for vibroacoustic applications. These findings established the scientific motivation and research gaps that guided the developments in the subsequent chapters. A consistent volumetric reconstruction technique based on Hierarchical B-Splines (HB-splines) is implemented. The proposed approach allows the direct generation of volumetric parametrizations from CAD boundary representations (B-Reps), overcoming one of the major bottlenecks in CAD-to-IGA integration. By exploiting the hierarchical structure of HB-splines, the method enables local refinement and adaptive resolution of geometric and physical features, significantly reducing the computational cost without compromising accuracy. This reconstruction framework was then coupled with a Kirchhoff–Love structural model, establishing a unified structural–acoustic formulation within a consistent IGA setting. A 3D coupling strategy was formulated to enable direct interaction between the reconstructed structural and acoustic domains, maintaining C^1-continuity where required and ensuring energy-consistent exchange across the interface. This formulation provides a rigorous foundation for coupled vibroacoustic analyses directly on

CAD-derived geometries, avoiding the traditional meshing and geometry-cleaning steps that often introduce approximation errors. Finally, the applicability and robustness of the proposed methodologies through several industrial case studies is demonstrated. Applications in the automotive, marine, and acoustic fields showcased the capability of immersed IGA to perform accurate modal and frequency response analyses directly on CAD models. The reduced-order approaches developed in this work preserve high fidelity with respect to full-order simulations, while dramatically decreasing the computational effort. In particular, the vibroacoustic coupling analyses revealed the method's ability to capture both structural and acoustic phenomena with excellent accuracy, validating the proposed CAD–IGA integration workflow.

Overall, the results obtained demonstrate that the integration between CAD and IGA can be achieved in a robust and automated manner, paving the way for next-generation simulation-driven design workflows. The methodologies developed herein not only enhance numerical accuracy and computational performance but also bring analysis capabilities closer to the design stage, thereby contributing to the realization of a truly unified CAD–CAE paradigm.

Final conclusion and future perspectives

11.1 Final conclusion

This doctoral research has explored the development of advanced isogeometric analysis (IGA) strategies for vibroacoustic simulations, with the comprehensive goal of bridging the gap between Computer-Aided Design (CAD) and numerical analysis. The work was articulated in two complementary parts: the first focusing on conformal NURBS-based IGA formulations and model reduction, and the second addressing the integration of CAD representations through immersed and hierarchical spline frameworks.

A significant contribution of this PhD concerns the extensive software development carried out throughout the project. For Part I, a complete and openly available IGA codebase has been implemented, providing a robust environment for NURBS-based vibroacoustic simulations and model reduction techniques vibroacoustic-iga-fem. Part II required the development of a new set of tools and numerical modules, effectively built almost entirely from scratch to support immersed IGA, hierarchical refinement, and CAD-embedded representations. The corresponding implementation, currently being finalized and validated, will be released publicly following the publication of the associated scientific results.

11.1.0.1 Summary of contributions

In the first part, the fundamental principles of IGA were revisited and compared to conventional Finite Element Methods (FEM), emphasizing the gains in accuracy–computational cost ratio of IGA in structural, acoustic, and vibroacoustic analyses. A modal-based Reduced Order Model (ROM) formulation was proposed to further enhance computational efficiency while preserving the high accuracy of the isogeometric discretization. The combination of IGA and ROM demonstrated significant reduc-

tions in computational cost and model size, enabling efficient yet precise prediction of vibroacoustic responses. These findings confirmed the suitability of IGA for high-fidelity simulations and highlighted its potential as a robust alternative to FEM in multi-physics contexts.

However, this first phase also exposed an important limitation: the strong dependency of conformal IGA on explicit NURBS parameterizations. While mathematically elegant, this requirement severely restricts applicability to simple geometries and prevents the use of complex industrial models typically represented as CAD B-Rep entities. This limitation motivated the second part of the research, dedicated to overcoming the conformal constraint and establishing a more direct link between CAD and analysis.

In the second part, a CAD-integrated IGA framework was developed based on immersed formulations and hierarchical B-splines (HB-splines). A volumetric reconstruction method was introduced to generate consistent spline-based parametrizations directly from CAD boundary representations. The proposed hierarchical structure enables local refinement and adaptive resolution of physical features, achieving substantial computational savings without loss of accuracy. The method was coupled with a Kirchhoff–Love shell formulation and extended to a fully 3D vibroacoustic setting, ensuring G^1-continuity and energetic consistency across interfaces. Through several industrial case studies, the immersed IGA framework demonstrated its robustness, accuracy, and scalability in handling complex geometries directly from CAD data—without the need for meshing or geometry simplification.

11.2 Limitations and open challenges

Despite these advances, several challenges remain open. From a geometric perspective, further work is required to ensure watertight CAD reconstructions and to extend the methodology to trimmed and non-manifold geometries, which are ubiquitous in industrial CAD models. From a computational standpoint, efficient quadrature and stabilization techniques for immersed elements must be refined to guarantee robustness across a wider range of applications. Moreover, the coupling between immersed structural and acoustic domains, while effective, can benefit from more general interface treatments and adaptive integration schemes to improve numerical conditioning and convergence.

11.3 Future Perspectives

Future research will aim to consolidate and extend the CAD–IGA integration achieved in this work. Potential developments include the extension to nonlinear and transient dynamics, enabling the simulation of complex time-dependent vibroacoustic phenomena, as well as the implementation of adaptive and goal-oriented refinement strategies for immersed and hierarchical IGA, driven by error estimators and physical indicators. Further improvements are expected in the coupling mechanisms for multi-domain and multi-physics problems, such as fluid–structure–acoustic interaction and thermoelastic effects. The integration of the proposed methodologies into industrial CAD–CAE pipelines will facilitate direct data exchange with CAD platforms and support simulation-driven design optimization. Finally, high-performance computing (HPC) implementations and parallel solvers tailored to hierarchical spline structures will be explored to enable efficient large-scale industrial analyses.

Bibliography

[1] R. Citarella, T. Landi, L. Caivano, G. D'Errico, F. Raffa, M. Romano et E. Armentani, "Structural and vibro-acoustics optimization of a car body rear part," *Applied Sciences*, vol. 13, p. 3552, 2023.

[2] J. A. Cottrell, T. J. R. Hughes et Y. Bazilevs, *Isogeometric Analysis: Toward Integration of CAD and FEA*. Wiley, 2009.

[3] D. Schillinger, L. Dedè, M. A. Scott, J. A. Evans, M. J. Borden, E. Rank et T. J. R. Hughes, "An isogeometric design-through-analysis methodology based on adaptive hierarchical refinement of nurbs, immersed boundary methods, and t-spline cad surfaces," *Computer Methods in Applied Mechanics and Engineering*, vol. 249–252, p. 116–150, 2012.

[4] D. Schillinger et E. Rank, "An unfitted *hp*-adaptive finite element method based on hierarchical b-splines for interface problems of complex geometry," *Computer Methods in Applied Mechanics and Engineering*, vol. 200, p. 3358–3380, 2011.

[5] J. Sobieszczanski-Sobieski, S. Kodiyalam et R. Yang, "Optimization of car body under constraints of noise, vibration, and harshness (nvh), and crash," *Struct Multidisc Optim*, vol. 22, p. 295–306, 2001.

[6] G. Fasulo, P. Vitiello, L. Federico et R. Citarella, "Vibro-acoustic modelling of aeronautical panels reinforced by unconventional stiffeners," *Aerospace*, vol. 9, p. 327, 2022.

[7] R. Citarella, L. Federico et M. Barbarino, "Aeroacustic and vibroacoustic advancement in aerospace and automotive systems," *Applied Sciences*, vol. 10, p. 3853, 2020.

[8] M. Drężek et M. Augustyniak, "Universal sea/fem based method for estimation of vibroacoustic coupling loss factors in realistic ship structures," *Polish Maritime Research*, vol. 31, p. 55–63, 2024.

[9] W. Sun, J. Zhou, D. Gong et T. You, "Analysis of modal frequency optimization of railway vehicle car body," *Advances in Mechanical Engineering*, vol. 8, p. 4, 2016.

[10] M. Barbarino et D. Bianco, "A bem–fmm approach applied to the combined convected helmholtz integral formulation for the solution of aeroacoustic problems," *Computer Methods in Applied Mechanics and Engineering*, vol. 342, p. 585–603, 2018.

[11] M. A. Panza, "A review of experimental techniques for nvh analysis on a commercial vehicle," *Energy Procedia*, vol. 82, p. 1017–1023, 2015.

[12] A. Fuchs, E. Nijman et H.-H. Priebsch, *Automotive NVH Technology.* Springer Cham, 2016.

[13] U.S. Product Data Association (US PRO), "Initial graphics exchange specification (iges) version 5.3," American National Standards Institute (ANSI), USA, Rapport technique, 1996, aNSI standard for the digital exchange of product data.

[14] International Organization for Standardization (ISO), *ISO 10303-21:2016 – Industrial automation systems and integration – Product data representation and exchange – Part 21: Implementation methods: Clear text encoding of the exchange structure*, ISO Norme, 2016.

[15] Coreform LLC, "Coreform flex – cad-to-analysis integration software," https://coreform.com/coreform-flex/, 2025.

[16] T. Landi, C. Hoareau, J. Deü, R. Citarella et R. Ohayon, "Projection based reduced order model of elasto-acoustic vibrations computed with isogeometric analyses," dans *9th ECCOMAS: Innovative Methods for Fluid-Structure Interaction*, Lisbon, 2024.

[17] A. Ciampaglia, A. Santini et G. Belingardi, "Design and analysis of automotive lightweight materials suspension based on finite element analysis," *Proceedings of the Institution of Mechanical Engineers, Part C: Journal of Mechanical Engineering Science*, vol. 235, n°. 9, p. 1501–1511, 2021.

[18] S. D. Rosa, "Some considerations about present and future of general aviation aircraft," *Aerotecnica & Missili e Spazio*, vol. 104, p. 169–170, 2025.

[19] H. J.-P. Morand et R. Ohayon, *Fluid-Structure Interaction: Applied Numerical Methods.* Wiley, 1995.

[20] R. Ohayon et C. Soize, "Computational vibroacoustics in low- and medium-frequency bands: Damping, rom, and uq modeling," *Applied Sciences*, vol. 7, p. 586, 2017.

[21] Y. Bazilevs, K. Takizawa et T. E. Tezduyar, *Computational Fluid-Structure Interaction: Methods and Applications.* Wiley-Blackwell, 2013.

[22] V. D'Alessandro, G. Petrone, F. Franco et S. D. Rosa, "A review of the vibroacoustics of sandwich panels: Models and experiments," *Journal of Sandwich Structures & Materials*, vol. 15, n°. 5, p. 541–582, 2013.

[23] S. D. Rosa, F. Franco, X. Li et T. Polito, "A similitude for structural acoustic enclosures," *Mechanical Systems and Signal Processing*, vol. 30, p. 330–342, 2012.

[24] Y. Bazilevs, M. C. Hsu, Y. Zhang et et al., "A fully-coupled fluid-structure interaction simulation of cerebral aneurysms," *Computational Mechanics*, vol. 46, p. 3–16, 2010.

[25] R. Rumpler, P. Göransson et J.-F. Deü, "A finite element approach combining a reduced-order system, padé approximants, and an adaptive frequency windowing for fast multi-frequency solution of poro-acoustic problems," *International Journal for Numerical Methods in Engineering*, vol. 97, p. 759, 2014.

[26] L. Rouleau, J.-F. Deü et A. Legay, "A comparison of modal reduction techniques based on modal projection for structures with frequency-dependent damping," *Mechanical Systems and Signal Processing*, vol. 90, p. 110, 2017.

[27] J.-F. Deü, W. Larbi, R. Ohayon et R. Sampaio, "Piezoelectric shunt vibration damping of structural-acoustic systems: Finite element formulation and reduced-order model," *Journal of Vibration and Acoustics*, vol. 136, p. 031007, 2014.

[28] S. Boily et F. Charron, "The vibroacoustic response of a cylindrical shell structure with viscoelastic and poroelastic materials," *Applied Acoustics*, vol. 58, p. 131, 1999.

[29] E. Manconi, A. Hvatov et S. V. Sorokin, "Numerical analysis of vibration attenuation and bandgaps in radially periodic plates," *Journal of Vibration Engineering & Technologies*, vol. 11, p. 2593–2603, 2023.

[30] E. Manconi et S. Sorokin, "On the effect of damping on dispersion curves in plates," *International Journal of Solids and Structures*, vol. 50, n°. 11–12, p. 1966–1973, 2013.

[31] K. A. Cunefare, S. D. Rosa, N. Sadegh et G. Larson, "State-switched absorber for semi-active structural control," *Journal of Intelligent Material Systems and Structures*, vol. 11, n°. 4, p. 300–310, 2000.

[32] T. J. R. Hughes, *The Finite Element Method: Linear Static and Dynamic Finite Element Analysis*. Dover, 2000.

[33] E. Manconi et B. R. Mace, "Estimation of the loss factor of viscoelastic laminated panels from finite element analysis," *Journal of Sound and Vibration*, vol. 329, n°. 19, p. 3928–3939, 2010.

[34] T. J. R. Hughes, J. A. Cottrell et Y. Bazilevs, "Isogeometric analysis: Cad, finite elements, nurbs, exact geometry and mesh refinement," *Computer Methods in Applied Mechanics and Engineering*, vol. 194, p. 4135, 2005.

[35] W. Li, Y. Chai, M. Lei et G. R. Liu, "Analysis of coupled structural-acoustic problems based on the smoothed finite element method," *Engineering Analysis with Boundary Elements*, vol. 42, p. 84, 2014.

[36] L. Piegl et W. Tiller, *The NURBS Book*. Springer, 1997.

[37] T. Dokken, V. Skytt, J. Haenisch et K. Bengtsson, "Isogeometric representation and analysis: Bridging the gap between cad and analysis," dans *47th AIAA Aerospace Sciences Meeting Including The New Horizons Forum and Aerospace Exposition*. Florida: American Institute of Aeronautics and Astronautics, 2009.

[38] S. Hartmann, D. Benson et A. Nagy, "Isogeometric analysis with ls-dyna," *Journal of Physics*, vol. 734, p. 032125, 2016.

[39] T. Elguedj, Y. Bazilevs, V. M. Calo et T. J. R. Hughes, "F-bar projection method for finite deformation elasticity and plasticity using nurbs-based isogeometric analysis," *International Journal of Material Forming*, vol. 1, p. 1091, 2008.

[40] R. N. Simpson, M. A. Scott, M. Taus, D. C. Thomas et H. Lian, "Acoustic isogeometric boundary element analysis," *Computer Methods in Applied Mechanics and Engineering*, vol. 269, p. 265, 2014.

[41] A. Buffa, G. Sangalli et R. Vázquez, "Isogeometric analysis in electromagnetics: B-splines approximation," *Computer Methods in Applied Mechanics and Engineering*, vol. 199, p. 1143, 2010.

[42] W. A. Wall, M. A. Frenzel et C. Cyron, "Isogeometric structural shape optimization," *Computer Methods in Applied Mechanics and Engineering*, vol. 197, p. 2976, 2008.

[43] D. Fußeder, B. Simeon et A.-V. Vuong, "Fundamental aspects of shape optimization in the context of isogeometric analysis," *Computer Methods in Applied Mechanics and Engineering*, vol. 286, p. 313, 2015.

[44] Y. Bazilevs, V. M. Calo, Y. Zhang et T. J. R. Hughes, "Isogeometric fluid–structure interaction analysis with applications to arterial blood flow," *Computational Mechanics*, vol. 38, p. 310, 2006.

[45] Y. Bazilevs, V. M. Calo, T. J. R. Hughes et Y. Zhang, "Isogeometric fluid-structure interaction: Theory, algorithms, and computations," *Computational Mechanics*, vol. 43, p. 3, 2008.

[46] S. B. Raknes, X. Deng, Y. Bazilevs, D. J. Benson, K. M. Mathisen et T. Kvamsdal, "Isogeometric rotation-free bending-stabilized cables: Statics, dynamics, bending strips and coupling with shells," *Computer Methods in Applied Mechanics and Engineering*, vol. 263, p. 127–143, 2013.

[47] X. Deng, A. Korobenko, J. Yan et Y. Bazilevs, "Isogeometric analysis of continuum damage in rotation-free composite shells," *Computer Methods in Applied Mechanics and Engineering*, vol. 284, p. 349, 2015.

[48] Y. Bazilevs, X. Deng, A. Korobenko, F. Lanza, M. D. Todd et S. G. Taylor, "Isogeometric fatigue damage prediction in large-scale composite structures driven by dynamic sensor data," *Journal of Applied Mechanics*, vol. 82, p. 091008, 2015.

[49] J. A. Cottrell, A. Reali, Y. Bazilevs et T. J. R. Hughes, "Isogeometric analysis of structural vibrations," *Computer Methods in Applied Mechanics and Engineering*, vol. 195, p. 5296, 2006.

[50] Y. Bazilevs, L. B. D. Veiga, J. A. Cottrell, T. J. R. Hughes et G. Sangalli, "Isogeometric analysis: Approximation, stability and error estimates for h-refined meshes," *Mathematical Models and Methods in Applied Sciences*, vol. 16, p. 1031, 2006.

[51] T. J. R. Hughes, A. Reali et G. Sangalli, "Duality and unified analysis of discrete approximations in structural dynamics and wave propagation: Comparison of p-method finite elements with k-method nurbs," *Computer Methods in Applied Mechanics and Engineering*, vol. 197, p. 4104, 2008.

[52] J. A. Cottrell, T. J. R. Hughes et A. Reali, "Studies of refinement and continuity in isogeometric structural analysis," *Computer Methods in Applied Mechanics and Engineering*, vol. 196, p. 4160, 2007.

[53] P. Antolin et T. Hirschler, "Quadrature-free immersed isogeometric analysis," *Engineering with Computers*, vol. 38, p. 4475, 2022.

[54] A. Reali et T. J. R. Hughes, "An introduction to isogeometric collocation methods," dans *Isogeometric Methods for Numerical Simulation*, G. Beer et S. Bordas, édit. Springer, 2015.

[55] L. Coox, O. Atak, D. Vandepitte et W. Desmet, "An isogeometric indirect boundary element method for solving acoustic problems in open-boundary domains," *Computer Methods in Applied Mechanics and Engineering*, vol. 316, p. 186, 2017.

[56] H.-J. Kim, Y.-D. Seo et S.-K. Youn, "Isogeometric analysis for trimmed cad surfaces," *Computer Methods in Applied Mechanics and Engineering*, vol. 198, p. 2982, 2009.

[57] M. J. Borden, M. A. Scott, J. A. Evans et T. J. R. Hughes, "Isogeometric finite element data structures based on bézier extraction of nurbs," *International Journal for Numerical Methods in Engineering*, vol. 87, p. 15, 2011.

[58] K. A. Johannessen, T. Kvamsdal et T. Dokken, "Isogeometric analysis using lr b-splines," *Computer Methods in Applied Mechanics and Engineering*, vol. 269, p. 471, 2014.

[59] Y. Bazilevs, V. M. Calo, J. A. Cottrell, J. A. Evans, T. J. R. Hughes, S. Lipton, M. A. Scott et T. W. Sederberg, "Isogeometric analysis using t-splines," *Computer Methods in Applied Mechanics and Engineering*, vol. 199, p. 229, 2010.

[60] O. C. Zienkiewicz et R. L. Taylor, *The Finite Element Method: Volume 1—The Basis*, 5^{e} éd. Oxford, UK: Butterworth-Heinemann, 2000.

[61] K.-J. Bathe, *Finite Element Procedures*. Englewood Cliffs, NJ: Prentice Hall, 1996.

[62] Y. Zhang, X. Hu, N. Duan et H. Hua, "A multidomain spectral method for analysis of interior vibroacoustic systems with segmented boundaries," *Mathematical Problems in Engineering*, vol. 2020, p. 6910174, 2020.

[63] R. Tielen, M. Möller, D. Göddeke et C. Vuik, "p-multigrid methods and their comparison to h-multigrid methods within isogeometric analysis," *Computer Methods in Applied Mechanics and Engineering*, vol. 372, p. 113347, 2020.

[64] B. Marussig et T. J. R. Hughes, "A review of trimming in isogeometric analysis: Challenges, data exchange and simulation aspects," *Computer Methods in Applied Mechanics and Engineering*, vol. 25, p. 1059–1127, 2018.

[65] T. Landi, C. Hoareau, J.-F. Deü, R. Ohayon et R. Citarella, "Comparative vibroacoustic analyses: Fem vs. iga," *Computational Mechanics*, vol. 75, p. 2103–2122, 2025.

[66] X. Song, G. Jin, S. Zhong, T. Ye et Y. Chen, "Isogeometric modeling and vibro-acoustic analysis of flow-excited irregular cavity-plate-exterior space coupled system," *Journal of Sound and Vibration*, vol. 595, p. 118712, 2025.

[67] E. Venås, T. Kvamsdal et T. Jenserud, "Isogeometric analysis of acoustic scattering using infinite elements," *Computer Methods in Applied Mechanics and Engineering*, vol. 335, p. 152–193, 2018.

[68] Y. Mi et H. Zheng, "An interpolation method for coupling nonconforming patches in isogeometric analysis of vibro-acoustic systems," *Computer Methods in Applied Mechanics and Engineering*, vol. 341, p. 551, 2018.

[69] Y. Mi, H. Zheng, Y. Shen et Y. Huang, "A weak form formulation for isogeometric analysis of vibro-acoustic systems with nonconforming interfaces," *International Journal of Applied Mechanics*, vol. 10, p. 1850073, 2018.

[70] W. Larbi et J.-F. Deü, "A 3d state-space solution for free-vibration analysis of a radially polarized laminated piezoelectric cylinder filled with fluid," *Journal of Sound and Vibration*, vol. 330, p. 162, 2011.

[71] A. Craggs, "The transient response of a coupled plate-acoustic system using plate and acoustic finite elements," *Journal of Sound and Vibration*, vol. 15, p. 509, 1971.

[72] S. Zhu, L. Dedè et A. Quarteroni, "Isogeometric analysis and proper orthogonal decomposition for the acoustic wave equation," *ESAIM: M2AN*, vol. 51, p. 1197, 2017.

[73] C. D. Falco, A. Reali et R. Vázquez, "Geopdes: A research tool for isogeometric analysis of pdes," *Advances in Engineering Software*, vol. 42, p. 1020, 2011.

[74] V. P. Nguyen, C. Anitescu, S. P. A. Bordas et T. Rabczuk, "Isogeometric analysis: An overview and computer implementation aspects," *Mathematics and Computers in Simulation*, vol. 117, p. 89, 2015.

[75] S. Gondegaon et H. K. Voruganti, "Static structural and modal analysis using isogeometric analysis," *Journal of Theoretical and Applied Mechanics*, vol. 46, p. 36, 2016.

[76] J.-F. Deü, W. Larbi et R. Ohayon, "Variational formulations of interior structural-acoustic vibration problems," dans *Computational Aspects of Structural Acoustics and Vibration*, ser. CISM International Centre for Mechanical Sciences, G. Sandberg et R. Ohayon, édit. Vienna: Springer, 2008, vol. 505, p. 1–44.

[77] W. Larby, J.-F. Deü et R. Ohayon, "A new finite element formulation for internal acoustic problems with dissipative walls," *International Journal for Numerical Methods in Engineering*, vol. 68, p. 381–399, 2006.

[78] X. Xie, L. Wang et J. Zhang, "A variational formulation for vibro-acoustic analysis of a panel backed by an irregularly-bounded cavity," *Journal of Sound and Vibration*, vol. 373, p. 147–166, 2016.

[79] M. Panzella, "Advanced finite element method for the vibro-acoustic response of plate-cavity systems," Thèse de doctorat, Politecnico di Torino, Turin, Italy, 2020. [En ligne]. Disponible: https://webthesis.biblio.polito.it/14670/1/tesi.pdf

[80] E. Tabak, "Methods for efficient analysis of vibro-acoustic problems," Thèse de doctorat, Delft University of Technology, Delft, The Netherlands, 2018. [En ligne]. Disponible: https://research.tudelft.nl/files/71117049/PhDThesis_tabak_final.pdf

[81] R. Ohayon, "Reduced models for fluid–structure interaction problems," *International Journal for Numerical Methods in Engineering*, vol. 60, p. 139, 2004.

[82] B. B. Smida, R. Majed, N. Bouhaddi et M. Ouisse, "Investigations for a model reduction technique of fluid–structure coupled systems," *Journal of Mechanical Engineering Science*, vol. 226, p. 42, 2012.

[83] L. Rouleau, J.-F. Deü et A. Legay, "Review of reduction methods based on modal projection for highly damped structures," dans *Proceedings of WCCM / ECCM / ECFD.* Vienna, Austria: Springer, 2014, pDF available online.

[84] *Industrial automation systems and integration – Product data representation and exchange – Part 42: Geometric and topological representation*, International Organization for Standardization (ISO) Norme ISO 10 303-42:1994, 1994, sTEP standard.

[85] R. Mittal et G. Iaccarino, "Immersed boundary methods," *Annual Review of Fluid Mechanics*, vol. 37, p. 239–261, 2005.

[86] E. Burman et P. Hansbo, "Fictitious domain finite element methods using cut elements: Ii. a stabilized nitsche method," *Applied Numerical Mathematics*, vol. 62, p. 328–341, 2012.

[87] E. Burman, S. Claus, P. Hansbo, M. G. Larson et A. Massing, "Cutfem: Discretizing geometry and partial differential equations," *International Journal for Numerical Methods in Engineering*, vol. 104, p. 472–501, 2015.

[88] T. Belytschko et T. Black, "Elastic crack growth in finite elements with minimal remeshing," *International Journal for Numerical Methods in Engineering*, vol. 45, p. 601–620, 1999.

[89] A. Legay, "The extended finite element method combined with a modal synthesis approach for vibro-acoustic problems," *International Journal for Numerical Methods in Engineering*, vol. 101, p. 329–350, 2014.

[90] J. Parvizian, A. Düster et E. Rank, "Finite cell method: h- and p-extension for embedded domain methods in solid mechanics," *Computational Mechanics*, vol. 41, p. 121–133, 2007.

[91] D. Schillinger, S. Kollmannsberger, R.-P. Mundani et E. Rank, "The finite cell method for geometrically nonlinear problems of solid mechanics," dans *Proceedings of the 9th World Congress on Computational Mechanics and 4th Asian Pacific Congress on Computational Mechanics*, vol. 10. IOP Publishing, 2010, p. 012170.

[92] D. Schillinger et M. Ruess, "The finite cell method: A review in the context of higher-order structural analysis of cad and image-based geometric models," *Archives of Computational Methods in Engineering*, vol. 22, p. 391–455, 2015.

[93] A. Düster, J. Parvizian, Z. Yang et E. Rank, "The finite cell method for three-dimensional problems of solid mechanics," *Computer Methods in Applied Mechanics and Engineering*, vol. 197, p. 3768–3782, 2008.

[94] A. Buffa, D. Cho et G. Sangalli, "Linear independence of the t-spline blending functions associated with some particular t-meshes," *Computer Methods in Applied Mechanics and Engineering*, vol. 199, p. 1437–1445, 2010.

[95] B. J. C. Giannelli et H. Speleers, "Thb-splines: The truncated basis for hierarchical splines," *Computer Aided Geometric Design*, vol. 29, p. 485–498, 2012.

[96] F. D. Prenter, C. Verhoosel, H. V. B. , J. Evans, C. Messe, J. Benzaken et K. Maute, "Multigrid solvers for immersed finite element methods and immersed isogeometric analysis," *Computational Mechanics*, vol. 85, p. 807–838, 2020.

[97] M. Schmidt, L. Noel, K. Doble, J. A. Evans et K. Maute, "Extended isogeometric analysis of multi-material and multi-physics problems using hierarchical b-splines," *Computational Mechanics*, vol. 71, p. 1179–1203, 2023.

[98] A. Falini, C. Giannelli, T. Kanduc, M. L. Sampoli et A. Sestini, "An adaptive iga-bem with hierarchical b-splines based on quasi-interpolation quadrature schemes," *International Journal for Numerical Methods in Engineering*, vol. 117, p. 1038–1058, 2018.

[99] S. C. Divi, P. H. van Zuijlen, T. Hoang, F. de Prenter, F. Auricchio, A. Reali, E. H. van Brummelen et C. V. Verhoosel, "Residual-based error estimation and adaptivity for stabilized immersed isogeometric analysis using truncated hierarchical b-splines," *Journal of Mechanics*, vol. 38, p. 204–237, 2022.

[100] J. Kiendl, K.-U. Bletzinger, J. Linhard et R. Wüchner, "Isogeometric shell analysis with kirchhoff–love elements," *Computer Methods in Applied Mechanics and Engineering*, vol. 198, p. 3902–3914, 2009.

[101] J. Kiendl, M.-C. Hsu, M. C. Wu et A. Reali, "Isogeometric kirchhoff–love shell formulations for general hyperelastic materials," *Computer Methods in Applied Mechanics and Engineering*, vol. 291, p. 280–303, 2015.

[102] A. B. Tepole, H. Kabaria, K.-U. Bletzinger et E. Kuhl, "Isogeometric kirchhoff–love shell formulation for biological membranes," *Computer Methods in Applied Mechanics and Engineering*, vol. 293, p. 328–347, 2015.

[103] M. Ambati, J. Kiendl et L. D. Lorenzis, "Isogeometric kirchhoff–love shell formulation for elasto-plasticity," *Computer Methods in Applied Mechanics and Engineering*, vol. 340, p. 320–339, 2018.

[104] E. Burman et M. A. Fernández, "Stabilized explicit coupling for fluid–structure interaction using nitsche's method," *Comptes Rendus Mathematique*, vol. 345, n°. 8, p. 467–472, 2007.

[105] E. Burman et P. Hansbo, "Fictitious domain methods using cut elements: Iii. a stabilized nitsche method for stokes' problem," *ESAIM: Mathematical Modelling and Numerical Analysis*, vol. 48, n°. 3, p. 859–874, 2014.

[106] D. Kamensky, M. C. Hsu, D. Schillinger, J. A. Evans, A. Aggarwal, Y. Bazilevs, T. J. R. Hughes et M. S. Sacks, "An immersogeometric variational framework for fluid–structure interaction: Application to bioprosthetic heart valves," *Computer Methods in Applied Mechanics and Engineering*, vol. 284, p. 1005–1053, 2015.

[107] E. Burman, M. A. Fernández et S. Frei, "A nitsche-based formulation for fluid–structure interactions with contact," *ESAIM: Mathematical Modelling and Numerical Analysis*, vol. 54, n°. 2, p. 503–528, 2020.

[108] D. Kamensky, M.-C. Hsu, D. Schillinger, J. A. Evans, A. Aggarwal, Y. Bazilevs, M. S. Sacks et T. J. Hughes, "An immersogeometric variational framework for fluid–structure interaction: Application to bioprosthetic heart valves," *Computer Methods in Applied Mechanics and Engineering*, vol. 284, p. 1005–1053, 2015.

[109] D. Kamensky, "Open-source immersogeometric analysis of fluid–structure interaction using fenics and tigar," *Computers & Mathematics with Applications*, vol. 81, p. 334–648, 2021.

[110] B. E. Griffith et N. A. Patankar, "Immersed methods for fluid–structure interaction," *Annual Review of Fluid Mechanics*, vol. 52, p. 421–448, 2020.

[111] A. Nitti, J. Kiendl, A. Reali et M. D. D. Tullio, "An immersed-boundary/isogeometric method for fluid–structure interaction involving thin shells," *Computer Methods in Applied Mechanics and Engineering*, vol. 364, p. 112977, 2020.

[112] G. Guarino, A. Milazzo, A. Buffa et P. Antolin, "The immersed boundary conformal method for kirchhoff–love and reissner–mindlin shells," *Computer Methods in Applied Mechanics and Engineering*, vol. 432, p. 117407, 2024.

[113] A. Farahat, M. Kapl, A. Kosmač et V. Vitrih, "A locally based construction of analysis-suitable g^1 multi-patch spline surfaces," *Computer Aided Geometric Design*, vol. 107, p. 102266, 2023.

[114] T. X. Duong, F. Roohbakhshan et R. A. Sauer, "Efficient contact computations based on isogeometric analysis of shells," *Computer Methods in Applied Mechanics and Engineering*, vol. 316, p. 43–72, 2017.

[115] M. S. Corporation, *MSC Patran Reference Manual, Part 5: Analysis Application*, Munich, Germany, 2021, reference manual for MSC Patran pre- and post-processor software.

[116] ——, *MSC Nastran Reference Guide*, Munich, Germany, 2021, reference manual for MSC Nastran finite-element solver.

[117] N. Cascone, L. Caivano, G. D'Errico et R. Citarella, "Vibroacoustic assessment of an innovative composite material for the roof of a coupe car," *Applied Sciences*, vol. 11, p. 1128, 2021.

[118] P. B. Bornemann et F. Cirak, "A subdivision-based implementation of the hierarchical b-spline finite element method," *Computer Methods in Applied Mechanics and Engineering*, vol. 253, p. 584–598, 2012.

[119] X. Xie, S. Wang, Q. Xie, C. Liu, Y. Ren et A. Yang, "Topology optimization using immersed isogeometric analysis and its software implementation," *Computer Methods in Applied Mechanics and Engineering*, vol. 432, p. 117374, 2024.

Appendix A

Appendix. Simplified vehicle model geometry data

This section is dedicated to the description of the geometry shown in Figure 5.19. Figure A.1 provides the 2D view of the simplified vehicle model's structure, and Table A.1 lists the coordinates and their corresponding weights. To complete the structure, it is assumed that the thickness of the structure is set to 0.035 m, directed inward from the geometry shown in Figure A.1. Furthermore, after performing these operations, it is possible to extrude the structure along the z-axis (perpendicular to the xy plane) by a distance of 1.2 m. After defining the structure, it is possible to construct the acoustic cavity inside the structure. It should be emphasized that the information provided in Tables A.1, A.2, the thickness of the structure and the extrusion distance are sufficient to fully describe the geometry. The choice of the number of patches used to divide the structure and the cavity can be made by the user and does not influence the solution in any way. Further details can be found in vibroacoustic-iga-fem within the functions `Car_Structure` and `Car_Cavity`.

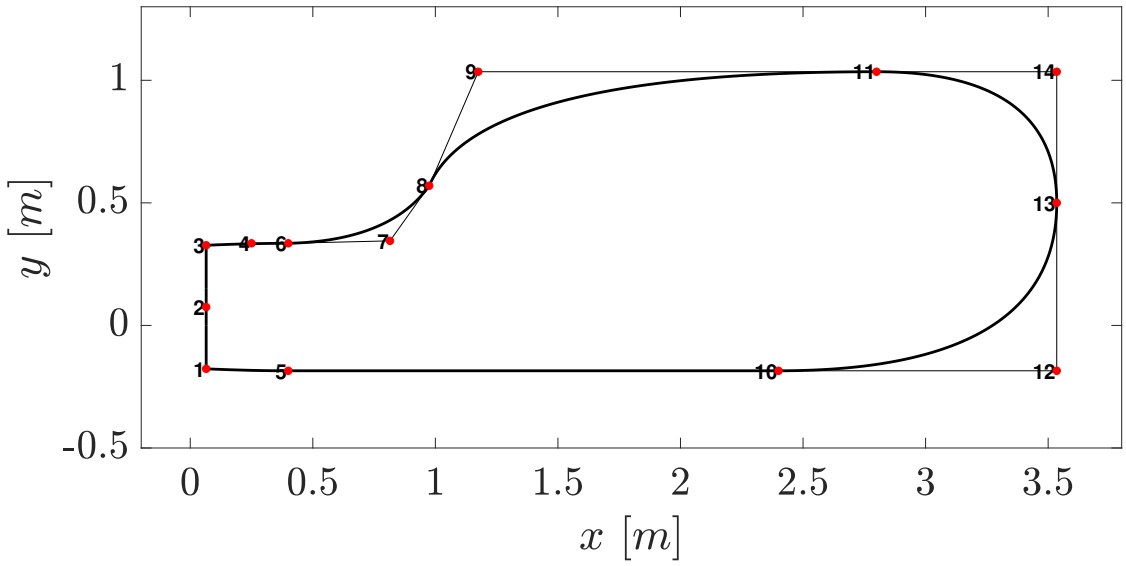

Figure A.1: 2D view for the simplified vehicle model geometry

Table A.1: Control points list and related weights

#Control points	x	y	weight	#Control points	x	y	weight
1	0.0650	-0.1770	1	8	0.9750	0.5700	1
2	0.0650	0.0750	1	9	1.1750	1.0350	1
3	0.0650	0.3270	1	10	2.4000	-0.1850	1
4	0.2500	0.3350	1	11	2.8000	1.0350	1
5	0.4000	-0.1850	1	12	3.5350	-0.1850	1
6	0.4000	0.3350	1	13	3.5350	0.5000	1
7	0.8150	0.3450	1	14	3.5350	1.0350	1

Table A.2: The B-Spline curves are constructed using 3 points. For the control points' numbering one must refer to Table A.1. The knot vector is {0 0 0 1 1 1} and p=2

B-Spline curve		
starting point	middle point	ending point
1	2	3
3	4	6
6	7	8
8	9	11
11	14	13
13	12	10
10	5	1

Appendix B

Appendix. Edge effect of Immersed IGA

The number of elements to split and the basis functions to be replaced depends on the edge effects. The number of elements to split is $[e_{stop} - p \leq e_{split} \leq e_{stop} + p]$. Indeed, the number of basis functions to be replaced changes and also depends on the current level.

For more details, see [118, 119].

Algorithm 7 Edge Effect Handling in Immersed IGA

procedure EDGEEFFECT(p, e_{split}, e_{stop}, $n_{\text{elem}}^{(l)}$, l)
  Determine the range of elements to split
  $e_{\text{split}} \in [\, e_{\text{stop}} - p,\ e_{\text{stop}} + p \,]$
  Compute number of basis functions to replace depending on level
  if $l = 0$ **then** ▷ Level 0
    if $e_{\text{split}} \leq p$ **and** $e_{\text{split}} \geq (n_{\text{elem}}^{(0)} - p)$ **then**
      Right: $n_{\text{right}} = p - (n_{\text{elem}}^{(0)} - e_{\text{split}})$
      Left: $n_{\text{left}} = p - e_{\text{split}} + 1$
    else if $e_{\text{split}} \leq p$ **and** $e_{\text{split}} < (n_{\text{elem}}^{(0)} - p)$ **then**
      Left: $n_{\text{left}} = p - e_{\text{split}} + 1$
    else if $e_{\text{split}} > p$ **and** $e_{\text{split}} \geq (n_{\text{elem}}^{(0)} - p)$ **then**
      Right: $n_{\text{right}} = p - (n_{\text{elem}}^{(0)} - e_{\text{split}})$
    end if
  else ▷ Levels higher than 0
    if $e_{\text{split}} \leq p$ **and** $e_{\text{split}} \geq (n_{\text{elem}}^{(l)} - p)$ **then**
      Right: $n_{\text{right}} = p - (n_{\text{elem}}^{(l)} - e_{\text{split}})$
      Left: $n_{\text{left}} = p - e_{\text{split}} + 1$
    else if $e_{\text{split}} \leq p$ **and** $e_{\text{split}} < (n_{\text{elem}}^{(l)} - p)$ **then**
      Left: $n_{\text{left}} = p - e_{\text{split}} + 1$
    else if $e_{\text{split}} > p$ **and** $e_{\text{split}} \geq (n_{\text{elem}}^{(l)} - p)$ **then**
      Right: $n_{\text{right}} = p - (n_{\text{elem}}^{(l)} - e_{\text{split}})$
    end if
  end if
  return $n_{\text{left}}, n_{\text{right}}$
end procedure

Appendix C

Contribution to the scientific community and attended conferences

C.1 Journal and conference publications

C.1.1 Journal articles

- R. Citarella, **T. Landi**, L. Caivano, G. D'Errico, F. Raffa, M. Romano, and E. Armentani, "Structural and Vibro-Acoustics Optimization of a Car Body Rear Part," *Applied Sciences*, vol. 13, p. 3552, 2023.

- **T. Landi**, C. Hoareau, J.-F. Deü, R. Ohayon, and R. Citarella, "Comparative Vibroacoustic Analyses: FEM vs. IGA," *Computational Mechanics*, vol. 75, pp. 2103–2122, 2025.

C.1.2 Conference papers

- T. Landi, C. Hoareau, J. Deü, R. Citarella and R. Ohayon, Projection Based Reduced Order Model of Elasto-Acoustic Vibrations Computed with Isogeometric Analyses, in: ECCOMAS 2024. URL: `https://www.scipedia.com/public/Landi_et_al_2024a`

- AIAS conference proceedings: on going

C.2 Participation in scientific events

Year	**Type**	**Event**	**Role**
Sept. 2023	Conference	AIAS Conf., Genova, Italy (*automotive* session)	Speaker
May 2024	Workshop	CSMA, Giens, France	Participant
June 2024	Conference	ECCOMAS Conf., Lisbon, Portugal (*innovative method for fluid-structure interaction* session)	Speaker
July 2024	Doctoral Shool	Isogeometric Analysis: Theory, Application and New Trends, Como, Italy	Remote Participant
Sept. 2024	Conference	AIAS Conf., Naples, Italy	Speaker
Febr. 2025	Workshop	AIAS Automotive workshop, Rome, Italy	Speaker
May. 2025	Conference	SURVISHNO Conf., Paris, France	Speaker
Sept. 2025	Conference	AIAS Conf., Florence, Italy (*automotive* session)	Speaker
Sept. 2025	Conference	IGA Conf., Eindhoven, Netherlands (*IGA for fluid structure interaction* session)	Speaker